Technische Universität München
TUM School of Engineering and Design

Objective Function Reformulation for Model Predictive Control of Electrical Drive Systems

Haotian Xie

Vollständiger Abdruck der von der TUM School of Engineering and Design der Technischen Universität München zur Erlangung des akademischen Grades eines

Doktors der Ingenieurwissenschaften

genehmigten Dissertation.

Vorsitz: Prof. Dr.-Ing. Markus Lienkamp
Prüfer der Dissertation:
1. Prof. Dr.-Ing. Dr. h.c. Ralph Kennel
2. Prof. Dr.-Ing. José Rodríguez Pérez

Die Dissertation wurde am 24.05.2022 bei der Technischen Universität München eingereicht und durch die TUM School of Engineering and Design am 21.12.2022 angenommen.

Acknowledgment

This dissertation is based on my doctoral project at the Chair of Electrical Drive Systems and Power Electronics (EAL), Technical University of Munich (TUM). My deepest gratitude goes first and foremost to my supervisor, Prof. Dr.-Ing. Ralph Kennel, for his guidance, support and encouragement throughout the whole doctoral project. In the past four years, I have not only learned fruitful academic knowledge but also broaden my horizon under the supervision of Prof. Kennel. His guidance enlightens me and shows me the direction. Without his support and encouragement, I can not overcome the obstacle and failures in the research. The proper freedom entrusted from him equipped me with the ability of independent working and efficient collaboration. The working experience at EAL will be a treasure for my life.

I would like to express my sincere gratitude to my mentor, Prof. Dr.-Ing. Fengxiang Wang. With his guidance and help, I understood the fundamental principle and conducted the experimental implementation at the very beginning of the doctoral project, which is very important for a beginner like me. I would like to show my sincere gratitude to Prof. Dr.-Ing. José Rodríguez. It is my great honor to coauthor several publications with Prof. Rodríguez. The detailed suggestions he shared with me really improve me a lot. I would also like to express my gratitude to Prof. Marcelo Heldwein for his support.

It is my pleasure to work with my colleagues at EAL. Eyke Liegmann and Darshan Manoharan are the leaders of MPC and sensorless team. I was inspired from the communication in the group meeting they organized. I feel grateful to Dr.-Ing. Julien Cordier for helping me familiar with our institute. I also appreciate the co-working experience with Dr.-Ing. Florian Bauer, Dr.-Ing. Mohamed Abdelrahem, Alexander Florian, Hannes Börngen, Stefan Klaß, etc. I really enjoy the excellent academic atmosphere, solid teamwork and cultural exchange in our institute. I appreciate the collaboration and support with the Chinese group: Prof. Dr.-Ing Zhenbin Zhang, Prof. Jianbo Gao, Dr.-Ing Xuezhu Mei, Dr.-Ing Xinbo Cai, Dr.-Ing Hui Sun, Wei Tian, Xiaonan Gao, Xicai Liu, Qing Chen, Yingjie He, Ying Tang, Lei Liu, Dehao Kong, Qifan Yang, Quan Zhang, Qi Li, Wei Zhang, Kunkun zuo, Shih-Wei Su, etc. The research and life experience with them will be an unforgettable memory for me. Many thanks to Heidi Jonas, Wolfgang Ebert, Dietmar Schuster and Anja Inzenhofer for their kindly help in the institute. I appreciate the co-working experiences with the Master students that I have supervised (Yao Zhang and Jianming Du), who have also helped me a lot. I would also like to appreciate the col-

laboration and friendship with Dr. Mateja Novak, Dr. Liming Yan, Qian Xun and Dongliang Ke.

Last but also the most sincere gratitude goes to my beloved parents. Thanks for their self-giving love, heartwarming encouragement and continuous support throughout my life, that grant me the courage to face the challenges. I would also like to give my thankful heart to my girlfriend for her love. Without them, I could hardly finish this work.

Munich, Germany in December 2021
Haotian Xie

Abstract

The dissertation aims at improving the control performance of finite control set model predictive control (FCS-MPC) for electrical drive systems. The main concept centers around the reformulation of the objective function as a set of easier optimization problems which can be solved efficiently, either in a sequential or concurrent manner.

In addition, the thesis presents a method using a derivative projection as well as an extended finite control set to improve the tracking performance of FCS-MPC in steady state and reduce the complexity of the control algorithm. The technique makes use of two voltage vectors instead of one in each sampling period. Moreover, thanks to a performant gradient descent, finding the minima of the objective function in the FCS-MPC scheme only requires a few steps, as a convex quadratic programming (QP) problem is considered.

Finally, the benefits of the proposed FCS-MPC method to encoderless drive control are investigated.

Kurzfassung

Die vorliegende Dissertation hat zum Ziel, die Performanz der direkten modellprädiktiven Regelung mit Finite Control Set (FCS-MPC) für elektrische Antriebssysteme zu erhöhen. Der Hauptansatz beruht auf der Umformulierung der Kostenfunktion als Satz einfacherer Optimierungsprobleme, die sich sequenziell oder gleichzeitig effizient lösen lassen.

Darüber hinaus stellt die Arbeit eine Methode zur Erhöhung der Regelgenauigkeit von FCS-MPC-Algorithmen vor, welche sich eine ableitungsbasierte Projektion sowie eine Erweiterung des Finite Control Sets zunutze macht. Das Verfahren verwendet, in jeder Abtastperiode, zwei Spannungszeiger anstelle von einem. Des Weiteren lassen sich die Minima der Kostenfunktion mithilfe eines effizienten Gradientenverfahrens in wenigen Schritten finden, da ein konvexes quadratisches Problem betrachtet wird.

Schließlich werden die Vorteile der vorgeschlagenen FCS-MPC-Methode für die geberlose Antriebsregelung untersucht.

Contents

CHAPTER 1

Introduction

This work focuses on the objective function reformulation for the model predictive control strategies of electrical drive system. The background, research motivation and the contribution of this dissertation are introduced in this chapter. Firstly, the electrical drives are introduced along with their industrial applications. The introduction of conventional control strategies for electrical drives, e.g., direct torque control (DTC) and field oriented control (FOC), as well as model predictive control (MPC) are summarized. Based on the research motivation, the contribution of the following chapters have been also summarized in the end of this chapter.

1.1 Background

1.1.1 DC and AC drive systems

Direct current (DC) machines and alternating current (AC) machines are the two mainstream categories in the family of electric machines [1]. The DC machines convert electrical energy into mechanical energy. The operating mechanism of DC machines centers around Faraday's principle that a conductor with current flow placed in a magnetic filed experiences a mechanical force. Based on the Fleming's "Left hand rule" that the motion of the conductor is in a direction perpendicular to the current flow and magnetic field, the pertinent conductors are forced to rotate in the stator magnetic field as the direction of current flow in the armature coils is reversed by the commutators and brushes [2]. However, such construction of commutator and brush results in the inherent drawbacks in the DC machines. The presence of commutator and brush not only increases the size and weight of the DC machines, restricts the capability of speed control, but also requires a higher maintenance cost due to the degraded safety. The AC machines mainly include asynchronous machines (induction machines, as shown in Fig. 1.1) and synchronous machines [3]. The operating principle of the induction machine (IM) is based on the electromagnetic induction between the rotor and the stator. The stator winding is connected to the AC power supply, and the rotor winding is short-circuited (in the squirrel-cage

machines) to generate the current flow and electromagnetic torque. Due to the absence of both the commutator and the brush, IM has the advantages of rugged construction, high efficiency, the ability to work in the harsh environment and so on. It is noteworthy that the rotation speed is slightly lower than the synchronous speed of IM. The featured applications of IM are lifts, cranes, household appliances, oil extraction and textile industries. Another category of AC machines is synchronous machine. The operating of a synchronous machine depends on the interaction of the magnetic field of the stator with that of the rotor. Although the synchronous machines require the measurements for start-up and synchronizing, it achieves the merits of higher power efficiency and higher torque density, which is most-frequently employed for the applications with constant speed, such as dc generators, electrical vehicles, centrifugal pumps and compressors.

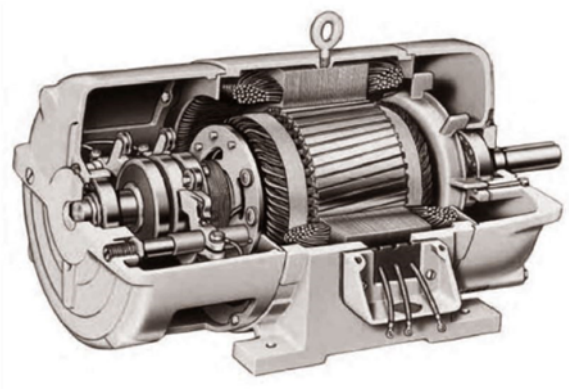

Figure 1.1: Induction machine (source: https://www.theengineeringprojects.com).

1.1.2 Control strategies for AC drives

1.1.2.1 Field oriented control (FOC)

FOC was firstly proposed by Hasse and Blaschke in the 1970s [4]. The concept is raised for solving the problem that flux and torque cannot be controlled independently in the AC machines. The stator current, which contains the coupled information of the exciting and armature current, can be represented as a vector with two orthogonal components. The decoupling is achieved by the decomposition of the vector [5]. One component, defines the magnitude of flux, while the other defines the torque. By doing so, the AC machine can be controlled by the similar method of a separately excited DC machine. The stator current is transformed from the two-phase stationary coordinate frame through Park transformation and the stator voltage is transformed from the three-phase stationary coordinate frame through the Clarke transformation, to project on the two-phase rotation coordinate frame. The torque and flux are indirectly controlled by the decoupled components of the stator current in FOC, to yield a better control performance of AC machines. However, the current and speed are regulated by the PI controllers in a cascaded structure. The dynamic response of FOC is restricted by the bandwidth of the inner-loop proportional-integral (PI) controller and the modulation stage.

1.1.2.2 Direct control with a look-up table

DTC was introduced by Takahashi and Noguchi in the 1980s, to control the torque and flux by directly applying the switching sequences in the inverter [6]. Accuracy and fast control of flux and torque can be achieved in DTC without the complex algorithm for coordinate transformation. Due to its intuitive concept and simple implementation, DTC has attracted increasingly attention in both academic and industrial communities [7]. More specifically, DTC shows less sensitivity against the parameter variations in the system model that only the knowledge or stator resistance is required. The selection of the vector is based on assigned region in the look-up table (LUT). Although DTC has the merits of quick dynamic response and low switching frequency, it still suffers from the drawback of large ripple at the steady state, especially in the scenario of a low speed range. To tackle the issue, DTC combined with a space vector modulation (SVM) algorithm is regarded as a promising solution.

1.1.2.3 Model predictive control

Arisen from the control of process industries in the 1970s, model predictive control (MPC) aims to solve an online optimization problem for a control system with constraints [8, 9]. The main concept of MPC centers around resolving the optimal solution by predicting the future behavior of the control plant in a receding horizon [10, 11]. As illustrated in Fig. 1.2, the action of the controller is based on the state of the control plant. MPC was first applied in the linear control system with slow dynamics, e.g., petroleum extraction and refining, chemical industry, supply chain management, control of energy efficiency in building and water treatment in urban [12]. The reason for this is the huge computational task can be allowed to be carried out in a long control period [13]. Thanks to the tremendous development of the digital controllers, i.e., digital signal processor (DSP), field-programmable-gate-array (FPGA) and dSPACE, the computational capability of the controller has been increased more than 100 times in the last three decades [14]. Therefore, the applications of MPC can be extended to the control of power electronics and electrical drive systems [15–17], as shown in Fig. 1.3.

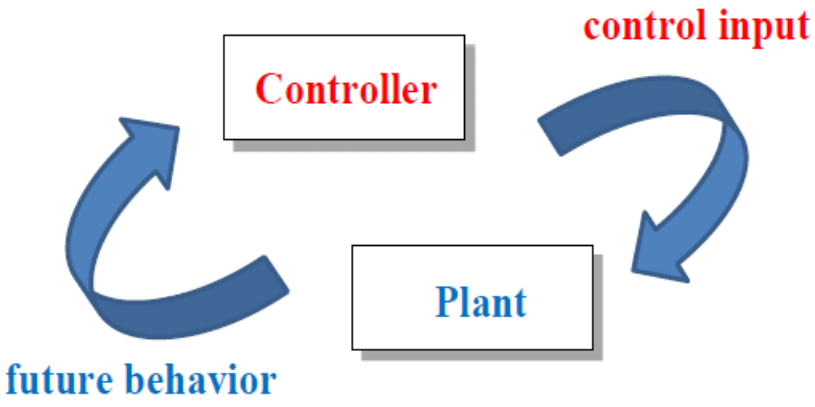

Figure 1.2: The close-loop structure of MPC.

To tackle the issue of high computational burden in MPC, an explicit MPC is proposed in 2002, to solve the multi-objective optimization problem with an offline method [18]. However, the offline computational complexity increases drastically when the scale of the NP-hard

problem increases, which leads to the exponential growth in the number of regions. In 2007, a MPC strategy with a finite control set (FCS) solution is proposed to control a voltage source inverter (VSI) [19]. Since that, finite control set MPC (FCS-MPC) has become one of the most frequently-used MPC strategy, and has been extensively investigated in the applications of power electronics and electrical drive systems [20]. In FCS-MPC, the objective function is formulated and determined according to the type of the control variables to be optimized. Thus, the control inputs are exhaustively searched to find the optimal solution for the objective function [21].

Based on the trend and research status of MPC, the existing problem that MPC suffers from, has become a major concern for further performance improvement [22]. First, MPC is still penalized by the high computational complexity, especially for the implementations with a longer prediction horizon. Moreover, the number of searched control inputs increases as the control plant is a multi-level or multiple-phase power converter. Second, the scale of the multi-objective optimization problem is larger when the additional constraints or specific system demands are taken into consideration. It is noteworthy that the relationship among the different control variables should be carefully dealt with in the objective function. Third, as a model-based controller, the control performance of MPC will be inevitably influenced by the parameter variations in the control system. Therefore, the robustness improvement against parameter mismatches is still an open discussion for MPC [23].

(a) source: https://www.thyssenkrupp-industrial-solutions.com/

(b) source: https://www.utwente.nl/en/news/2021/6/1095055/

(c) source: https://www.autonomousvehicleinternational.com

Figure 1.3: The applications of MPC.

1.2 Research motivations

The research motivations of MPC for the applications of electrical drive systems are summarized in this section. This work mainly focuses on the optimization problem underlying FCS-MPC strategies for electrical drives, especially the implementation on the IMs as a case study. In FCS-MPC, all the contol inputs are exhaustively searched to find the optimal solution in the optimization stage, while only one vector is executed in the whole sampling period. Moreover, the objective function aims to minimize the tracking deviations of the different control variables, e.g., torque, flux, current and speed. Problem formulation of FCS-MPC is summarized as follows.

1.2.1 Regulation principle among the control variables

The most attractive feature of FCS-MPC lies in its ability to handle flexible constraints and specific system demands. The constraints are explicitly incorporated in the online optimization problem when they are flexibly included in the objective function. More specifically, the control variables are determined by the specific demands in the varied applications. Although FCS-MPC shows its superiority in dealing with complicated control systems incorporated with constraints, the multiple control targets are conflicted in the optimization process of the objective function. Normally, the trial-and-error weighting parameters are introduced to modify the relationship among the control variables. However, they are not easy to be fine-tuned. The regulation principle among the control variables in the objective function should be further investigated.

1.2.2 Computational burden reduction

The high computational complexity is an inherent drawback of FCS-MPC along with its development. The FCS-MPC strategies, search all the possible control inputs in an enumeration-based approach, to find to optimal solution for the online optimization problem. In the implementations of simple control system, the issue can be mitigated by the advanced digital

controllers. However, the number of control inputs increases when the control system is more complicated, i.e., for the multi-level converters or multi-phase motor drives. Specifically, the algorithm complexity grows exponentially with an increased number of prediction horizon. Although lots of computationally efficient FCS-MPC algorithms have been proposed in the literature review, how to realize the trade-off among the feasible set, computational burden and control performance of FCS-MPC, is still an open issue.

1.2.3 Performance improvement at the steady state

Compared with the counterpart FOC strategy, FCS-MPC has the merits of fast dynamic response and relatively lower switching frequency. However, only one control input is carried out in the entire sampling period, which leads to the unsatisfactory control performance at the steady state, i.e., higher torque and current ripples in the electrical machine drives. Another reason relates to this is the varied switching frequency in FCS-MPC. Therefore, a potential research trend for FCS-MPC is to improve the steady-state performance while retains the fast dynamic response.

1.2.4 Robustness improvement against parameter mismatches

The dynamic model of the control plant is employed in the prediction stage of FCS-MPC, to predict the future behavior of the control system. As the parameter variation occurs in the system model, it will inevitably leads to the error of the predicted value and deteriorated control performance of the controller. To cope with this issue, the observer-based technologies should be applied in FCS-MPC for robustness improvement.

1.3 Main work of this thesis

The main work of this thesis is to solve the aforementional issues in the optimization problem underlying FCS-MPC for the applications of power electronics and electrical drive systems. Following the description of the control plant, problem formulation of FCS-MPC is investigated. The FCS-MPC algorithms with single control objective and multi-objective are experimentally verified on the lab-constructed platform. Several regulation principles are evaluated in the multi-objective FCS-MPC, to tackle the issue of weighting parameters tuning.

Furthermore, the objective function is reformulated to improve the steady-state performance of FCS-MPC. The optimization problem underlying FCS-MPC is regarded as a quadratic programming (QP) problem, to be solved by a gradient descent solution. Moreover, the extension of the feasible set, iterative algorithms and computationally efficient solutions are investigated.

The encoderless technology for FCS-MPC is also presented, for the elimination of an encoder as well as robustness improvement against parameter mismatches. The MRAS estimator is implemented in the constrained parallel structure FCS-MPC as a case study.

CHAPTER 2

Description of the control plant

In this chapter, the control plant description for the MPC schemes is presented. As a case study, the squirrel-cage induction machines (IMs) fed by a two-level voltage source inverter (2-L VSI) are introduced in this work. The mathematical model of the induction machine is derived, followed by the principles of coordinate transformations. Afterwards, the topology of a 2-L VSI as well as its discrete vectors are described.

2.1 Mathematical modelling of IM

The dynamic model of the squirrel-cage IM is described in the following equations (2.1-2.5) using the stationary $\alpha\beta$ frame.

$$\boldsymbol{u}_{s\alpha,\beta} = R_s \cdot \boldsymbol{i}_{s\alpha,\beta} + \frac{d\boldsymbol{\psi}_{s\alpha,\beta}}{dt} \tag{2.1}$$

$$0 = R_r \cdot \boldsymbol{i}_{r\alpha,\beta} + \frac{d\boldsymbol{\psi}_{r\alpha,\beta}}{dt} - j \cdot \omega \cdot \boldsymbol{\psi}_{r\alpha,\beta} \tag{2.2}$$

$$\boldsymbol{\psi}_{s\alpha,\beta} = L_s \cdot \boldsymbol{i}_{s\alpha,\beta} + L_m \cdot \boldsymbol{i}_{r\alpha,\beta} \tag{2.3}$$

$$\boldsymbol{\psi}_{r\alpha,\beta} = L_m \cdot \boldsymbol{i}_{s\alpha,\beta} + L_r \cdot \boldsymbol{i}_{r\alpha,\beta} \tag{2.4}$$

$$T_e = \frac{3}{2} p \cdot \mathit{Im}\left\{\boldsymbol{\psi}_s^* \cdot \boldsymbol{i}_s\right\} \tag{2.5}$$

where $\boldsymbol{u}_{s\alpha,\beta}$ denotes the stator voltage vector, $\boldsymbol{i}_{s\alpha,\beta}$ and $\boldsymbol{i}_{r\alpha,\beta}$ are the stator and rotor currents, respectively. L_s, L_r and L_m are the stator, rotor and magnetizing inductances, and $\boldsymbol{\psi}_{s\alpha,\beta}$ and $\boldsymbol{\psi}_{r\alpha,\beta}$ are the stator and rotor flux-linkages, respectively. R_s and R_r are the equivalent stator and rotor resistances, p denotes the number of pole pairs and ω is the electrical angular speed. It is noteworthy that the rotor winding is short circuited in the squirrel-cage IMs. Thereby, the rotor voltage $\boldsymbol{u}_{r\alpha,\beta}$ in (2.2) is zero.

For the number of pole pairs p = 1, the relationship between the electromagnetic torque and the derivative of the rotor speed can be expressed as

$$J\frac{d\omega}{dt} = T_e - T_L \tag{2.6}$$

where J is the moment of inertia and T_L represents the load torque.

Assuming that the control system is linear time-invariant, we consider that $\boldsymbol{\psi}_{s\alpha,\beta}$ and $\boldsymbol{\psi}_{r\alpha,\beta}$ are the control variables and $\boldsymbol{u}_{s\alpha,\beta}$ is the control input, the dynamic model of IM can be converted to the space-state model, as shown in (2.7-2.8)

$$\frac{d\boldsymbol{\psi}_{s\alpha,\beta}}{dt} = \boldsymbol{u}_{s\alpha,\beta} - R_s \cdot \boldsymbol{i}_{s\alpha,\beta} \tag{2.7}$$

$$\frac{d\boldsymbol{\psi}_{r\alpha,\beta}}{dt} = -R_r \cdot \boldsymbol{i}_{r\alpha,\beta} + j \cdot \omega \cdot \boldsymbol{\psi}_{r\alpha,\beta} \tag{2.8}$$

where $\boldsymbol{i}_{s\alpha,\beta}$ and $\boldsymbol{i}_{r\alpha,\beta}$ can be substituted by the control variables in (2.3-2.4).

2.2 Three-phase two-level voltage source inverter

The topology of a three-phase two-level voltage source inverter (2-L VSI) is shown in Fig. 2.1(a). The dc-link voltage of the 2-L VSI is defined by $\boldsymbol{u}_{DC}$. S_a, S_b and S_c represent the signal of power devices in the upper side of the bridge configuration. S_a, S_b and S_c = 1 means the corresponding power device turns on, while S_a, S_b and S_c = 0 means the corresponding power device turns off. Therefore, the voltage vector can be calculated by (2.9).

$$\boldsymbol{u} = \frac{2}{3}U_{DC}(\mathrm{S}_a\text{+}a \cdot S_b\text{+}a^2 \cdot S_c) \tag{2.9}$$

where $a = e^{j\frac{2\pi}{3}}$, $\boldsymbol{u}_{s\alpha,\beta}$ is the applied voltage vector, $\boldsymbol{u}_i = S_i \cdot \boldsymbol{u}_{DC}$, $i = a, b, c$. Based on the above, the combinations of the discrete control set for the 2-L VSI are shown in Fig. 2.1(b). As can be understood, there are six discrete voltage vectors $(u_1 - u_6)$ and two zero vectors (u_0, u_7).

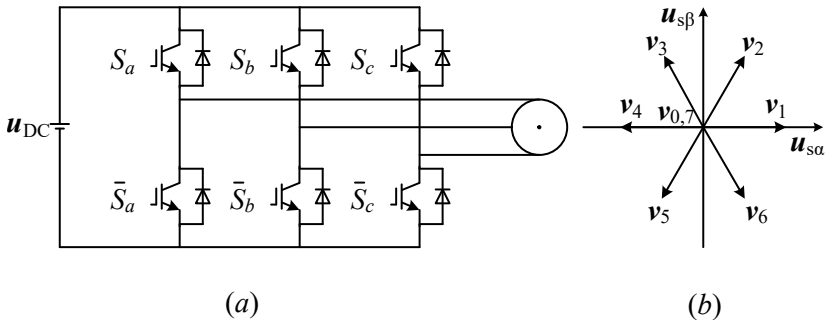

(*a*) (*b*)

Figure 2.1: 2-level voltage source inverter. (a) the topology. (b) the generated voltage vectors.

2.3 Principles of coordinate transformations

As can be seen, the state-space model of IM is built in the stationary $\alpha\beta$ frame, while the voltage vectors in the abc-frame is generated in the 2-L VSI. To cope with this issue, the principles of coordinate transformations i.e., Clarke transformation, is proposed. The description of the Clarke transformation is shown in Fig. 2.2. The stationary $\alpha\beta$ frame is represented by the black lines, while the abc-frame is described by the red dashed lines.

Therefore, we use matrix K to transform the voltage vectors in the abc-frame to that in the stationary $\alpha\beta$ frame, through Clarke transformation in (2.10).

$$\boldsymbol{u}_{\alpha,\beta} = K\boldsymbol{u}_{abc} \tag{2.10}$$

$$K = \frac{2}{3} \cdot \begin{bmatrix} 1 & -\frac{1}{2} & -\frac{1}{2} \\ 0 & \frac{\sqrt{3}}{2} & -\frac{\sqrt{3}}{2} \end{bmatrix} \tag{2.11}$$

To transform the voltage vectors $(\boldsymbol{u}_{dq})$ in the rotation dq frame to that $(\boldsymbol{u}_{\alpha,\beta})$ in the stationary $\alpha\beta$ frame, the Park transformation is applied by using $K(\theta)$, as shown in (2.12)

$$\boldsymbol{u}_{dq} = K(\theta)\boldsymbol{u}_{\alpha,\beta} \tag{2.12}$$

$$K(\theta) = \frac{2}{3} \cdot \begin{bmatrix} cos(\theta) & sin(\theta) \\ -sin(\theta) & cos(\theta) \end{bmatrix} \tag{2.13}$$

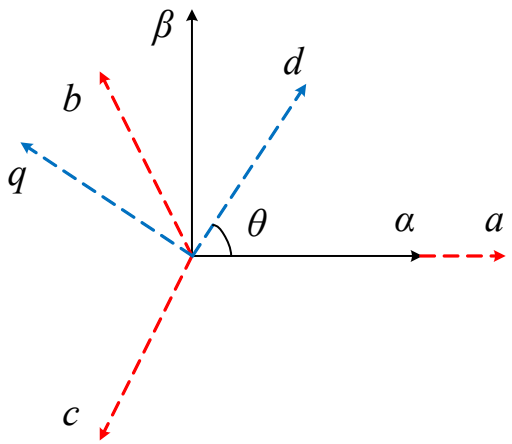

Figure 2.2: Description of coordinate transformations. (black lines denote the stationary $\alpha\beta$ frame, red dashed lines denote the abc-frame, blue dashed lines represent the rotation dq frame.

2.4 Lab-constructed testbench and real-time control system

In this section, the lab-constructed testbench and the real-time control system are introduced. The description of the experimental platform is shown in Fig. 2.3. The lab-constructed experimental platform is consisted of a 3.0 kW Danfoss VT-302 inverter with a control panel, a

14 kVA IGBT-based Servostar620 inverter, 1.4 GHz Linux-based real-time control system and two 2.2 kW squirrel-cage IMs. The dc-link voltage u_{DC} is 582 V and the low-voltage power supply for the gate drive and control board is 24 V. The high-performance controller can be operated with a sampling frequency ranges from 5 kHz to 48 kHz, to achieve a competitive control performance. A 1024-point incremental encoder is employed for the measurement of rotor position. The parameters of the IMs are illustrated in TABLE 2.1.

Figure 2.3: Description of the lab-constructed testbench and real-time control system (A) 3.0 kW Danfoss VT-302 inverter for load machine (B) 14 kVA IGBT-based Servostar620 inverter for main machine (C) Control panel (D) 1.4 GHz Linux-based real time controller (E) Main machine (F) Load machine.

Table 2.1: The parameters of the IMs

Parameters	Values
dc-link voltage $\boldsymbol{u}_{dc}[V]$	582
stator resistance R_s $[\Omega]$	2.68
rotor resistance R_r $[\Omega]$	2.13
magnetizing inductance L_m [H]	0.275
stator inductance L_s [H]	0.283
rotor inductance L_r [H]	0.283
number of pole pairs $P[/]$	1
norminal rotor speed ω_{nom} [rad/s]	290
nominal flux ψ_{nom} [Wb]	0.71
norminal torque T_{nom} [Nm]	7.5
moment of inertia J [kg $\cdot m^2$]	0.005

CHAPTER 3

MPC problem formulation

The MPC problem formulation is introduced in this chapter. First, a brief instruction as well as the classification of MPC problem is proposed. Following, the optimization problem underlying MPC with finite control set (FCS) in the electrical drive systems, is presented. To solve the MPC problem from a mathematical perspective, a geometric description of the MPC problem is derived.

3.1 Classification of MPC problem

The evolution of MPC (also referred as to "receding horizon control") is revisited in this section. MPC has been firstly proposed in the 1970s, to solve the optimization problem in the control system with slow dynamic, i.e., process industry. With the tremendous development of the commercial digital controllers (such as DPS, FPGA and dSPACE), MPC has extended its applications to power electronics and electrical drive systems [24]. It is one of the mainstream categories of predictive control, the other two are hysteresis-based predictive control and trajectory-based predictive control. The future behavior of MPC is predicted based on the model of the control plant, combined with the past state and the control input in the future [25]. The concept of MPC is similar to that of Kalman filter rather than the abovementioned predictive controller. Thereby, MPC resolves the optimal solution by evaluating a customized objective function over a receding horizon. The block diagram of MPC is shown in Fig. 3.1, which consists of the control plant and its model, the prediction stage and the optimization stage.

In the MPC family, the schemes can be categorized as follows: explicit MPC, continuous control set MPC (CCS-MPC) and finite control set MPC (FCS-MPC) [26]. Explicit MPC has been proposed by Bemporad $etal$ in 2002, to offline solve a multi-parametric programming problem [18]. The control inputs are piecewise affine in the state space which is divided into several regions. A feedback control law is designed, to solve the desired control inputs which are piecewise affine (PWA) in the state space with divided regions. However, the computational

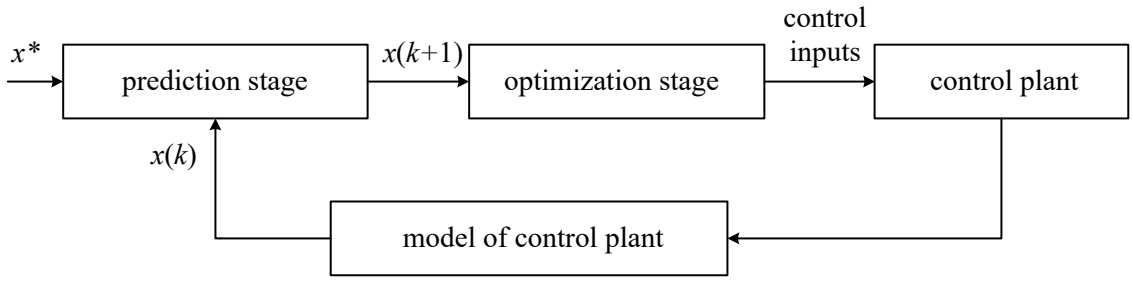

Figure 3.1: Block diagram of MPC.

burden as well as the memory requirement of the controller suffer from an exponential growth, with the increased scale of the optimization problem. Regarding the features of controlling a power converter or an electrical drive system, CCS-MPC and FCS-MPC has been extensively investigated for decades. The former CCS-MPC schemes require an additional modulation stage, to generate the applied voltage vectors with their corresponding duty cycles. Therefore, CCS-MPC has a fixed switching frequency and resolve the solution in a continuous control set. The latter FCS-MPC schemes bypass the modulation stage, directly apply the discrete voltage vectors by the optimization of the objective function with a minimum value. The switching frequency of FCS-MPC is varied and its control set is discrete. The main concepts of CCS-MPC and FCS-MPC schemes are shown in Fig. 3.2.

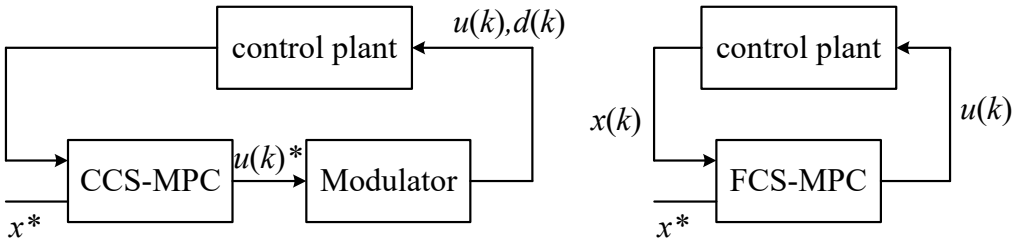

(a) CCS-MPC (b) FCS-MPC

Figure 3.2: The concepts of CCS-MPC and FCS-MPC schemes.

3.2 Optimization problem underlying FCS-MPC

As a mainstream category in the MPC family, FCS-MPC has become a predominant control strategy for the electrical drive systems, due to the discrete nature of the inverter. Compared with the counterpart CCS-MPC, FCS-MPC does not require any modulators. FCS-MPC has the merits of simple concept, straightforward implementation, fast dynamic response and flexible inclusion of constraints. The main concept of FCS-MPC centers around evaluating the future behavior of the control plant by the optimization of the formulated objective function with the predicted control variables. FCS-MPC is consist of the prediction stage and the optimization stage, which are explained in detail as follows.

3.2.1 Prediction stage

3.2.1.1 Forward Euler discretization

In the prediction stage, the predicted control variable in the next interval $x(k+1)$ can be calculated by the known information, i.e., the control variable in the current interval $x(k)$ and the applied switching sequence $u(k)$. The space-state model of the control plant in (2.7-2.8) can be rewritten as

$$\frac{dx(k)}{dt} = Ax(k) + Bu(k) \tag{3.1}$$

where the matrices A, B are the parameters of the control plant. The first-order forward Euler discretization is applied to calculate the predicted control variable $x(k+1)$

$$\frac{dx(k)}{dt} = \frac{x(k+1) - x(k)}{T_s} \tag{3.2}$$

$$x(k+1) = (AT_s + I)x(k) + BT_s u(k) \tag{3.3}$$

where T_s is the sampling period, I is the identity matrix. Similarly, the predicted control variable in the $k+h$ interval can be obtained in (3.4) for the FCS-MPC schemes with a longer prediction horizon h.

$$x(k+h) = (AT_s + I)x(k+h-1) + BT_s u(k+h-1) \tag{3.4}$$

3.2.1.2 Time-delay compensation

It is noteworthy that not merely the prediction of the control variables but also the optimization for every switching sequence are time-consuming in the real-time implementations [27]. To address this issue, a compensation strategy for time-delay is proposed for the FCS-MPC schemes. For FCS-MPC with a prediction horizon of 1 (h = 1), the predicted control variable in $k+2$ interval is calculated and to be optimized.

$$x(k+2) = (AT_s + I)x(k+1) + BT_s u(k+1) \tag{3.5}$$

where $x(k+1)$ is obtained in (3.3), $u(k+1)$ is the switching sequence in $k+1$ interval. The description of time-delay compensation is illustrated in Fig. 3.3. As shown in Fig. 3.3(a), the control variable $x(k-1)$ and are measured at the same time ($k-1$ interval) in the idealized implementation. Therefore, the optimal solution $u(k)$ can be obtained at k interval. However, we still require computational effort for optimization in the real-time implementation. By doing so, the optimal solution $u(k)$ will be obtained at $k+1$ interval. To cope with this issue, a time-delay compensation strategy is proposed. As shown in Fig. 3.3(b), $u[(k)|(k-1)]$ denotes the optimal solution for k interval which is obtained at $k-1$ interval. As can be understood, $x(k)$ is predicted with the known information $x(k-1)$ and $u[(k)|(k-1)]$ between $k-1$ to k. Afterwards, $x(k+1)$ is predicted and optimized between k to $k+1$. Therefore, the optimal solution $u[(k+1)|(k)]$ can be applied at $k+1$ interval.

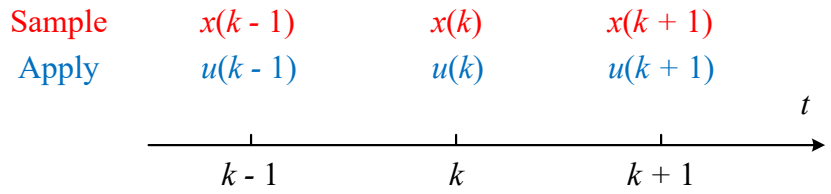

(a) Idealized implementation

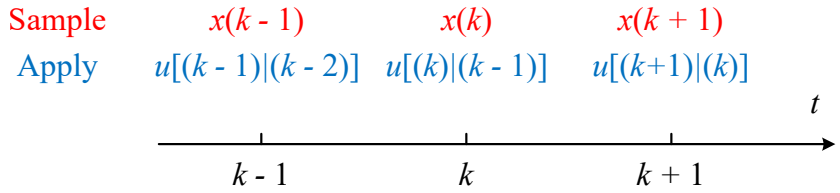

(b) With time-dealy compensation

Figure 3.3: Description of time-delay compensation.

3.2.2 Optimization stage

To evaluate the future behavior of the control plant, a customized objective function is formulated in the optimization stage. As we can understand, the objective function is designed according to the specific requirements of the control system. As shown in Fig. 3.4, the multiple control targets of the control system includes the core control targets, specific system demands and the physical constraints.

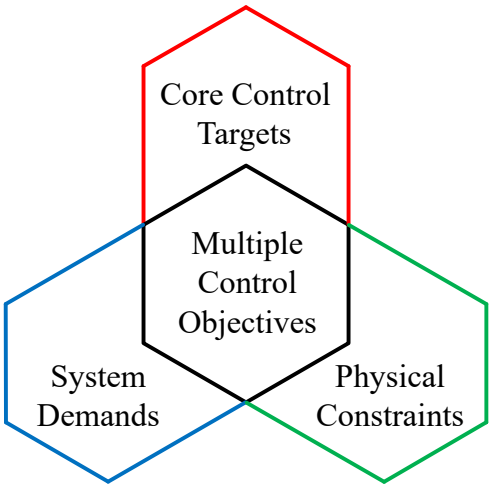

Figure 3.4: Multiple control targets of the control system.

(1) *Core control targets*: The core control targets are the predominate terms in the objective function, which determine the control performance of the control system. Classified by dimension of the core control targets, the the number of core control targets can be one (single control target), or more than one (multiple control targets). It should be mentioned that the multiple control targets require the weighting parameters to modify their importance in the objective

function. Considering the control plant is the IM drives as a case study, the core control targets can be torque, stator flux, stator current, rotor speed and so on.
(2) *Specific system demands*: The specific system demands are regarded as the soft constraints of the control plant, which are also penalized in the objective function. The system demands included in the objective function are flexible, according to the different type of control plant. For instance, the switching frequency is specifically concerned in the power converters applications, to avoid a high switching frequency. In the applications of multilevel converters, the neural-point voltage is regarded as the specific system demand for voltage balancing.
(3) *Physical constraints*: Apart from the soft constraints (specific system demands), the physical constraints (hard constraints) are handling in the objective function. The most frequently-used physical constraint in the applications of the power converters is the limitation of current magnitude. The physical constraints must be satisfied when the optimal solution is selected. Otherwise, the control system does not work or breakdown, due to the severe failure.

Based on the above, the objective function of FCS-MPC can be formulated as:

$$g_j = \lambda_{x1}\left[x_1^* - x_1(k+2)_j\right]^2 + \lambda_{x2}\left[x_2^* - x_2(k+2)_j\right]^2 + \cdots + \lambda_{x(l+m)}\left[x_{(l+m)}^* - x_{(l+m)}(k+2)_j\right]^2 + F_1(k+2)_j + F_2(k+2)_j + \cdots + F_n(k+2)_j \tag{3.6}$$

$$F_i(k+2)_j = \begin{cases} 0, & \textit{if } |x_{l+m+i}(k+2)_j| \leq |x_{l+m+i_{max}}| \\ \infty, & \textit{if } |x_{l+m+i}(k+2)_j| > |x_{l+m+i_{max}}| \end{cases} \tag{3.7}$$

where x_1, $x_2 \cdots x_l$ are the core control targets, x_{l+1}, $x_{l+2} \cdots x_{l+m}$ are the system demands, x_{l+m+1}, $x_{l+m+2} \cdots x_{l+m+n}$ are the physical constraints, λ_{x1}, $\lambda_{x2} \cdots \lambda_{x(l+m)}$ are their corresponding weighting parameters, F_1, $F_2 \cdots F_n$ are the physical constraint functions, l, m and n are integers. * denotes the reference trajectory, j is the applied switching state, $j \in 0, 1, \ldots, 6$.

In this work, the FCS-MPC schemes are applied for controlling the IM drives as a case study. The formulated objective functions are designed as follows

$$g_j = \left[T^* - \hat{T}(k+2)_j\right]^2 + \lambda_\psi^2 \cdot \left[\, \| \boldsymbol{\psi}_s^* \| - \| \hat{\boldsymbol{\psi}}_s(k+2)_j \| \,\right]^2 + \lambda_{sw}^2 \cdot n_{sw}^2 \quad + Im(k+2)_j \tag{3.8}$$

$$I_m(k+2)_j = \begin{cases} 0, & \textit{if } |\boldsymbol{i}_s(k+2)_j| \leq |\boldsymbol{i}_{smax}| \\ \infty, & \textit{if } |\boldsymbol{i}_s(k+2)_j| > |\boldsymbol{i}_{smax}| \end{cases} \tag{3.9}$$

when the torque and stator flux are regarded as the core control targets. λ_ψ and λ_{sw} are the weighting parameters, n_{sw} is the number of switching, $Im(k+2)$ is the current limitation term, i_{smax} is the maximum value of stator current magnitude. The objective function of FCS-MPC is formulated in (3.10)

$$g_j = [(\boldsymbol{i}_{s\alpha}(k+2)^* - \boldsymbol{i}_{s\alpha}(k+2)_j)^2 + (\boldsymbol{i}_{s\beta}(k+2)^* - \boldsymbol{i}_{s\beta}(k+2)_j)^2] + \lambda_{sw} \cdot {n_{sw}}^2 + Im(k+2)_j \tag{3.10}$$

when the stator current is considered as the core control target.

3.3 Geometric description of FCS-MPC problem

In this section, the FCS-MPC problem is described from a geometric perspective. As can be understood, the optimization problem underlying FCS-MPC aims to search the optimal control input, which minimizes the tracking deviation of the control variable between its predicted and reference value. As shown in Fig. 3.5, the orthogonal components of control variable x in the stationary $\alpha\beta$ frame are displayed. The black points $(x_\alpha(k), x_\beta(k))$, $(x_\alpha(k+2), x_\beta(k+2))$ and (x_α^*, x_β^*) represent the control variable at k and $k+2$ interval as well as its reference value, the red dashed lines $d(k)$ and $d(k+2)$ denote the distance of the control variable between its predicted and reference value at k and $k+2$ interval.

From a geometric perspective, the tracking deviation of the control variable is regarded as the quadratic Euclidean norm of the distance $d(k+2)$ between x^* and $x(k+2)$. Therefore, the optimization problem underlying FCS-MPC is converted to find the solutions that geometrically reduce the distance $d(k+2)$.

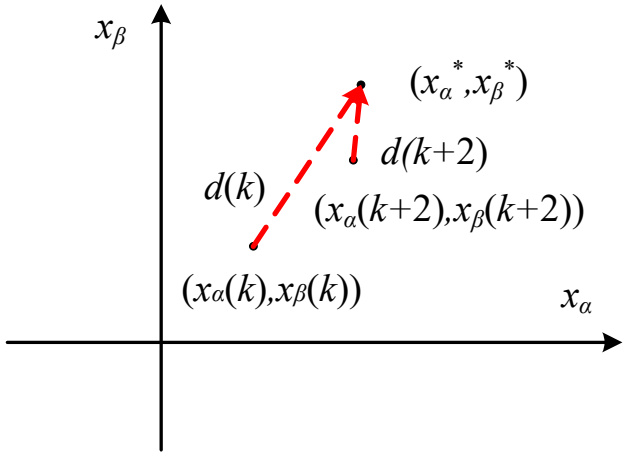

Figure 3.5: Geometric description of the FCS-MPC optimization problem

$$f(k+2) = ||d(k+2)||_2^2 = [x_\alpha^* - x_\alpha(k+2)]^2 + [x_\beta^* - x_\beta(k+2)]^2 \tag{3.11}$$

CHAPTER 4

Multi-objective FCS-MPC schemes

In this chapter, the principle of the multi-objective FCS-MPC schemes for IM drives are introduced. We focus on the two predominant schemes: finite control set predictive torque control (FCS-PTC) and finite control set predictive current control (FCS-PCC). Following, the differences between the control variables in the two schemes are investigated in detail. The control performance of FCS-PTC and FCS-PCC at both the steady state and transient state are experimentally validated. Moreover, an experimental assessment is conducted to evaluate the advantages of the two proposed multi-objective FCS-MPC schemes.

4.1 Principle of FCS-PTC

The electrical drive systems in the traction applications (e.g., railway applications, electrical vehicles) raise special concern on the torque performance [28]. The main control objectives in the abovementioned applications are electromagnetic torque and stator flux-linkage [29]. Therefore, the tracking deviations of torque and stator flux-linkage are optimized in the formulated objective function. The close-loop control schematic of FCS-PTC is depicted in Fig. 4.1. The FCS-PTC scheme is consist of flux-linkage estimation, prediction stage and optimization stage, which are described as follows.

4.1.1 Flux-linkage estimation

The measured stator current $i_{s\alpha,\beta}(k)$ is the known information in the real-time implementation of IM drive. However, the stator and rotor flux-linkage $\hat{\boldsymbol{\psi}}_{s\alpha,\beta}(k)$ and $\hat{\boldsymbol{\psi}}_{r\alpha,\beta}(k)$ can not be directly measured by the controller. According to (4.1-4.2), the stator and rotor flux-linkage are

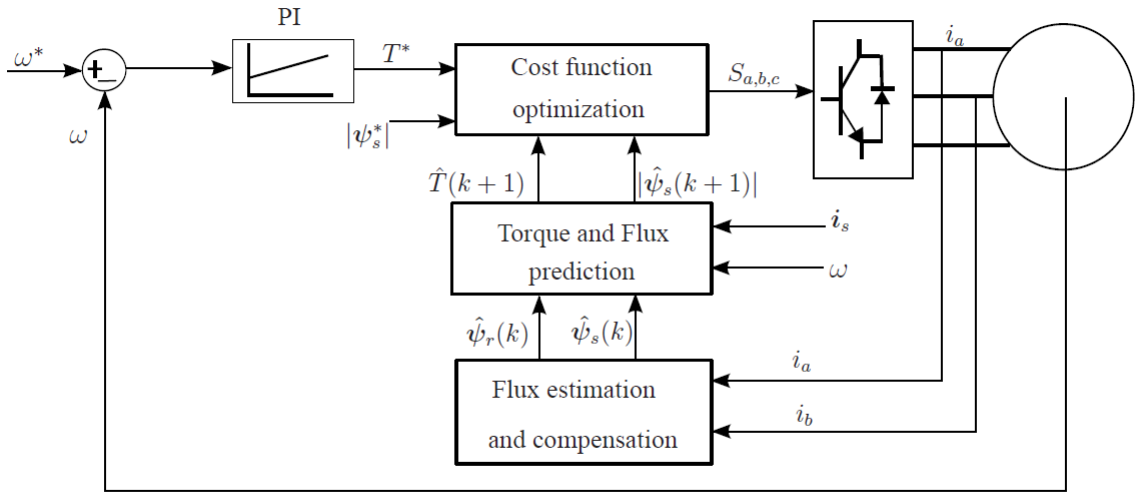

Figure 4.1: The close-loop control schematic of FCS-PTC.

estimated by the dynamic model of IM.

$$\hat{\boldsymbol{\psi}}_{s\alpha,\beta}(k) = L_s \cdot i_{s\alpha,\beta}(k) + L_m \cdot i_{r\alpha,\beta}(k) \tag{4.1}$$

$$\hat{\boldsymbol{\psi}}_{r\alpha,\beta}(k) = L_m \cdot i_{s\alpha,\beta}(k) + L_r \cdot i_{r\alpha,\beta}(k) \tag{4.2}$$

The estimated stator and rotor flux-linkages $\hat{\boldsymbol{\psi}}_{s\alpha,\beta}(k)$ and $\hat{\boldsymbol{\psi}}_{s\alpha,\beta}(k)$ are subsequently employed in the prediction stage.

4.1.2 Prediction stage

To evaluate the future behavior of the control plant, the predicted values of the control variables are calculated in the prediction stage. In the FCS-PTC algorithm, the predicted electromagnetic torque and stator flux-linkage is required. The predicted values can be obtained by two discretization methods: the first-order forward Euler discretization or the Taylor discretization.

4.1.2.1 First-order forward Euler formula

Assuming that the derivatives of the control variables are constant in a sampling period when the sampling period T_s is enough small, the derivatives $dx(k)/dt$ are applied in the first-order forward Euler formula, as described in (4.3).

$$\frac{dx(k)}{dt} = \frac{x(k+1) - x(k)}{T_s} = Ax(k) + Bu(k) \tag{4.3}$$

Therefore, the predicted value of the control variable can be rewritten as

$$x(k+1) = x(k) + T_s \cdot \frac{dx(k)}{dt} = (AT_s + I)x(k) + BT_s u(k) \tag{4.4}$$

where the control variables $x = [i_{s\alpha,\beta}, \psi_{s\alpha,\beta}]^T$. According to the state-space model of the IM in (2.1-2.4), the derivatives of stator current and flux-linkage can be obtained as

$$\frac{di_{s\alpha,\beta}(k)}{dt} = \frac{1}{\tau_\sigma} i_{s\alpha,\beta}(k) + \frac{1}{\tau_\sigma R_\sigma} \cdot [k_r \cdot (\frac{1}{\tau_r} - j\omega(k)) \cdot \hat{\psi}_{r\alpha,\beta}(k) + u_{s\alpha,\beta}(k)] \tag{4.5}$$

$$\frac{d\psi_{s\alpha,\beta}(k)}{dt} = u_{s\alpha,\beta}(k) - R_s \cdot i_{s\alpha,\beta}(k) \tag{4.6}$$

The predicted stator current $\hat{i}_{s\alpha,\beta}(k+1)$ can be expressed as

$$\hat{i}_{s\alpha,\beta}(k+1) = (1 - \frac{T_s}{\tau_\sigma}) i_{s\alpha,\beta}(k) + \frac{T_s}{\tau_\sigma R_\sigma} \cdot [k_r \cdot (\frac{1}{\tau_r} - j\omega(k)) \cdot \hat{\psi}_{r\alpha,\beta}(k) + u_{s\alpha,\beta}(k)] \tag{4.7}$$

where the system parameters $k_r = L_m/L_r$, $R_\sigma = R_s + k_r^2 \cdot R_r$, $L_\sigma = \sigma \cdot L_s$ and $\tau_\sigma = \sigma \cdot L_s/R_\sigma$. Similarly, the predicted stator flux-linkage $\hat{\psi}_{s\alpha,\beta}(k+1)$ is expressed by (4.8).

$$\hat{\psi}_{s\alpha,\beta}(k+1) = \psi_{s\alpha,\beta}(k) + T_s \cdot (u_{s\alpha,\beta}(k) - R_s \cdot i_{s\alpha,\beta}(k)) \tag{4.8}$$

Based on the above, the predicted electromagnetic torque is calcualted by (4.9).

$$\hat{T}(k+1) = \frac{3}{2} \cdot p \cdot Im \left\{ \hat{\psi}_s(k+1)^* \cdot \hat{i}_s(k+1) \right\} \tag{4.9}$$

Considering the time-delay compensation, the predicted values at $k+2$ interval are further calculated in (4.10-4.12).

$$\hat{\psi}_{s\alpha,\beta}(k+2) = \hat{\psi}_{s\alpha,\beta}(k+1) + T_s \cdot (u_{s\alpha,\beta}(k) - R_s \cdot i_{s\alpha,\beta}(k+1)) \tag{4.10}$$

$$\hat{i}_{s\alpha,\beta}(k+2) = (1 - \frac{T_s}{\tau_\sigma}) \hat{i}_{s\alpha,\beta}(k+1) + \frac{T_s}{\tau_\sigma R_\sigma} \cdot [k_r \cdot (\frac{1}{\tau_r} - j\omega(k)) \cdot \hat{\psi}_{r\alpha,\beta}(k+1) + u_{s\alpha,\beta}(k)] \tag{4.11}$$

$$\hat{T}(k+2) = \frac{3}{2} \cdot p \cdot Im \left\{ \hat{\psi}_s(k+2)^* \cdot \hat{i}_s(k+2) \right\} \tag{4.12}$$

where the predicted values at $k+1$ interval are obtained in (4.7-4.9). We assume that the switching sequence and rotor speed are unchanged in the consecutive (k and $k+1$) intervals.

4.1.2.2 Taylor's formula

Apart from first-order forward Euler formula, the predicted values of the control variables can also be obtained by the Taylor's formula. The main concept of Taylor's formula centers around (4.13).

$$\begin{aligned} x(k+1) &= x(k) + \frac{dx(k)}{dt} T_s + \frac{1}{2!} \frac{d^2x(k)}{dt^2} T_s^2 + \cdots + \frac{1}{n!} \frac{d^n x(k)}{dt^n} T_s^n \\ &= e^{AT_s} x(k) + \int_0^{T_s} e^{At} dt \cdot u(k) \end{aligned} \tag{4.13}$$

where $o(t) = \frac{1}{2!} \frac{d^2x(k)}{dt^2} T_s^2 + \cdots + \frac{1}{n!} \frac{d^n x(k)}{dt^n} T_s^n$ is the reminder term. As the reminder term $o(t)$ is considered as zero ($o(t) \approx 0$), the Taylor's formular is simplified as the first-order forward Euler formula.

4.1.3 Optimization stage

The tracking errors between the predicted value of the control variables and their reference values are evaluated in the optimization stage. It is noteworthy that the multiple control variables to be evaluated in the optimization stage are very flexible, including the core control targets, specific system demands and physical constraints. (as described in Chapter 3.2.2). The customized formulation of the objective function in the optimization stage are illustrated as follows.

4.1.3.1 Objective function with absolute value norm

In the objective function with absolute value norm (l_1-norm), the tracking deviations of the control variables are optimized by their absolute values. The objective function is formulated as the sum of the absolute values of the tracking deviation terms. To balance the relationship among the different control variables, the tracking error terms are normalized by a predefined weighting parameter. The formulated l_1-norm objective function in the FCS-PTC algorithm is rewritten in (4.14).

$$g_j = (\hat{T}(k+2) - T^*) + \lambda_\psi(||\hat{\psi}_s(k+2)|| - \psi_s^*) + \lambda_{sw} \cdot n_{sw} + Im(k+2) \tag{4.14}$$

where λ_ψ and λ_{sw} are the weighting parameters for the terms of stator flux-linkage and switching frequency. $Im(k+2)$ is the current limitation term, which has been introduced in (3.9). The tracking errors of the control variables in the l_1-norm objective function are intuitively optimized that the normalized tracking errors are directly added up. The optimal solution that minimizes the sum of the tracking errors is delivered to the inverter.

4.1.3.2 Objective function with quadratic norm

The tracking deviations of the control variables can also be evaluated in the objective function with quadratic norm (l_2-norm) [30]. Instead of the absolute values, the squared values of the tracking deviations are applied in the l_2-norm objective function formulation. The sum of the squared values are minimized in the objective function. However, it is worth mentioned that the weighting parameters of the squared tracking error terms should be modified by their squared values, i.e., λ_ψ^2 and λ_{sw}^2. Therefore, the l_2-norm objective function in the FCS-PTC algorithm is described as

$$g_j = (\hat{T}(k+2) - T^*)^2 + \lambda_\psi^2(||\hat{\psi}_s(k+2)|| - \psi_s^*)^2 + \lambda_{sw}^2 \cdot n_{sw}^2 + Im(k+2) \tag{4.15}$$

4.2 Principle of FCS-PCC

Current quality is of great importance for the applications of electrical drive systems [31]. High distortion in the stator current will lead to the deteriorated performance in the control system [32]. Therefore, finite control set predictive current control (FCS-PCC) is one of the FCS-MPC strategies, in which reducing the current distortion is regarded as the predominant task [33]. Although FCS-PTC can effectively decrease the tracking deviation of electromagnetic torque, the error of stator current is not directly optimized in its objective function. Thus, the stator current distortion in the FCS-PTC algorithm is still relatively high. On the contrary, the stator

current is considered as the main control target in the FCS-PCC. The block diagram of FCS-PCC is demonstrated in Fig. 4.2.

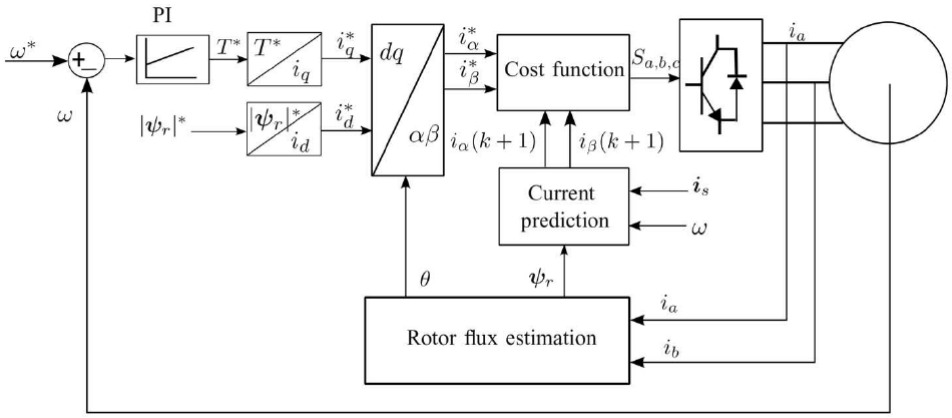

Figure 4.2: The close-loop control schematic of FCS-PCC.

4.2.1 Prediction stage

The stator and rotor flux-linkage are estimated by (4.1-4.2) in FCS-PCC, which is similar to that of FCS-PTC. The predicted stator current in the stationary $\alpha\beta$ frame is calculated in (4.16), as the first-order forward Euler discretization is applied.

$$\begin{aligned}\hat{i}_{s\alpha,\beta}(k+1) &= i_{s\alpha,\beta}(k) + T_s \cdot \frac{di_{s\alpha,\beta}(k)}{dt} \\ &= (1-\frac{T_s}{\tau_\sigma})i_{s\alpha,\beta}(k) + \frac{T_s}{\tau_\sigma R_\sigma} \cdot [k_r \cdot (\frac{1}{\tau_r} - j\omega(k)) \cdot \hat{\psi}_{r\alpha,\beta}(k) + u_{s\alpha,\beta}(k)]\end{aligned} \tag{4.16}$$

where the system parameters $k_r = L_m/L_r$, $R_\sigma = R_s + k_r^2 \cdot R_r$, $L_\sigma = \sigma \cdot L_s$ and $\tau_\sigma = L_\sigma/R_\sigma$. The predicted stator current $\hat{i}_{s\alpha,\beta}(k+2)$ at $k+2$ interval is calculated with the time-delay compensation, as shown in (4.17).

$$\hat{i}_{s\alpha,\beta}(k+2) = (1-\frac{T_s}{\tau_\sigma})\hat{i}_{s\alpha,\beta}(k+1) + \frac{T_s}{\tau_\sigma R_\sigma} \cdot [k_r \cdot (\frac{1}{\tau_r} - j\omega(k)) \cdot \hat{\psi}_{r\alpha,\beta}(k+1) + u_{s\alpha,\beta}(k)] \tag{4.17}$$

4.2.2 Optimization stage

As the stator current is the main control target in the FCS-PCC algorithm, the tracking deviations of the stator current in the stationary $\alpha\beta$ frame are evaluated in the objective function of FCS-PCC [34, 35]. It is noteworthy that the stator current components in the stationary $\alpha\beta$ frame have the equal priority. Therefore, it is not required to design a weighting parameter for the modification between the stator current terms. However, the weighting parameter that balances the importance between the terms of stator current and specific system demand, i.e.,

switching frequency, is still required. Based on the above, the l_1-norm objective function in the FCS-PCC algorithm is formulated as

$$g_j = (\hat{i}_{s\alpha}(k+2) - i^*_{s\alpha}) + (\hat{i}_{s\beta}(k+2) - i^*_{s\beta}) + \lambda_{sw} \cdot n_{sw} + Im(k+2) \tag{4.18}$$

where $i^*_{s\alpha}$ and $i^*_{s\beta}$ are the reference value of the stator current in the stationary $\alpha\beta$ frame. The reference values can be expressed as

$$i^*_{sd} = \frac{|\psi^*_r|}{L_m} \tag{4.19}$$

$$i^*_{sq} = \frac{2L_r}{3L_m} \cdot \frac{T^*}{|\psi^*_r|} \tag{4.20}$$

$$\begin{bmatrix} i^*_{s\alpha} \\ i^*_{s\beta} \end{bmatrix} = \begin{bmatrix} cos(\theta) & -sin(\theta) \\ sin(\theta) & cos(\theta) \end{bmatrix} \begin{bmatrix} i^*_{sd} \\ i^*_{sq} \end{bmatrix} \tag{4.21}$$

where $\theta = arctan(\hat{\psi}_{r\alpha}/\hat{\psi}_{r\beta})$ is the rotation angle. The formulation of the l_2-norm objective function can be described as

$$g_j = (\hat{i}_{s\alpha}(k+2) - i^*_{s\alpha})^2 + (\hat{i}_{s\beta}(k+2) - i^*_{s\beta})^2 + \lambda^2_{sw} \cdot n^2_{sw} + Im(k+2) \tag{4.22}$$

4.3 Assessment of FCS-PTC and FCS-PCC algorithms

4.3.1 Performance evaluation of FCS-PTC

In this section, the control performance of FCS-PTC is evaluated by both the simulation and experimental results. The simulation is conducted in the Matlab/Simulink environment with a sampling period of 62.5 μs. The applied parameters of the induction machine in the simulation model are the same with that applied in the experimental testbench, as shown in TABLE. 2.1.

4.3.1.1 Simulation results

Fig. 4.3 presents the performance of FCS-PTC during a simulated load disturbance. The proposed method operates at a medium rotor speed (1000 rpm), and the torque reference alters from 2 to 5 Nm. The electromagnetic torque rises from 2 Nm to 5 Nm in 0.4 ms with approximately 5 rpm variation in rotor speed. The FCS-PTC method shows a fast dynamic response due to the inherent advantages of predictive control. The ripples of the electromagnetic torque and stator flux-linkage in the FCS-PTC method are approximated 2.3 Nm and 0.05 Wb, respectively.

Fig. 4.4 illustrates the FCS-PTC's performance during a flux disturbance. The simulation operates at a 1000 rpm rotor speed with a 2 Nm load torque, and the flux magnitude decreases from 0.91 to 0.71 Wb at t = 0.2 s. As can be seen, the torque ripple drops from 2.8 to 2.4 Nm with the FCS-PTC method when the flux magnitude $\|\psi_s\|$ is varied. Moreover, it can be observed that the ripple of stator flux magnitude is 0.06 Wb. Considering the current quality, the stator current THD in the FCS-PTC method is 5.9 % in this simulational scenario. The simulation results indicate that FCS-PTC achieves a fast dynamic response during the transient state, and performs well before and after the transient state.

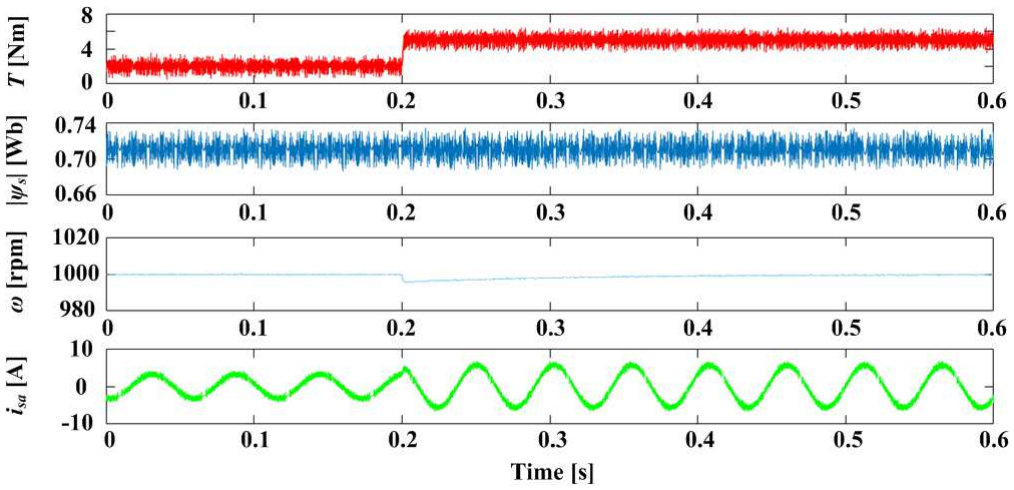

Figure 4.3: Load step performance of the FCS-PTC algorithm (ω = 1000 rpm, T rises from 2 to 5 Nm).

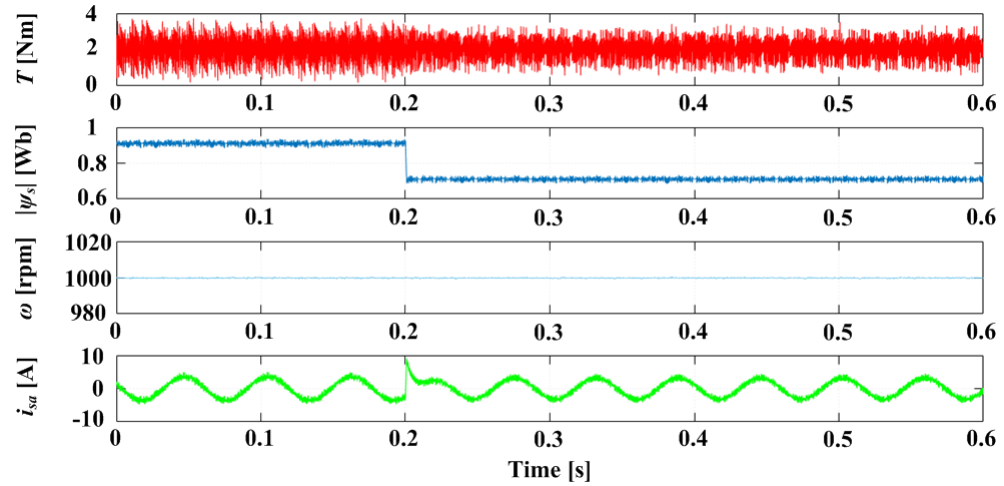

Figure 4.4: Flux step performance of the FCS-PTC algorithm (ω = 1000 rpm, T = 2 Nm, $\|\psi_s\|$ decreases from 0.91 to 0.71 Wb).

4.3.1.2 Experimental verification

Corresponding to the simulations, the torque step performance of the FCS-PTC method is evaluated in Fig. 4.5. The main motor operates at torque control mode that torque reference is directly set in the algorithm. The rotor speed of 1000 rpm is given by the Danfoss load inverter. In the testing controller, the torque reference is altered from 2 Nm to 5 Nm for the use of cost function. It can be seen that the FCS-PTC method achieves a fast dynamic performance. The load torque increases in 0.4 ms, and rotor speed rises to about 1100 rpm and then drops back within 80 ms. The torque and flux ripple of the FCS-PTC method are 2.0 Nm and 0.16 Wb, respectively. Accordingly, the torque squared mean error of FCS-PTC algorithm is 0.40. Moreover, the switching frequency of the FCS-PTC algorithm is 2.0 kHz.

The flux step performances are investigated in Fig. 4.6 at a rotor speed of 1000 rpm with a

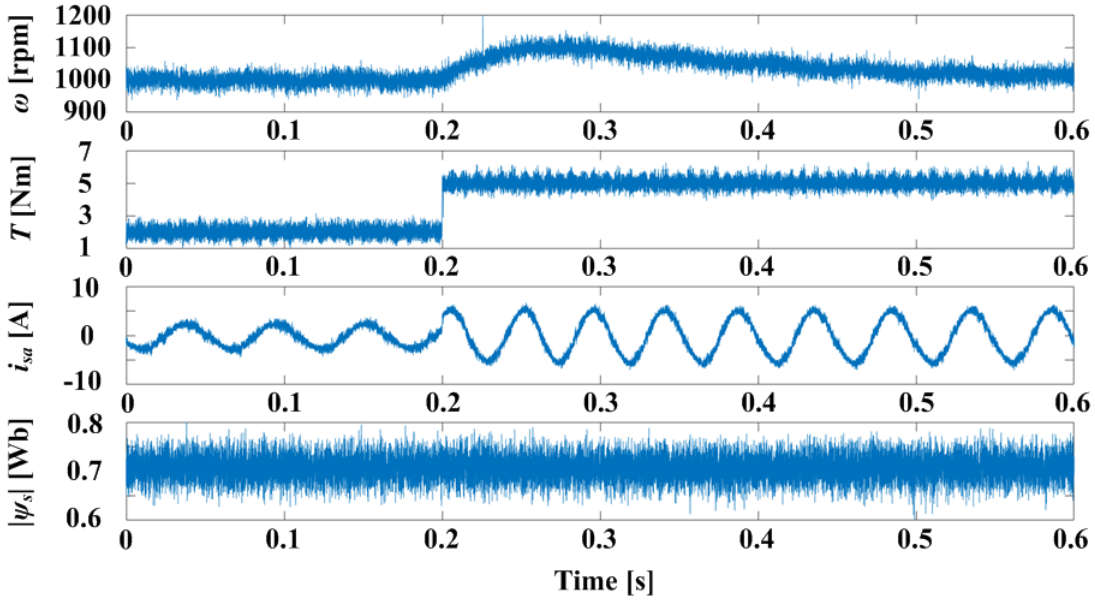

Figure 4.5: Experimental performance of the FCS-PTC algorithm with a load torque step (ω = 1000 rpm, T rises from 2 to 5 Nm).

2 Nm load torque. Since electromagnetic torque is proportional to the q-axis flux, the torque ripple increases in the direct relation to the flux magnitude (from 0.71 to 0.91 Wb). The torque ripple of FCS-PTC alters from 1.9 Nm to 2.2 Nm as flux magnitude rises. The stator current THD of the FCS-PTC method in this test scenario is 6.1 %. The maximum ripple in the stator flux-linkage magnitude is 0.22 Wb.

The load disturbance performance of FCS-PTC is given in Fig. 4.7. The FCS-PTC method is implemented with a 300 rpm rotor speed and a 4 Nm load disturbance. In the FCS-PTC method, as the torque disturbance occurs, rotor speed shows a slight reduction of 100 rpm and then stabilizes, returning to the original speed within 250 ms. More specifically, the tracking error of stator flux-linkage in the FCS-PTC method is 0.05 Wb. It can be observed that FCS-PTC performs well at the steady state after the load disturbance that the stator current THD is 6.0 %.

The induction machine's stator and rotor resistances are varied to evaluate the parameter sensitivity of the FCS-PTC scheme. The results of R_s mismatch are illustrated in Fig. 4.8. The rotor speed is set at 300 rpm, with a R_s variation from 2.68 to 3.5 Ω (30 % mismatch). It can be seen that the FCS-PTC controller becomes instability when R_s rises to 3.5 Ω, that the control performance is dramatically deteriorated when R_s reaches the peak.

In Fig. 4.9 the robustness validation of an R_r mismatch is presented at the same rotor speed of 300 rpm. The rotor resistance is varied from 2.13 to 3.5 Ω (65 % mismatch). It is shown that the FCS-PTC algorithm achieves a strong robustness to R_r variations. More specifically, the FCS-PTC method obtains a 1.6 Nm torque ripple and 90 rpm speed variation. It is indicated that the FCS-PTC scheme achieves a satisfactory steady-state performance at a low speed.

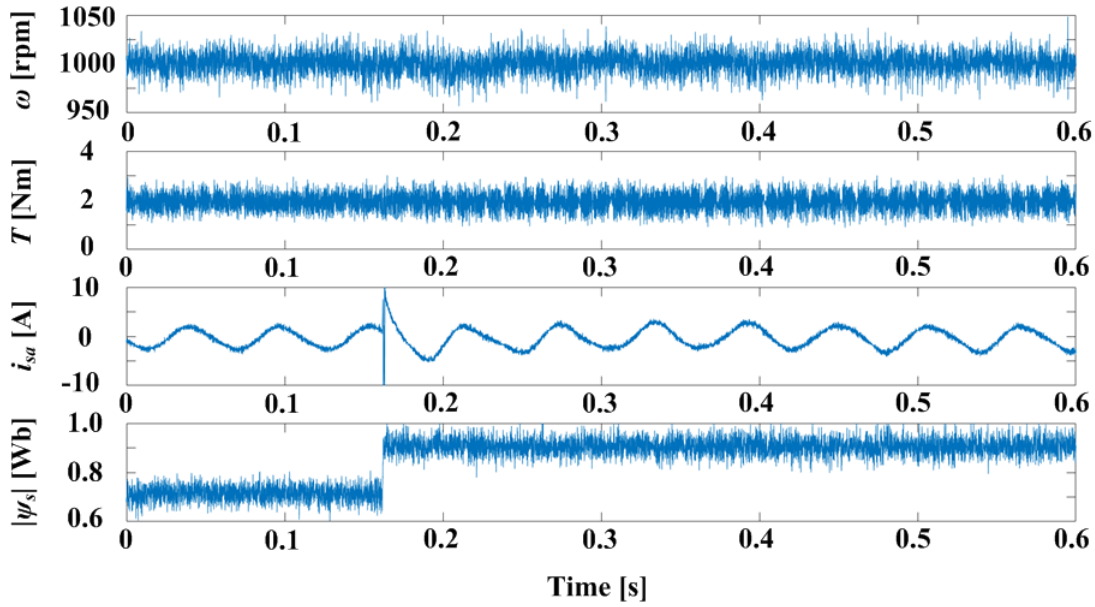

Figure 4.6: Experimental performance of the FCS-PTC algorithm with a flux-linkage step (ω = 1000 rpm, T = 2 Nm, $\|\psi_s\|$ decreases from 0.91 to 0.71 Wb).

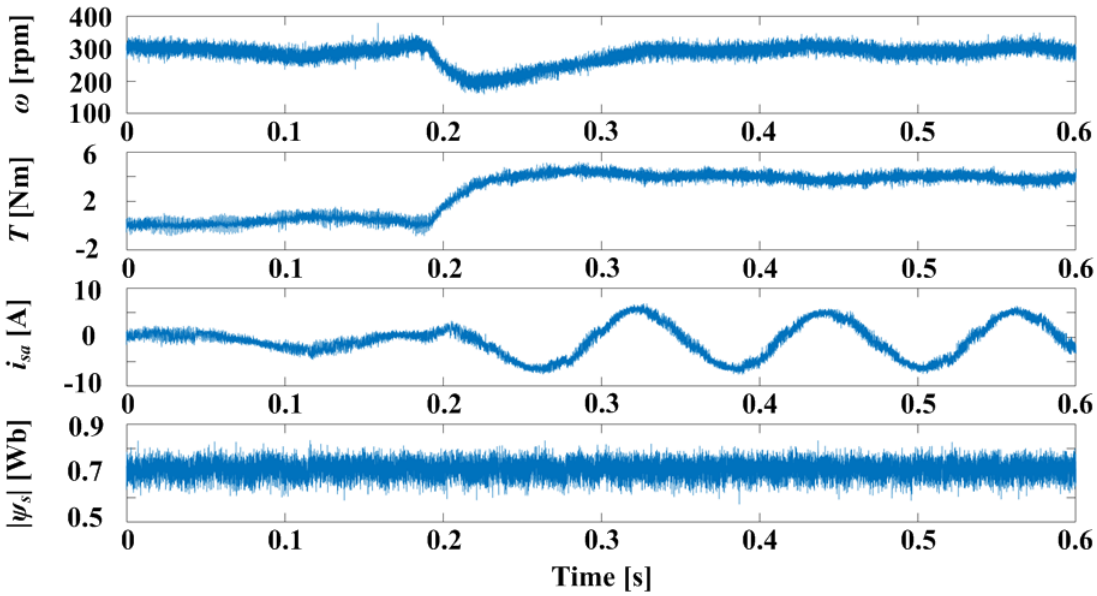

Figure 4.7: Experimental performance of the FCS-PTC algorithm with a load disturbance (ω = 300 rpm, T alters from 0 to 4 Nm).

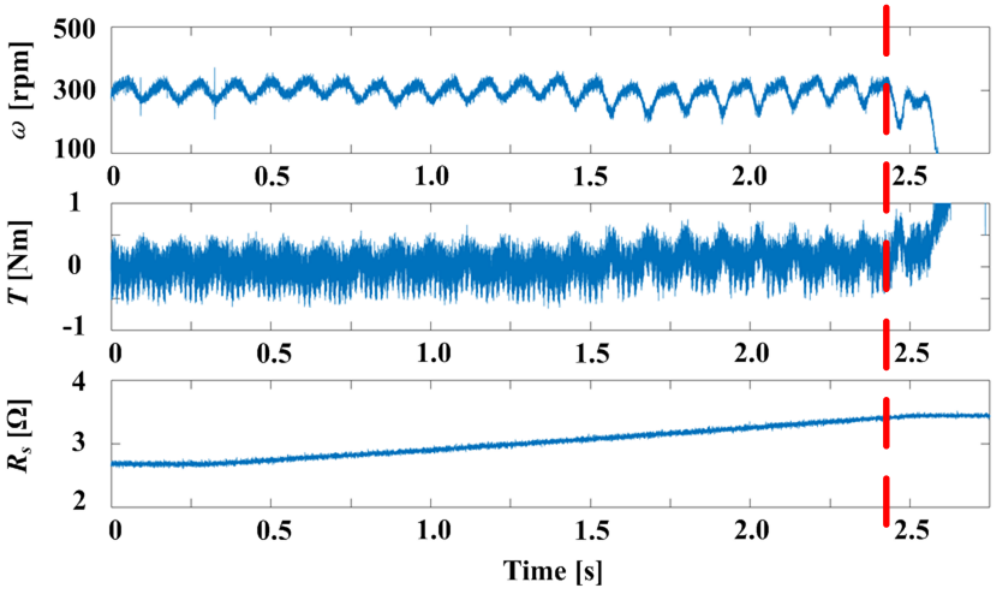

Figure 4.8: Robustness validation of the FCS-PTC algorithm with a R_s mismatch (ω = 300 rpm, R_s increases from 2.68 to 3.5 Ω).

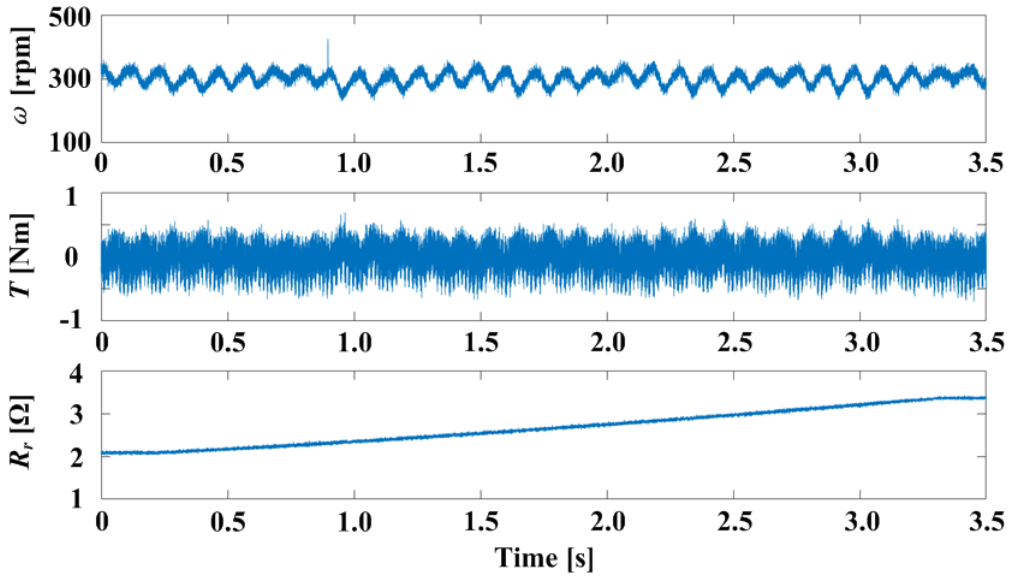

Figure 4.9: Robustness validation of the FCS-PTC algorithm with a R_r mismatch (ω = 300 rpm, R_r increases from 2.13 to 3.5 Ω).

4.3.2 Performance Evaluation of FCS-PCC

In this section, the control performance of the FCS-PCC algorithm is evaluated by the experimental assessment. The FCS-PCC algorithm is conducted with a 16 kHz sampling frequency. The test scenarios at both the steady state and transient state are conducted.

Fig. 4.10 illustrates the steady-state performance of the FCS-PCC method, from up to down

are the measured waveforms of rotor speed, electromagnetic torque, rotor flux and stator current. In the first steady-state test scenario, the IM operates at 50 rad/s with a 3 Nm load torque. The electromagnetic torque and stator current errors of the FCS-PCC method is obtained in Fig. 4.10, which are T_{err} = 1.68 Nm and i_{serr} = 0.47 A ($i_{serr}/||i_s||$ = 12.3 %), respectively. Compared with the abovementioned FCS-PTC method, FCS-PCC achieves a relatively lower stator current error, while the torque error becomes higher. The reason for this is that the term of stator current has the highest priority in the objective function of FCS-PCC.

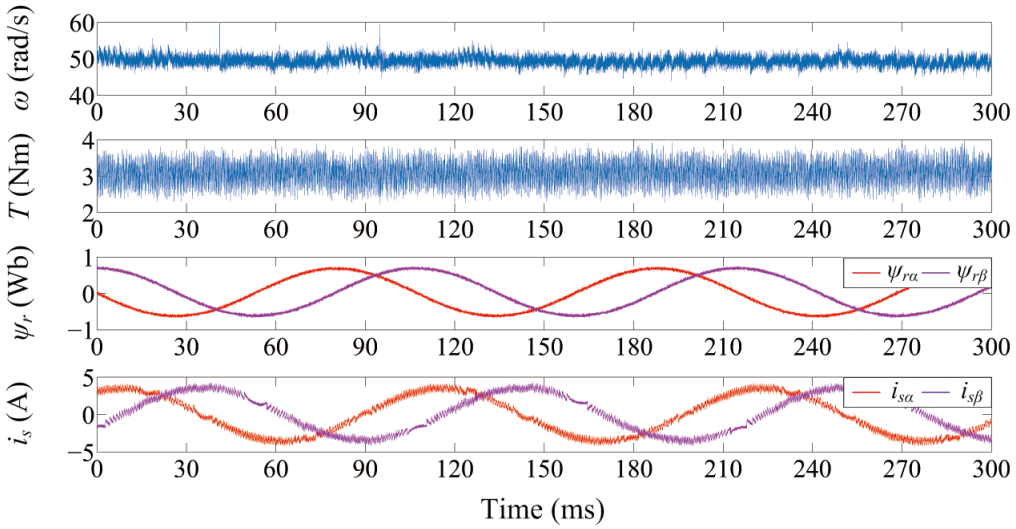

Figure 4.10: Experimental results: steady-state performance of the FCS-PCC method at 50 rad/s with a 3 Nm load torque.

The second test scenario for the FCS-PCC method is conducted at 200 rad/s with a 5 Nm load torque, as shown in Fig. 4.11. Compared with the first steady-state scenario, a larger torque error (T_{err} = 1.83 Nm) and a smaller stator current deviation (i_{serr} = 0.51 A, $i_{serr}/||i_s||$ = 10.4 %) are obtained in the FCS-PCC method. Similar trend can be found in the comparative results between FCS-PTC and FCS-PCC in the second scenario. In FCS-PTC, less torque deviation is achieved because torque and stator flux are considered as the main control targets. On the contrary, a better stator current quality is found in the FCS-PCC algorithm, in which the stator current error is formulated as the penalty term in the objective function. It can be concluded that the control objectives are customized and flexible included in the objective function of the FCS-MPC schemes.

The transient-state performance of the FCS-PCC method is investigated, which includes speed step test and load step test. The speed step performance is initially evaluated. The IM works at a rotor speed of 100 rad/s, and a 3 Nm load torque is provided by the control panel. A speed step from 100 rad/s to 150 rad/s is suddenly carried out by the algorithms at t = 80 ms. As can be seen in Fig. 4.12, the rotor speed rises from 100 rad/s to 150 rad/s in about 60 ms. Due to its merit of quick dynamic response, it is obvious that FCS-PCC achieves a short settling time during the transient state. It can be seen that the FCS-PCC algorithm performs very well both during and after the transient state, which indicates that the FCS-PCC algorithm not merely obtains a fast dynamic response but also retains a satisfactory steady-state performance.

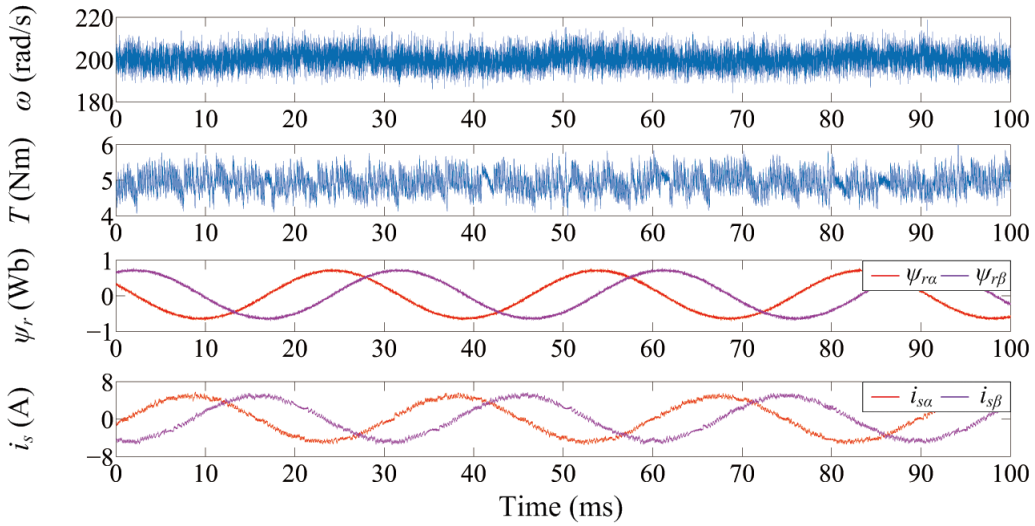

Figure 4.11: Experimental results: steady-state performance of the FCS-PCC method at 200 rad/s with a 5 Nm load torque.

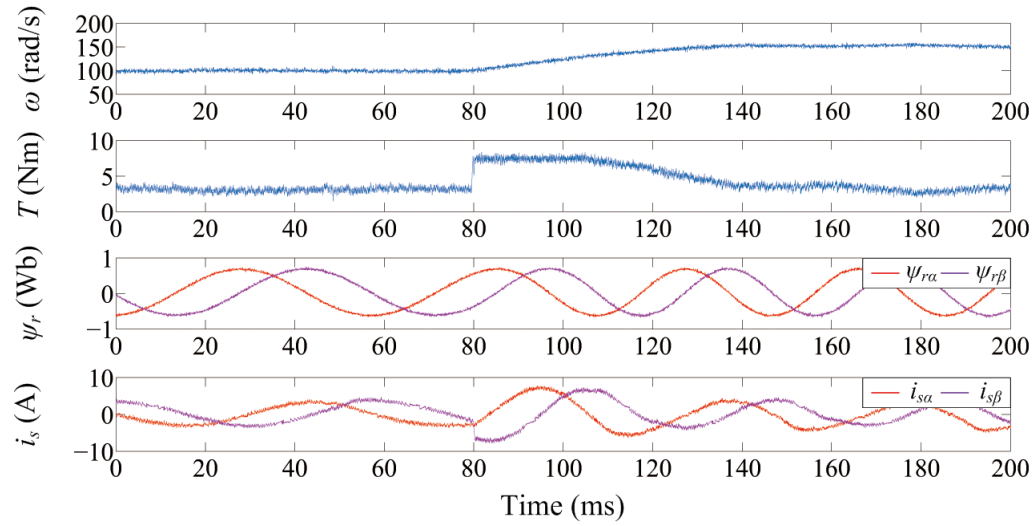

Figure 4.12: Experimental results: speed step performance of the FCS-PCC method from 100 rad/s to 150 rad/s with 3 Nm load toque.

The load step performance of the FCS-PCC method is shown in Fig. 4.13. As shown, the IM operates at the given rotor speed 100 rad/s which is provided by the control panel. As can be understood, the initial value of the torque reference is 5 Nm, which suddenly drops to 3 Nm within 400 μs as the load step takes place. As shown in Fig. 4.13, the rotor speed decreases to about 81 rad/s and then recovers to the original value within 200 ms simultaneously. The errors of torque and stator current after the transient state are 1.30 Nm and 0.48 A, respectively.

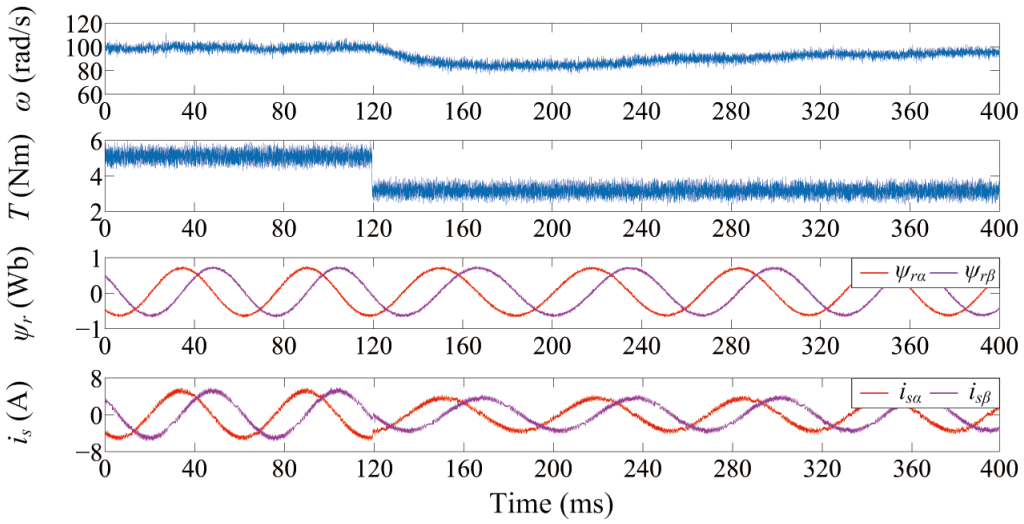

Figure 4.13: Experimental results: load step performance of FCS-PCC from 5 Nm to 3 Nm at 100 rad/s.

4.4 Conclusion

In this chapter, the FCS-MPC schemes with multiple control targets for IM drives are investigated. Categorized by the type of control targets, FCS-PTC and FCS-PCC are the two mainstream control strategies in the FCS-MPC family. The formulation of FCS-PTC and FCS-PCC, especially the prediction stage and optimization stage, are introduced in detail. Finally, the control performance of the two FCS-MPC algorithms at the steady state, transient state and speed reversal maneuver are tested by an experimental assessment.

CHAPTER 5

Multi-objecitve FCS-MPC without weighting parameters

In the FCS-MPC schemes with multiple control targets, we aim to resolve the optimal solution by minimizing the tracking deviations of the control variables. To do so, multiple control variables are flexibly included in the formulated objective function of FCS-MPC. However, how to balance the relationships among the different control variables in the objective function, i.e., the design of the weighting parameters has become an open discussion. In this chapter, the multi-objective FCS-MPC schemes without weighting parameters are introduced.

5.1 Introduction

The FCS-MPC schemes has shown the superiority of resolving an optimization problem with multiple control objectives. Therefore, multiple control variables are included in the customized objective function of FCS-MPC. The weighting parameters are required to define the contribution of each control variable. However, the design of the weighting parameters is still a challenging task. The most frequently-used approach is to design the weighting parameters as the empirical values, by normalizing the different control variables. An obvious drawback of the empirical weighting parameter is that it can not be always fine-tuned in the varied operating conditions. To cope with the aforementioned issue, the weighting parameter design in the FCS-MPC schemes with multiple objectives are discussed in this chapter in detail.

5.2 Classification of the weighting parameter optimization solutions

Several literature review has extensively investigated the methods of weighting parameter optimization in the FCS-MPC schemes. Apart from the empirical values obtained by the trial-and-

error method, from elimination of the weighting parameters by unifying the dimension of the control variables, to the adaption of the weighting parameter via an online/offline approach.

5.2.1 Elimination of the weighting parameters

The first category of the weighting parameter optimization solutions is to eliminate the weighting parameters directly. As we reduce the dimension of the control objectives in the objective function to one, the usage of the weighting parameters is avoided. The weighting parameter elimination methods are very simple that they do not increase the computational burden as well as algorithm complexity. However, it is obvious that the methods become less effectiveness in a complex control system, in which the number of multiple control targets in the objective function is high. In [36], a weighting factor-less FCS-PTC using virtual vector for PMSM drives is presented. The cost function is constructed as the deviation between the desired and applied voltage vector. It is worth noting that the applied voltage vectors are selected by the deadbeat (DB) technology in advance. In [37], a two-vector based FCS-PTC without weighting factors for IM drives is proposed, which obtains the similar reference vector of stator flux with [36]. More specifically, two optimal vectors as well as the least-squares optimized duty cycles are carried out in the inverter. The aforementioned weighting parameter elimination strategies with DB solution show weak robustness against parameter variations, and the switching frequency is higher when more vectors are executed in a sampling interval. Recently, a very simple sequential structure FCS-MPC for IM drives is presented in [38]. The torque and flux tracking error terms in the cost function are separated and evaluated in a sequential order. However, the global optimal solution is not guaranteed because only two optimal vectors are selected according to the torque criterion. Based on the above, a generalized sequential FCS-MPC (GS-FCSMPC) is proposed in [39] for performance improvement. The priorities of the control targets are assigned in the GS-FCSMPC and the field-weaken ability is experimentally validated. In [40], an even-handed sequential FCS-MPC is studied, in which the priorities of the control targets are determined by the obtained cross-error. To conclude, how to assign the priorities of control targets in the objective function is still an open discussion for sequential FCS-MPC strategies. Moreover, the number of the optimal switching sequences is reduced in the sequential FCS-MPC algorithms as the specific control objective is optimized. As more control targets are included, the global optimal state is difficult to be achieved.

5.2.2 Online adaptation of the weighting parameters

Another category of weighting parameter optimization solutions is to adapt the weighting parameters via an online approach. The main concept of online weighting parameter adaption methods is to select the optimal solution by a predefined regulation. In the conventional FCS-MPC schemes, the objective function is designed as the sum of the normalized tracking deviations. On the contrary, the online adaption methods, such as ranking criteria or searching the mutual elements are employed to modify the tracking error terms instead of the weighting parameters. In [41], a FCS-PTC strategy without weighting parameters is developed. The tuning of weighting parameters is replaced by the multi-objective optimization based on the ranking criterion. However, the additional weighting parameters are introduced to modify the ranking values. In [42], a parallel structure FCS-PTC without weighting factor for IM drives

is proposed, which optimizes the torque and flux tracking error terms simultaneously. The weighting parameter is eliminated in the parallel FCS-PTC, but the constraints for torque and flux are required to be carefully designed. A fuzzy decision-making approach for FCS-PTC is presented in [43], by evaluating the normalized membership functions. The similar concept of fuzzy control for online weighting parameter adjustment is investigated in [44]. However, an importance matrix among the different control targets is assigned to evaluate the normalized membership functions. In [45], a simulated annealing algorithm is proposed to solve the open issue of weighting factor selection in FCS-PTC. The convergence criterion is achieved by the formulated energy function as well as the tracking error terms. Although the online optimization solutions bypass the process of weighting parameters selection, the additional data is indirectly applied instead of the weighting parameters.

5.2.3 Offline adaptation of the weighting parameters

The weighting parameters can also be adapted offline in the FCS-MPC schemes. In [46], the weighting parameters in the multi-objective FCS-MPC are adjusted by the empirical approach. The amount of multiple simulational procedures is reduced by a branch and bound algorithm. Recently, the offline search based on artificial neural network (ANN) has attracted much attention in weighting parameter tuning. In [47], the weighting parameters are dynamically adapted by the trained ANN within the safe margin. However, performance metrics for electrical drive systems such as torque and flux tracking error are not considered. In [48], an ANN approach is proposed to design the parameters in the objective function for FCS-PTC. In this application, both the weighting parameters and the reference of stator flux are obtained by the fitness function in varied testing scenarios. The offline design for weighting parameters depends on the trial and error procedures or large scale data based on the repetitive simulational results, which is both resource-consuming and lack of theoretical analysis.

5.3 Artificial neural network (ANN) based FCS-MPC

In the ANN based FCS-MPC scheme, the weighting parameters for the stator flux-linkage term and the switching frequency term as well as the reference of the stator flux-linkage are designed by the ANN approach [48]. The proposed ANN structure has 3 neurons in the input layer, 12 neurons in the first hidden layer, 5 neurons in the second hidden layer and 5 neurons in the output layer. The training data are generated from repetitive simulation results with the combination of different weighting parameters. To select the optimal combination of the weighting parameters, a fitness function (f_{ANN}) is formulated to evaluate the performance metrics, as described in (5.1). It can be seen that the following performance metrics, i.e., the errors of torque, stator current and stator flux-linkage (T_{err}, i_{serr}, ψ_{serr}), the average switching frequency (f_{swavg}) are evaluated in the fitness function f_{ANN}.

$$f_{ANN} = {\psi_{serr}}^2 + i_{serr}^2 + T_{err}^2 + (f_1 - f_{swavg})^2 \tag{5.1}$$

The block diagram of ANN is illustrated in Fig. 5.1. The first step is to collect the training data generated from the simulation results with various weighting parameter combinations.

Subsequently, the performance metrics are trained in the proposed ANN to find the optimal solution, which minimizes the fitness function (5.1). The optimal combination of the parameters are delivered to the FCS-MPC scheme.

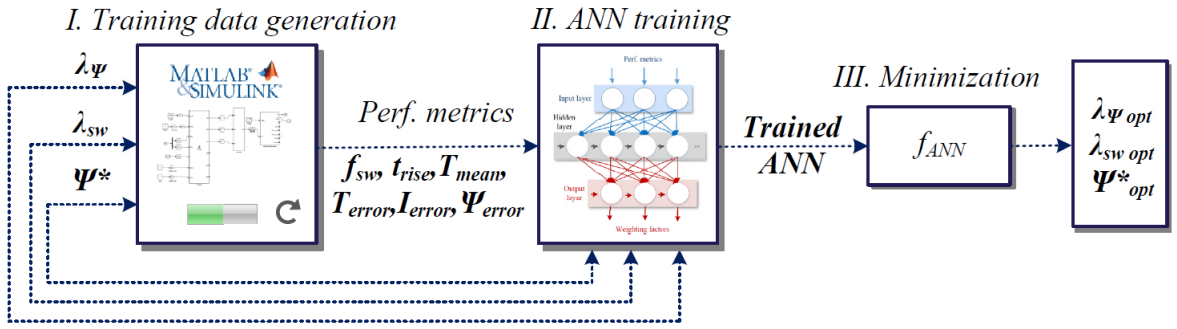

Figure 5.1: Block diagram of ANN.

As a case study, 200 rad/s with a 2 Nm load torque and 150 rad/s with a 5 Nm load torque are tested as the two steady-state scenarios for the proposed ANN. The combinations of the optimal parameters can be observed in the plots of the fitness function, as shown in Fig. 5.2 and Fig. 5.3. As the load torque becomes higher, it can be seen that the region of optimal parameters moves towards the direction of a higher value of λ_ψ and a lower value of λ_{sw}. The optimal parameter combination for the first test scenario is λ_ψ = 10, λ_{sw} = 0.1, ψ_s^* = 0.675, while that for the second test scenario is λ_ψ = 6.88, λ_{sw} = 0.07, ψ_s^* = 0.66. The moving trend indicates the change of designed parameters with various working conditions.

Fig. 5.4 shows the steady-state performance of the proposed ANN-based FCS-MPC conducted at 200 rad/s with 2 Nm. The test scenario is conducted at a sampling frequency f_{samp} = 16 kHz. From up to down the waveforms of rotor speed, electromagnetic torque, stator flux, stator current and the applied switching state are presented. As can be seen, the ANN-based FCS-MPC with a group of optimal weighting parameters (λ_ψ = 10, λ_{sw} = 0.1, ψ_s^* = 0.675) achieves an improved tracking performance in terms of electromagnetic torque and stator current (0.48 Nm and 11.6 %). More specifically, the appropriate tuning of λ_{sw} leads to a significant lower average switching frequency (2.53 kHz) than the conventional method. The tracking error of the stator flux-linkage magnitude is 0.055 Wb. As shown in Fig. 5.4, it can be claimed that the proposed ANN-based FCS-MPC algorithm outperforms the conventional FCS-MPC in this test scenario.

The steady-state performance at 150 rad/s with 5 Nm is investigated as the second experimental scenario. For a fair and comprehensive comparison, the ANN-based FCS-MPC is conducted with an average switching frequency of 2.5 kHz. As shown in Fig. 5.5, a higher tracking deviation is obtained by the conventional FCS-MPC using fixed weighting parameters. Compared with ANN-based FCS-MPC, the tracking deviations of the conventional FCS-MPC are 36.8 % and 2.1 % higher in terms of torque and stator current. The torque and stator current errors of the ANN-based FCS-MPC are 0.57 Nm and 8.65 %, respectively. A similar trend can be ob-

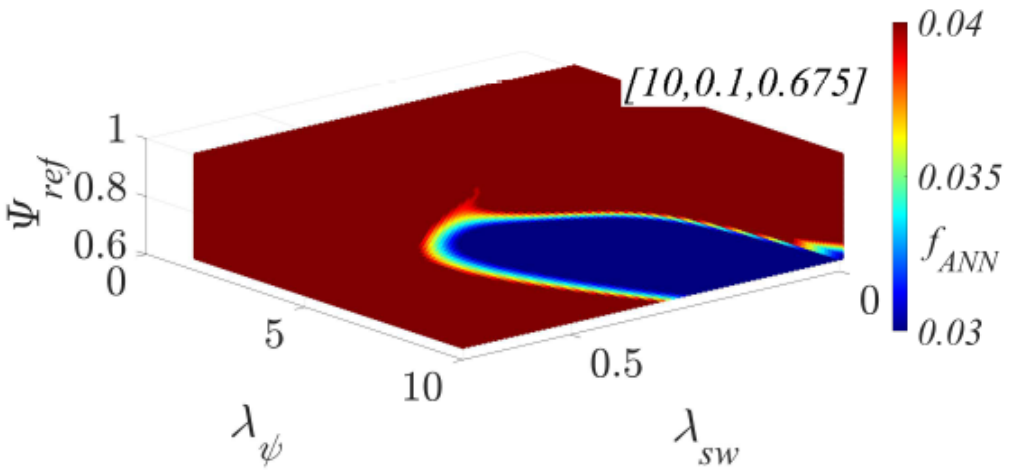

Figure 5.2: Plot of the fitness function in the test scenario of 200 rad/s with a 2 Nm load torque, f_1 = 2.5 kHz.

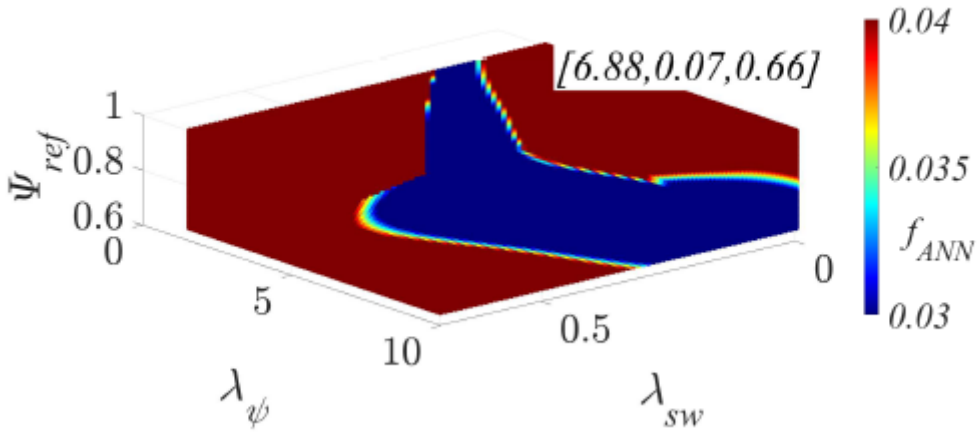

Figure 5.3: Plot of the fitness function in the test scenario of 150 rad/s with a 5 Nm load torque, f_1 = 2.5 kHz.

served between the conventional and ANN-based FCS-MPC methods in both the steady-state scenarios that a better tracking performance is achieved by the proposed ANN-based FCS-MPC algorithm.

5.4 FCS-MPC with a sequential structure

To cope with the issue of weighting parameter design in the FCS-MPC schemes, a sequential structure is proposed in the optimization stage to avoid the usage of the weighting parameters.

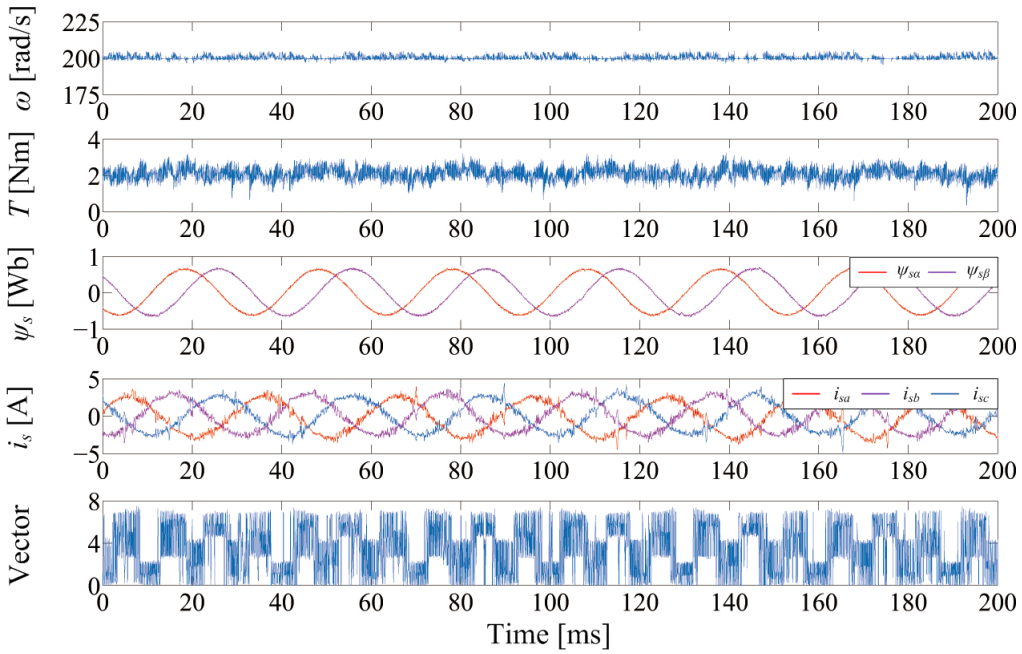

Figure 5.4: Steady-state performance of ANN-based FCS-MPC at 200 rad/s with 2 Nm.

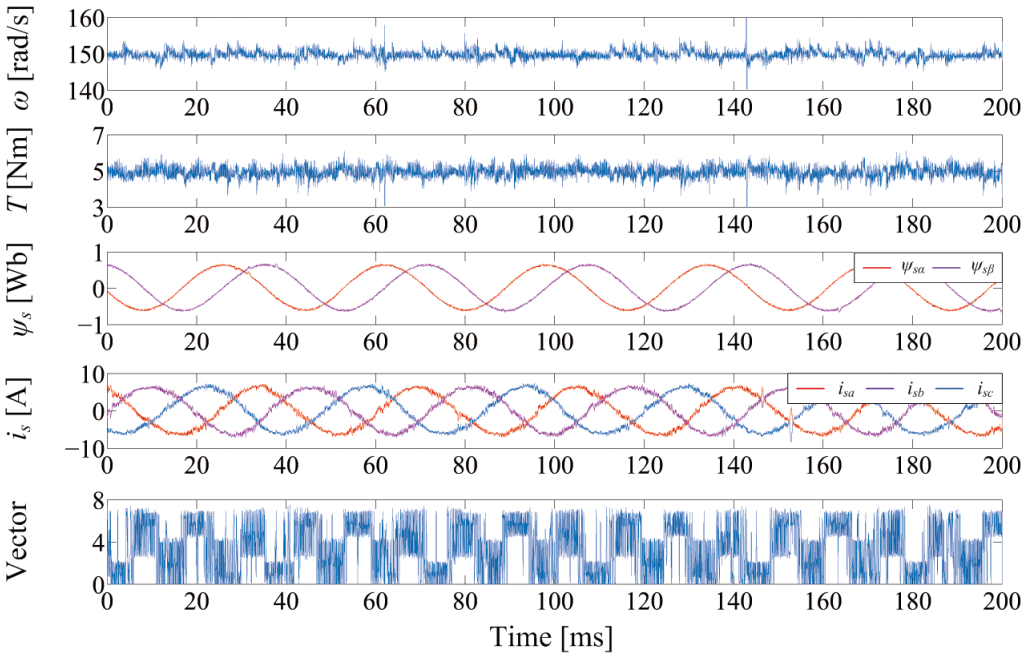

Figure 5.5: Steady-state performance of ANN-based FCS-MPC at 150 rad/s with 2 Nm.

The weighting parameters are eliminated by unifying the dimension of the control variables in the objective function. By splitting the objective function (4.15) in the conventional FCS-MPC, two tracking error terms are formulated in the optimization stage of the FCS-MPC with a sequential structure. The torque and stator flux-linkage error terms g_T and g_F are described

in (5.2).

$$\begin{aligned} g_T &= (\hat{T}(k+2) - T^*)^2 + Im(k+2) \\ g_F &= (||\hat{\psi}_s(k+2)|| - \psi_s^*)^2 + Im(k+2) \end{aligned} \tag{5.2}$$

In the FCS-MPC with a sequential structure (SMPC), the control variables are separately optimized in sequence. As can be understood, only one control variable is optimized in each optimization stage. All the control inputs are searched in the first optimization stage, and the feasible set is gradually narrowed according to the results of the former optimization stage. The block diagram of SMPC is described in Fig. 5.6. It can be seen that the torque error term is initially optimized, in which the two voltage vectors that minimize the torque error the most are selected. Subsequently, the two voltage vectors are delivered to the second stage. The voltage vector which obtains a minimum stator flux-linkage error is selected as the optimal solution.

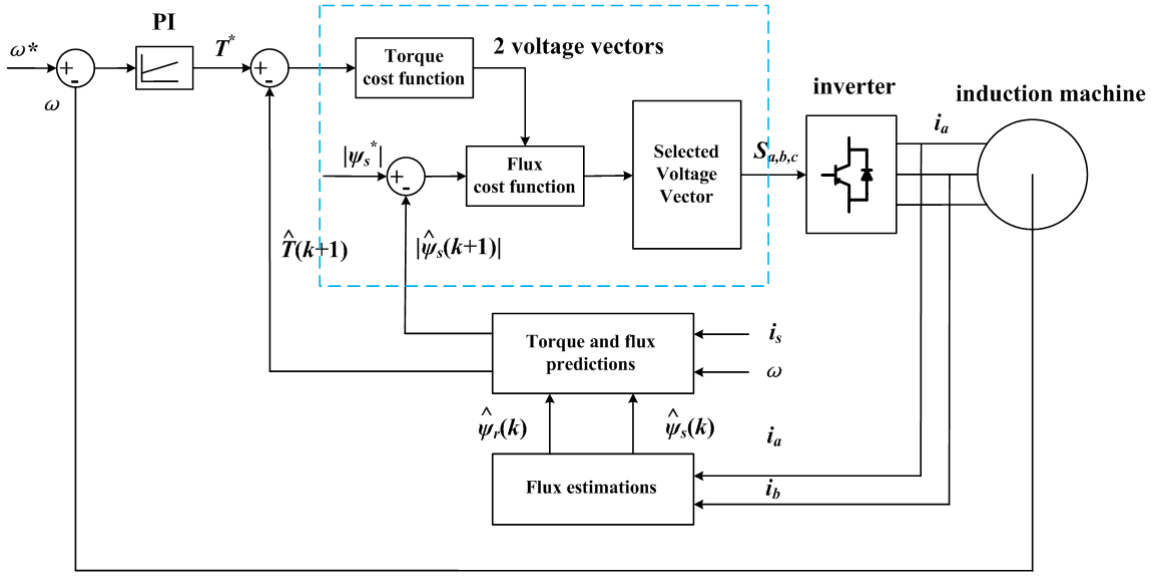

Figure 5.6: Block diagram of FCS-MPC with a sequential structure.

The SMPC algorithm can be conducted in a generalized approach that the torque and flux terms obtain the priority in turns [39]. The GS-FCSMPC algorithm is experimentally validated in both the steady-state scenarios. As shown in Fig. 5.7, the GS-FCSMPC algorithm achieves a 26.8 %, 19.7 % and 6.5 % reduction in terms of torque, stator current and flux error, when compared with the conventional FCS-MPC. Nevertheless, it has to be mentioned that the inherent feature of the sequential structure restricts its ability to handle more complicated cost function (with multiple conflicting targets). Compared with the ANN-based FCS-MPC, the GS-FCSMPC is penalized by a higher average switching frequency. The reason for this relates to the absence of the conflicting targets (e.g. switching frequency) in the objective function. It can be observed that the average switching frequency (2.69 kHz) is slightly higher than that of ANN-based FCS-MPC. A similar trend can be observed in Fig. 5.8 that a better tracking performance is achieved by the GS-FCSMPC algorithm. The T_{err} and i_{serr} of the GS-FCSMPC algorithm are 0.62 Nm and 6.71 %, respectively.

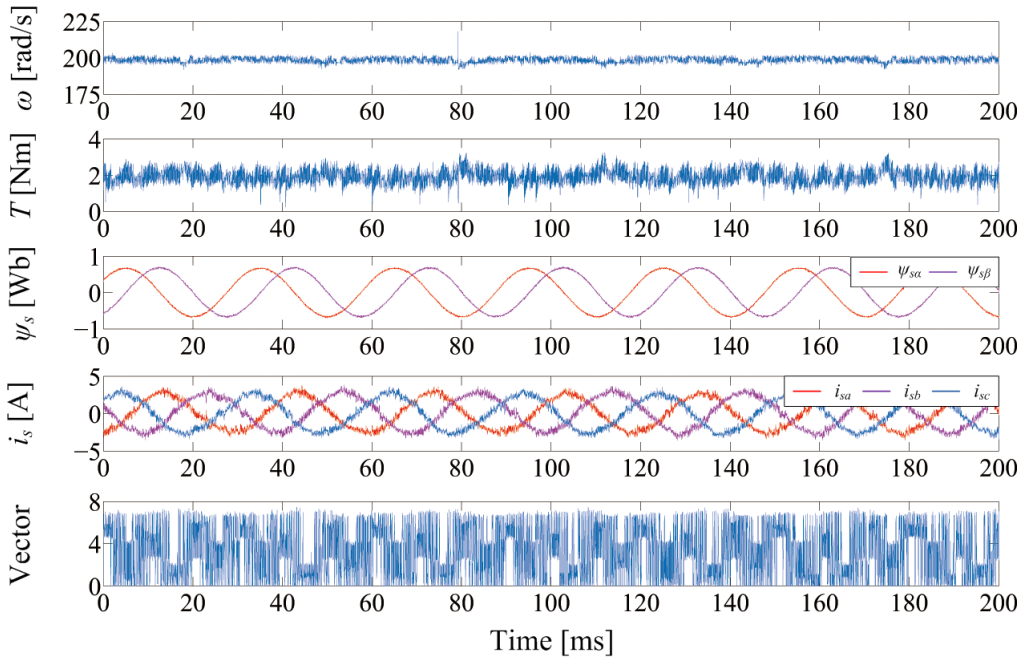

Figure 5.7: Steady-state performance of FCS-MPC with a generalized sequential structure at 200 rad/s with 2 Nm.

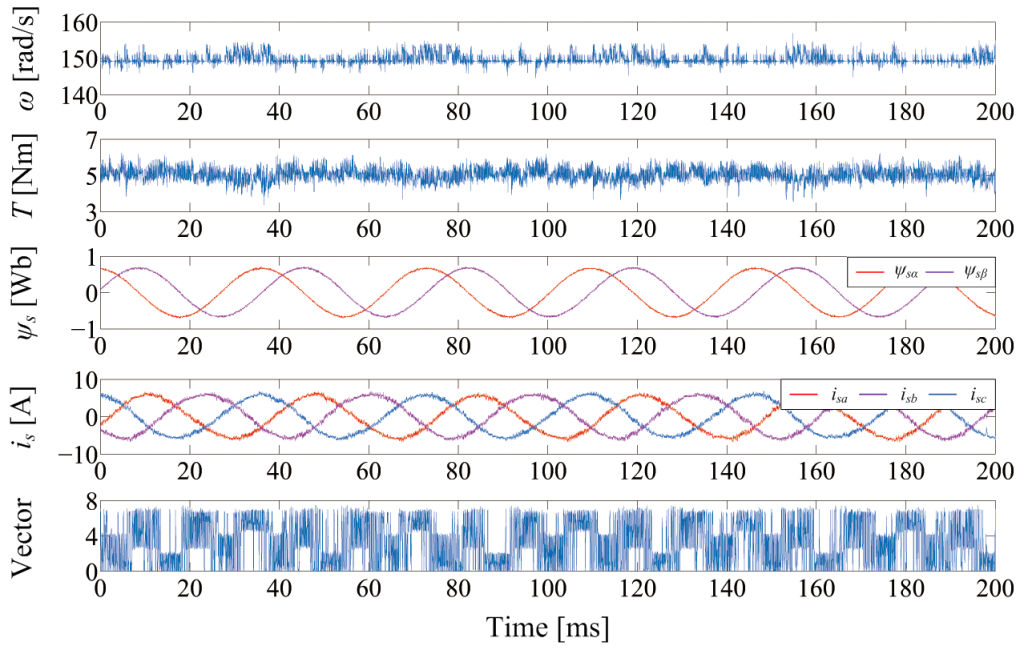

Figure 5.8: Steady-state performance of FCS-MPC with a generalized sequential structure at 150 rad/s with 5 Nm.

5.5 FCS-MPC with a constrained parallel structure

Apart from the FCS-MPC with a sequential structure, a constrained parallel structure can be applied in the FCS-MPC schemes to eliminate the weighting parameters. The proposed constrained parallel FCS-MPC method (PPTC) is implemented in a parallel structure in order to optimize the torque and flux cost functions. Instead of handling a cost function with multiple control objectives and fixed weighting parameters, the control objectives are achieved simultaneously but independently. When the operating conditions shift, the relationship between torque and flux should be adjusted accordingly. To further improve the performance of the proposed control method, one important factor is to constrain the torque and flux tracking errors within the boundaries. Those vector candidates which make the torque and flux magnitude errors within the predefined boundaries are then evaluated by an adaptive selection mechanism.

The block diagram of the proposed PPTC strategy is shown in Fig. 5.9. The reference torque T_{ref} is generated by a speed PI controller that measures the tracking error of the speed reference and the measured rotor speed. Although the tracking error terms employed in the proposed PPTC algorithm are the same with that of SMPC algorithm, the optimization principle is different.

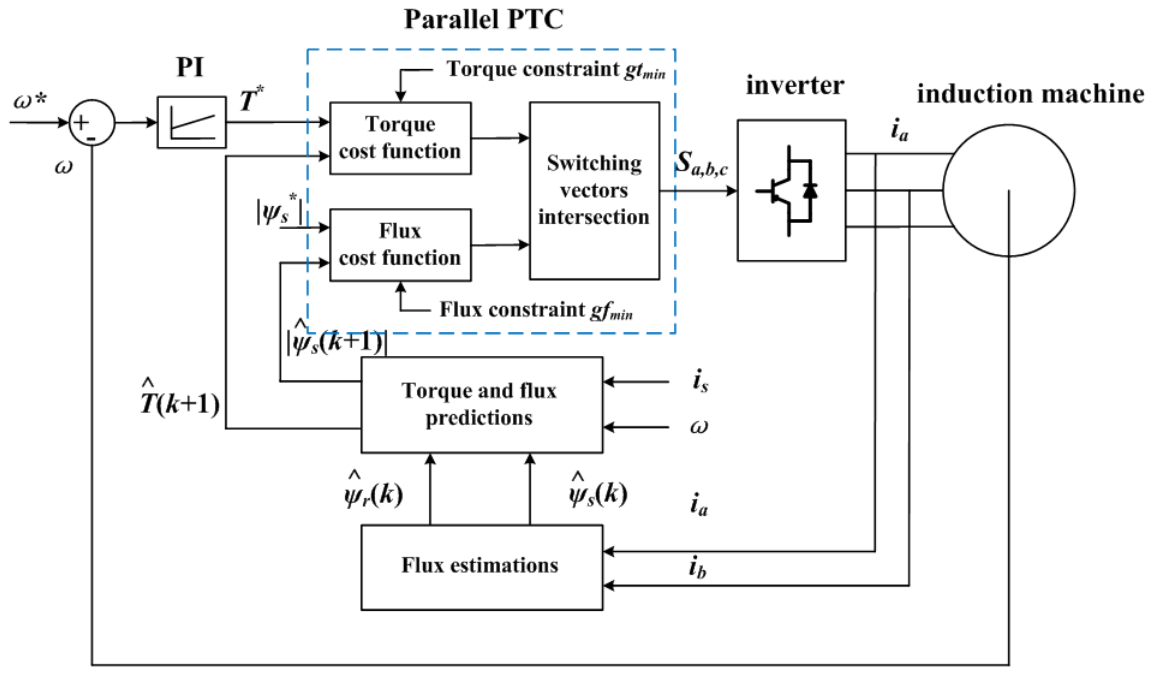

Figure 5.9: Block diagram of FCS-MPC with a constrained parallel structure.

To enhance the proposed PPTC's performance, g_{tmin} and g_{fmin} are designed as the initial boundaries for torque and flux constraints, respectively. The first step is to choose candidate vectors for optimal torque (OT), best-optimal flux (BF) and sub-optimal flux options (SF). For every switching state (i = 0-7), the torque cost function term is compared with g_{tmin}. The candidates are registered as elements in the OT array when g_{ti} is less than g_{tmin}. Simultaneously,

the enumerative vectors are inserted into the BF array if the corresponding g_{fi} is within the g_{fmin} boundary, while the rest are categorized as SF. The candidates in each array are sorted by ascending cost function value.

Regarding that the uncertain number of the candidates in the three arrays, there are some possibilities. The best possibility is that there are some mutual candidates both in OT and BF, the vector that minimize torque error is selected. It is reasonable that torque is more crucial than flux in the PPTC method. The other condition is that there are no mutual candidates between OT and BF, then the optimal choice is the mutual vector with minimize flux error between OT and SF. In very few occasions such as starting process, there are no candidates in OT. In that case the vector that minimize the torque error is delivered, so as to track the reference value T_{ref} instantly.

To guarantee both torque and flux magnitude are optimized in the proposed PPTC method, the amount of vector candidates within each boundary should be 2-4. If there is less than 2 candidates within one boundary, the other term can not be effectively optimized. Otherwise, the boundary is too high if there are more than 4 candidates within it. When the amount of vector candidate within optimal-torque (OT) is less than 2, the torque boundary g_{tmin} should have a 5 % increase. On the contrary, if the amount is more than 4, g_{tmin} should have a 5 % reduction. The same adaption is employed for flux boundary g_{fmin}. The flowchart of the proposed algorithm is introduced in Fig. 5.10.

To ensure the proper number of VVs in V_T and V_F, the constraints for electromagnetic torque and flux-linkage should be carefully designed. To do so, the values of tracking deviations g_T and g_F are obtained in the different test scenarios. The number in the square bracket means the sorted sequence for tracking deviation. For example, $g_T[2]$ is the torque deviation which is the second smallest, and $g_F[2]$ is the stator flux-linkage deviation which is the second smallest and so on. The values of $g_T[2-4]$ and $g_F[2-4]$ can be seen in Fig. 5.11. It can be observed from Fig. 5.11(a) that the average $g_T[2]$, $g_T[3]$, $g_T[4]$ in 2.0 ms are 0.7 Nm, 1.1Nm and 1.8Nm, respectively. The average $g_F[2]$, $g_F[3]$, $g_F[4]$ are 0.01 Wb, 0.02 Wb and 0.035Wb, respectively. As can be understood, the constraints in PPTC aim to register a proper number (2-4) of control inputs in V_T and V_F. Therefore, T_{min} should ranges from 0.7 to 1.8 Nm, F_{min} should ranges from 0.01 to 0.035 Wb, to guarantee that there are 2-4 VVs in V_T and V_F. Similarly, the average $g_T[2]$, $g_T[3]$, $g_T[4]$ are 0.8 Nm, 1.8 Nm and 2.5 Nm, and the average $g_F[2]$, $g_F[3]$, $g_F[4]$ are 0.01 Wb, 0.02 Wb and 0.04 Wb in Fig. 5.11(b). In the test scenario of 2772 rpm with 7.5 Nm, T_{min} should ranges from 0.8 to 2.5 Nm, F_{min} should ranges from 0.01 to 0.04 Wb. Based on the above, T_{min} = 1.2 Nm and F_{min} = 0.03 Wb are selected as the initial constraints.

In order to verify the proposed PPTC's feasibility, performances in the entire speed range are investigated. Rotor speed, torque, and stator flux are shown in the $\alpha\beta$-axis in Fig. 5.12. The rotor speed reverses from 2600 rpm to -2600 rpm within about 400 ms. The results indicate that the proposed PPTC method achieves fast dynamic response and performs well in the whole speed range.

The steady-state performance of the proposed constrained PPTC algorithm is shown in Fig. 5.13 and Fig. 5.14. As shown in Fig. 5.13, the torque and stator current error of the proposed method are 0.40 Nm and 9.23 %, respectively. However, the average switching frequency is slight higher (2.68 kHz) when compared with the conventional FCS-MPC method. As can

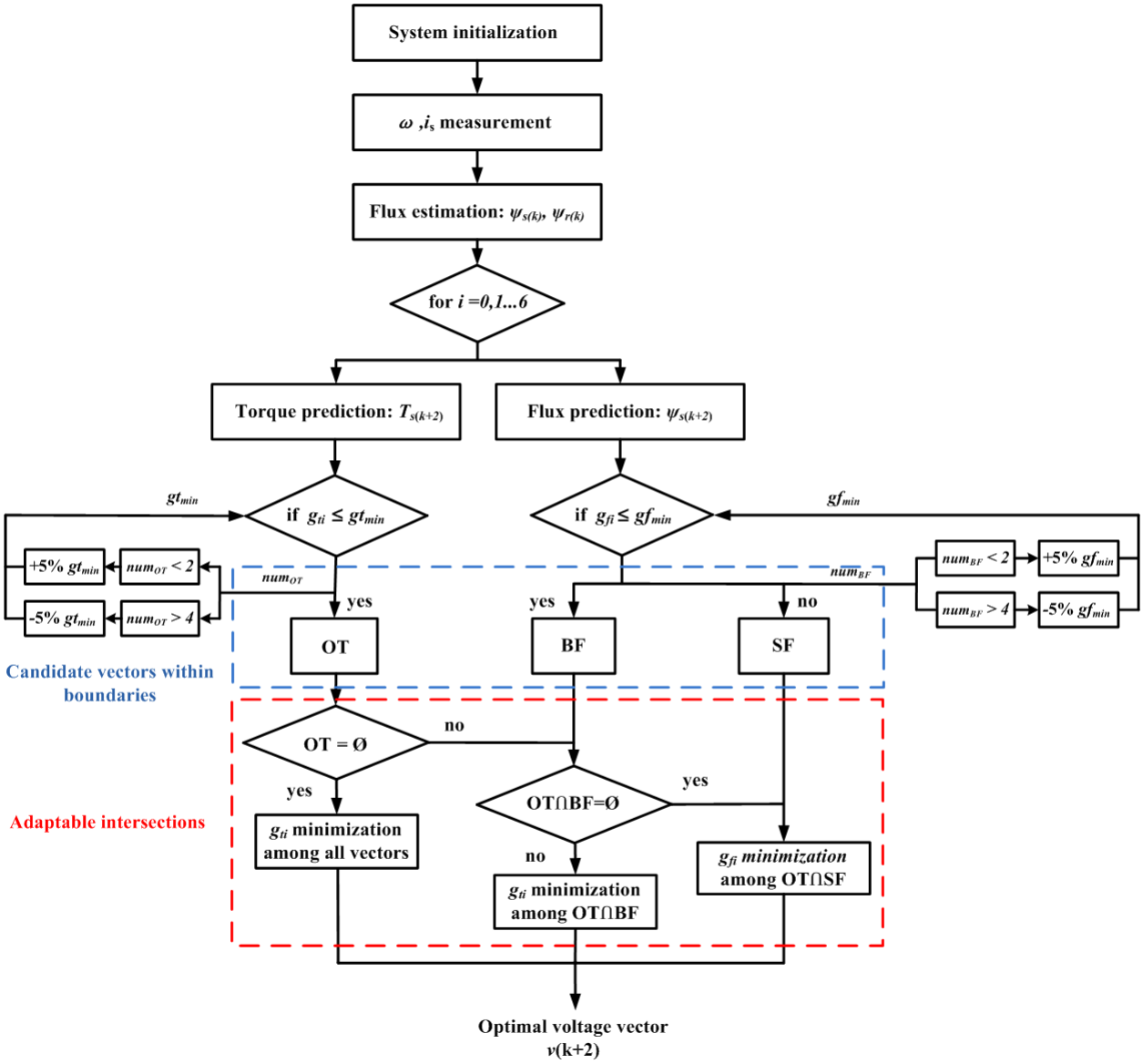

Figure 5.10: Flowchart of FCS-MPC with a constrained parallel structure.

be seen in Fig. 5.14, the tracking errors are 0.55 Nm and 7.07 %, which are smaller than that of conventional FCS-MPC with the fixed weighting parameters. The reason for this is the self-tuning of the weighting parameters in the parallel optimization principle.

The transient state performance of the proposed PPTC is investigated as follows. In Fig. 5.15, a load step occurs that the load torque alters from 2 Nm to 5 Nm. The torque and flux ripple of the proposed PPTC algorithm are 1.5 Nm and 0.12 Wb, respectively. The values are less than that of the conventional FCS-MPC method (2.0 Nm and 0.16 Wb). As shown in Fig. 5.16, The proposed PPTC method's torque ripple alters from 1.5 Nm to 1.7 Nm as flux magnitude rises. It is shown that, compared with conventional PTC, the proposed PPTC reduces torque and flux

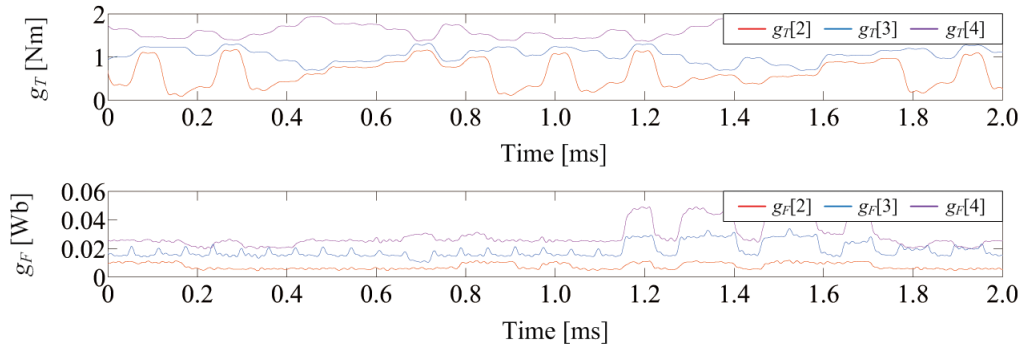

(a)

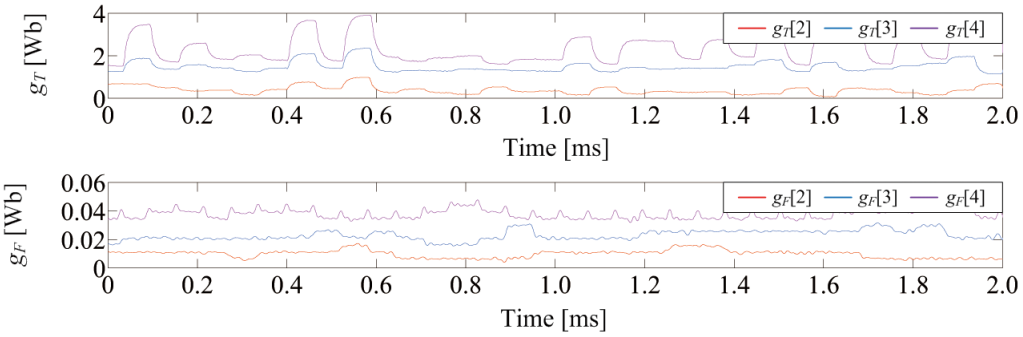

(b)

Figure 5.11: The values of g_T and g_F in two test scenarios. (a) 300 rpm with 4 Nm. (b) 2772 rpm with 7.5 Nm.

error by approximately 23 % and 36 %, respectively.

5.6 FCS-MPC with an ensemble regulation principle

As the multiple control targets are tackled in the multi-objective FCS-MPC, it is essential that the importance of both the core control targets and system demands are carefully regulated. In this section, the concept of the proposed ensemble regulation approach is presented. The proposed ensemble regulation principle for multi-objective FCS-MPC consists of priority evaluation, sorting algorithm and ensemble regulation mechanism. More specifically, the proposed ensemble regulation principle requires neither additional penalty coefficients nor knowledge of offline data resources.

Instead of incorporating multiple control targets in the objective function of the multi-objective FCS-MPC algorithm, the splitting of the objective function into multiple terms of single control target is proposed in (5.3). Therefore, the dimensions of the single terms are reduced to 1. It is obvious that no penalty coefficients are required in these one-dimension terms. It should be noted that a control system has both the major and supplement objectives.

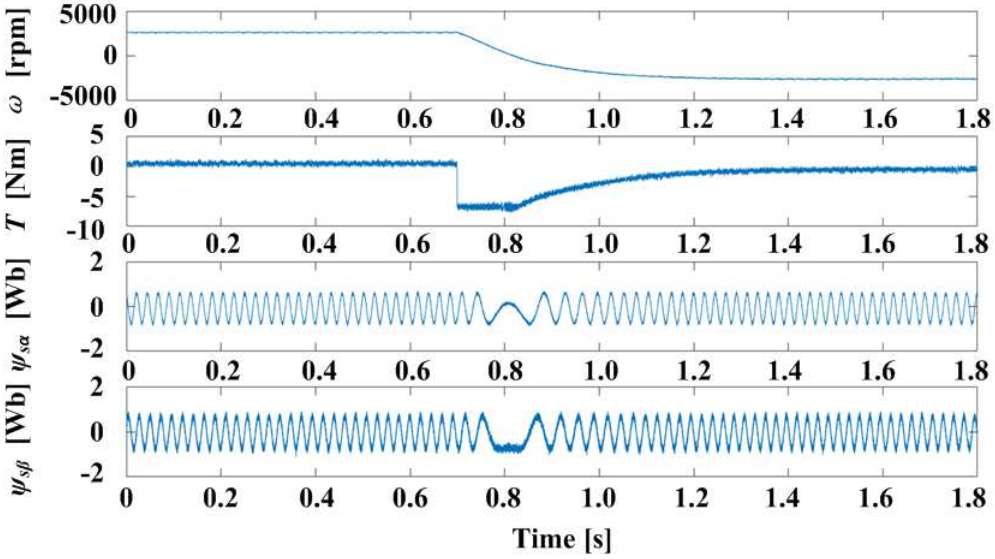

Figure 5.12: Speed reversal maneuver of FCS-MPC with a constrained parallel structure (from 2600 rpm to -2600 rpm without load torque).

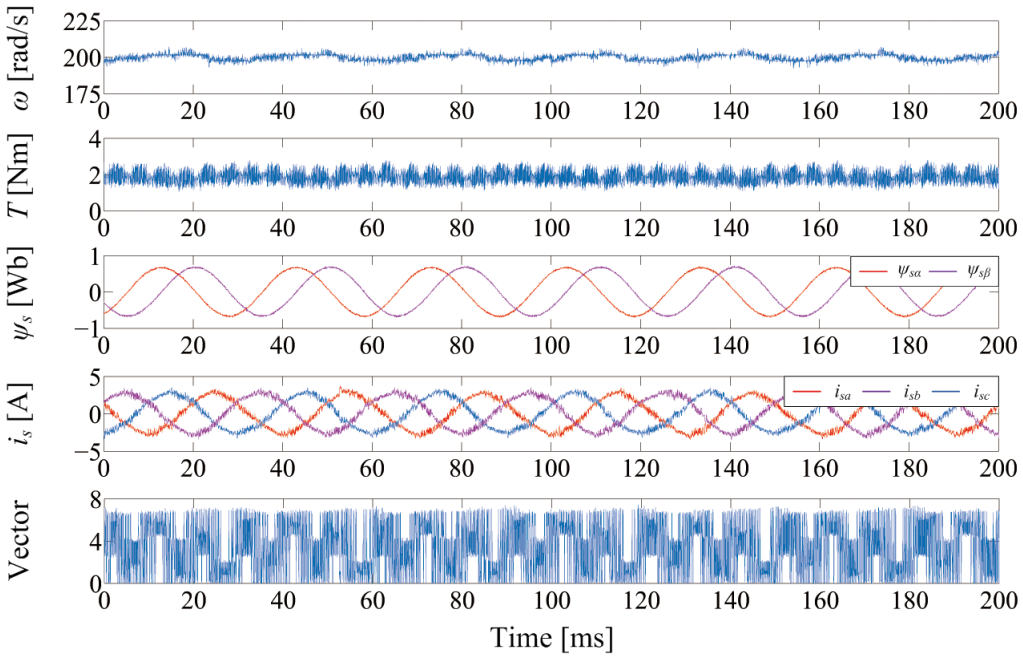

Figure 5.13: Steady-state performance of FCS-MPC with a constrained parallel structure at 200 rad/s with 2 Nm.

The priority of the major (more prior) objectives is higher than that of supplement (less prior) objectives. Although the one-dimension terms are optimized simultaneously, the sequence of applying the optimal solutions is determined by the priority of the specific control target. The priority of each control target in the multi-objective FCS-MPC algorithm is evaluated in

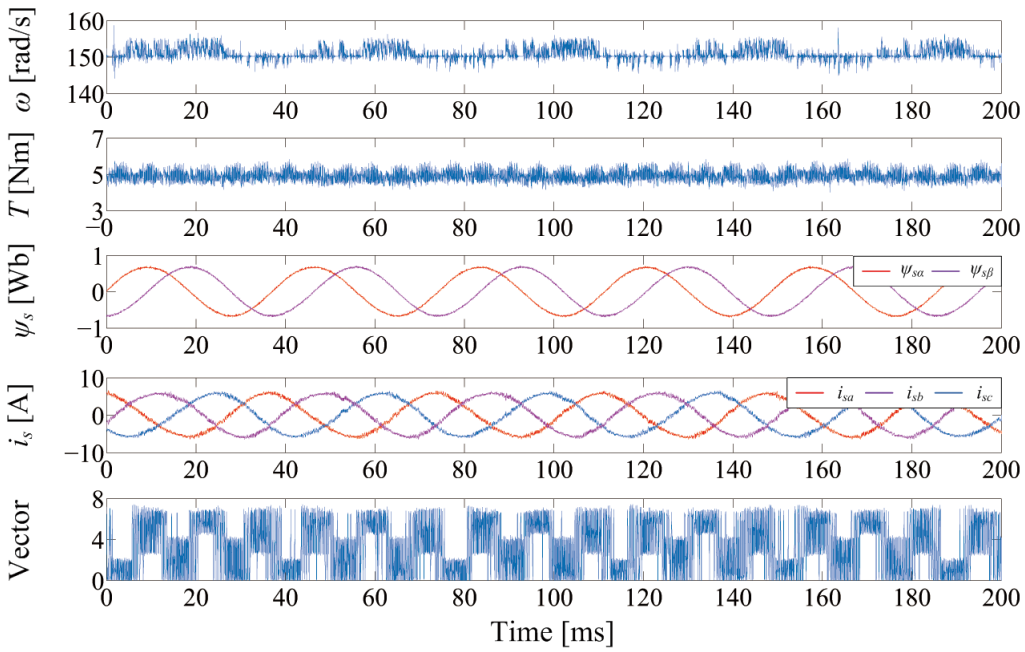

Figure 5.14: Steady-state performance of FCS-MPC with a constrained parallel structure at 150 rad/s with 5 Nm.

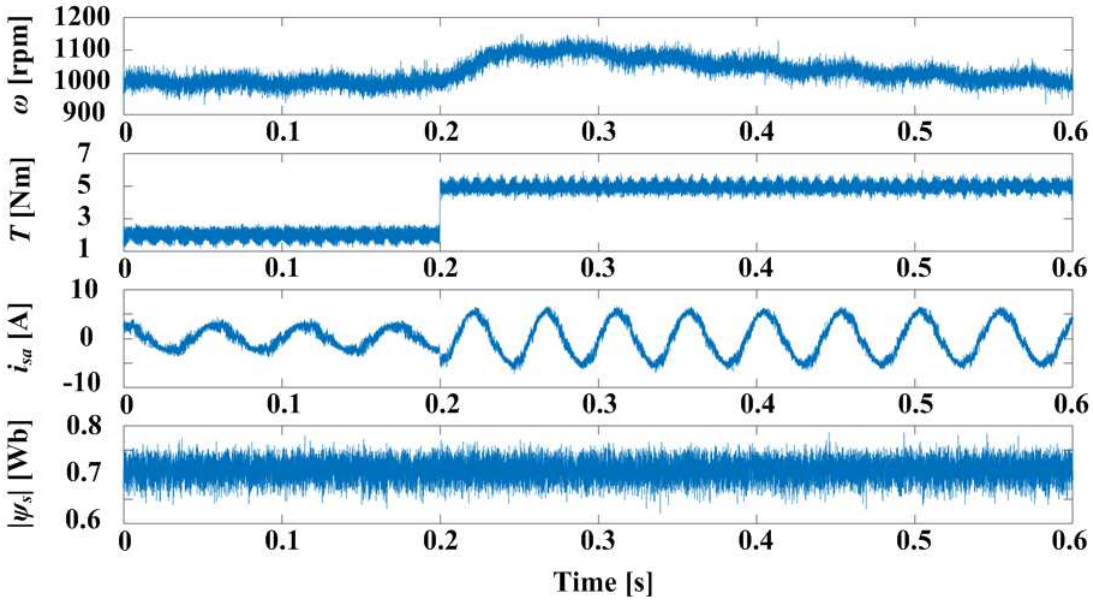

Figure 5.15: Load step performance of FCS-MPC with a constrained parallel structure. (ω = 1000 rpm, T alters from 2 to 5 Nm).

Fig. 5.17.

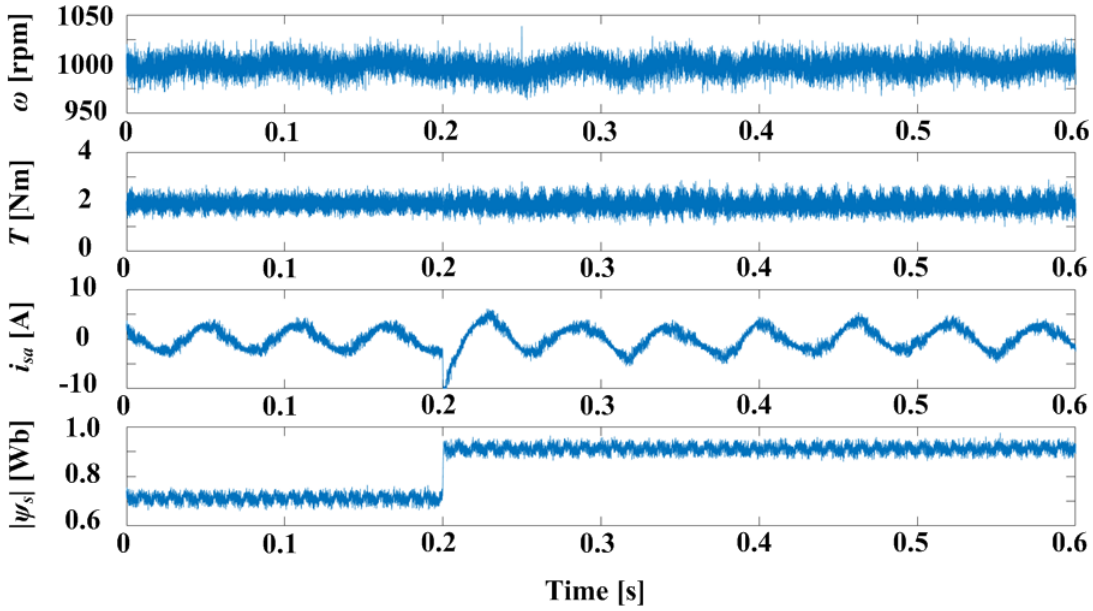

Figure 5.16: Load step performance of FCS-MPC with a constrained parallel structure. (ω = 1000 rpm, T = 2 Nm, flux magnitude decreases from 0.91 to 0.71 Wb).

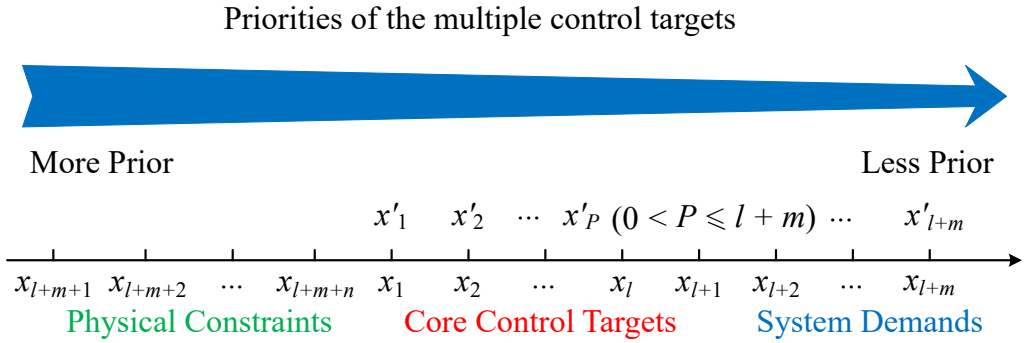

Figure 5.17: Priority evaluation of the multiple control targets in the FCS-MPC.

$$
\begin{aligned}
g(x_1)_j &= [x_1^* - x_1(k+2)_j]^2 \\
g(x_2)_j &= [x_2^* - x_2(k+2)_j]^2 \\
&\vdots \\
g(x_{l+m})_j &= \left[x_{l+m}^* - x_{l+m}(k+2)_j\right]^2 \\
g(x_{l+m+1})_j &= F_1(k+2)_j \\
g(x_{l+m+2})_j &= F_2(k+2)_j \\
&\vdots \\
g(x_{l+m+n})_j &= F_n(k+2)_j
\end{aligned}
\tag{5.3}
$$

As shown in Fig. 5.17, the multiple control targets in the multiobjective FCS-MPC algorithm are categorized as the core control targets, system demands and physical constraints. Among them the physical constraints take the highest priority to guarantee the safety of the control system, which are satisfied by the selected optimal solutions. The core control targets show a significant influence on the control performance of the multi-objective FCS-MPC algorithm, which are less prior than the physical constraints. The system demands are supplemented in the objective function for a certain application, which are of the least importance to be optimized. Based on the above, the physical constraint terms are inserted in the homogeneous terms $g(x_1)_j$, $g(x_2)_j$,...,$g(x_{l+m})_j$, as rewritten in (5.4).

$$g(x'_P)_j = [x'^*_P - x'_P(k+2)_j]^2 + \sum_{i=1}^{n} F_i(k+2)_j \tag{5.4}$$

where the integer P represents the priority of the control target, $0 < P \leq l + m$. The control target x'_P is more prior as P is smaller.

A sorting algorithm (SA) is conducted for each homogeneous objective term $g(x'_P)_j$, where P is integer, $0 < P \leq l + m$. The tracking deviations $g(x'_P)_j$ in (5.4) are compared among all the switching states, $\forall\, j \in 0, 1, \ldots, 6$. Three optimal switching states $b_P[0]$, $b_P[1]$ and $b_P[2]$ are regarded as the best-optimal solutions (stored in the array b_P), while the rest ($s_P[0]$, $s_P[1]$, $s_P[2]$ and $s_P[3]$) are the elements of the sub-optimal solutions (stored in the array s_P). It is noted that the tracking deviation $g(x'_P)$ is the smallest as $j = b_P[0]$, while it obtains the largest value as $j = s_P[3]$. Namely, the elements in b_P and s_P are sorted according to the tracking performance of the control target x'_P. The formulation of the best-optimal and suboptimal solutions is described in Fig. 5.18. Based on the above, an ensemble regulation mechanism (Step 3) is employed for the collected data in b_P and s_P, to obtain the optimal solution of the multi-objective FCS-MPC.

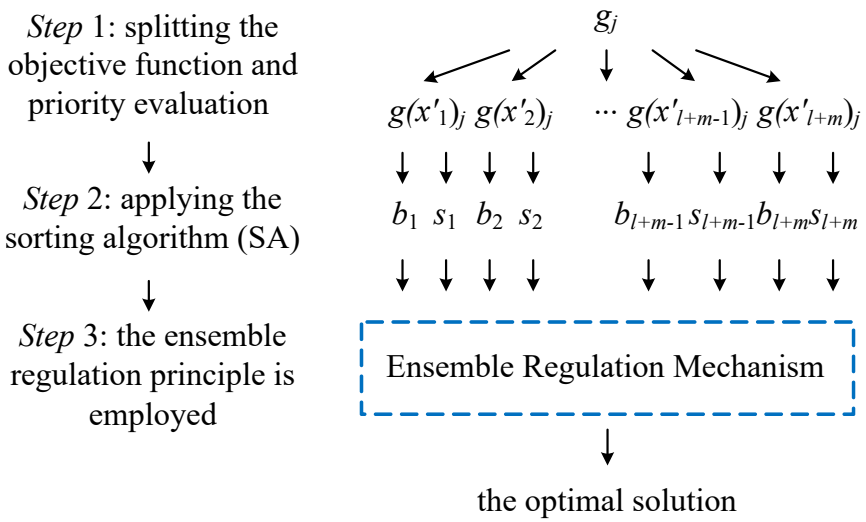

Figure 5.18: The formulation of the best-optimal and suboptimal solutions.

Finally, an ensemble regulation mechanism is established for the swept weighting parameters in the objective function of multi-objective DMPC. The optimal solution is generated

by searching the mutual switching states among b_1, b_2,..., and b_{l+m}. The concept is simple and straightforward that the mutual switching states among all the best-optimal solutions can achieve satisfactory performance for every control target. Considering that x'_1 is the control target with the most priority in x'_P, the switching state with minimum tracking deviation $g(x'_1)$ is selected when there are more than one mutual solutions. The reason for constraint tightening is, we expect to achieve better tracking performance of the control objective, which is of more importance. For example, $b_1[0]$ and $b_1[1]$ are the mutual best-optimal solutions among b_1, b_2,..., and b_{l+m}. $b_1[0]$ is selected as the optimal switching state to be delivered to the inverter, because the value of $g(x'_1)$ is smaller when $b_1[0]$ is applied.

Providing that there are no mutual switching states among all the best-optimal solutions, the constraint of the least important control target x'_{l+m} is preliminarily relaxed. To explore the potential mutual element, the sub-optimal solution s_{l+m} is applied instead of b_{l+m}. Therefore, the ensemble regulation mechanism is adjusted to find the mutual solution among b_1, b_2,..., and b_{l+m-1} and s_{l+m}. Likewise, the constraint of the control target with less priority is relaxed in sequence to search among b_1, b_2,..., b_{P-1} and s_P ($0 < P \leq l + m$), until the mutual solution is obtained. Two criteria are proposed to resolve the optimal solution as there are multiple mutual solutions. First, the mutual solutions are compared with the elements from b_{P+1} to b_{l+m} in the order of priority. The mutual solutions which are also the elements in the best optimal solutions of the more prior target are selected. To alleviate the negative influence of the sub-optimal solution s_P, the switching state with the smallest $g(x'_P)$ is regarded as the optimal solution. The flowchart of the proposed ensemble regulation mechanism is illustrated in Fig. 5.19.

The block diagram of multi-objective FCS-MPC combined with the proposed ensemble regulation principle is depicted in Fig. 5.20. The control objectives are predicted by the discrete model of the control plant. The priorities of the control targets are evaluated and the multiple homogeneous terms are constructed. The switching states are categorized by the sorting algorithm. Finally, the elements in the best-optimal and sub-optimal solutions are optimized by the ensemble regulation mechanism, to generate the optimal solution.

The proposed FCS-MPC with an ensemble regulation principle shows a competitive control performance at both the steady-state scenarios. For the first test scenario (as shown in Fig. 5.21), the tracking errors are T_{err} = 0.36 Nm , i_{serr} = 8.54 % and ψ_{serr} = 0.049 Wb, respectively. The tracking errors in the second scenario (as shown in Fig. 5.22) are T_{err} = 0.40 Nm , i_{serr} = 6.28 % and ψ_{serr} = 0.052 Wb. The turnaround time of the proposed FCS-MPC with an ensemble regulation principle is 37 μs.

The transient-state performance of the proposed FCS-MPC algorithm is tested. The IM starts at t = 0.9 s and a speed reversal maneuver is conducted at t = 2.9 s. Thereafter, a 5 Nm load torque disturbance is provided at t = 6.17 s. As shown in Fig. 5.23, it is confirmed that the proposed method shows fast transient response and performs well at a wide speed range. It can be observed that the electromagnetic torque rises from 0 to 5 Nm in 50 ms. The rotor speed suffers from a 15 rad/s drop and returns in 80 ms.

Finally, the principle of the proposed ensemble regulation method is analyzed. As shown in Fig. 5.24, three best solutions for both torque and stator flux optimization ($b_1[0-2]$ and $b_2[0-2]$) as well as the selected switching states are presented. It can be seen that the optimal voltage vectors are entirely selected from the torque best-optimized solutions (b_1). For selecting the flux best-optimized solutions (b_2), the possibility is approximately 62 %. Moreover, the distribution of the selected switching sequences is illustrated in Fig. 5.25. As concluded, the least torque

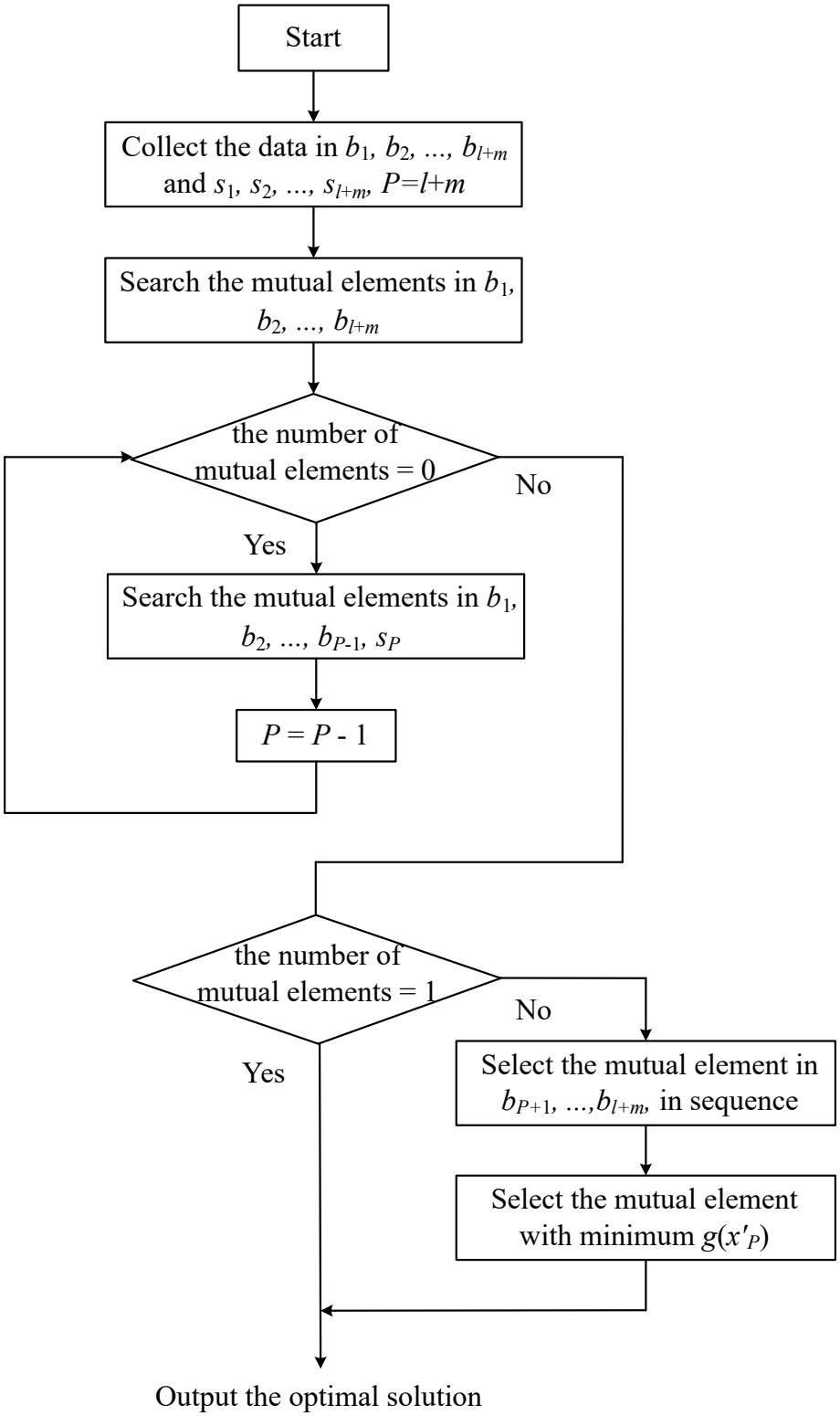

Figure 5.19: Flowchart of the ensemble regulation mechanism.

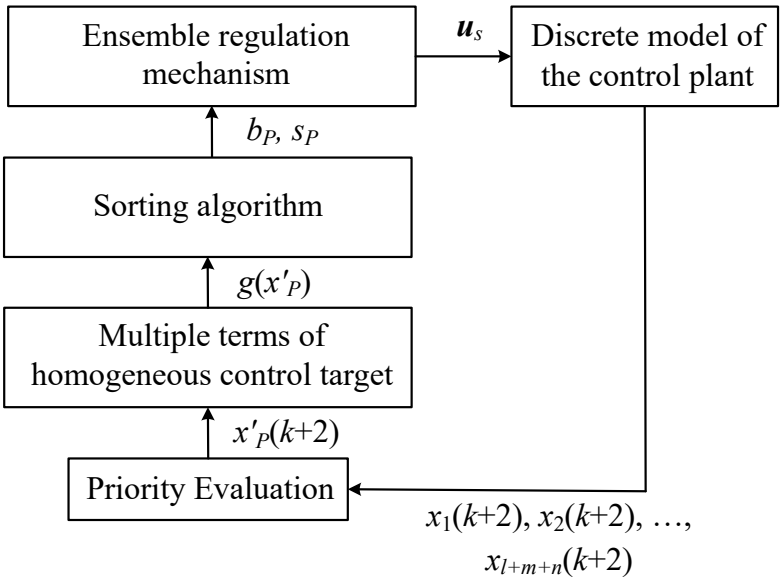

Figure 5.20: Block diagram of multi-objective FCS-MPC combined with ensemble regulation principle.

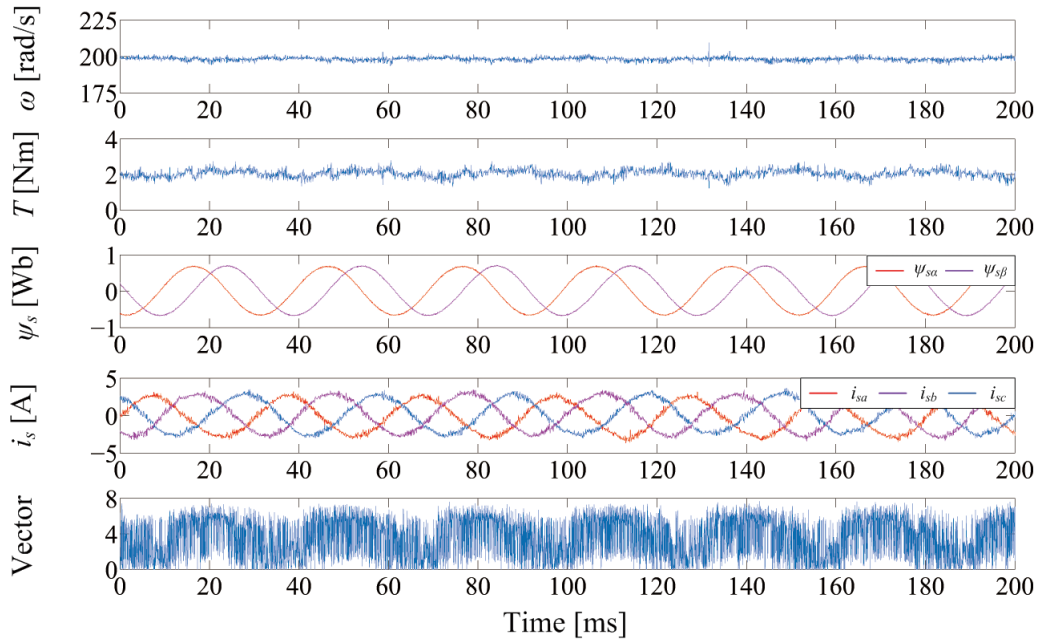

Figure 5.21: Steady-state performance of FCS-MPC with an ensemble regulation principle at 200 rad/s with 2 Nm.

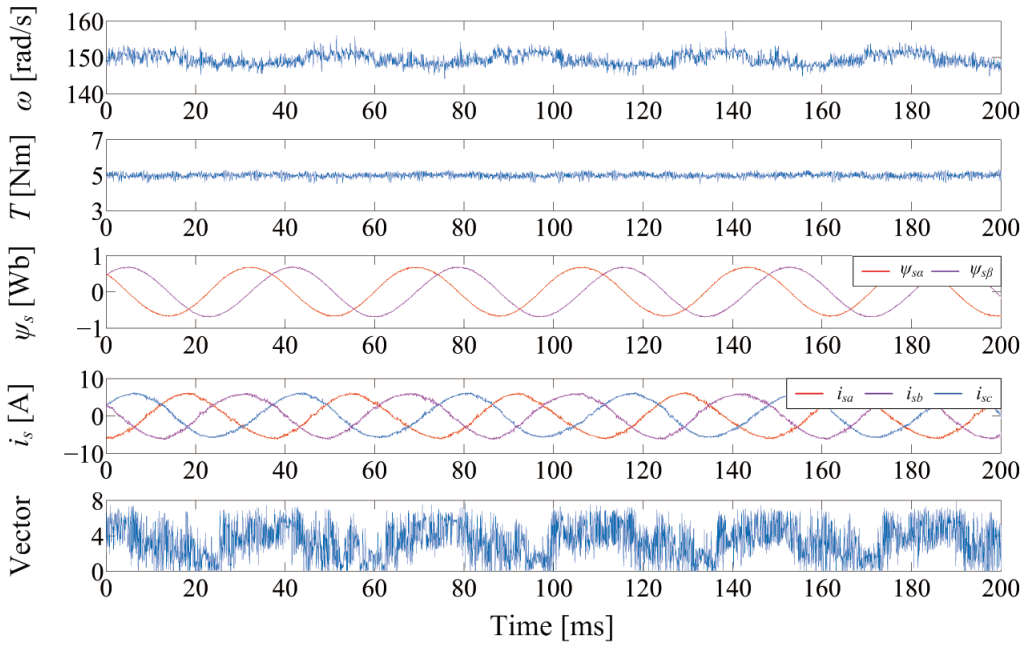

Figure 5.22: Steady-state performance of FCS-MPC with an ensemble regulation principle at 150 rad/s with 5 Nm.

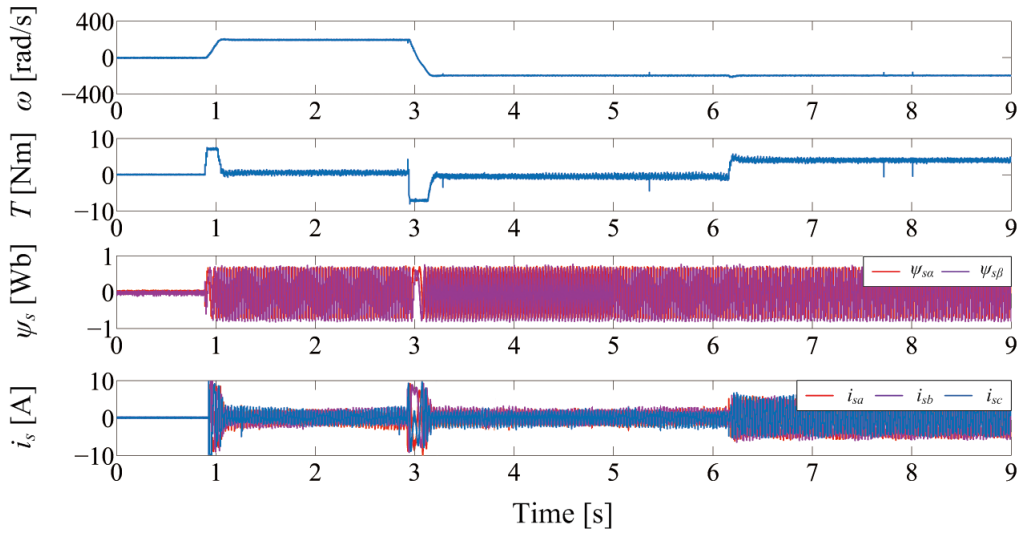

Figure 5.23: Dynamic performance of the proposed FCS-MPC algorithm. The IM starts at 0.9 s, the rotor speed reverses at 2.9 s with a 5 Nm load torque at 6.17 s.

error is obtained by 66 % of the optimal solutions, while the percentage for the smallest flux error is 26 %. Compared with the conventional method, the proposed FCS-MPC algorithm has more possibility to select the solutions with less tracking error.

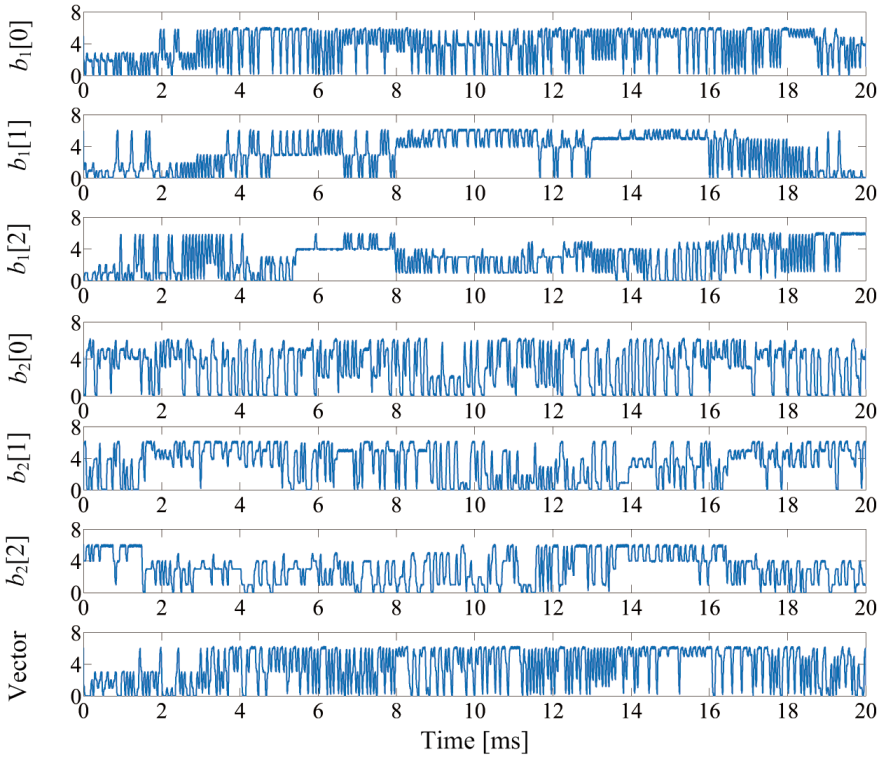

Figure 5.24: Comparisons between the best-optimal solutions for torque/flux and the selected switching sequences.

5.7 Conclusion

In this chapter, the solutions for the modification of the multiple control targets in the FCS-MPC schemes are investigated. First, the classification of the weighting parameter optimization solutions are proposed. Based on the above, several weighting parameter solutions for the FCS-MPC are evaluated and experimentally validated.

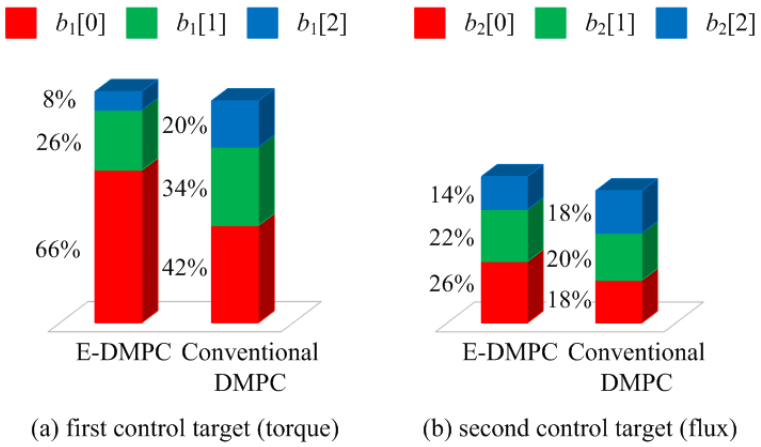

Figure 5.25: Comparisons between the percentage of selecting the best-optimal solutions.

CHAPTER 6

Objective function reformulation in FCS-MPC using a derivative projection

Multiple control targets, e.g., electromagnetic torque, stator current, voltage balance in the neural point and average switching frequency, are optimized in the objective function of the FCS-MPC schemes. The optimal switching sequence is selected by minimizing the predefined objective function, to reduce the tracking errors. Thus, an improved control performance is achieved in FCS-MPC. However, the conventional FCS-MPC schemes still suffers from the inherent drawbacks, i.e., high ripples at the steady state and high computational burden. In this chapter, the objective function is reformulated in the FCS-MPC schemes using a derivative projection, to tackle the abovementioned issues.

6.1 Introduction

The state-of-the-art FCS-MPC algorithms can be considered as an emerging control strategy for the electrical drive systems, due to its flexible definition of the control targets. FCS-MPC shows the superiority on straightforward concept, simple implementation, fast dynamic response and low switching frequency, which has become an attractive alternative to the conventional control strategies, e.g., direct torque control (DTC) and field oriented control (FOC).

One of the drawbacks in the FCS-MPC schemes is the high computational burden. In FCS-MPC, all the possible control inputs are enumerated in the prediction and optimization stage, to resolve an optimal solution in the optimization problem. However, the computational effort will be very high via an exhaustive search, especially in the multilevel converters and multistep implementations. It is noteworthy that the number of searched control inputs grows exponentially with an increased number of the prediction horizon. As we can understood, some of the control inputs are not likely to be the optimal solution in the implementation. For example, the tracking errors will be definitely larger with the movement in a prediction horizon, when the direction of the movement is opposite to that of the reference. Based on the above, the preselection principle

is designed to distinguish the desired and undesired control inputs. The computational effort of FCS-MPC can be significantly reduced without the sacrifice of the control performance, as the undesired control inputs are unvisited in the prediction and optimization stage. Several computationally-efficient methods have been investigated in the previous work. [49] introduces a Quasi-centralized direct MPC scheme incorporates with computationally efficient concept for the back-to-back converter based PMSG wind turbine system. The DC-link voltage tracking errors are eliminated by a flexible cost function using revised dynamic reference. In [50], a low-complexity approach for single vector based MPC is proposed. Unfortunately, it is limited by special applications. In [51], a weighting factor-less FCS-PTC with reduced complexity for five-phase PMSM is presented. Furthermore, a three-vector based direct predictive power control for doubly fed induction generators is proposed in [52]. However, the comparisons between the three-vector method and one-vector method are conducted at the different switching frequencies.

The latter drawback is, the tracking deviations is relatively high at the steady state, because only one switching state is employed in the entire sampling period in FCS-MPC. The reason relates to this is the discrete nature of the finite control set. In [53], the multistep FCS-MPC scheme for the three-level inverter is investigated as a case study and its performance is further evaluated in [54]. Although a simple rounding scheme is developed to alleviate the exponential growth of the switching sequences, the computational effort of multistep FCS-MPC is still larger than that of conventional FCS-MPC. In [55], a computationally efficient multistep direct predictive torque control (DPTC) is proposed for surface-mounted permanent magnet synchronous motor (PMSM). The number of candidates is reduced by the look-up table to avoid exhaustive searching. However, the multistep DPTC approach still suffers from high computational complexity that the computational time of the algorithm is about 50 μs with 3 horizons. [56] introduces a multistep MPC with voltage and current constraints for linear induction machine (LIM), to yield better closed-loop performance and reduced calculation burden. However, the FCS-MPC with a longer predictive horizon shares the same drawbacks with [53], which have not been fundamentally solved. Authors in [57] present a FPGA-implemented longhorizon FCS-MPC with a nonrecursive sphere decoding algorithm (SDA). The effectiveness of the controller at a prediction horizon of 5 is experimentally verified. It is noted that the amount of switching sequences is decreased by the SDA in a non-recursive manner, However, the long-horizon FCS-MPC strategies rely on the emerging high-performance controllers such as system-on-chip based FPGA (SOC-based FPGA) and dSPACE, especially for the multi-level converter applications. In [58], a long-horizon FCS-MPC algorithm combined with a branch-and-bound strategy and moving blocking scheme, is adopted to control the quasi-Z-source inverter (qZSI). However, the tradeoff between the length of horizon and the computational burden is required in the long-horizon FCS-MPC strategies. In [59], the optimization problem underlying multistep FCS-MPC is formulated to be solved by a fast SDA, in order to show a significant improvement in the current THD of the cascaded H-bridge inverters. Moreover, it is potential to further reduce the amount of control inputs over a prediction horizon. As concluded in [60], a fixed switching frequency based multi-vector predictive torque control for six phase PMSM is proposed. However, the deadbeat principle is employed to select the optimal vectors and calculate their duty ratios, which raises more concern on robustness improvement. In [61], a multi-vector MPC algorithm with geometric solution for five-phase flux-switching permanent magnet motor is experimentally verified. In [62], a two-vector based MPC is presented for

performance improvement of the PWM rectifier. The average switching frequency is reduced by 30 % compared to the prior algorithm due to the modulated deadbeat solution. In order to control a three-level inverter with LC filter, MPC combined with modulated optimal vector is introduced in [63], but the additional space-vector modulation stage is also required.

6.2 Objective function reformulation using a derivative projection

The proposed computationally efficient predictive current control (PCC) with an extension of finite set (PCC-II) is consist of the following components: current derivative calculation, preselection principle, duty cycles optimization by the least-squares (LS) method and objective function minimization. The components of the proposed controller are introduced in detail as follows.

6.2.1 Derivation projection

Instead of the predicted values calculated by the forward Euler discretization in the conventional FCS-PCC algorithms, the proposed method directly generates the desired stator current derivative for zero-error tracking as the reference, which is defined in (6.1).

$$\frac{dx^*(k)}{dt} = \frac{x^*(k) - x(k)}{T_s} \tag{6.1}$$

where T_s is the sampling period, $x = [i_{s\alpha}, i_{s\beta}]^T$, $x^*(k) - x(k)$ denotes the forward difference of the state variable at k interval. The derivative of $x(k)$ can be directly obtained by the state-space model in (3.1). The geometric description of the optimization problem underlying FCS-PCC is shown in Fig. 6.1(a), while the control variable $x(k)$ and the its reference value x^* are projected on their derivatives $dx(k)/dt$ and $dx^*(k)/dt$ in Fig. 6.1(b). It is noteworthy that the derivative of the control variable dx/dt can be formulated in the objective function using current derivative projection. As shown in the stationary frame in Fig. 6.1(b), the desired stator current derivative $dx^*(k)/dt$ is calculated by (6.1). Simultaneously, for every switching sequence the stator current derivative $dx(k)/dt_j$, $\forall j = 0, 1, \ldots, 6$, is achieved.

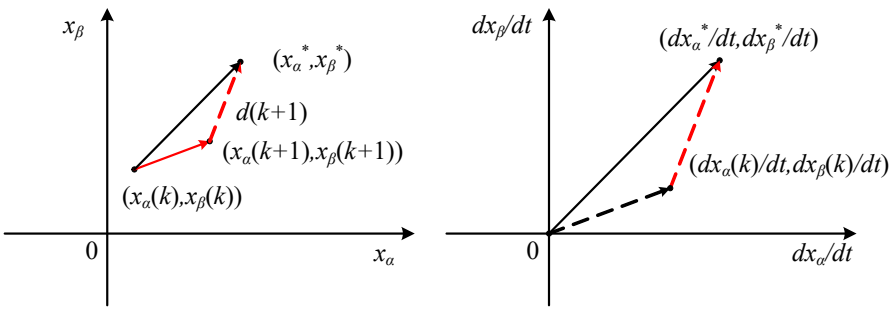

Figure 6.1: Geometric description of the derivative projection in the optimization problem underlying FCS-PCC. (a) without derivative projection. (b) with derivative projection.

It is noteworthy that the FCS-PCC scheme can mitigate the discretization error using a derivative projection instead of forward Euler formula, because the predicted values are not required in the reformulated objective function of the proposed scheme. Considering that the derivatives of variables are also applied in the prediction stage of the conventional FCS-PCC, the derivative projection will not result in the wrong selection of the optimal solution.

6.2.2 Formulation of the objective function

To obtain a satisfactory control performance, it is required to reduce the tracking error between the calculated and the desired stator current derivative in the proposed algorithm. Unfortunately, the discrete nature of both the switching sequences and the corresponding stator current derivatives inevitably yields a high tracking deviation. Considering that the time-delay compensation, the selected stator current derivative $dx(k)/dt$ at k interval and $dx(k+1)/dt_j$ (for optimization) are introduced to synthesize the potential solution. As shown in Fig. 6.2(b), the synthesized solution is constructed by $dx(k)/dt$ and $dx(k+1)/dt_j$ as an example. Their duty cycles $t(k)_j$ and $t(k+1)_j \in [0,1]$ are optimized by the LS method to minimize the quadratic objective function g_j, which is rewritten as the squared Euclidean-norm of the tracking derivation $d(k+1)_j$.

$$\begin{aligned} g_j &= \|d(k+1)_j\|_2^2 \\ &= (t(k)_j \frac{dx_\alpha(k)}{dt} + t(k+1)_j \frac{dx_\alpha(k+1)}{dt}_j - \frac{dx_\alpha^*(k+1)}{dt})^2 \\ &+ (t(k)_j \frac{dx_\beta(k)}{dt} + t(k+1)_j \frac{dx_\beta(k+1)}{dt}_j - \frac{dx_\beta^*(k+1)}{dt})^2 \end{aligned} \tag{6.2}$$

$$subject\ to\ t(k)_j + t(k+1)_j = 1 \tag{6.3}$$

where the derivative of reference at the instance $k+1$ is calculated with the known information at the instance k (assuming that $x^*(k) = x^*(k+1)$).

6.2.3 Optimization of the duty cycle

As expressed in (6.4), the objective function g_j is partial differentiated with $t(k)_j$ and $t(k+1)_j$. To optimize the duty cycles, the minimal value of the objective function g_j is achieved by solving its partial derivatives to zero.

$$\frac{\partial g_j}{\partial t(k)_j} = 0, \quad \frac{\partial g_j}{\partial t(k+1)_j} = 0 \tag{6.4}$$

which is rewritten as

$$\begin{aligned} \frac{\partial g_j}{\partial t(k)_j} &= 2\frac{dx_\alpha(k)}{dt} d_\alpha(k+1)_j + 2\frac{dx_\beta(k)}{dt} d_\beta(k+1)_j = 0 \\ \frac{\partial g_j}{\partial t(k+1)_j} &= 2\frac{dx_\alpha(k+1)}{dt}_j d_\alpha(k+1)_j + 2\frac{dx_\alpha(k+1)}{dt}_j d_\beta(k+1)_j = 0 \end{aligned} \tag{6.5}$$

where $d_\alpha(k+1)_j$ and $d_\beta(k+1)_j$ are the components of stator current derivative tracking deviation in the $\alpha\beta$ frame. Therefore, the duty cycles $t(k)_j$ and $t(k+1)_j$ are solved with the

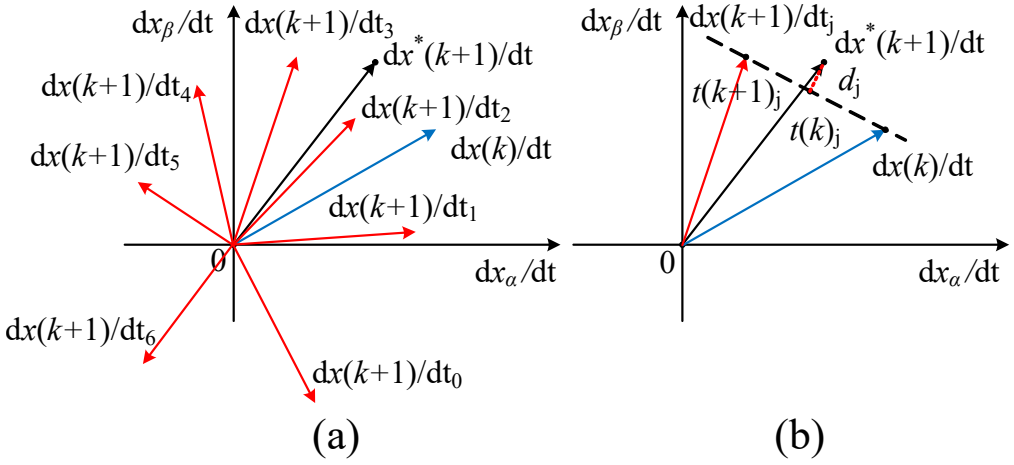

Figure 6.2: Description of the stator current derivatives in the stationary $\alpha\beta$ frame. (a) The desired and applied stator current derivatives. The black line is the desired current derivative, the blue line is the optimal current derivative at k interval, the red lines are the applied current derivatives at $k+1$ interval. (b) The synthesis of current derivatives with least-squares optimized duty cycles. The tracking deviation d_j is represented by the red dashed line.

constraint (6.3). At last, the optimal stator current derivative incorporated with the corresponding duty cycles are selected via sorting the minimal value of the objective function $g_j(min)$. The optimal solution minimizes $g_j(min)$ most is delivered to the inverter.

6.2.4 Preselection principle

To avoid exhaustive search, a preselection principle is introduced in the proposed PCC-II algorithm to alleviate the computational burden by reducing the number of searched control inputs. As shown in Fig. 6.3(a), seven control inputs are exhaustive searched without the preselection principle, to resolve the optimal solution in the reformulated objective function. It is noteworthy that the directions of several current derivatives (i.e., $dx(k+1)/dt_{0,5,6}$ in Fig. 6.3(a)) are opposite to that of the desired derivative $dx^*(k+1)/dt$. The tracking deviation d_j is larger when the current derivative with an opposite direction is applied with the former optimal solution $dx(k)/dt$. Therefore, the current derivative with an opposite direction can not be selected as the optimal solution. Based on the above, the finite set is divided into two regions according to the angle θ between the applied and desired current derivative. As shown in Fig. 6.3(b), the angle θ is an acute angle $(\theta \leq \pi/2)$ in the red region, while θ is an obtuse angle $(\theta \geq \pi/2)$ in the purple region. The current derivatives in the red region are employed in the formulation of the objective function and the optimization stage. On the contrary, the derivatives in the purple region are unvisited in the preselection principle. It can be observed that the proposed preselection principle can significantly reduce the computational burden of the proposed PCC-II algorithm while retains the optimal tracking performance.

The close-loop control schematic of the proposed PCC-II is shown in Fig. 6.4, which includes four control components, i.e., current derivative calculation, preseletion principle, duty cycles optimization and objective function minimization. First, the desired and applied current derivatives are calculated by the system model. Based on the above, the finite set is divided into two

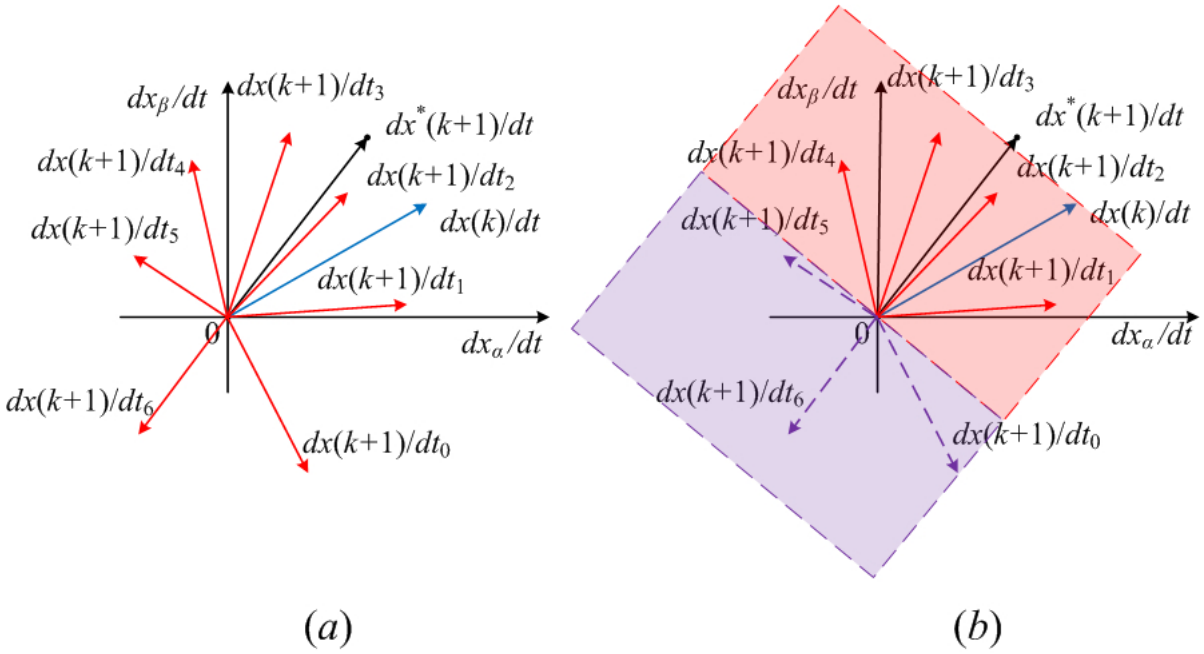

Figure 6.3: Comparisons between the two search approaches in the proposed PCC-II algorithm. (a) exhaustive search (b) preselection principle.

separate regions to preselect the control inputs. The control inputs in the red region are used for the formulation and optimization of the objective function, while those in the purple region are unvisited. Therefore, the computational burden of the proposed algorithm can be significantly reduced by the preselection principle. Subsequently, the objective function is formulated as the quadratic Euclidean norm of the tracking deviation, in which the duty cycles are optimized by the LS method. The current derivatives as well as their duty cycles that minimize the objective function the most are selected as the optimal solutions for the controller.

The flowchart of the proposed PCC-II algorithm is illustrated in Fig. 6.5. Moreover, the execution steps in the proposed algorithm are described in Algorithm 1.

6.3 Experimental validation

6.3.1 Speed reversal maneuver

First, the feasibility of the proposed PCC-II algorithm is verified by the experimental implementing during a full speed reversal maneuver, as reported in Fig. 6.6. The IM initially operates at 290 rad/s, and a speed step change to -290 rad/s occurs at t = 0.86 s subsequently. Owing to that the quick dynamic response of FCS-MPC schemes, it is indicated that the speed reversal duration of the proposed PCC-II algorithm is 270 ms. Due to the LS optimized tracking deviations, it is obvious that the proposed method shows the benefits for reduced electromagnetic torque and stator current errors (T_{err} = 0.85 Nm and $i_{serr}/||i_s||$ = 6.6 %). Compared with that of conventional FCS-PCC (T_{err} = 1.21 Nm and $i_{serr}/||i_s||$ = 13.4 %), the values are decreased by 29.8% and 50.7%. The turnaround time and average switching frequency of the proposed

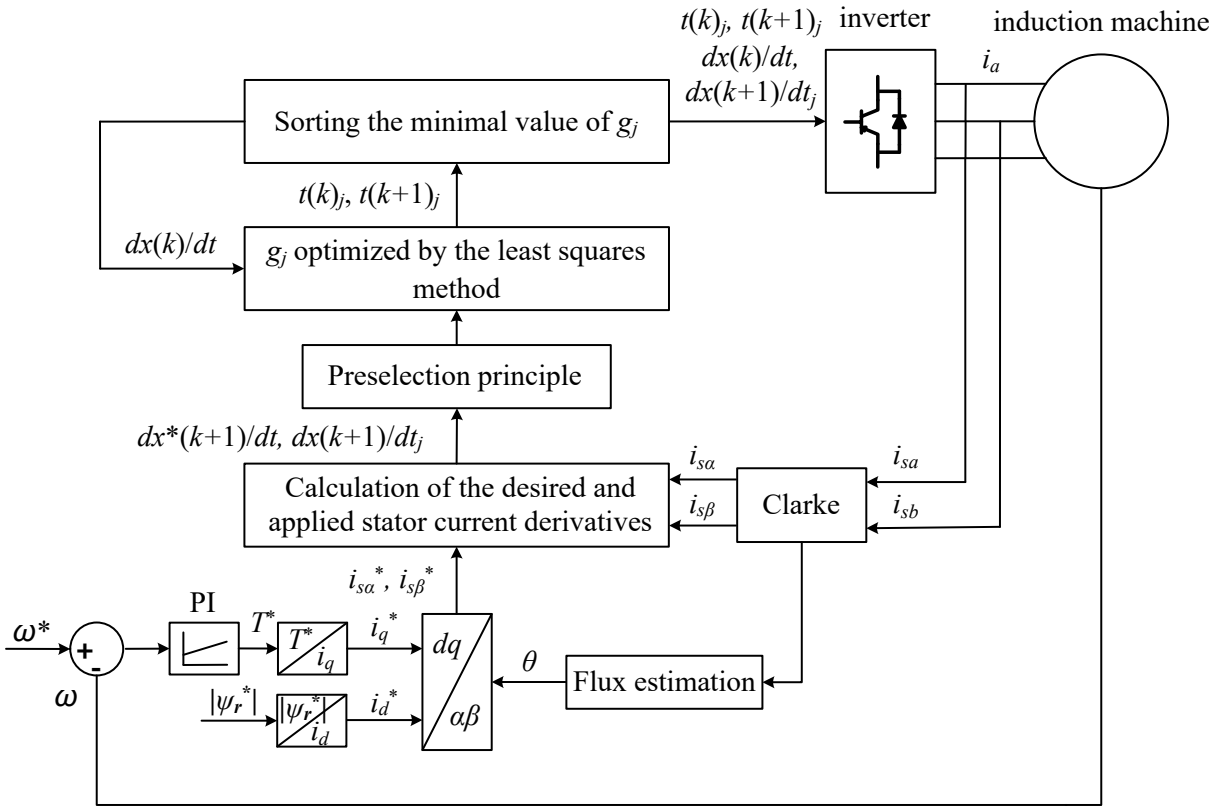

Figure 6.4: Block diagram of the proposed PCC-II algorithm.

algorithm are 27 μs and 3.8 kHz, respectively. The comparative performance metrics between the conventional FCS-PCC and PCC-II algorithms during the speed reversal maneuver are summarized in TABLE.6.1. More specifically, it is confirmed that the proposed PCC-II algorithm performs well at the whole speed range.

Table 6.1: The comparative performance metrics between conventional FCS-PCC and PCC-II during the speed reversal maneuver

Metrics	FCS-PCC	PCC-II
speed reversal duration [ms]	300	270
T_{err} [Nm]	1.21	0.85
ψ_{rerr} [Wb]	0.04	0.03
$i_{serr}/\|\|i_s\|\|$ [%]	13.4	6.6
f_{sw} [kHz]	3.3	3.8

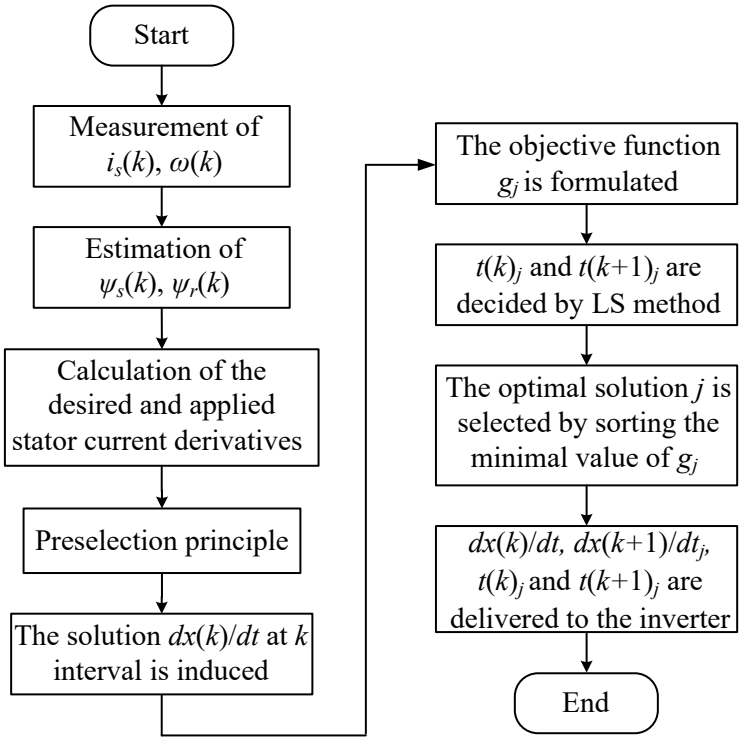

Figure 6.5: Flowchart of the proposed PCC-II algorithm.

Algorithm 1 The execution of the proposed PCC-II algorithm

1: System initialization, rotor speed and stator current measurement, stator and rotor flux estimation.
2: Calculation of the desired and applied stator current derivatives $dx^*(k+1)/dt$ in (6) and $dx(k+1)/dt_j$ in (10), $\forall j = 0, 1...6$.
3: A preselection principle is introduced to divide the finite control set into two separate regions. The control inputs in the purple region are unvisited.
4: The synthesized current derivative is achieved by $dx(k)/dt$ and $dx(k+1)/dt_j$. The objective function g_j is further formulated.
5: The duty cycles $t(k)_j$ and $t(k+1)_j$ for the applied current derivatives $dx(k)/dt$ and $dx(k+1)/dt_j$ are optimized by the least-squares method to yield the minimal value of g_j.
6: The minimal value of the objective function $g_j(min)$ is sorted within the preseleted control set. The control input that minimizes $g_j(min)$ most is selected as the optimal solution.
7: The optimal switching sequences in the continuous sampling periods incorporated with their duty cycles are delivered to the inverter.

6.3.2 Steady-state performance

Fig. 6.7 illustrates the steady-state performance of the conventional FCS-PCC, duty-cycle based FCS-PCC and the proposed PCC-II algorithm, from up to down are the measured waveforms of rotor speed, electromagnetic torque, rotor flux and stator current. In the first steady-state test scenario, the IM operates at 50 rad/s with a 3 Nm load torque. As shown in Fig. 6.7(a), the conventional FCS-PCC suffers from the largest torque and stator current errors, which are

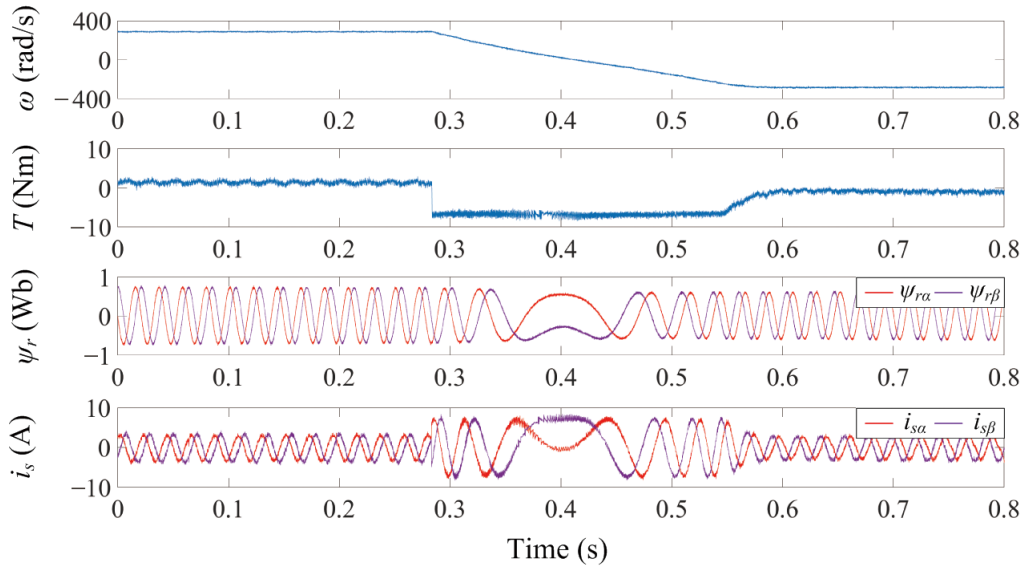

Figure 6.6: Experimental results: speed reversal performance of the proposed PCC-II algorithm from 290 rad/s to -290 rad/s.

T_{err} = 1.68 Nm and i_{serr} = 0.47 A ($i_{serr}/||i_s||$ = 12.3 %), respectively. The duty-cycle based FCS-PCC achieves the advantages of smaller torque and current tracking errors, due to the extension of the finite set. Compared with the conventional FCS-PCC, the values are decreased by 27.4 % and 46.8 %. However, the duty-cycle based FCS-PCC is penalized by a higher f_{sw} because the number of applied vectors in a sampling period is more than 1. The proposed PCC-II algorithm improves the steady-state performance without the increased number of applied switching states in each sampling period. The reason for this is at most one vector is employed in a sampling period averagely. Compared with the duty-cycle based FCS-PCC at the same switching frequency f_{sw} = 2.0 kHz, the proposed PCC-II algorithm obtains a further reduction on torque and current by 13.1 % and 24.0 %, respectively. It can be observed that the proposed PCC-II achieves the least tracking deviations among the three algorithms in the first test scenario.

The second test scenario is conducted among the three algorithms at 200 rad/s with a 5 Nm load torque, as shown in Fig. 6.8. Compared with the first steady-state scenario, a larger torque error (T_{err} = 1.83 Nm) and less stator current deviation (i_{serr} = 0.51A, $i_{serr}/||i_s||$ = 10.4 %) is obtained in the conventional FCS-PCC. Similar trend can be found in the comparative results among the three algorithms in the second scenario. As depicted in Fig. 6.8(b), the tracking errors of torque and stator current in the duty-cycle based FCS-PCC is reduced by 8.7 % and 35.3 %, when compared with the values of the conventional FCS-PCC. Moreover, it can be observed in Fig. 6.8(c) that the proposed PCC-II algorithm achieves the least tracking errors (T_{err} = 1.15 Nm and i_{serr} = 0.24A). The comparative performance metrics of three algorithms at the steady state are summarized in TABLE 6.2.

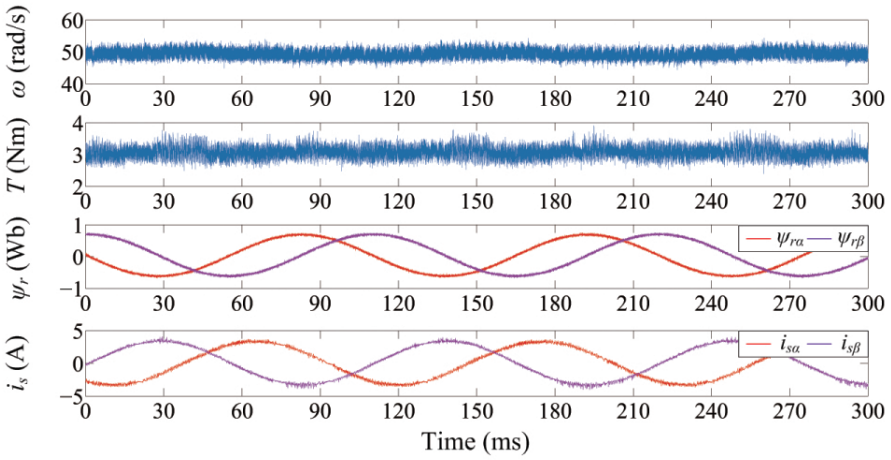

(a)

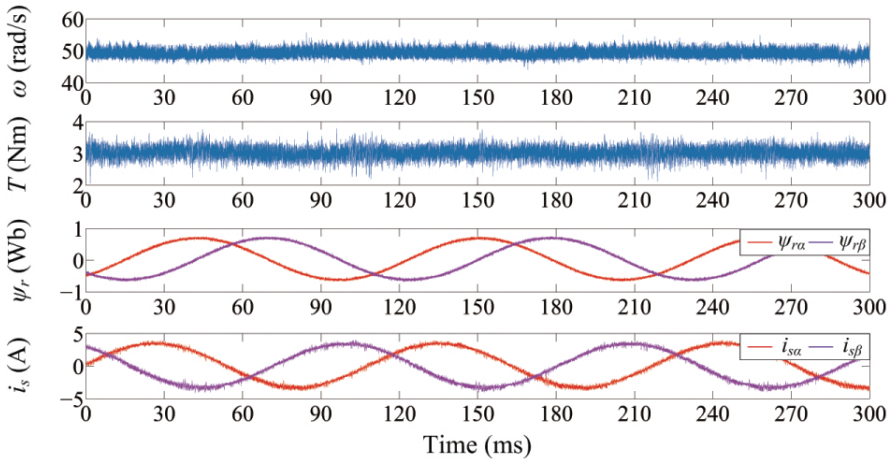

(b)

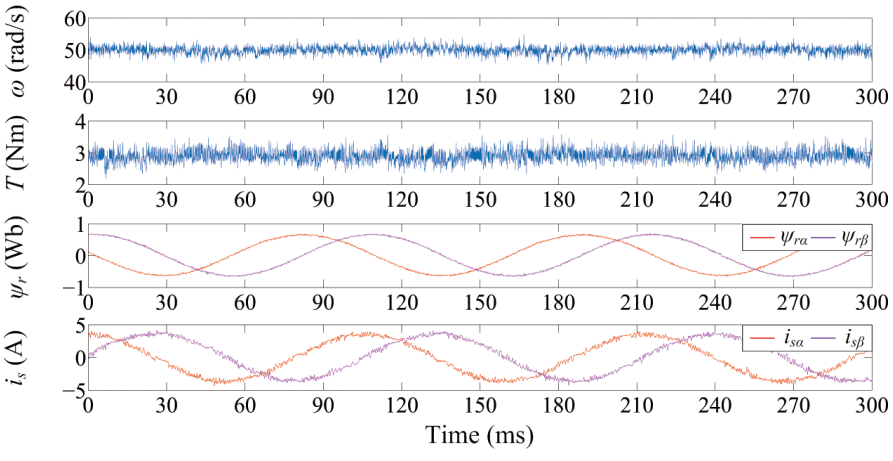

(c)

Figure 6.7: Experimental results: steady-state performance at 50 rad/s with a 3 Nm load torque. (a) conventional FCS-PCC. (b) duty-cycle based FCS-PCC. (c) the proposed PCC-II algorithm.

Table 6.2: The comparative performance metrics among the three algorithms at the steady state

50 rad/s, 3 Nm	FCS-PCC	duty-cycle based FCS-PCC	PCC-II
T_{err} [Nm]	1.68	1.22	1.06
ψ_{rerr} [Wb]	0.045	0.039	0.034
i_{serr} [A]	0.47	0.25	0.19
200 rad/s, 5 Nm	FCS-PCC	duty-cycle based FCS-PCC	PCC-II
T_{err} [Nm]	1.83	1.67	1.15
ψ_{rerr} [Wb]	0.048	0.044	0.036
i_{serr} [A]	0.51	0.33	0.24

6.3.3 Transient-state performance

The transient-state performance among the three algorithms are investigated, which includes speed step test and load step test. The speed step performance is initially evaluated. The IM works at a rotor speed of 100 rad/s, and a 3 Nm load torque is provided by the control panel. A speed step from 100 rad/s to 150 rad/s is suddenly carried out by the algorithms at t = 80 ms. As can be seen in Fig. 6.9(c), the rotor speed rises from 100 rad/s to 150 rad/s in 58 ms. A similar rise time of rotor speed (about 60 ms) can be found in the conventional FCS-PCC and duty-cycle based FCS-PCC, due to the same parameters (k_p = 0.23, k_i = 5.38) in the speed PI regulator. Compared with the conventional FCS-PCC, the proposed algorithm shows the superiority of 23.7 % and 51.8 % reduction in terms of torque and current errors. The proposed PCC-II algorithm achieves the least tracking deviations at the steady state, while retains a fast dynamic response during the transient state.

The load step performance of the conventional FCS-PCC, duty-cycle based FCS-PCC and the proposed PCC-II algorithm are compared in Fig. 6.10. As shown, the IM operates at the given rotor speed 100 rad/s which is provided by the control panel. The initial value of the torque reference is 5 Nm, which suddenly drops to 3 Nm within 400 μs as the load step takes place. As shown in Fig. 6.10(c), the rotor speed decreases to about 83 rad/s and then recovers to the original value within 200 ms simultaneously. It can be observed that the proposed algorithm retains the merit of fast dynamic response of its counterpart FCS-PCC algorithms. The error of rotor flux magnitude in the proposed PCC-II algorithm is 0.03 Wb. Compared with the conventional FCS-PCC algorithm, the torque and stator current errors of the proposed algorithm is decreased by 41.5 % and 37.5 %, respectively.

6.3.4 Robustness validation

In this section, the robustness validation to parameter variations (i.e. R_r and L_m) of the proposed PCC-II algorithm is presented. As shown in Fig. 6.11, the IM runs at 15 rad/s without load torque, and the stator resistance R_r changes from $2.13\ \Omega$ to $4.26\ \Omega$ (100 % variation) in 0.7 s. During the R_r variation, the proposed PCC-II algorithm shows strong robustness against

the parameter mismatch that all the measured waveforms keep stable. It is revealed by the experimental results that the proposed algorithm shows weak sensitivity to varied stator resistance.

The robustness performance of the proposed algorithm with $10\ \%\ L_m$ variation is evaluated in Fig. 6.12. As shown, the mutual inductance is increased by 10% in 1 s. Due to the negative impact of L_m variation on the reference value of stator current, the control performance of the proposed algorithm is significantly deteriorated that the measured waveforms become instability at t = 0.8s. The robustness performance of the proposed PCC-II algorithm shows a similar trend with that of the conventional FCS-PCC.

6.3.5 Computational burden analysis

Finally, the computational burden of the three FCS-PCC algorithms are analyzed. In the conventional FCS-PCC and duty-cycle based FCS-PCC, the control inputs are exhaustive searched in every sampling period. Compared with the conventional FCS-PCC, the duty-cycle based FCS-PCC improves the steady-state performance using extended finite set. However, the turnaround time of duty-cycle based FCS-PCC (40 μs) is much longer than that of conventional FCS-PCC (24 μs). In the proposed PCC-II algorithm, the number of searched control inputs is significantly reduced by the preselection principle. The turnaround time of the proposed algorithm is 27 μs. The turnaround time and the average number of searched control inputs of the three algorithms are compared in TABLE 6.3. As can be understood, the number of searched nodes in the proposed algorithm is reduced by 45.7 % and 78.3 % averagely, when compared wtih the conventional and duty-cycle based FCS-PCC algorithms. More specifically, the preselection principle will not result in the selection of the suboptimal solutions, which degrades the control performance.

Table 6.3: Comparisons of turnaround time and the average number of searched control inputs η among the three algorithms

Metrics	FCS-PCC	duty-cycle based FCS-PCC	PCC-II
η [/]	7	17.5	3.8
T_{algo} [μs]	24	40	27

6.4 Conclusion

In this chapter, a computationally efficient FCS-PCC with an extension of finite set (PCC-II) for IM drives is proposed. The optimization problem underlying FCS-PCC is resolved using a current derivative projection from a geometric perspective. By doing so, the objective function is formulated as the quadratic Euclidean norm of the tracking deviation. An extension of finite set is formed by applying the current derivatives in the consecutive sampling periods. The corresponding duty cycles are optimized by the LS method. Moreover, a preselection principle is introduced for computational burden reduction that the control inputs in the purple region

are unvisited. The optimal solution is solved by minimizing the formulated objective function. Compared with conventional and duty-cycle based FCS-PCC, the proposed PCC-II algorithm achieves a significant improvement on steady-state performance while retains the merit of fast response at the transient state. More specifically, the number of searched control inputs is significantly reduced in the proposed algorithm.

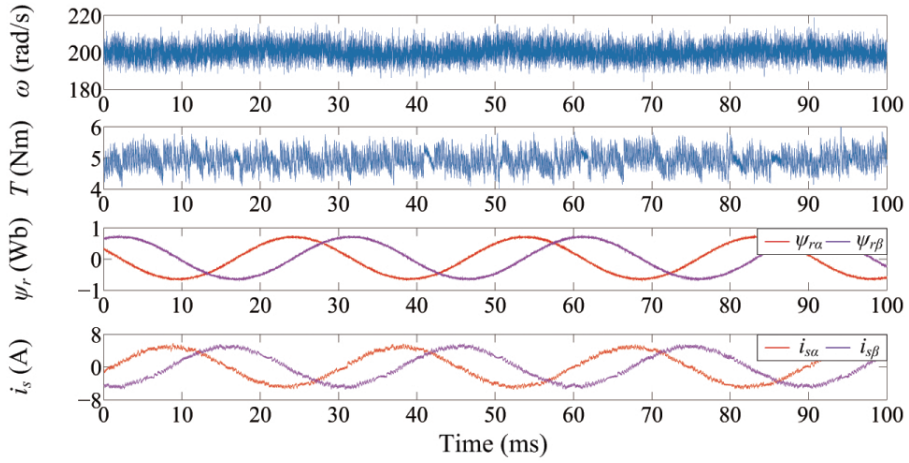

(a)

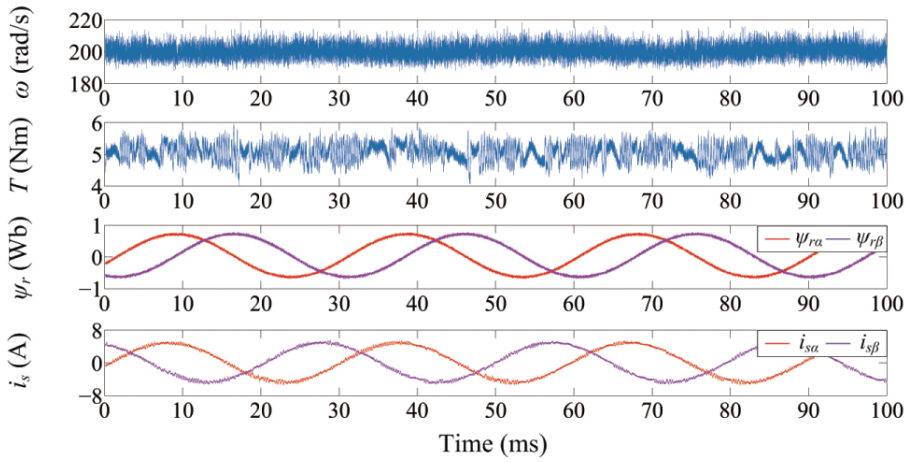

(b)

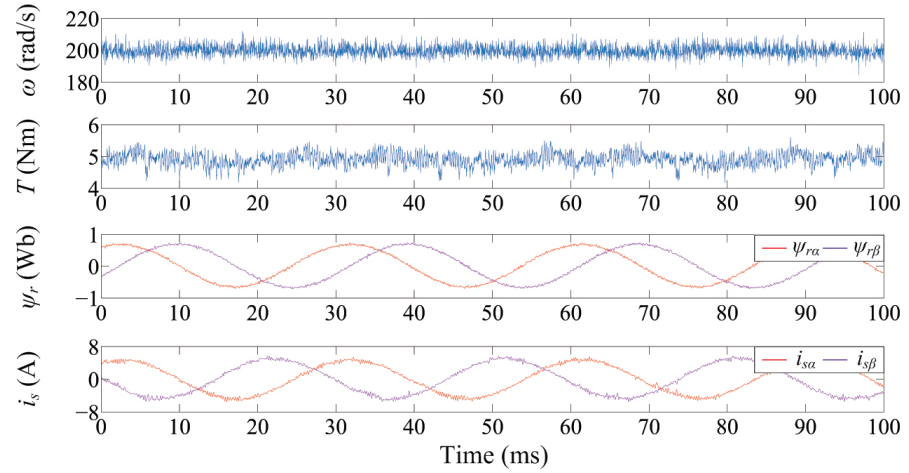

(c)

Figure 6.8: Experimental results: steady-state performance at 200 rad/s with a 5 Nm load torque. (a) conventional FCS-PCC. (b) duty-cycle based FCS-PCC. (c) the proposed PCC-II algorithm.

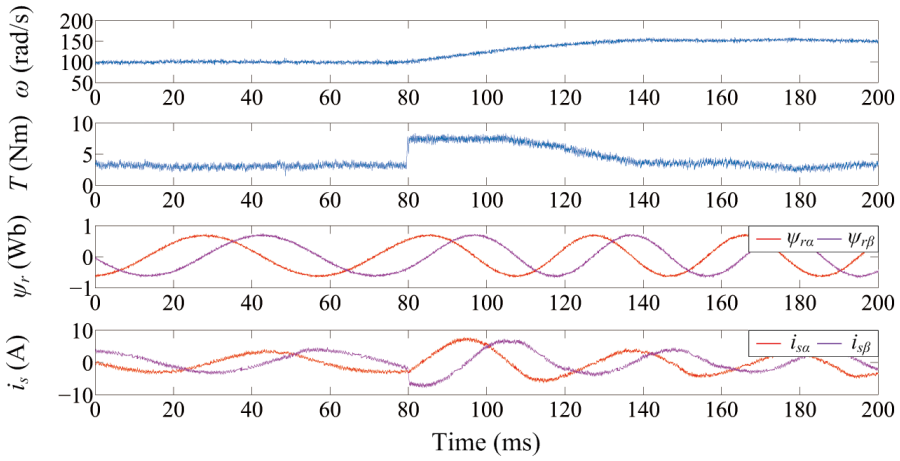

(a)

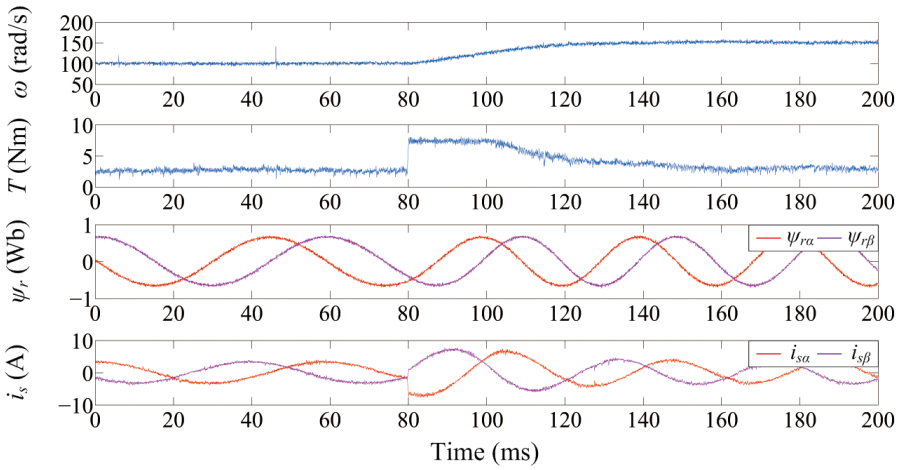

(b)

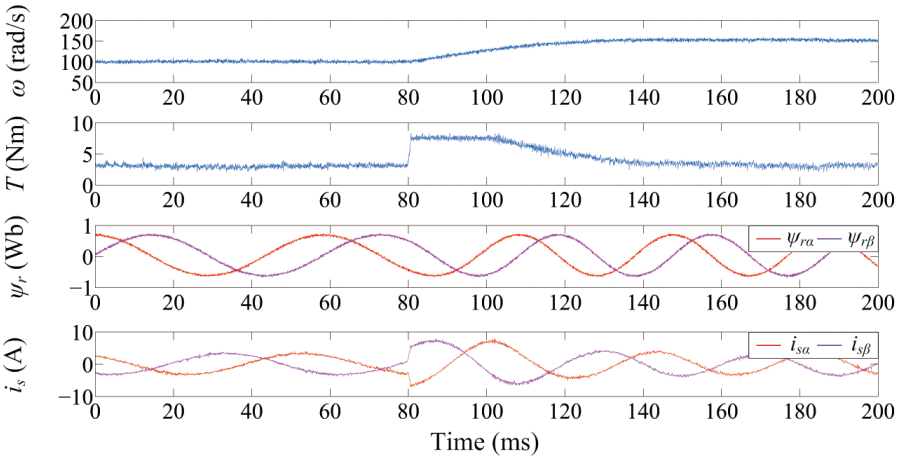

(c)

Figure 6.9: Experimental results: speed step performance from 100 rad/s to 150 rad/s with 3 Nm load toque. (a) conventional FCS-PCC. (b) duty-cycle based FCS-PCC. (c) the proposed PCC-II algorithm.

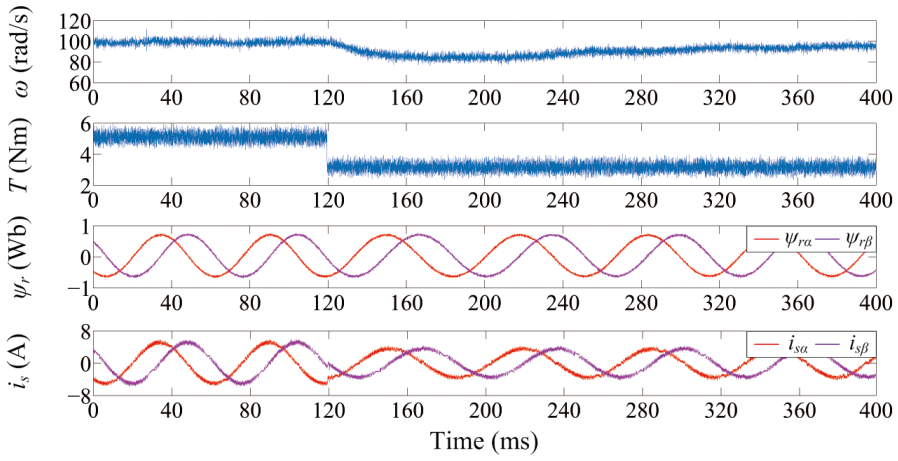

(a)

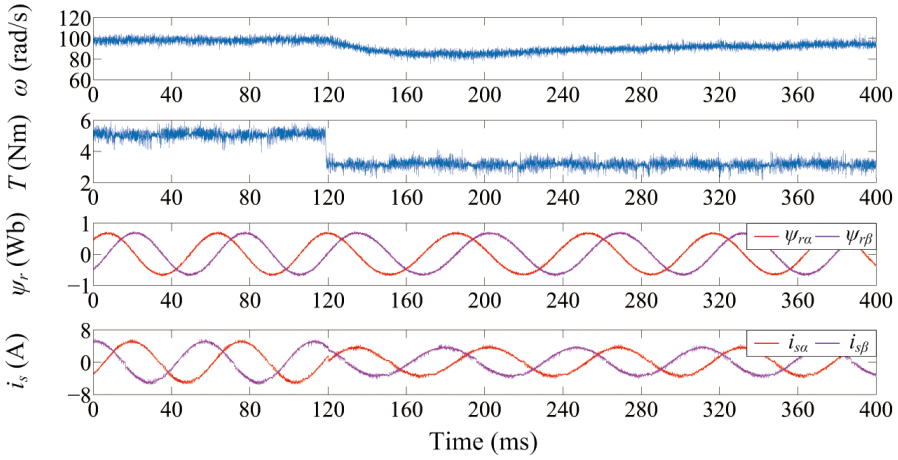

(b)

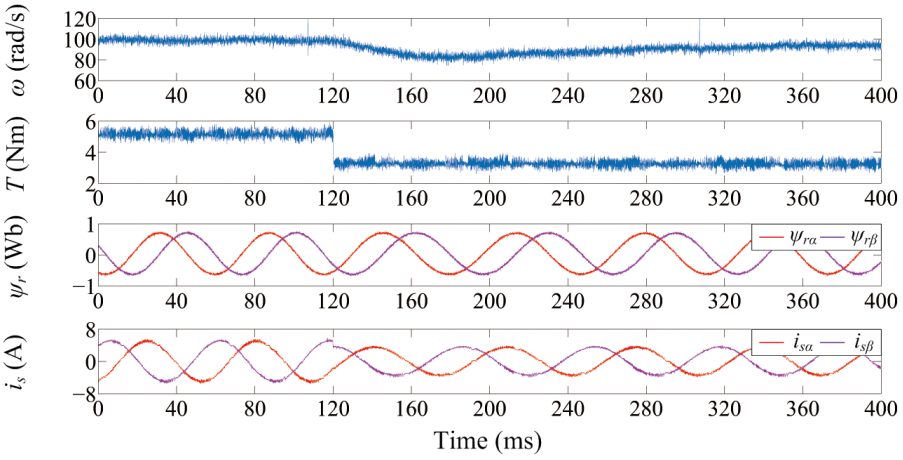

(c)

Figure 6.10: Experimental results: load step performance from 5 Nm to 3 Nm at 100 rad/s. (a) conventional FCS-PCC. (b) duty-cycle based FCS-PCC. (c) the proposed PCC-II algorithm.

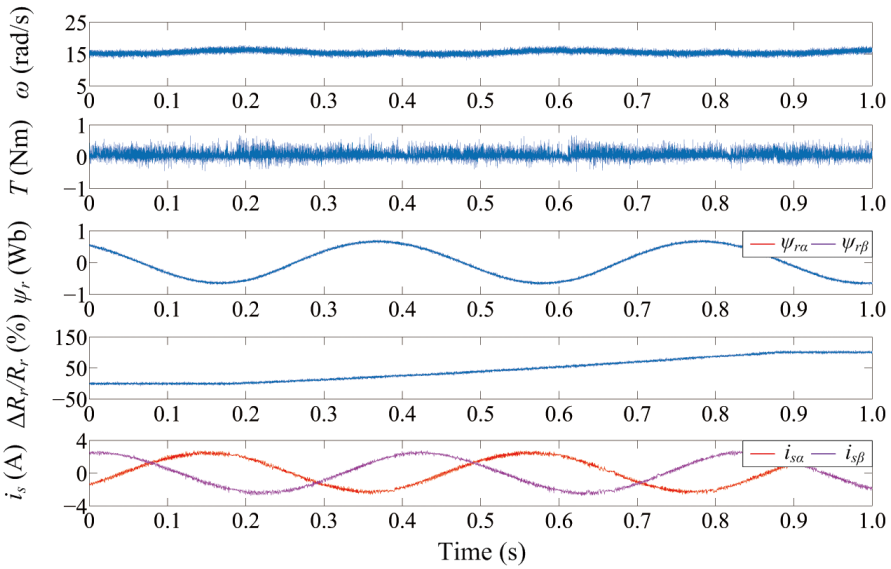

Figure 6.11: Experimental results: robustness evaluation of the proposed PCC-II algorithm at 15 rad/s, R_r changes from 2.13 Ω to 4.26 Ω (100 % R_r variation).

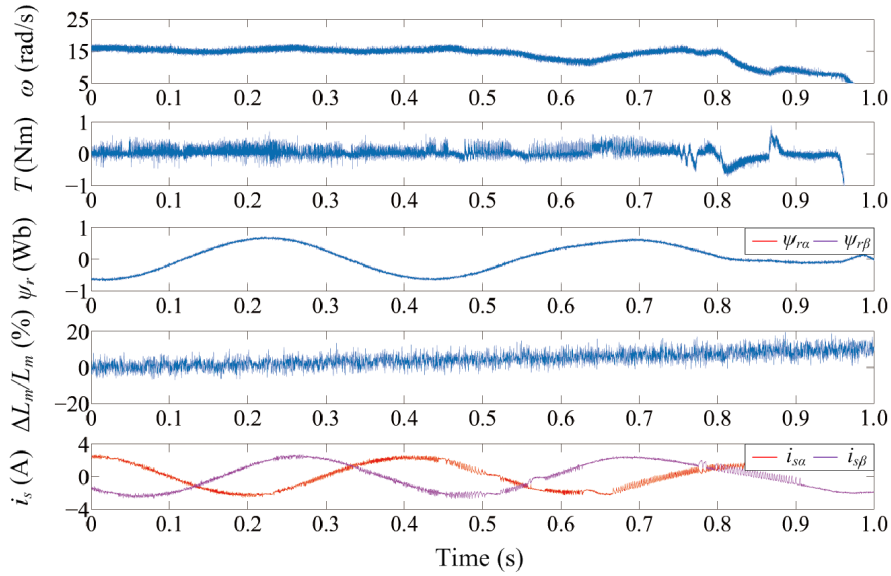

Figure 6.12: Experimental results: robustness evaluation of the proposed PCC-II algorithm at 15 rad/s, L_m changes from 275 mH to 302.5 mH (10 % L_m mismatch).

CHAPTER 7

Gradient descent solutions for FCS-MPC problems

Increasingly attention on the performance improvement of FCS-MPC has been arisen by the power electronic applications. The optimization problem underlying FCS-MPC can be geometrically considered as a quadratic programming (QP) problem. In this chapter, a gradient descent solution is proposed to solve the constrained QP problem that the value of the objective function can be effectively decreased. The effectiveness and feasibility of the gradient descent solution for FCS-MPC optimization problems has been verified on the lab-built 2.2 kW IM drive test-bench. Special issues on the gradient descent solution, i.e., extension of finite set and selection of step lengths have also been discussed.

7.1 Introduction

FCS-MPC has drawn widespread attention, due to its merits of straightforward concept, flexible inclusion of constraints and the ability to handle multiple conflicting criteria [16, 24, 64]. As mentioned, due to the single control input employed in the entire sampling interval, FCS-MPC suffers from the major drawback of unsatisfactory control performance at the steady state, i.e., high current distortion and large torque fluctuations, which remains an open issue [65, 66].

To tackle the abovementioned challenge, one of the intuitive solutions is to implement a finite control set model predictive controller combined with multiple-vector method. The concept centers around the extension of the feasible set with the combination of multiple control inputs, to track the reference trajectory (i.e., the desired control input). Zhang $et\ al$ [67] propose a generalized multiple-vector based FCS-MPC for PMSM drives. Although the result has found smaller tracking deviations at the steady state, the number of switching actions in a sampling period is increasing. In [60], a fixed switching frequency PTFC with multiple vectors for six-phase permanent magnet synchronous machine (PMSM) drive is proposed. Similarly, the proposed control scheme is conducted at a higher switching frequency with a longer sampling period, whereas the comparisons with the conventional method are not fair to some extent. In [68],

a voltage pre-selection based PTFC with multi-vector for PMSM drive is presented, aiming to reduce the number of active voltage vectors. However, specific concerns are required in such technology to alleviate the sensitivity to parameter variations, which makes the algorithm more complicated. A possible solution to enhance the steady-state performance is investigated in [69], but the main control objectives are the active and reactive power at the common coupling point. To suppress the influence of nonsinusoidal back EMF in the five-phase PMSM, a constant switching frequency FCS-PCC with virtual vector tracking is proposed in [70]. Since the virtual vector strongly depends on the accuracy of the system parameter, it is worth noted that a discrete-time disturbance observer is designed to improve the robustness performance. In addition, a model predictive direct duty cycle control (MPD2C) with varied control set for PMSM is introduced in [71]. The duty cycles of the optimal vectors are regarded as the control variables, to be directly regulated in the objective function without the modulator. In [72], a space-vector modulation (SVM) based PTFC using a deadbeat solution is proposed. In [73], a deadbeat-based FCS-MPC with symmetrical modulation for interior PMSM (IPMSM) is presented. However, the merit of quick dynamic response in FCS-MPC is sacrificed, in the presence of a modulation stage. Furthermore, a multiple vector FCS-MPC for multilevel inverter is proposed in [74], to reduce the algorithm complexity through mapping the reference vector into a large sector. The proposed method eliminates the weighting parameter, but the issue of robustness against parameter mismatches has not been addressed. To conclude, the multiple vector solution can be a promising choice for FCS-MPC to decrease the steady-state tracking error. Nevertheless, there is still one limitation (e.g., higher switching frequency) due to the higher number of switching in a control cycle. Moreover, the algorithm complexity of the multiple-vector FCS-MPC becomes higher, to alleviate the sensitivity against parameter variations.

Over the last decade, the optimization problem underlying FCS-MPC is rearranged as an integer least-squares (ILS) problem, can be solved over a longer prediction horizon. To improve the current quality at the steady state while retaining a low switching frequency, such FCS-MPC control schemes with long-horizon (namely, multistep FCS-MPC) have attracted substantial interest from the researchers. Geyer and Quevedo [53] propose a multistep FCS-MPC algorithm for the three-level inverter. It is worth mentioning that the computational effort grows exponentially along with the increased number of horizon. To address this issue, a sphere decoding algorithm (SDA) is introduced to significantly reduce the number of searched control inputs. In [57], a resource-efficient long-horizon FCS-MPC for a three-level converter with a passive load is proposed. This work mainly focuses on the reduction of computational burden with a nonrecursive SDA on a field-programmable gate array (FPGA), to implement the proposed algorithm with a horizon of 5 in 13.4 μs. An exposition of the experimental results in the long-horizon FCS-MPC for an H-bridge inverter is provided in [59]. The redundant elements are unvisited by control inputs transformation from a cube-lattice to a hexagon. Beyond that, the long-horizon FCS-MPC extends its application to various topologies of the power converters, e.g., seven-level H-bridge inverter in [75]. To eliminate the objective function and weighting parameters, the proposed method directly calculates the optimal vector with the best current performance while retaining the minimum common-mode voltage. To the best of our knowledge, the concept shares the similar weakness with the deadbeat technology. [76] analyzes the impact of the transient state on the effectiveness of multistep FCS-MPC. Based on the above, a box-constrained quadratic programming (QP) solver is applied for transients.

Recently, the gradient descent (GD) solution has been extensively investigated, due to its

merits of fast tracking performance for resolving a convex problem [77]. In [78], an updating mechanism based on the current gradient is proposed to improve the control performance of FCS-MPC, in the absence of model parameters. It is worth noted that the proposed model-free FCS-MPC performs well as the machine knowledge is not provided. In [79], the GD optimization is employed for parameter identification, to enhance the robustness against parameter mismatches in FCS-MPC for a grid-connected converter. In [80], a computational efficiency model predictive pulse pattern control (MP3C) combined with a gradient method is conducted on an FPGA. The results have shown an impressive resource reduction by 17 times compared with the existing solutions. In [20], a GD method based FCS-PCC with least-squares duty cycles is presented. However, the algorithm in this work has not been implemented with a longer horizon, i.e., the exponential growth of computational burden has not been taken into consideration. Although the least-squares method can minimize the tracking deviation in the objective function, the control objective that searches along with the direction of GD, is still not guaranteed. In [81–84], a fast-gradient solution for computational complexity reduction has been extensively researched, in which the explicit MPC is considered as an ILS problem. However, the offline computational burden and resource requirements will grow dramatically with the increased scale of the explicit MPC problem. The advantages of the GD method for FCS-MPC schemes have not been fully investigated.

Motivated by the above, a GD-based objective function reformulation for FCS-MPC with extended prediction horizon is proposed, to achieve lower tracking deviations at the steady state while retaining a short settling time at the transient state. First, the convexity of the quadratic programming (QP) problem underlying FCS-MPC is proved. Thereby, the optimization problem is resolved by the GD method. The reason for this is, the tracking deviations of the control objectives can be minimized more efficiently, as they search along with the direction of GD. Based on the above, the objective function is reformulated as the deviation between the normalized gradient descent and derivative with an extension of the feasible set. The latter is, the abovementioned procedures are iteratively learned in an extended prediction horizon of 3 for the convergence of the tracking deviations. More specifically, a pruning algorithm is introduced to reduce the computational burden with decreased number of searched control inputs. Compared with the conventional and multi-vector FCS-MPC, the proposed algorithm tracks the reference in a faster and more efficient way. A deepest decrease occurs in the objective function as the control variables search along the direction from the gradient descent.

7.2 Proof of convexity

It is noted that the main objective of FCS-PCC is to regulate the current trajectory along with its reference in the stationary $\alpha\beta$ frame. The tracking deviation is regarded as the Euclidean norm between $i_{s\alpha,\beta}$ and $i^*_{s\alpha,\beta}$ from a geometric perspective. Therefore, the quadratic Euclidean norm of the tracking deviation expressed in (7.1) is included in the objective function, to reformulate FCS-PCC as a QP problem.

$$F(k) = (i^*_{s\alpha} - i_{s\alpha}(k))^2 + (i^*_{s\beta} - i_{s\beta}(k))^2 \tag{7.1}$$

$F(k)$ is partially differentiated with $i_{s\alpha,\beta}$ in (8) and its Hessian matrix H is defined as

$$\frac{\partial F(k)}{\partial i_{s\alpha,\beta}(k)} = -2(i^*_{s\alpha,\beta} - i_{s\alpha,\beta}(k)) \tag{7.2}$$

$$H = \begin{bmatrix} 2 & 0 \\ 0 & 2 \end{bmatrix} \tag{7.3}$$

The following lemma and theorem are introduced to confirm the convexity of $F(k)$.

Lemma 1: For the twice differentiable function f:$\boldsymbol{X} \rightarrow \mathbb{R}^n$, if its Hessian matrix is positive semidefinite, f is convex.

Theorem 1: For the function f:$\boldsymbol{X} \rightarrow \mathbb{R}^n$, if$f(\theta x_1 + (1-\theta)x_2) \leq \theta f(x_1) + (1-\theta)f(x_2), \forall\, x_1,\ x_2 \in \boldsymbol{X}, \forall\, \theta \in [0,1]$, the function f is convex.

7.2.1 Proof 1

Proof 1: The quadratic function $f(x) = x^2$ is regarded as each term of $F^{(k,n)}$, as x is denoted by the forward difference of the stator current. The convexity of $f(x)$ is proved by Theorem 1.

$$\begin{aligned} & f(tx_1 + (1-t)x_2) - tf(x_1) + (1-t)f(x_2) \\ =& -(t-t^2){x_1}^2 - (t-t^2){x_2}^2 + 2t(t-1)x_1x_2 \\ \leq& 0 \end{aligned} \tag{7.4}$$

Therefore, each term of $F^{(k,n)}$ is convex. Owing to that $F^{(k,n)}$ is the sum of the quadratic functions with non-negative weightings, $F^{(k,n)}$ is convex [85].

7.2.2 Proof 2

Proof: To proof Lemma 1, the Taylor expansions of $F(x_0)$ with Peano form of the remainder is rewritten as

$$\begin{aligned} F(x_0) = F(x) + \nabla F(x)(x_0 - x) + \frac{1}{2}(x_0 - x)^T H(x_0 - x) \\ + o((x - x_0)^T(x - x_0)) \end{aligned} \tag{7.5}$$

where d denotes the forward difference $x_0 - x$. It is noted that the remainder $\lim\limits_{d\rightarrow 0} \frac{o(d^2)}{d^2} = 0$. Owing to that H is positive semidefinite, we have $\frac{1}{2}(x_0 - x)^T H(x_0 - x) \geq 0$, yields

$$F(x_0) \geq F(x) + \nabla F(x)(x_0 - x) \tag{7.6}$$

As $x_1 < x < x_2$, it is obtained that $x = \theta x_1 + (1-\theta)x_2$, $\theta \in [0,1]$. By substituting x_1, x_2 into x_0 and multiply the coefficient θ, $1-\theta$ on both sides, (7.6) is rewritten as

$$\begin{aligned} \theta F(x_1) &\geq \theta F(x) + \theta \nabla F(x)(x_1 - x) \\ (1-\theta)F(x_2) &\geq (1-\theta)F(x) + (1-\theta)\nabla F(x)(x_2 - x) \end{aligned} \tag{7.7}$$

Thus, we obtain that

$$\begin{aligned} \theta F(x_1) + (1-\theta)F(x_2) \geq F(x) + \nabla F(x) \\ ((\theta x_1 + (1-\theta)x_2) - x) \end{aligned} \tag{7.8}$$

where the right term is rewritten as

$$\begin{aligned} F(x) + \nabla F(x)(x - (\theta x_1 + (1-\theta)x_2) \\ = F(x) = F(\theta x_1 + (1-\theta)x_2) \end{aligned} \tag{7.9}$$

The convexity of $F(x)$ is proved by (7.10) according to Theorem 1.

$$\theta F(x_1) + (1-\theta)F(x_2) \geq \ F(\theta x_1 + (1-\theta)x_2) \tag{7.10}$$

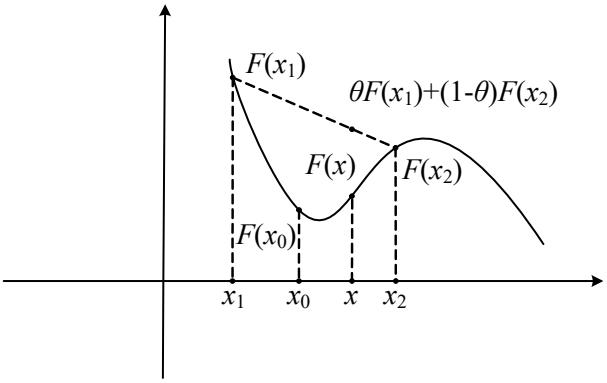

Figure 7.1: Definitions of the function $F(x)$ and the variables.

Conversely, it is noted that if $F(x)$ is convex, the Hessian matrix H is positive semidefinite. *Remark 1:* The convexity of the objective function is of importance that the minimum value of the convex function is unique within its feasible set. The gradient descent represents the negative partial derivative of the objective function, which is the direction to search for the convergence of the objective function to zero in a most effective manner. A deepest decrease in the value of the objective function occurs as the control variable moves along with the direction of the gradient descent.

7.3 Objective function reformulation

7.3.1 With finite control set

As can be understood, a deepest decrease in the tracking deviation of the stator current can be achieved, when the stator current is iteratively learned in the direction of gradient descent. By doing so, the reference trajectory in the convex objective function, i.e., equation (7.1), can be effectively tracked. As described in Fig. 7.2, the stator current moves with the predetermined step size in every iteration, and the gradient descent $-\nabla F(k)$ is updated accordingly. To force the tracking deviation to zero in the fastest manner, the normalized stator current derivative and gradient descent are compared for every switching sequence, as described in (7.11). The optimal switching state that minimizes g_j the most is selected to be carried out.

$$g_j = \left(\frac{-\frac{\partial F(k,n)}{\partial i_{s\alpha}}}{|-\nabla F(k,n)|} - \frac{\frac{di_{s\alpha}(k,n)}{dt}}{|\frac{di_s(k,n)}{dt}|}\right)^2 + \left(\frac{-\frac{\partial F(k,n)}{\partial i_{s\beta}}}{|-\nabla F(k,n)|} - \frac{\frac{di_{s\beta}(k,n)}{dt}}{|\frac{di_s(k,n)}{dt}|}\right)^2 \tag{7.11}$$

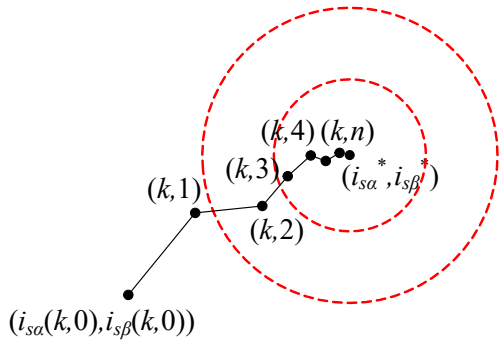

Figure 7.2: Iterative learning of stator current in the direction of gradient descent to solve the convex QP problem in (7.1). The dashed lines denote the contour lines of tracking derivation.

where n denotes the number of iterations, j is the switching state, h = 0 represents FCS-MPC with one prediction horizon, a tilde " ~ " is derived as the symbol for the normalized values. As shown in Fig. 7.3, the stator current derivative which tracks the gradient descent best is selected as the optimal solution. Considering that the proposed algorithm cannot be executed in one iteration period, the adverse effect of time-delay should be compensated. Akin to conventional FCS-PCC, we update the value of gradient descent $-\nabla F(k, n+1)$ instead of $-\nabla F(k, n)$ by (7.12).

$$-\nabla F(k, n+1) = -\nabla F(k, n) - H \begin{bmatrix} \Delta i_{s\alpha} \\ \Delta i_{s\beta} \end{bmatrix} \tag{7.12}$$

Therefore, the reformulated objective function with time-delay compensation is rewritten as

$$g_j = \left(\frac{-\frac{\partial F(k,n+1)}{\partial i_{s\alpha}}}{|-\nabla F(k,n+1)|} - \frac{\frac{di_{s\alpha}(k,n)}{dt}}{|\frac{di_s(k,n)}{dt}|}\right)^2 + \left(\frac{-\frac{\partial F(k,n+1)}{\partial i_{s\beta}}}{|-\nabla F(k,n+1)|} - \frac{\frac{di_{s\beta}(k,n)}{dt}}{|\frac{di_s(k,n)}{dt}|}\right)^2 + \lambda_{sw}^2 \cdot n_{sw}^2 \tag{7.13}$$

7.3.2 With an extension of finite control set

Noted that the discrete nature of the control inputs, it is a challenging task to search exactly along with GD by the discrete current derivatives. To address this issue, the expansion of feasible set (of current derivative) is achieved, in a combination of normalized derivative and the optimal one in the former iteration. For simplification, we assume that (α_1, β_1) represents the normalized optimal derivative $(d\tilde{\boldsymbol{i}}_{s\alpha}^{(n-1)}(k+h)/dt,\ d\tilde{\boldsymbol{i}}_{s\beta}^{(n-1)}(k+h)/dt)$ in $n-1^{th}$ iteration, (α_2, β_2) represents the normalized derivative $(d\tilde{\boldsymbol{i}}_{s\alpha}^{(n)}(k+h)/dt,\ d\tilde{\boldsymbol{i}}_{s\beta}^{(n)}(k+h)/dt)$ in n^{th} iteration to be evaluated, and (α_3, β_3) is defined as the updated GD $-\nabla f^{n+1}(k+h)$. $\forall i = 1, 2, 3,\ (\alpha_i, \beta_i \in \mathbb{R})$. As shown in Fig. 7.4(a), the duty cycles of (α_1, β_1) and (α_2, β_2) are t and $(1-t)$ $(t \in \mathbb{R}, 0 \leq t \leq 1)$, respectively. The direction of GD can be approached by the regulation of duty cycle t in (7.16). It should be mentioned that (α_1, β_1) is applied in the entire iteration (i.e., $t = 1$) when $t \geq 1$. On the other hand, t is set as 0 when $t \leq 0$.

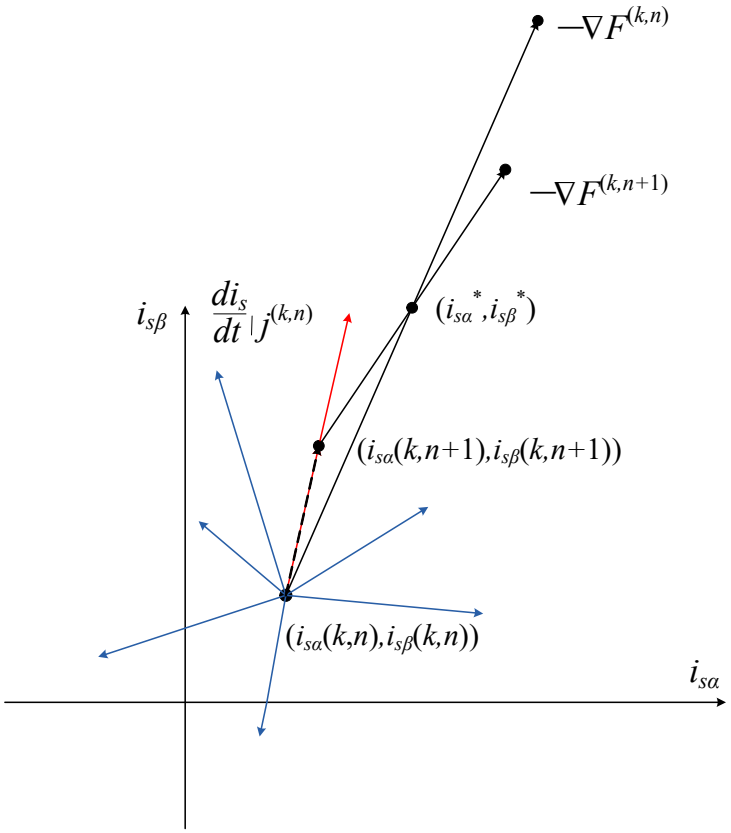

Figure 7.3: Description of stator current derivatives and the gradient descent. The red line is the selected stator current derivative, the blue lines are the rest derivatives of stator current, the black dashed line represents the movement of the stator current, the black solid lines are the gradient descent at n and $n+1$ iterations.

To track the direction of the gradient descent, the following equation (7.14) should be satisfied.

$$\begin{aligned} \alpha_1 t + \alpha_2(1-t) &= \kappa\alpha_3 \\ \beta_1 t + \beta_2(1-t) &= \kappa\beta_3 \\ 0 \;\leq\; t \;&\leq 1 \end{aligned} \tag{7.14}$$

where κ is the coefficient. By eliminating the parameter κ, we can obtain the function with one freedom that

$$\beta_1 t + \beta_2(1-t) = \frac{\beta_3}{\alpha_3} \cdot (\alpha_1 t + \alpha_2(1-t)) \tag{7.15}$$

The duty cycle t is solved by

$$t = \frac{\beta_2 - \alpha_2 \cdot \dfrac{\beta_3}{\alpha_3}}{(\beta_2 - \beta_1) + (\alpha_1 - \alpha_2) \cdot \dfrac{\beta_3}{\alpha_3}} \tag{7.16}$$

The objective function J is reformulated to minimize the tracking deviation between GD and the combination of stator current derivatives in the continuous iterations after normalization. To

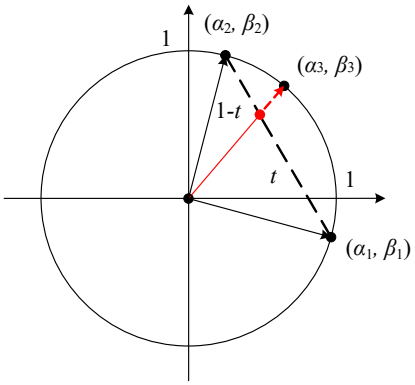

(*a*) $0 < t < 1$

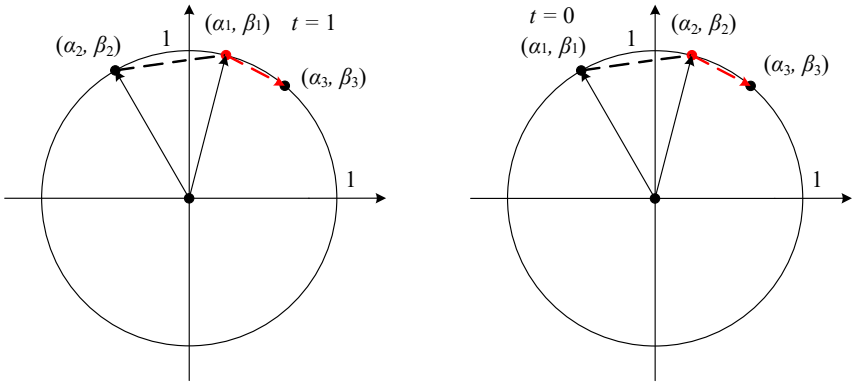

(*b*) $t = 1$ (*c*) $t = 0$

Figure 7.4: The combination of normalized derivatives in the continuous iterations and the updated GD. (a) $0 < t < 1$. (b) $t = 1$. (c) $t = 0$.

do so, J is rewritten as

$$J = (\alpha_3 - t\alpha_1 - (1-t)\alpha_2)^2 + (\beta_3 - t\beta_1 - (1-t)\beta_2)^2 + \lambda_{sw} \cdot n_{sw}^2 \tag{7.17}$$

where λ_{sw} is applied for switching frequency modification, n_{sw} represents the number of switching in an iteration, $n_{sw} = \sum_{v=a,b,c} |S_v^n(k+h) - S_v^{n-1}(k+h)|$. The current derivative (α_2, β_2) (as well as the corresponding control input) that minimizes J most is selected as the optimal.

7.4 Design of the step lengths

The proposed FCS-PCC algorithm solved by the gradient descent method is essentially an iterative learning method. The optimal voltage vector does not manipulate in the entire sampling period because the gradient descent only indicates the movement direction for the convergence of stator current tracking deviation. As can be understood, GD is only a vector that indicates the searching direction. Therefore, the period for each iteration (namely step length η) is required

to be further designed. If η is small enough, it is obvious that the stator current can track the reference value very well. However, the algorithm is penalized by the weakness of high computationally demanding ability caused by the increased number of iterations. On the other hand, the convergence of tracking deviation is not satisfied when η is too large. The design of the step length η is discussed as follows.

7.4.1 Dichotomy-based approach

A simple dichotomy-based approach is introduced in this section. As can be understood, the period of the nth iteration is $1/2^{n+1}$ of the sampling period T_s. As shown in Fig. 7.5, each iteration period in the dichotomy-based approach with 2 iterations is T_s/2, and the periods with 3 iterations are T_s/2, T_s/4 and T_s/4, respectively. The number of iterations is determined by the stopping criterion, as described in (7.18).

$$T_s^{(n)} \leq \eta T_s, T_s^{(n+1)} < \eta T_s \tag{7.18}$$

where η is the coefficient in the stopping criterion.

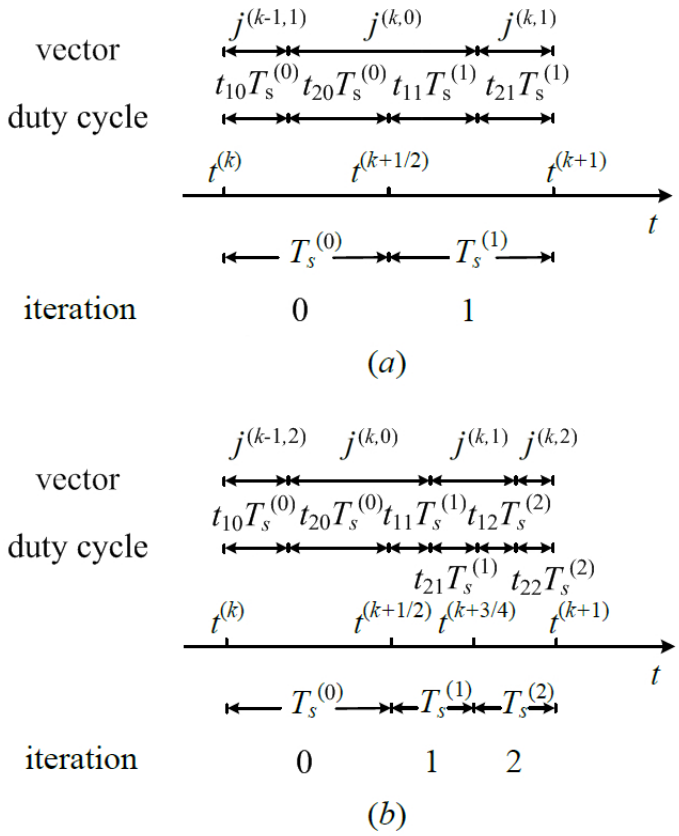

Figure 7.5: The applied iteration periods in a sampling period. (a) with 2 iterations (b) with 3 iterations.

To determine the step lengths of the iterations, the dichotomy-based method is one of the simple choices that the step length of the $n + 1^{th}$ iteration is half of that of the former iteration

(n^{th}). The first reason is that the stator current tracks the reference in an effective manner in the first several iterations because their step lengths are relatively larger. The latter is that the tracking performance of stator current is improved by the increased number of iterations. Considering that the computational ability of the real-time control system, the number of iterations in a sampling period is limited by the stopping criterion (7.18).

7.4.2 Backtracking approach

The relationship between the control variables and the objective function is shown in Fig 7.6, in which x denotes $(i_{s\alpha}(k,n), i_{s\beta}(k,n))$, d is defined as the direction of stator current derivative using optimal voltage vector, $\lambda \in (0,1]$ represents the coefficient. As described in (7.19), the inequality is constructed to evaluate whether the tracking error is converging, as well as its convergence rate. The step length $\eta(k,n)$ should be modified by ϵ as (7.20) is not satisfied. Otherwise, $\eta(k,n)$ is set as the same value of $\eta(k,n-1)$.

$$F(x+\eta d) \leq F(x) + \eta\lambda \frac{dx}{dt} d \tag{7.19}$$

$$\eta(k,n) = \epsilon \cdot \eta(k,n-1), \epsilon \in (0,1] \tag{7.20}$$

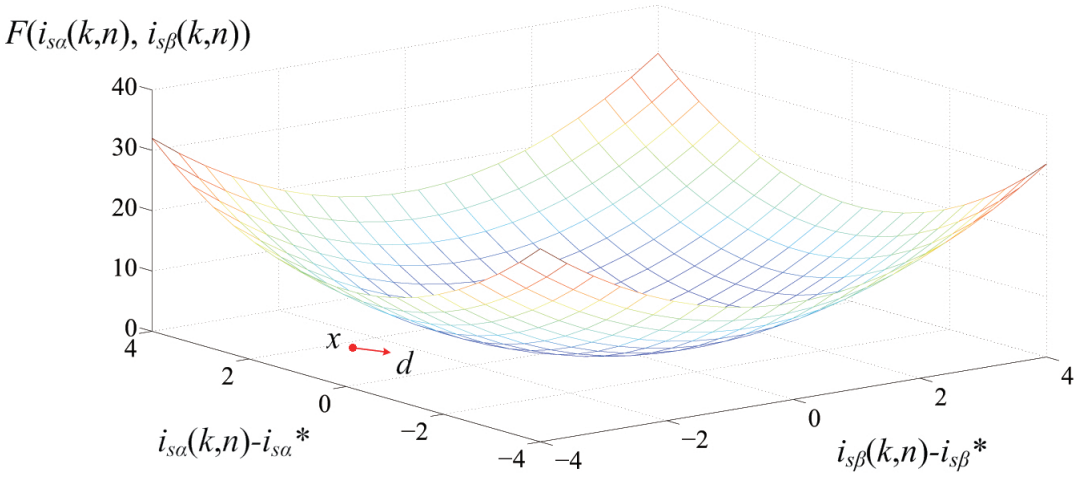

Figure 7.6: Relationship between the control variables and the objective function.

The stopping criteria of the proposed iterative algorithm are shown in (7.21) and (7.22). Regarding that the execution time, it is noted that the iterative learning stops when the step length $\eta(k,n)$ is less than the predefined value ρT_s. The latter criterion is that the 2-norm of gradient descent is enough small, to guarantee the algorithm to be efficiently iterated. Therefore, the last iteration operates in the rest of the sampling period once either stopping criterion is satisfied.

$$\eta(k,n) \leq \rho T_s, \rho \in (0,1] \tag{7.21}$$

$$||-\nabla F(k,n+1)||_2 \leq \delta \tag{7.22}$$

where T_s is the sampling period.

7.4.3 Convergence analysis

The convergence of the gradient descent solution can be obtained by the backtracking approach. As can be seen in Fig. 7.7, we assume that the control variable is x_1 and the corresponding value of $f(x)$ is $f(x_1)$. $\nabla f(x)$denotes the slop of $f(x)$, d represents the step direction. Based on the above, we consider a coefficient $\lambda \in (0, 1]$, to adjust the gradient to the slope of red dashed line. It can be observed that there is an intersection point $f(x_2)$ between $f(x)$ and the red dashed line. The equation (7.19) is satisfied when the control variable $x_1 < x_1 + \eta d < x_2$. In such circumstances, the function $f(x)$ is below the red dashed line. The step length η is decreased by (7.20), when (7.19) is not satisfied.

According to Fig. 7.7, we can obtain (7.23) that

$$f(x_1 + \eta d) \leq f(x_1) + \eta\lambda \cdot \nabla f(x_1)d \leq f(x_1) \tag{7.23}$$

Therefore, the convergence of the proposed algorithm is confirmed that the updated value of function $f(x)$ is smaller in each iteration and finally converges to 0.

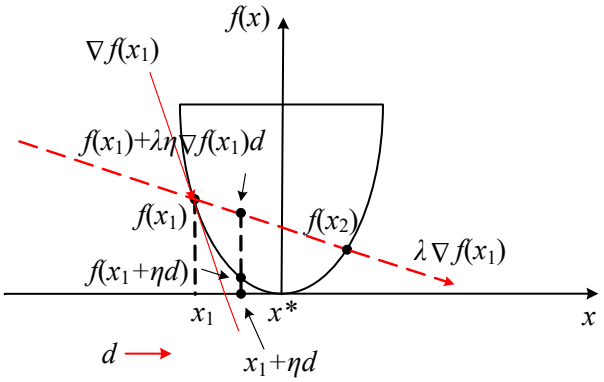

Figure 7.7: The relationship between $f(x)$ and its control variable in the cross-section of d.

7.5 Decision variables reduction methods

7.5.1 Generalized search tree for decision making

Although the optimal switching sequence can be achieved via exhaustive enumeration, the computational complexity of the proposed algorithm multiplies with the increased number of iteration. As the conventional FCS-PCC is applied in the 2-L VSI, the number of decision variables to be enumerated in the abc framework is 8 (as shown in the cube lattice in Fig. 7.8(a)). The redundant decision variables are excluded in [59] that a hexagon with 7 control inputs in the $\alpha\beta$ framework is formulated. Based on the above, the two-layer decision-making approach is proposed to further reduce the number of control inputs. According to (3.4), the predicted stator current in the $\alpha\beta$ framework are calculated. It is worth noting that the control variables with different $u_{s\alpha}$ share the same value of $i_{s\beta}(k+1)$, and those with different $u_{s\beta}$ share the same $i_{s\alpha}(k+1)$. Therefore, the $\alpha\beta$ components of predicted stator current can be optimized in the two-layer structure independently. As shown in Fig. 7.8(c), the control inputs in Fig. 7.8(b)

are projected in the β axis, to make decision for $u_{s\beta}$ in the first layer. Once the optimal $u_{s\beta}$ is decided by minimizing the objective function $g_{j\beta}$ in (18), the elements in the selected branch are optimized by $g_{j\alpha}$ minimization in the next layer. On the other hand, the decision-making algorithm with $i_{s\alpha}$ priority is shown in Fig. 7.8(d). It can be observed that there are five different $u_{s\alpha}$ to be optimized in the first layer. Namely, the tree has five branches that the elements in the same branch share the same $u_{s\alpha}$ and $i_{s\alpha}(k+1)$. The optimal branch is visited in the second layer to decide the optimal $u_{s\beta}$.

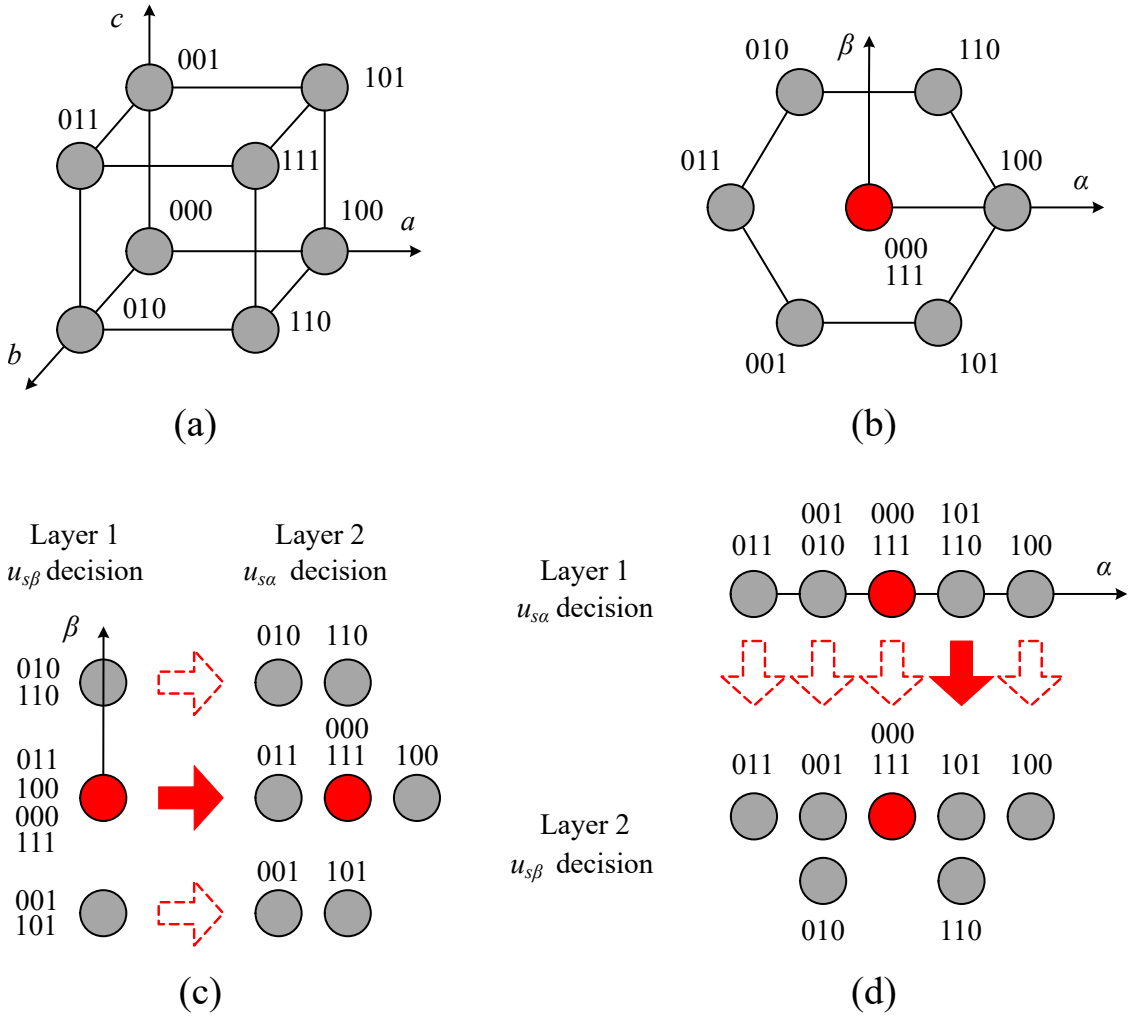

Figure 7.8: Principle of decision variables reduction algorithm. (a) 8 decision variables in the conventional FCS-PCC. (b) redundant candidates reduction in [59]. (c) the proposed two-layer decision making algorithm with $i_{s\beta}$ priority. (d) the proposed two-layer decision making algorithm with $i_{s\alpha}$ priority.

$$g_{j\beta} = \left(\frac{-\dfrac{\partial F(k,n)}{\partial i_{s\beta}}}{|-\nabla F(k,n)|} - \frac{\dfrac{di_{s\beta}(k,n)}{dt}}{\left|\dfrac{di_s(k,n)}{dt}\right|}\right)^2 \tag{7.24}$$

$$g_{j\alpha} = \left(\frac{-\dfrac{\partial F(k,n)}{\partial i_{s\alpha}}}{|-\nabla F(k,n)|} - \frac{\dfrac{di_{s\alpha}(k,n)}{dt}}{\left|\dfrac{di_s(k,n)}{dt}\right|}\right)^2 \tag{7.25}$$

A generalized approach is introduced to determine the priorities of the control variables in the cascaded structure. As demonstrated in Fig. 7.9, $u_{s\beta}$ is optimized before $u_{s\alpha}$ in the first iteration at k interval, while $u_{s\alpha}$ obtains the priority in the next iteration. As shown in Fig. 5, a simple two-layer decision-making algorithm for decision variables selection is introduced to reduce the algorithm complexity. The cascade structure decision-tree has two layers. The first layer is used for the decision of one control variable, while the latter layer is employed for selection of the other variable. Thus, the split terms in the objective function (7.11) are optimized in the first and second layer, respectively. For the iterations with $i_{s\beta}$ priority, seven switching sequences are served as the input elements of the decision-tree, to be classified as the three branches in the first layer. The branch that minimizes (7.24) is selected as the optimal solution in the first layer and the another two branches are discarded. The elements in the selected branch are subsequently used for the optimization of (7.25). In the case that $i_{s\alpha}$ is optimized in the first layer, the optimal branch is selected (from the five branches) by optimizing (7.25) in the first layer and (7.24) is subsequently optimized in the second layer. The concept of

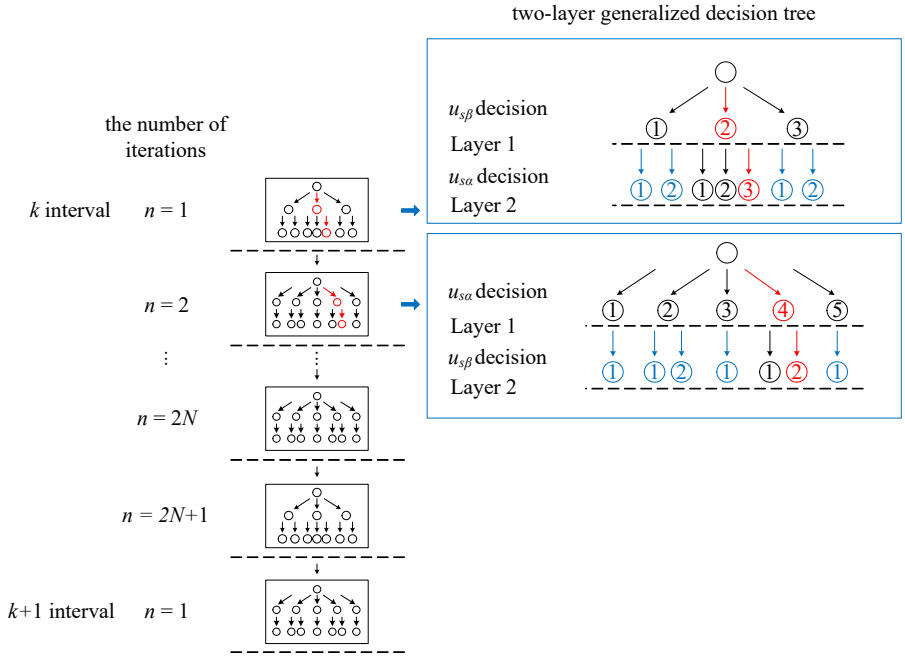

Figure 7.9: Two-layer generalized search tree for optimal switching sequence selection. The red elements represent the selected optimal solutions, the blue elements represent the discarded solutions, the black elements are the searched solutions but not selected.

the proposed two-layer generalized decision-making algorithm is simple and intuitive that the number of decision-variables is reduced by discarding the undesired branches. The proposed low-complexity decision-making method is even promising in the field of multi-level power converters to overcome the obstacle of computational burden.

7.5.2 Pruning algorithm

The generalized search tree can reduce the number of searched control inputs in one prediction horizon. However, the algorithm complexity grows exponentially with the increased length of horizon, which still remains a challenge for FCS-MPC with a longer prediction horizon. To address this issue, a pruning algorithm (PA) based on branch-and-bound (BB) is introduced to reduce the number of searched control inputs. As shown in Fig. 7.10, a decision tree with branches and leaves is built. Owing to that the 2-L VSI has 7 control inputs with different current derivatives in the case study, there are 7 leaves in each branch of the decision tree. The leaf is applied to predict the outcome of the control plant, which grows as a branch in the next prediction horizon. Therefore, the amount of leaves increases significantly to 7^N with a horizon of N.

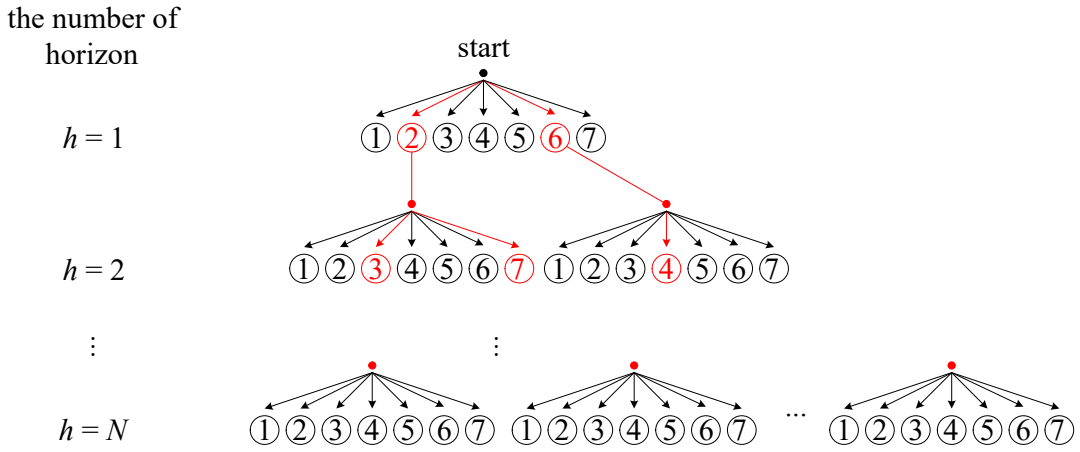

Figure 7.10: The pruning algorithm in the decision tree to select the optimal solution. The red elements represent the selected optimal solutions (within the boundary), the black elements are the searched solutions but not selected.

The concept of PA centers around discarding the undesired branches, in which the outcome of leaf exceeds the predefined constraint C_h. It is worth noted that the boundary for each horizon C_h is tighten with the increased h ($C_m < C_l, l < m, \forall\, l, m \in h$). To evaluate whether a certain branch is required to be visited in the $(h+1)^{th}$ horizon, the outcome of leaf $f^n(k+h)$ is compared with the constraint C_h. The leaf terminates, i.e., the corresponding branch in the $(h+1)^{th}$ horizon is unvisited, as (7.26) is not satisfied. The pseudo code of PA is summarized as follows.

$$f^n(k+h) \; < \; C_h \tag{7.26}$$

$$C_h \; = \; A \cdot B^{(h-1)} \cdot ||i_s^*||^2 \tag{7.27}$$

where A and B are the coefficients to design the boundaries in PA.

7.6 Experimental verifications

In this section, several case studies of the gradient descent solution for FCS-MPC are proposed. Subsequently, the feasibility and effectiveness are experimentally verified.

7.6.1 Case study

Three gradient descent solutions for FCS-MPC are investigated, regarding the differences in extension of finite control set, design of step lengths and the number of prediction horizon. The description of the three gradient descent solutions are illustrated in TABLE. 7.1. As can be seen, GD-FCSMPC1 applies single switching state with a backtracking iteration approach and a prediction horizon of 1. In GD-FCSMPC2, an extension of control set with a dichotomy-based method is applied in one prediction horizon. GD-FCSMPC3 employs an extended control set with a backtracking algorithm and a long prediction horizon.

Table 7.1: Description of three gradient descent solutions for FCS-MPC

GD solutions	Finite set extension	Step lengths design	Prediction horizon
GD-FCSMPC1	No	Backtracking	one
GD-FCSMPC2	Yes	Dichotomy-based	one
GD-FCSMPC3	Yes	Backtracking	Multiple

7.6.2 Experimental assessment

7.6.2.1 GD-FCSMPC1

The block diagram of the GD-FCSMPC1 algorithm is demonstrated in Fig. 7.11 and the algorithm description is shown in Algorithm 2.

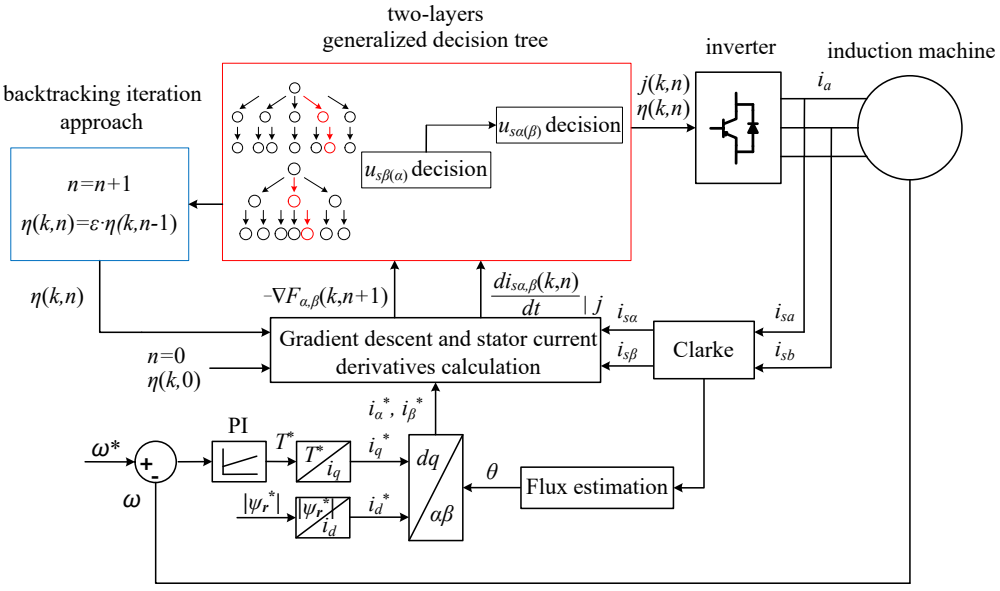

Figure 7.11: Block diagram of the proposed GD-FCSMPC1.

Algorithm 2 GD-FCSPCC algorithm with backtracking iteration approach

1: System initialization, i_s and ω measurement, $\hat{\psi}_s(k)$ and $\hat{\psi}_r(k)$ estimation.
2: Gradient descent and stator current derivatives for every switching state calculation.
3: By minimizing the deviation functions $g_{j\beta}$ and $g_{j\alpha}$ in the two-layer cascade structure decision tree, the optimal solution is selected.
4: The abovementioned procedures are iteratively repeated according to a backtracking approach, until the stopping criterion is satisfied.
5: The optimal vector and the step length for every iteration are delivered to the inverter.

The first experimental test is implemented to validate the control performance during a nominal speed reversal maneuver (from 2772 rpm to -2772 rpm). In Fig. 7.12, the measured waveforms of rotor speed, electromagnetic torque, rotor flux and stator current are illustrated. The speed reversal maneuver starts at t = 0.82 s, and the rotor speed reaches -2772 rpm at t = 1.11 s. It is noted that the proposed GD-FCSPCC has the advantage in terms of fast dynamic response that the settling time is only 290 ms. More specifically, the feasibility of the proposed algorithm is verified at the whole speed range.

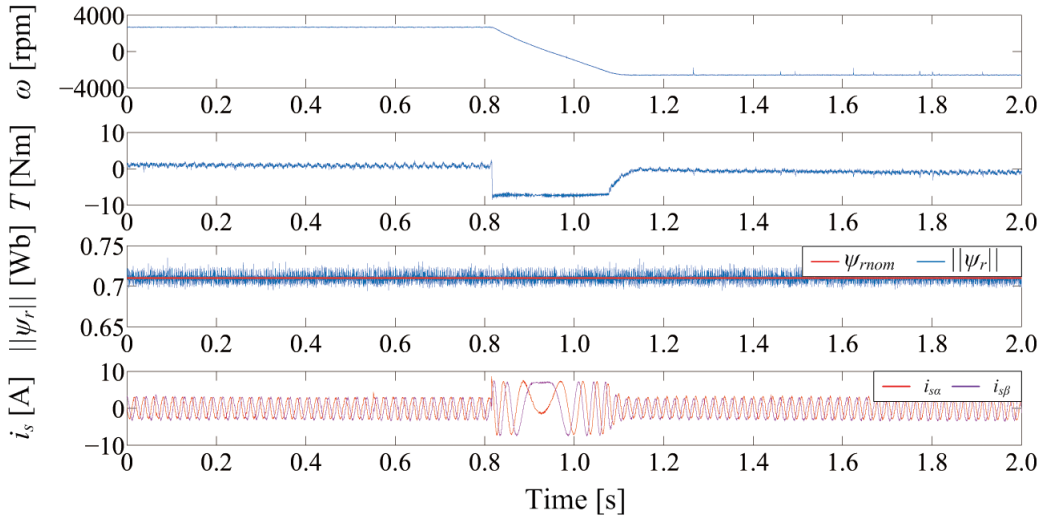

Figure 7.12: Speed reversal performance of the proposed GD-FCSMPC1 at full speed range.

The performance of the proposed GD-FCSMPC1 is investigated at the steady-state of 150 rpm with 4 Nm as well as rated rotor speed and load torque (2772 rpm with 7.5 Nm), respectively. The measured waveforms of rotor speed, electromagnetic torque, rotor flux, stator current and selected switching state at 150 rpm with 4 Nm are shown in Fig. 7.13. As we can see, the torque mean squared error (T_{mse} = 0.21 Nm) of the proposed GD-FCSPCC is lower than that of the conventional FCS-PCC (0.25 Nm), multistep FCS-MPC (0.48 Nm) as well as multi-vector based FCS-MPC (0.30 Nm). It is also observed that the proposed method obtains a slightly lower error of stator current magnitude ($||i_{serr}||$ = 0.23 A) due to its fast and effective convergence of tracking deviation. Compared with $||i_{serr}||$ of the conventional FCS-PCC, multistep FCS-MPC as well as multi-vector based FCS-MPC, the value is decreased by 20.7%, 39.5% and 11.5%, respectively. The stator current tracking performance is also shown

in Fig. 7.13. As can be seen, the stator current of the proposed algorithm tracks its reference value very well both in α and β-axis.

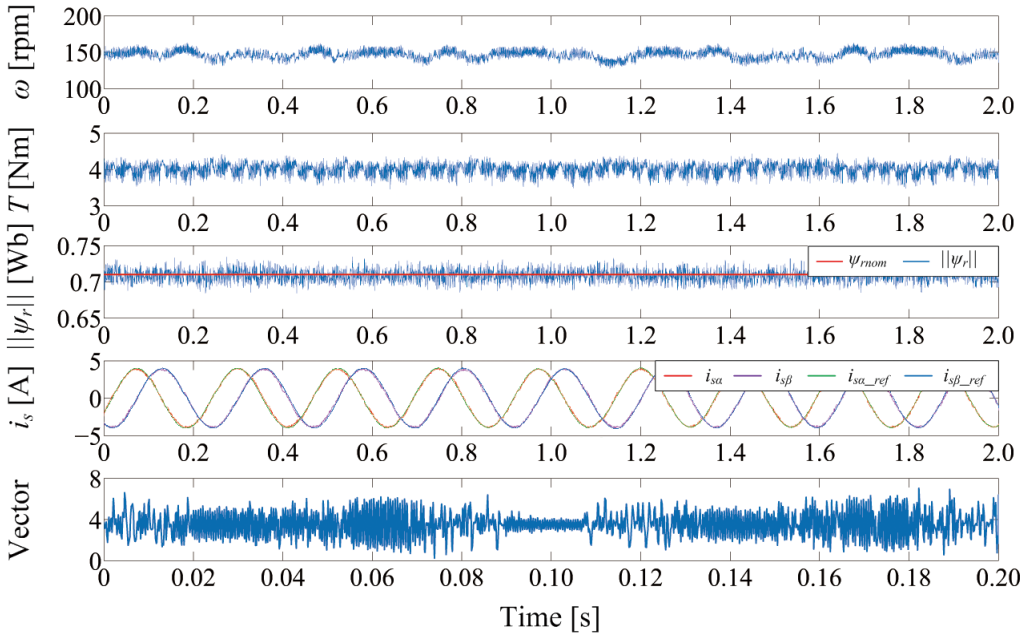

Figure 7.13: Steady-state performance of the proposed GD-FCSMPC1 at 150 rpm with 4 Nm.

The comparisons among the steady-state performance of the four algorithms at nominal rotor speed and load torque are shown in Fig. 7.14. As can be seen in Fig. 7.14, the mean squared error of electromagnetic torque is 0.31 Nm when FCS-PCC employs the gradient descent solution combined with a backtracking iterative approach. The value achieves a significant reduction than the conventional FCS-PCC (0.55 Nm), multistep FCS-MPC (0.68 Nm) as well as multi-vector based FCS-MPC (0.47 Nm). It is indicated that the error of rotor flux magnitude is 0.033 Wb. Moreover, the proposed method improves the performance in terms of stator current THD. The $||i_{serr}||$ of the proposed GDFCSMPC1 as well as methods in [32], [53] and [86] are 0.46 A, 0.67 A, 0.80 A and 0.58 A, respectively. Furthermore, the stator current of the proposed method tracks its reference value better than the other three algorithms. The steady-state performance of IM operates at rated speed and torque shares the similar trend with that of 150 rpm with 4 Nm. The trend of switching frequency versus rotor speed and torque for the proposed algorithm is illustrated in Fig. 7.15.

To validate the dynamic behavior of the proposed GD-FCSMPC1, the load step and load disturbance tests are carried out with the applied 10 kHz sampling frequency. Firstly, the IM operates at the torque control mode that 1000 rpm rotor speed is provided by the control panel and a constant 5 Nm torque reference is directly set in the algorithm. At the time instant 0.96 s, the electromagnetic torque decreases to 2 Nm in 0.3 ms. As the load step occurs, the rotor speed decreases to 790 rpm correspondingly. It is observed in Fig. 7.16 that the rotor speed returns to the original value in 300 ms thanks to the MPC's merit of quick transient response. In addition, the proposed method shows a significant improvement in very low T_{mse} (0.30 Nm) and stator current tracking error (0.14 A).

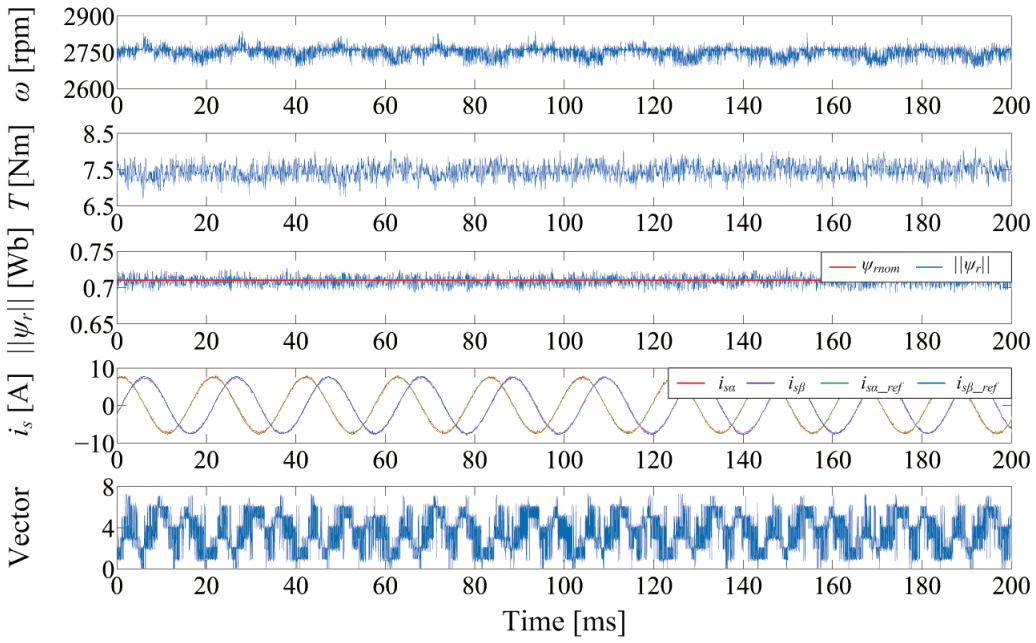

Figure 7.14: Steady-state performance of the proposed GD-FCSMPC1 at 2772 rpm with 7.5 Nm.

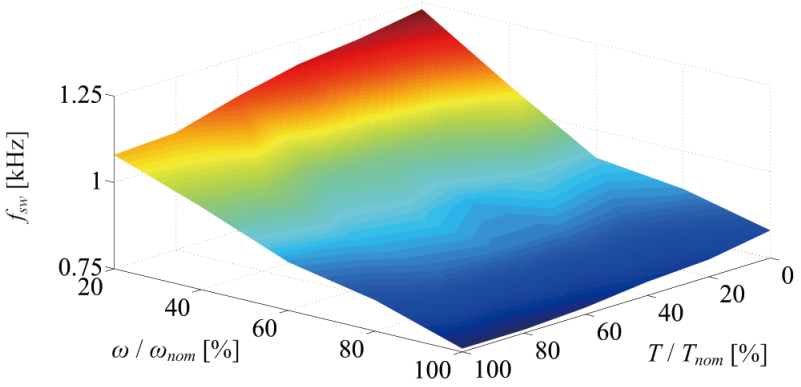

(a)

The load disturbance performance of the proposed method is evaluated subsequently. The IM runs at a constant rotor speed of 1500 rpm, and a 5 Nm load disturbance is further implemented. As shown in Fig. 7.17, the electromagnetic torque rises from 0 Nm to 5 Nm within 30 ms. Meanwhile, the rotor speed suffers from a 100 rpm decrease. The recovery time of rotor speed is approximately 90 ms. The T_{mse} and $||i_{serr}||$ of the proposed GD-FCSPCC are 0.43 Nm and 0.39 A, respectively. It can be seen that the proposed method performs well at the transient state.

Finally, the execution time of the four algorithms are collected in the 10 consecutive sampling periods from the controller, as shown in Fig. 7.18. The average algorithm time (defined as T_{algo}) is calculated and listed in TABLE 7.2. The T_{algo} of the proposed GD-FCSPCC is 38.426 μs,

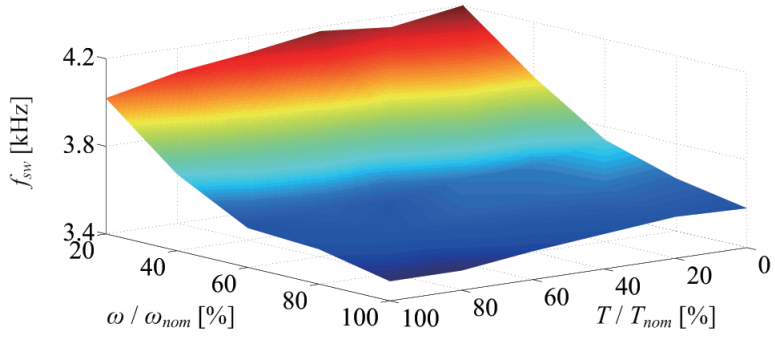

(b)

Figure 7.15: Switching frequency versus rotor speed and torque for the proposed algorithm. (a) 5 kHz sampling frequency. (b) 10 kHz sampling frequency.

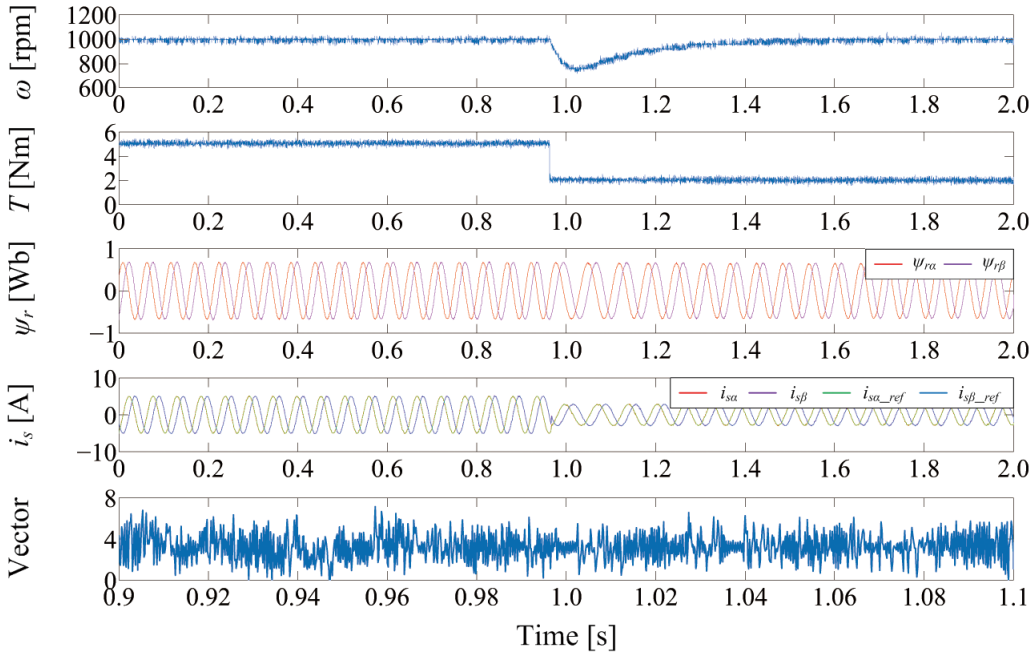

Figure 7.16: Load step performance of the GD-FCSMPC1 (ω = 1000 rpm, T decreases from 5 Nm to 2 Nm). From up to down are the measured waveforms of rotor speed, electromagnetic torque, rotor flux, stator current and the selected switching state.

and the value of the multi-vector based FCS-MPC is slightly lower (28.045 μs). The multistep FCS-MPC suffers from the longest T_{algo} (49.500 μs) while the conventional FCS-PCC achieves the least (22.459 μs).

7.6.2.2 GD-FCSMPC2

The block diagram of the GD-FCSMPC2 algorithm is demonstrated in Fig. 7.19 and the algorithm description is shown in Algorithm 3.

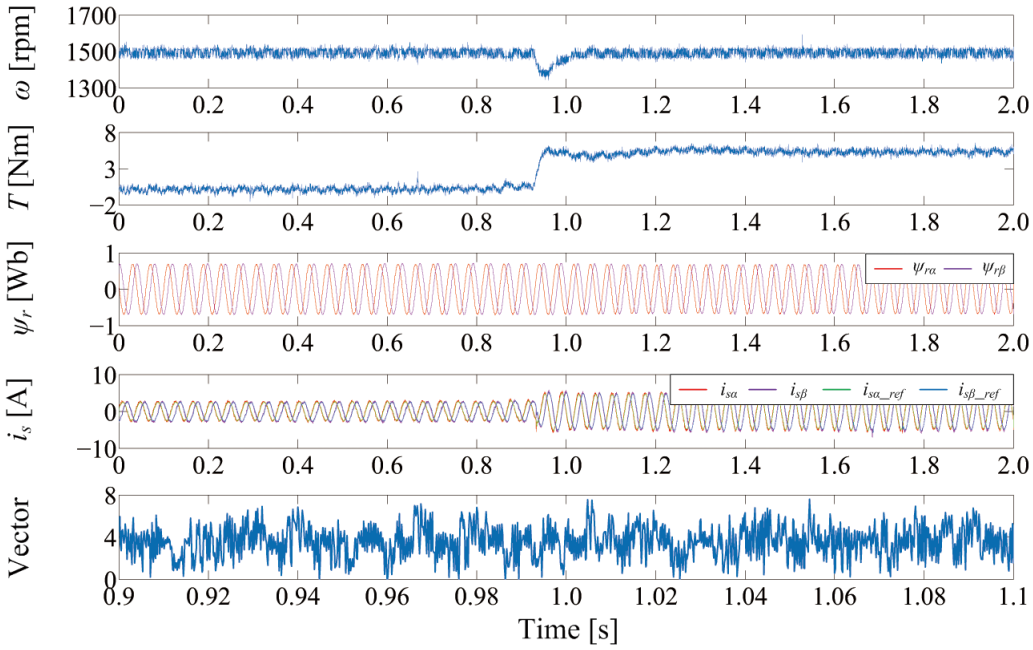

Figure 7.17: Load disturbance performance of the GD-FCSMPC1 (ω = 1500 rpm, T rises from 0 Nm to 5 Nm). From up to down are the measured waveforms of rotor speed, electromagnetic torque, rotor flux, stator current and the selected switching state.

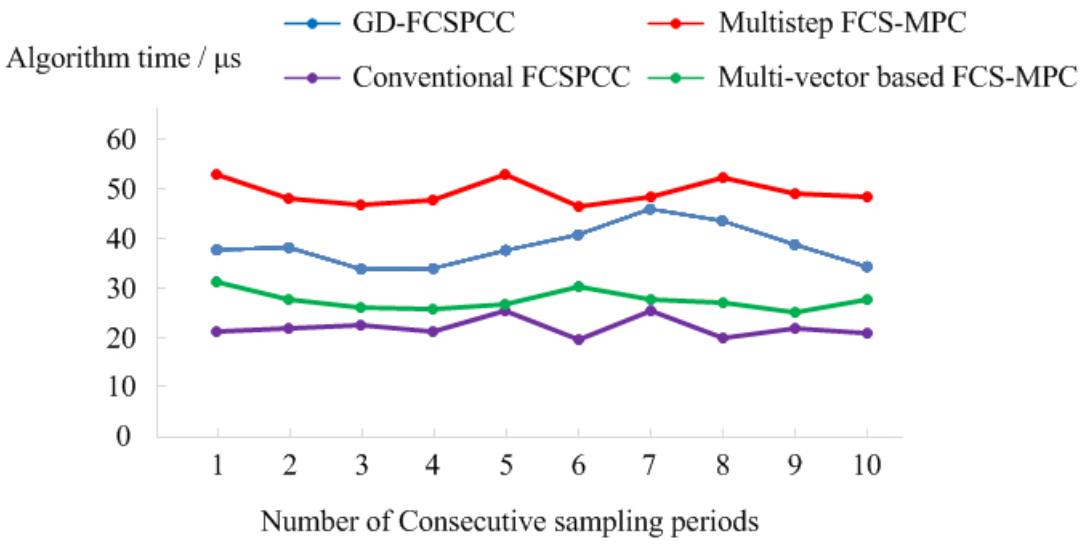

Figure 7.18: The execution time of the four algorithms in the 10 consecutive sampling periods.

The experimental implementation is firstly conducted to investigate the steady-state performance. The IM operates at the working condition of 50 rad/s with 4 Nm. As shown in Fig. 7.20, the measured waveform of vector is described as the decimal value (from 0 to 7) of the three-digit binary number from 000 to 111. It is indicated in Fig. 7.20 that the proposed

Table 7.2: The comparative issues among the average execution time of the four algorithms

Algorithms	Ref [32]	Ref [53]	Ref [86]	GD-FCSMPC1
T_{algo} [μs]	22.459	49.500	28.045	38.426

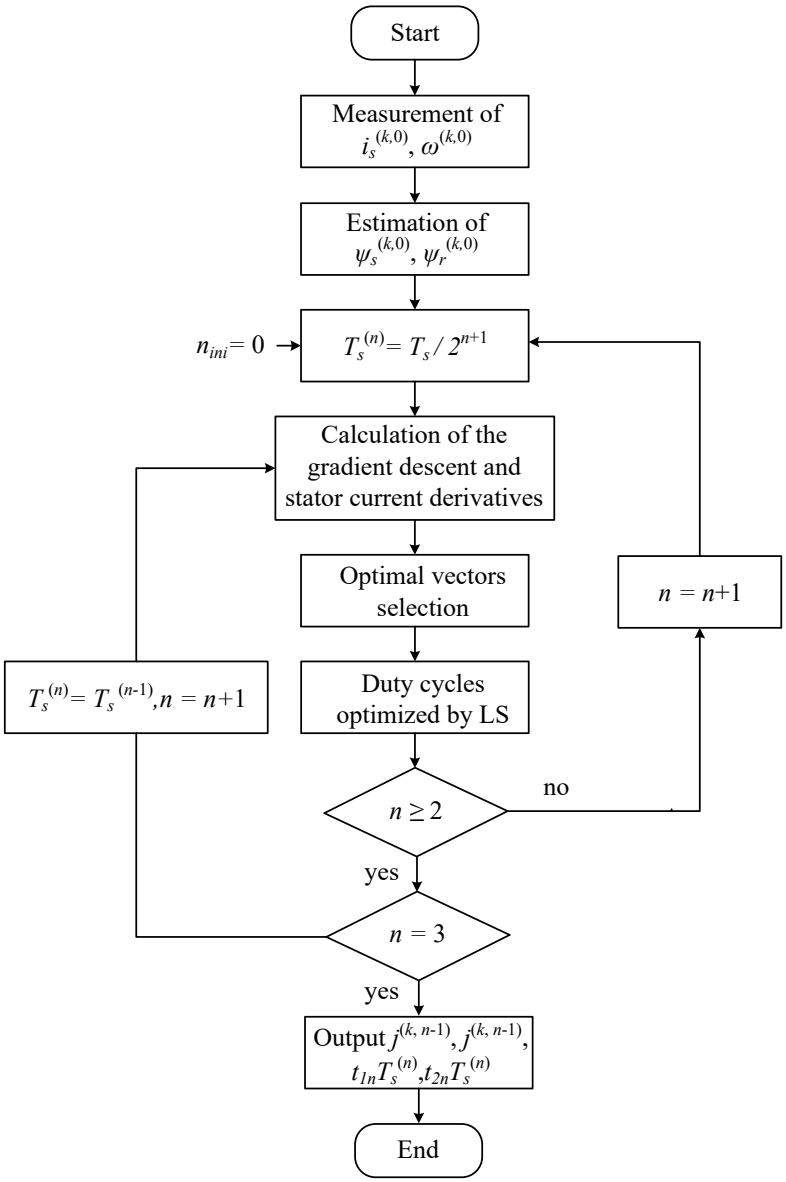

Figure 7.19: Flow diagram of the proposed GD-FCSMPC2 algorithm.

GD-FCSMPC2 algorithm obtains the lowest torque ripple (T_{ripple} = 0.91 Nm) and stator current magnitude error ($||i_{serr}||$ = 0.25 A). The aforementioned values are significantly reduced, compared with that of FCS-PCC (60.7 % and 48.3 %). Therefore, the steady-state performance of the GD-FCSMPC2 is improved at an affordable cost of increased algorithm complexity (47 μs) and averaged switching frequency (1.15 kHz).

Experimental verification is conducted on the proposed GD-FCSMPC2 at the nominal speed

Algorithm 3 The execution of the proposed GD-FCSMPC2 algorithm

1: System initialization, measurement of $\omega^{(k,0)}$ and $\boldsymbol{i}_s^{(k,0)}$, estimations of $\hat{\boldsymbol{\psi}}_s^{(k,0)}$ and $\hat{\boldsymbol{\psi}}_r^{(k,0)}$.
2: Calculation of the gradient descent and stator current derivatives for every switching state.
3: The optimal vector is selected by minimization the deviation function J.
4: Calculation of the duty cycles of the optimal vectors in the $n-1^{th}$ and n^{th} iterations by least squares optimization to polyfit the required gradient descent.
5: The abovementioned procedures are iterated by a dichotomy-based method until the stopping criterion is satisfied.
6: The optimal vectors with their duty cycles in a sampling period are delivered to the inverter.

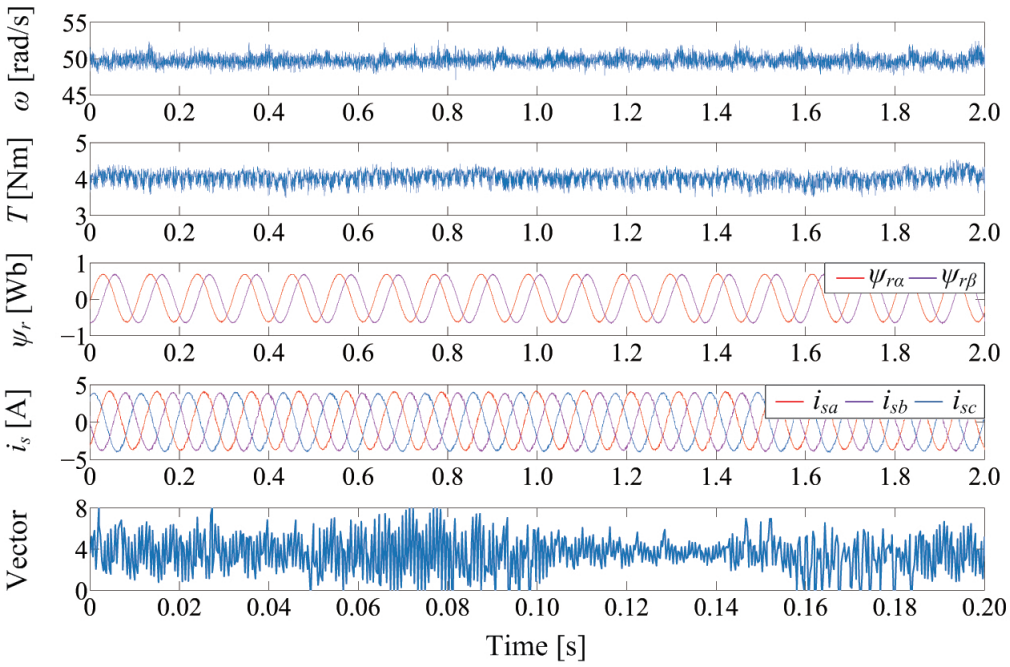

Figure 7.20: Steady-state performance of the proposed GD-FCSMPC2 at 50 rad/s with 4 Nm.

and torque afterwards. As shown in Fig. 7.21, a significant reduction (44.4 %) is achieved in terms of electromagnetic torque ripple by GD-FCSMPC2 than the conventional FCS-PCC. Moreover, the stator current magnitude error of GD-FCSMPC2 and FCS-PCC at rated speed and torque, are 0.52 A and 0.87 A, respectively. The reasons that the proposed algorithm achieves better control performance are twofold. First, the iterative gradient descent method tracks the reference value more efficiently than the conventional FCS-PCC. Second, the discrete switching state is directly applied in the conventional and dichotomy-based FCS-PCC. Contrary to this, the optimal solution in the proposed is optimized by the least squares method to achieve a smaller tracking deviation.

The speed reversal maneuver is carried out to verify the feasibility of the proposed GD-FCSMPC2 algorithm at the whole speed range. Measured waveforms of rotor speed, electromagnetic torque, rotor flux in $\alpha\beta$ frame and stator current are shown in Fig. 7.22. It can be seen that the proposed algorithm performs well that the torque mean squared error is 0.35 Nm and

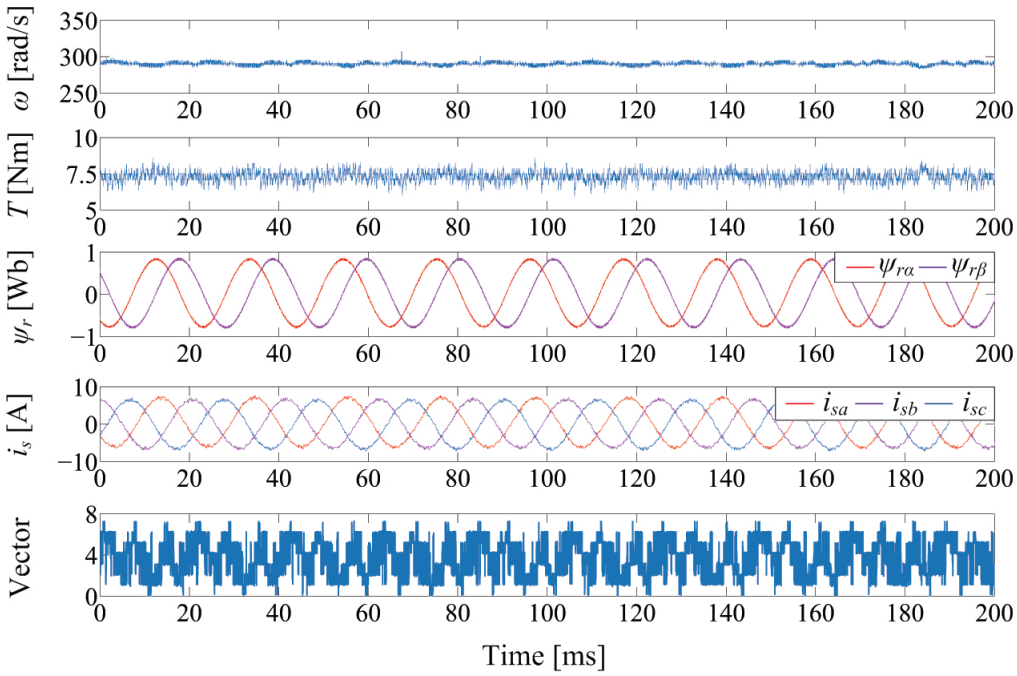

Figure 7.21: Steady-state performance of the proposed GD-FCSMPC2 at 290 rad/s with 7.5 Nm.

$||i_{serr}||$ is 0.46 A. The fast dynamic response of the proposed method is revealed that the speed reversal maneuver is completed within 260 ms. More specifically, the error of the rotor flux magnitude is 4.3%.

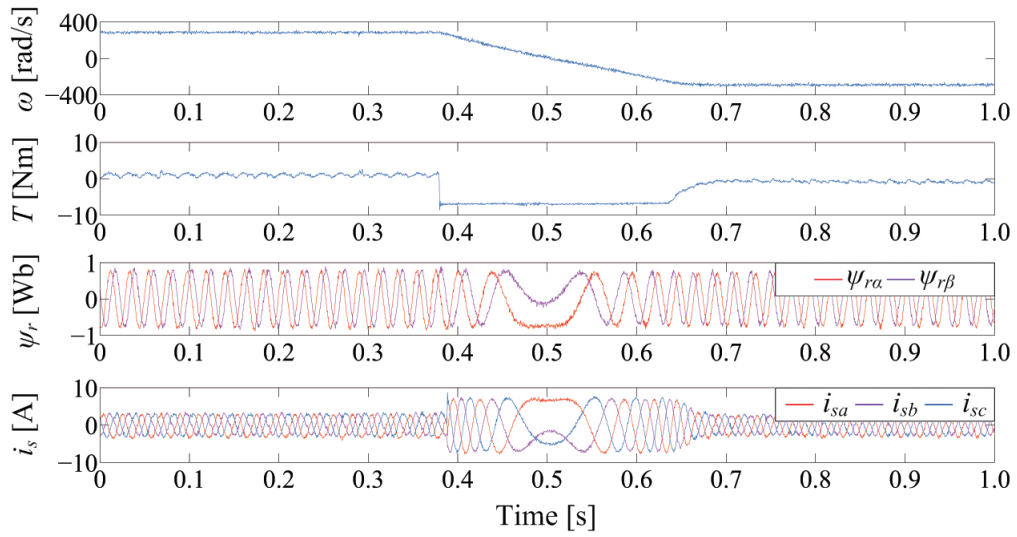

Figure 7.22: Speed reversal maneuver performance of GD-FCSMPC2.

In order to investigate the dynamic behavior of the proposed algorithm, load disturbance test is conducted that the induction machine operates at 200 rad/s against a 5 Nm load disturbance.

As depicted in Fig. 7.23, the fast dynamic response of the proposed method is validated that the electromagnetic torque rises from 0 to 5 Nm in 30 ms. At the same time, the rotor speed suffers from a 10 rad/s reduction and recovers to the original value in 75 ms. It can be observed that the proposed algorithm achieves a low torque ripple and stator current magnitude error (1.58 Nm, 0.32 A).

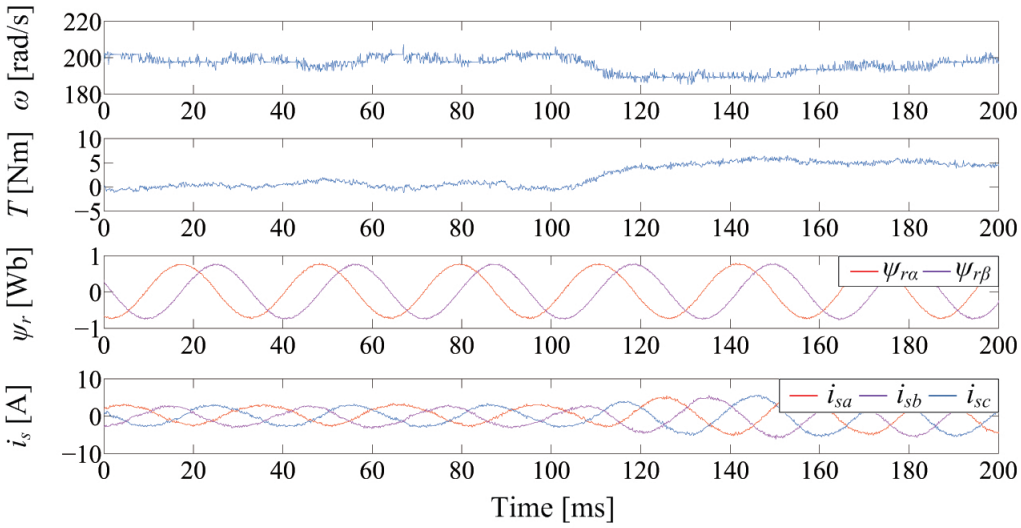

Figure 7.23: Load disturbance performance of GD-FCSMPC2.

A load step test is implemented on the testbench that the IM runs at the rotor speed of 50 rad/s. At t = 0.98 s, the electromagnetic torque increases from 2 to 5 Nm in 300 s, with a step change of load torque. It is exhibited in Fig. 7.24 that the rotor speed climbs to the peak of 80 rad/s. As the load step is completed, the electromagnetic torque ripple of the proposed algorithm is 1.04 Nm, which is lower than that of the conventional FCS-PCC (49.7 %). Similarly, the proposed method obtains the a lower stator current magnitude error (0.36 A), while the $||i_{serr}||$ of FCS-PCC is 0.58 A.

7.6.2.3 GD-FCSMPC3

A closed-loop block diagram of the proposed algorithm is shown in Fig. 7.25. The proposed algorithm has several control components including the prediction stage, the optimization stage of the gradient descent based objective function, the extension of finite set and the pruning algorithm. To describe the full implementation step, the flowchart of the proposed algorithm is demonstrated in Fig. 7.26.

Firstly, the effectiveness of the proposed GD-FCSMPC3 algorithm is validated. The measured waveforms of rotor speed, torque and rotor flux are investigated in Fig. 7.27. It can be observed that the rotor speed reverse from 290 rad/s to -290 rad/s at t = 0.84 s. The settling time of speed reversal maneuver is 250 ms. The experimental results verify that GD-FCSMPC3 obtains excellent performance includes small tracking errors and a very short settling time in a wide speed range [87–89].

The investigation of steady-state performance is carried out in the scenario of 30 rad/s with a 3 Nm load torque. As shown in Fig. 7.28, the measured waveforms of speed, torque, rotor flux

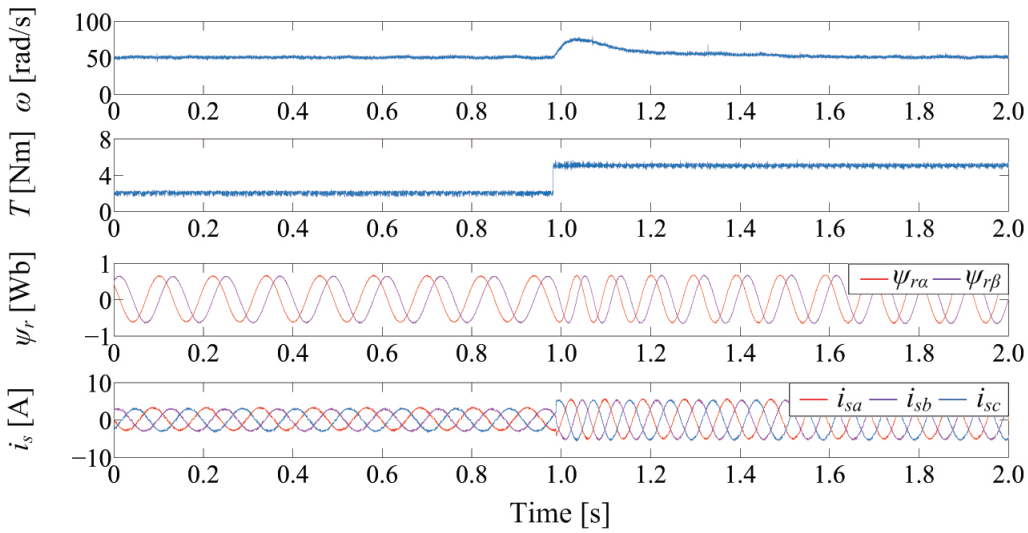

Figure 7.24: Load step performance of GD-FCSMPC2.

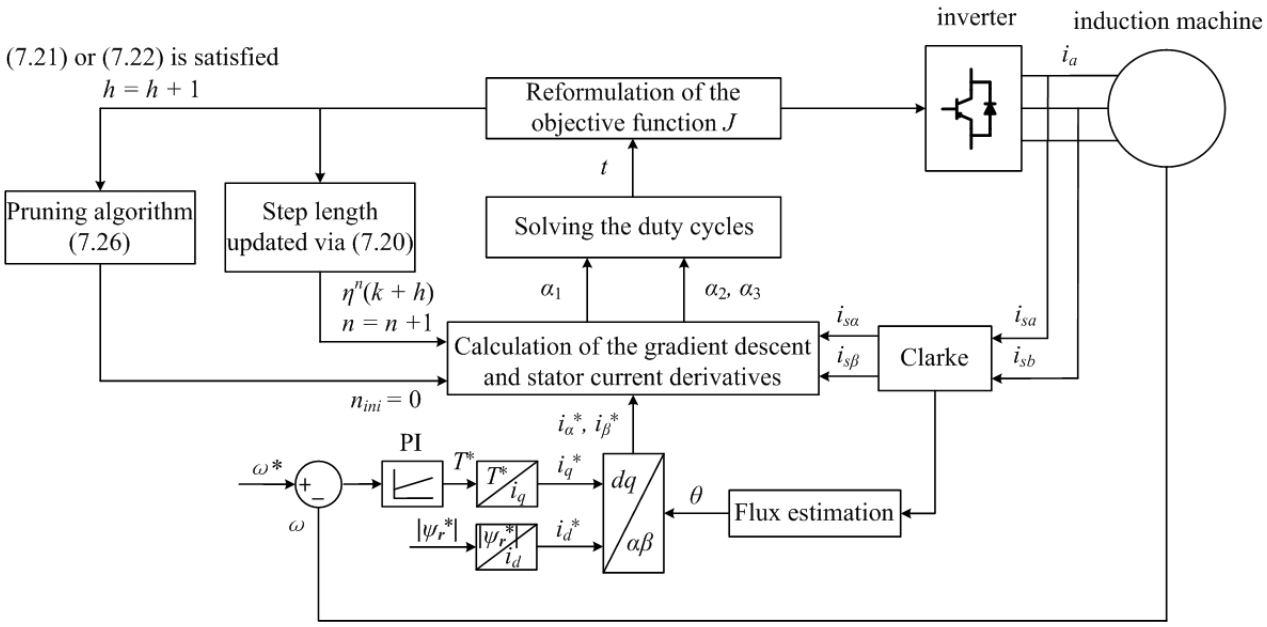

Figure 7.25: The closed-loop block diagram of the proposed algorithm.

and stator current are presented from up to down. The proposed algorithm with a prediction horizon of 3 achieves a lower torque and stator current error (T_{err} = 0.15 Nm, i_{serr} = 4.7 %). The reason relates to this is, the control objective iteratively searches along with the direction of GD, which minimizes the value of convex function F (the stator current deviation) more efficiently.

To validate the advantages of the proposed algorithm in the varied operating conditions, three FCS-PCC algorithms are compared in another test scenario of 200 rad/s with 5 Nm subse-

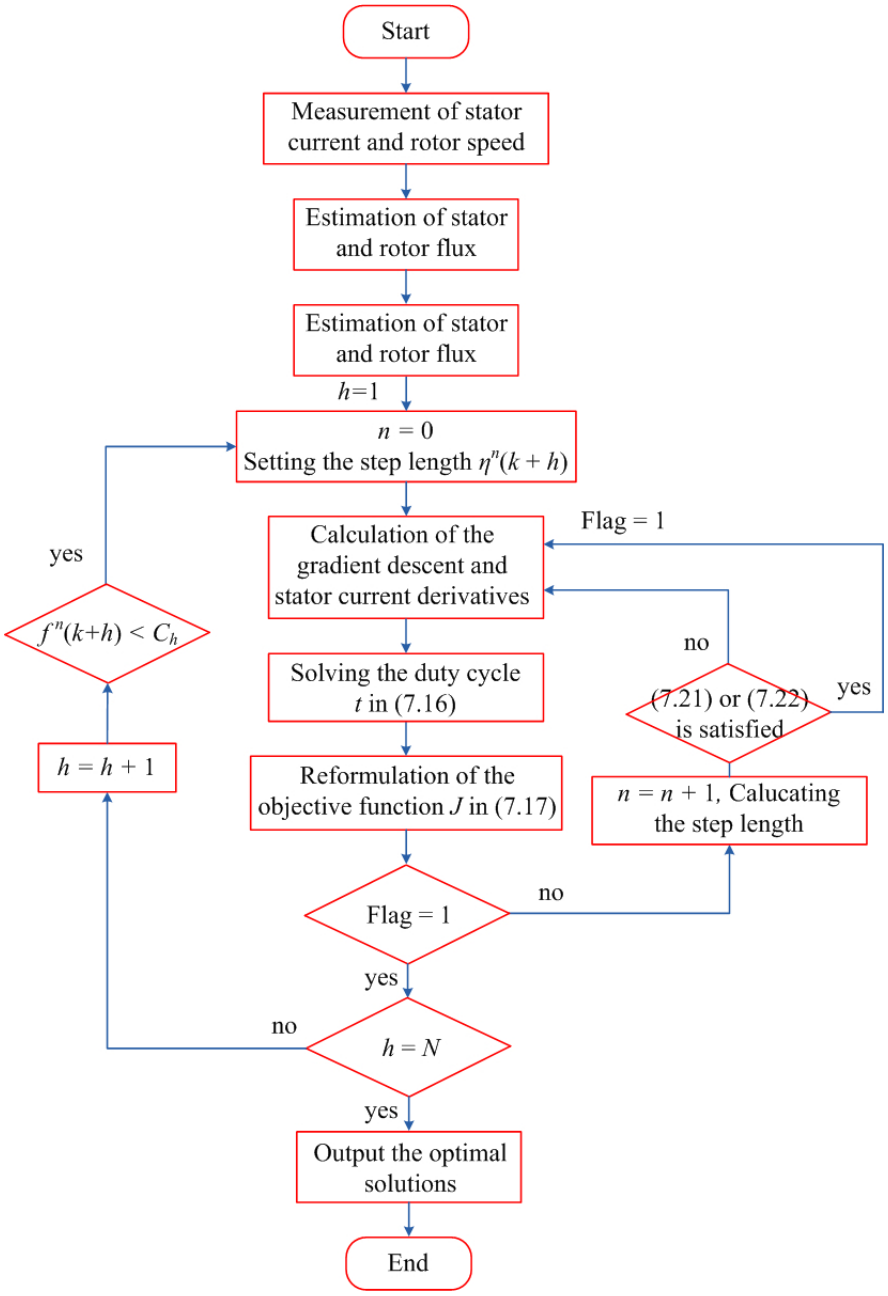

Figure 7.26: The flowchart of the proposed algorithm.

quently. As shown in Fig. 7.29, a similar conclusion can be drawn at a higher rotor speed with a 1.5 kHz switching frequency. Compared with the first test scenario, the proposed GD-FCSMPC3 algorithm achieves a slight higher i_{serr} (4.8 %) and torque error (T_{err} = 0.48 Nm). The performance metrics of the conventional FCS-PCC, long-horizon FCS-PCC and the proposed GD-FCSMPC3 algorithms in both scenarios are demonstrated in Fig. 7.30. It can be observed from the performance metrics that the current and torque tracking deviation of long-horizon FCS-PCC is increased by 29.2 % and 10.4 %, when compared with the proposed algorithm at 200 rad/s with 5 Nm. Moreover, the conventional FCS-PCC is penalized by the highest

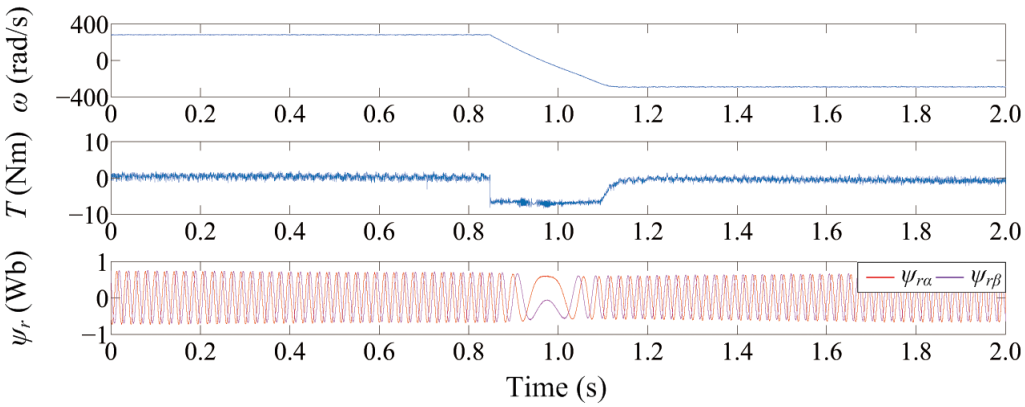

Figure 7.27: Speed reversal performance of the proposed algorithm (from 290 rad/s to -290 rad/s).

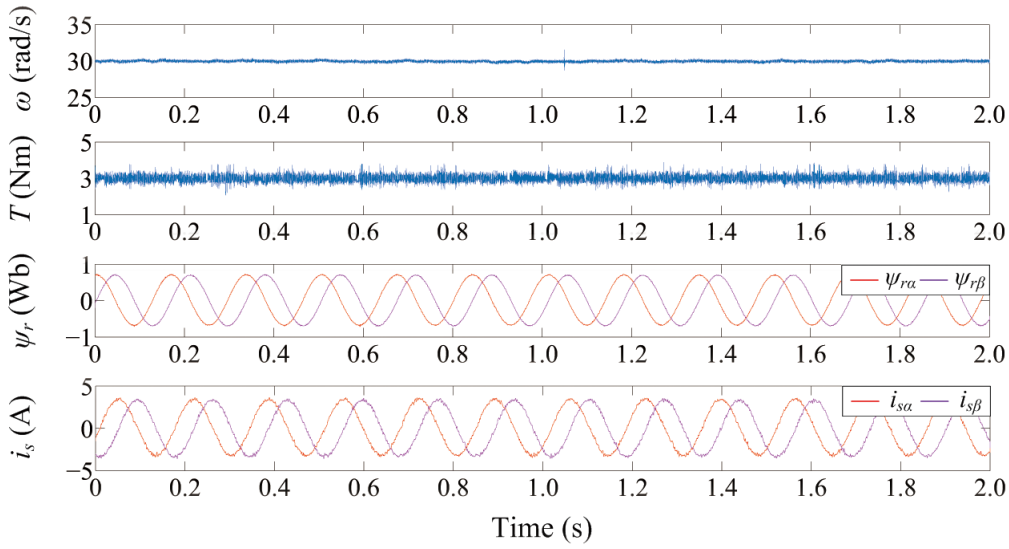

Figure 7.28: Steady-state performance of the proposed GD-FCSMPC3 in the test scenario of 30 rad/s with 3 Nm.

tracking deviations that i_{serr} is 7.5 % and T_{err} is 0.65 Nm. It is worth noted that the proposed algorithm only obtains about 46 % of the known information (i.e., measured stator current) from the control plant, when compared with the two prior FCS-PCC algorithms.

The load disturbance test of GD-FCSMPC3 is carried out, to evaluate the transient-state performance. In this scenario, the main machine runs at a constant rotor speed of 150 rad/s, which is given by the algorithm. Meanwhile, a 5 Nm load torque disturbance is applied to the load machine by the control panel. As shown in Fig. 7.31, it can be observed that the proposed algorithm retains the merit of fast dynamic response. As the load disturbance occurs, the rotor speed suffers from a slight 5 % decrease (7.5 rad/s), and returns to the original value within 80 ms afterwards. The load torque, rises from 0 Nm to 5 Nm in 30 ms with an 8 % overshoot. It can be concluded that the proposed algorithm achieves very short settling time

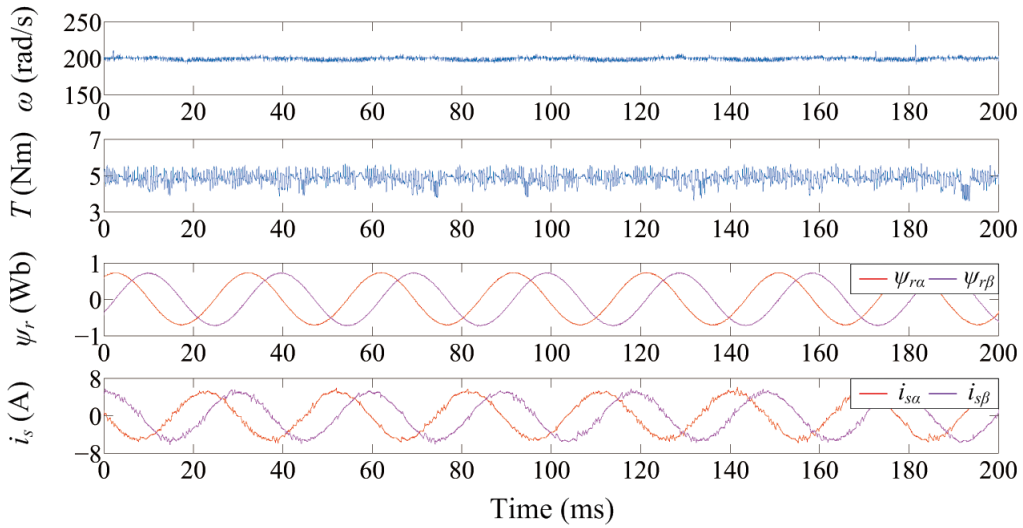

Figure 7.29: Steady-state performance of the proposed GD-FCSMPC3 in the test scenario of 200 rad/s with 5 Nm.

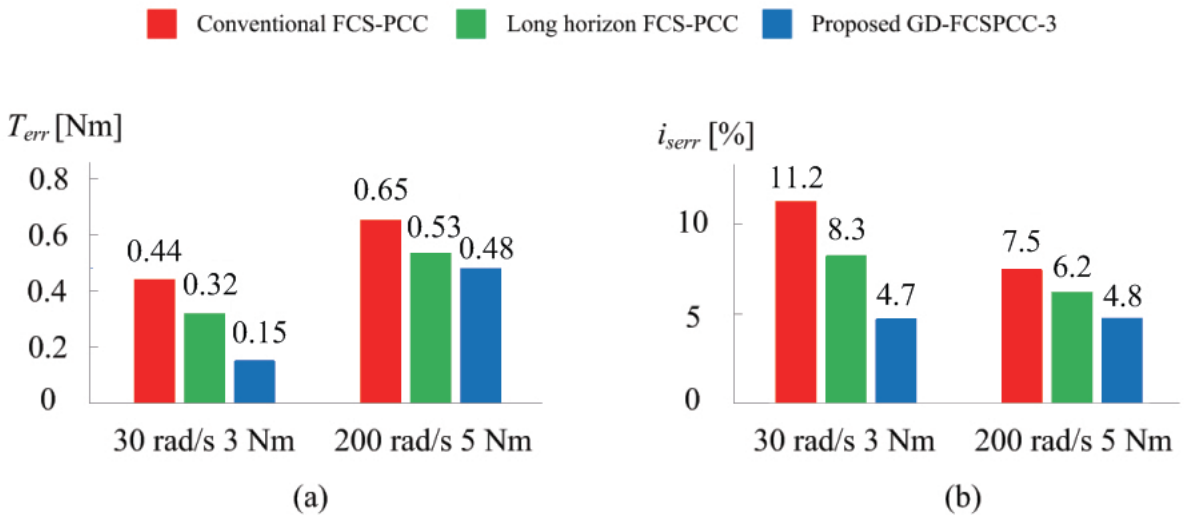

Figure 7.30: Performance metrics of the three algorithms in the steady-state scenarios. (a) comparison of torque deviations (b) comparison of stator current deviations.

and competitive control performance at the transient state when compared with the conventional and long-horizon FCS-PCC methods, due to the same speed PI parameters. The performance metrics of the proposed GD-FCSMPC3 at the transient state are summarized in TABLE. 7.3.

The robustness performance of the proposed GD-FCSMPC3 algorithm against variations of the system parameters (i.e., R_r and L_m), is validated. As shown in Fig. 32, the IM runs at a low rotor speed of 20 rad/s with a 200 % R_r mismatch, by increasing the rotor resistance from the nominal value $2.13\ \Omega$ to $6.4\ \Omega$. It can be observed that the proposed algorithm shows strong

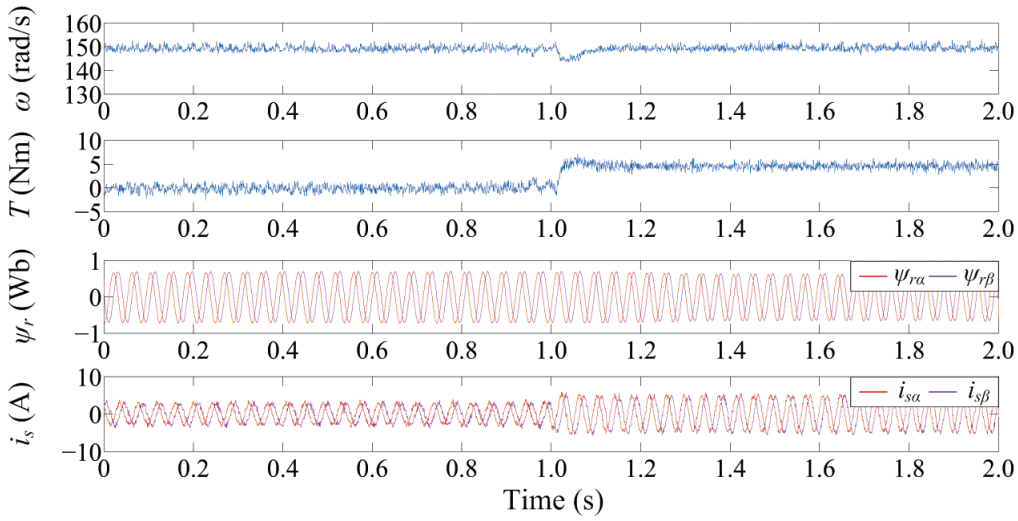

Figure 7.31: Transient-state performance of GD-FCSMPC3 at 150 rad/s with a 5 Nm load disturbance.

Table 7.3: Transient-state performance of the proposed GD-FCSMPC3

Performance metrics	GD-FCSMPC3
Rotor speed drop	7.5 rad/s
Speed recovery time	80 ms
Settling time of T	30 ms
Torque overshoot	8 %

robustness against R_r parameter mismatch. As a 200 % R_r mismatch occurs, the torque and flux tracking deviations keep stable, which are 0.18 Nm and 0.05 Wb, respectively.

The parameter sensitivity of the proposed algorithm against L_m mismatch is investigated in Fig. 7.33. As can be seen, the proposed controller becomes significant unstable, as a 20 % L_m variation takes place. The rotor speed and torque suffer from a larger ripple, while the magnitude of rotor flux is reduced by 60 %. The reason relates to this is the impact of L_m mismatch on the reference trajectory of stator current, as well as the calculation of GD. This conclusion is consistent with that has been drawn in [32].

Finally, the computational efforts of the three algorithms are evaluated in TABLE 7.4. It can be observed that the conventional FCS-PCC achieves the smallest algorithm time ($T_{algo} = 21.6$ μs), due to its simple concept. The pruning algorithm is used in both the long-horizon FCS-PCC and the proposed GD-FCSPCC-3, to dramatically reduce the number of searched control inputs with a prediction horizon of 3. The T_{algo} of long-horizon FCS-PCC is 48.8 μs. The algorithm time of the proposed GD-FCSPCC-3 with exhaustive search is 458 μs, which can be reduced to 69.3 μs by appling the pruning algorithm. As shown in Fig. 7.34, a pie chart illustrates the percentage of the computational requirements for each control component in the three algorithms. The percentages of calculation and optimization stage in the long-horizon

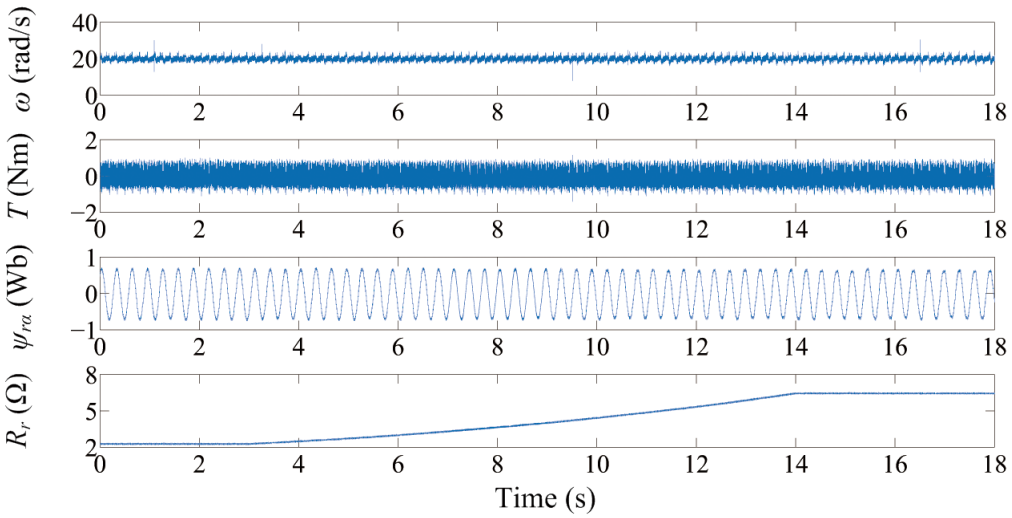

Figure 7.32: Robustness performance of the proposed GD-FCSMPC3 with a 200 % R_r mismatch.

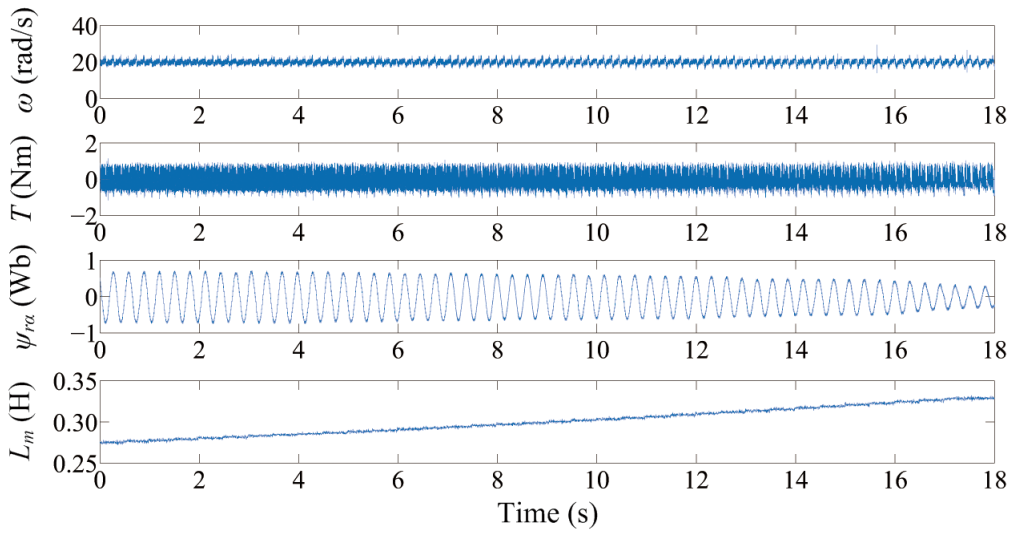

Figure 7.33: Robustness performance of the proposed GD-FCSMPC3 with a 200 % L_m mismatch.

FCS-PCC and the proposed algorithm are higher than that in the conventional FCS-PCC.

Table 7.4: Comparisons among the algorithm time of the three algorithms

Algorithms	Ref [32]	Ref [53]	GD-FCSPCC3	Exhaustive Search
T_{algo} [μs]	21.6	48.8	69.3	458

To evaluate the effectiveness of the pruning algorithm, the number of searched nodes in the GD-FCSPCC-3 is compared with the proposed algorithm with exhaustive search and the

Lenstra-Lenstra-Lovasz (LLL) method in [90]. As illustrated in TABLE 7.5, the number of searched nodes decreases from 517 to 14 by the LLL method for a three-level power converter, while the value declines from 1197 to 80 by the proposed PA. The results indicate that the proposed PA shows a competitive effectiveness compared with the LLL method.

Table 7.5: Comparative issues among the maximum number of nodes by exhaustive search, LLL and PA

Algorithms	Exhaustive Search in [90]	LLL
number [/]	517	14
Algorithms	GD-FCSMPC3 without PA	GD-FCSMPC3 with PA
number [/]	1197	80

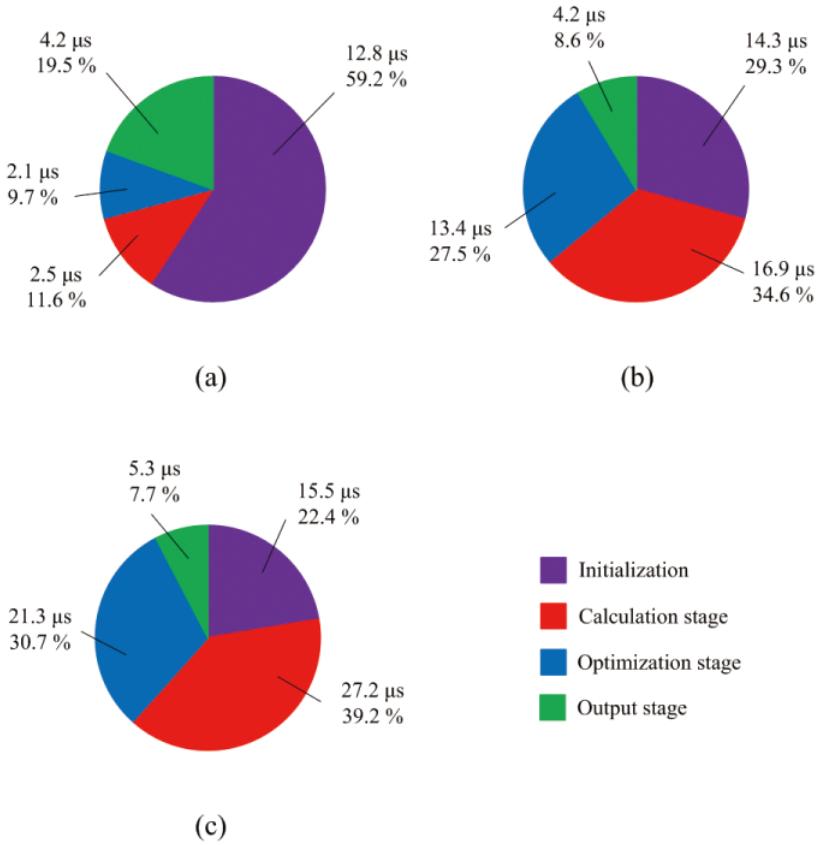

Figure 7.34: The computational requirements of the controller components in the three algorithms. (a) conventional FCS-PCC (b) long-horizon FCS-PCC (c) the proposed GD-FCSMPC3.

7.7 Conclusion

In this chapter, the potential of performance improvement for the FCS-MPC schemes is investigated. Firstly, the FCS-MPC optimization problem is regarded as a QP problem from a geometric perspective. Based on the above, the convexity of the QP problem is proved, to employ the gradient descent solution in FCS-MPC, in which a deepest decrease occurs as the control variable searches along with the direction of gradient descent. Furthermore, the convergence of the gradient descent solution has been analyzed. Finally, three gradient descent solutions for FCS-MPC are evaluated as the case studies. The effectiveness of the proposed solutions are validated on the testbench.

CHAPTER 8

Encoderless technology for FCS-MPC

MPC has explored its advantages of very intuitive concept, straightforward implementation, flexible inclusion of constraints, fast dynamic response and the capability to handle with multiple conflicting targets in the power electronic applications. As a model-based strategy, MPC still requires the known information, i.e., rotor angular speed in the electrical drive systems, to predict the behavior of the control variables. Although an encoder can be used to measure the rotor speed, it will result in the increased cost of installation and maintenance and degraded system reliability. Moreover, the parameter mismatches in the system model will inevitably lead to the prediction error and deteriorated control performance. In this chapter, the encoderless technologies for FCS-MPC scheme with a reformulated objective function are introduced instead of an encoder, which bring the merits of cost reduction, high reliability, easy installation and maintenance, the ability to operate in harsh environment and strong robustness against parameter variations.

8.1 Introduction

As a model-based control strategy, FCS-MPC calls for the inherent requirement on the rotor position, which is normally measured by an encoder [34]. However, the installation of the encoder results in the increased system complexity, wherein the significant degradation of stability takes place [91]. Thus, several model-based speed estimator has been intensively researched in recent years, such as Luenberger observer, adaptive full-order observer (AFO), sliding mode observer (SMO), model reference adaptive system (MRAS) and extended Kalman filter (EKF). In [92], AFO with the corresponding feedback gain is developed for IM. It is confirmed that the estimated error of rotor speed caused by the system parameter variations, is reduced. A robust sensorless scheme based on flux observer is proposed in [93], which improves robustness by the approach of parameter compensation. In [94], a sensorless FCS-PTC for IM using extended Kalman filter (EKF) is proposed, to reduce the speed error in a wide speed range. In [95], a

compensated MRAS estimator based FCS-PTC for IM is presented. However, the influence of rotor time constant on speed estimation is ignored. Yang $et\ al$ [96] proposed a MRAS current observer for sensorless control of a doubly-fed induction machine. The stability and feasibility of the proposed method are confirmed by simulation and experimental results. As concluded in [97], the rotor time constant is modified in the MRAS estimator for IM drives. However, the tuning of stator resistance is simple but not satisfactory. In [98], a MRAS estimator is designed to estimate the rotor speed and flux for the PPTC algorithm. However, the mismatch of rotor time constant has not been taken into consideration, and the influence of parameter uncertainties on PPTC has not been theoretically analyzed. A discrete hybrid prediction model is presented in [99] to improve the robustness performance of PTC for PMSM drives, to establish the close-loop prediction models for stator current and flux. In [100], a robust predictive torque and flux control for N*3-phase PMSM drives is proposed. The robustness against load torque disturbance and parameter uncertainties of the proposed algorithm is effectively strengthened by the unknown torque disturbance observer. In [101]. the impressing results on simultaneous stator and rotor resistance identification for sensorless IM drives are presented. The topic is explored according to a novel direction that the IM dynamic is transformed into the form of adaptive observer (AO). More specifically, an alternative solution is proposed in [102] to solve the issue of parameter sensitivity in high gain AO. The proposed algorithm yields the merits that the two-way coupling is removed and less computational resources are consumed. However, the prediction error in FCS-MPC is not considered in the aforementioned strategies, which is required to be further investigated.

As can be understand, the encoderless technology for FCS-MPC schemes not only estimates the rotor speed but also improves the robustness against parameter variations. In this chapter, a model reference adaptive system (MRAS) is employed for the FCS-PTC and constrained parallel structure FCS-PTC, respectively. The reasons for choosing MRAS are the shared IM model with the FCS-PTC schemes, the improved estimation accuracy in stator flux-linkage and easier parameter tuning. The proposed algorithms are experimentally carried out on the 2.2 kW IM drive testbench for further evaluation.

8.2 MRAS for FCS-PTC

8.2.1 MRAS estimator

The block diagram of the MRAS estimator is shown in Fig. 8.1. To estimate the rotor speed for FCS-PTC scheme, the voltage and current model are employed as the reference and adjustable model. In the stationary reference frame, the voltage model is calculated as

$$\hat{\psi}_s = \int (u_s - i_s \hat{R}_s) dt \tag{8.1}$$

$$\hat{\psi}_r = \frac{L_r}{L_m}(\hat{\psi}_s - L_s \sigma i_s) \tag{8.2}$$

The current model is described as

$$\frac{d\hat{\boldsymbol{\psi}}_{\boldsymbol{rI}}}{dt} = \frac{L_r R_r}{L_m} \cdot \boldsymbol{i}_s - (\frac{R_r}{L_r} - j\hat{\omega} \cdot \boldsymbol{i}_s)\hat{\boldsymbol{\psi}}_{\boldsymbol{rI}} + f(\hat{e}) \tag{8.3}$$

Thus, the error term between the reference model and the adjustable model is

$$\hat{e}_{\psi r} = \hat{\boldsymbol{\psi}}_{\boldsymbol{rI\alpha}}\hat{\boldsymbol{\psi}}_{\boldsymbol{r\beta}} - \hat{\boldsymbol{\psi}}_{\boldsymbol{rI\beta}}\hat{\boldsymbol{\psi}}_{\boldsymbol{r\alpha}} \tag{8.4}$$

As can be seen, a PI controller is designed as the adaptation mechanism in the MRAS estimator. It is employed for modification in the adjustable model. The adaptation mechanism of MRAS is constructed as (8.5)

$$f(\hat{e}) = k_{p\omega}\hat{e}_{\psi r} + k_{i\omega}\int \hat{e}_{\psi r}dt \tag{8.5}$$

The stator resistance compensation is described as

$$\begin{aligned} \hat{e}_{Rs} &= \boldsymbol{i}_{s\alpha}\cdot(\hat{\boldsymbol{\psi}}_{\boldsymbol{rI\alpha}} - \hat{\boldsymbol{\psi}}_{\boldsymbol{r\alpha}}) + \boldsymbol{i}_{s\beta}\cdot(\hat{\boldsymbol{\psi}}_{\boldsymbol{rI\beta}} - \hat{\boldsymbol{\psi}}_{\boldsymbol{r\beta}}) \\ \hat{R}_s &= k_{pRs}\hat{e}_{Rs} + k_{iRs}\int \hat{e}_{Rs}dt \end{aligned} \tag{8.6}$$

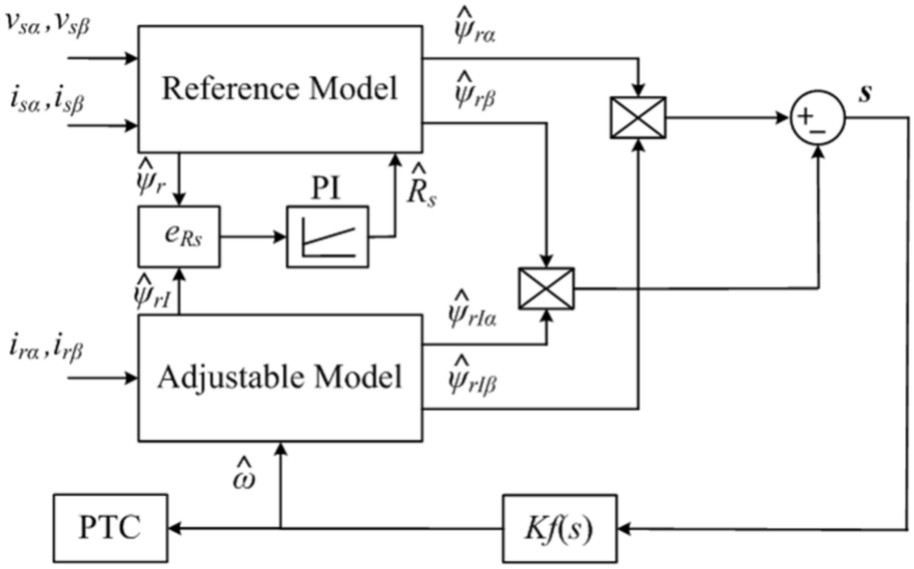

Figure 8.1: Block diagram of the MRAS estimator.

8.2.2 Encoderless FCS-PTC scheme

The encoderless FCS-PTC scheme selects torque and stator flux as the control objectives. As shown in Fig. 8.2, the block diagram of the encoderless FCS-PTC scheme is presented. The predicted stator current and flux-linkage are calculated as

$$\hat{\psi}_s(k+1) = \hat{\psi}_s(k) + T_s(u_s(k) - \hat{R}_s \cdot i_s(k)) \tag{8.7}$$

$$\hat{i}_s(k+1) = (1 - \frac{T_s}{\tau_\sigma})i_s(k) + \frac{T_s}{\tau_\sigma R_\sigma}\cdot[k_r\cdot(\frac{1}{\tau_r} - j\omega(k))\cdot\hat{\psi}_r(k) + u_s(k)] \tag{8.8}$$

The predicted electromagnetic torque is calculated by the predicted current and flux.

$$\hat{T}(k+1) = \frac{3}{2} \cdot p \cdot Im\left\{\hat{\psi}_s(k+1)^* \cdot \hat{i}_s(k+1)\right\} \tag{8.9}$$

For every switching candidates, the tracking error between the predicted stator flux and torque and their reference value is calculated in the cost function g_j, as shown in (8.10). The optimized switching state which minimizes the cost function will be chosen as the optimal solution.

$$g_j = (\hat{T}(k+2) - T^*)^2 + \lambda_\psi^2(||\hat{\psi}_s(k+2)|| - \psi_s^*)^2 + Im(k+2) \tag{8.10}$$

where T^* is the torque reference generated by the speed PI controller, and ψ_s^* is the stator flux magnitude reference. λ is the weighting factor to modify the torque and flux terms in accordance with the working conditions.

Considering that the time delay compensation in the encoderless FCS-PTC scheme, the predicted values of torque and flux in the $k+2$ period are compared with the reference values in the objective function. More specifically, the constraint for current limitation is designed as follows

$$I_m(k+2)_j = \begin{cases} 0, & if\ |\boldsymbol{i}_s(k+2)_j| \leq |\boldsymbol{i}_{smax}| \\ \infty, & if\ |\boldsymbol{i}_s(k+2)_j| > |\boldsymbol{i}_{smax}| \end{cases} \tag{8.11}$$

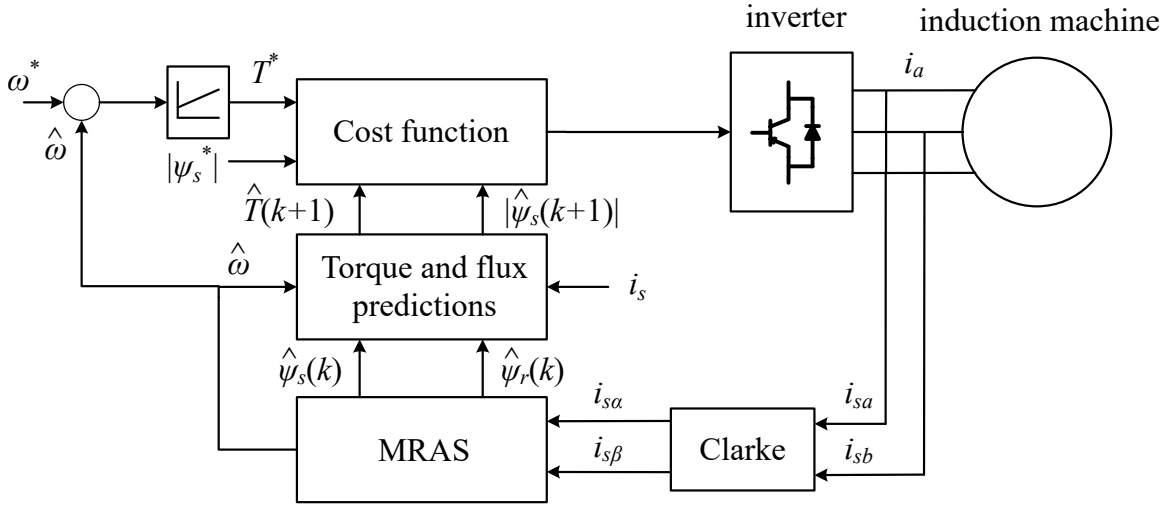

Figure 8.2: Block diagram of the encoderless FCS-PTC scheme.

8.3 Robust MRAS for constrained parallel structure FCS-MPC

The principle description of the proposed constrained parallel structure FCS-MPC has been introduced in Chapter. 5.5. In this section, the issues on robustness as well as the encoderless technology for the proposed method are discussed in detail.

8.3.1 Parameter sensitivity analysis

As a model-based control strategy, the control performance of PPTC is detrimentally influenced by the inevitable predicted errors, due to the parameter variations in the control plant. Therefore, the sensitivity analysis of the algorithm to the parameters such as the stator resistance R_s and rotor time constant τ_r is of great importance to improve the robustness of PPTC. In this paper, the parameter sensitivity is studied according to the following assumptions.
(1) R_r has the same changing rate with that of R_s.
(2) The measured noise of stator current is ignored that $i_s(k)$ is accuracy.

Hence, ΔR_s and $\Delta\tau_r$ are the errors between the actual and mismatched parameters. When the stator resistance deviation ΔR_s is considered, the actual values of the predicted stator flux-linkage and current are rewritten as

$$\hat{\boldsymbol{\psi}}_s^R(k+1) = \hat{\boldsymbol{\psi}}_s(k) + T_s\left(\boldsymbol{v}_s(k) - \boldsymbol{i}_s(k)\cdot(R_s+\Delta R_s)\right) \tag{8.12}$$

$$\hat{\boldsymbol{i}}_s^R(k+1) = (1-\frac{T_s}{\tau_\sigma+\Delta\tau_\sigma})\cdot i_s(k) + \frac{T_s}{\sigma L_s}\cdot[k_r(\frac{1}{\tau_r}-j\hat{\omega})\hat{\psi}_r(k) + v_s(k)] \tag{8.13}$$

Thus, the unknown disturbances of the predicted values are denoted by $\Delta\hat{\boldsymbol{\psi}}_s^R(k+1)$ = $\boldsymbol{\psi}_s^R(k+1)$ - $\hat{\boldsymbol{\psi}}_s(k+1)$ and $\Delta\boldsymbol{i}_s^R(k+1)$ = $\hat{\boldsymbol{i}}_s^R(k+1)$ - $\hat{\boldsymbol{i}}_s(k+1)$, which are deduced as

$$\Delta\boldsymbol{\psi}_s^R(k+1) = -T_s\boldsymbol{i}_s(k)\Delta R_s \tag{8.14}$$

$$\Delta\boldsymbol{i}_s^R(k+1) = \frac{\Delta\tau_\sigma}{\tau_\sigma(\tau_\sigma+\Delta\tau_\sigma)}T_s i_s(k) \tag{8.15}$$

As the deviation of rotor time constant $\Delta\tau_r$ occurs, it does not lead to the stator flux-linkage error in the prediction stage. The predicted value $\hat{\boldsymbol{i}}_s^\tau(k+1)$ are described as follows:

$$\begin{aligned}\hat{\boldsymbol{i}}_s^\tau(k+1) =& (1-\frac{T_s}{\tau_\sigma})\cdot i_s(k) + \frac{T_s}{\sigma L_s}\cdot[k_r(\frac{1}{\tau_r+\Delta\tau_r}\\ &- j\hat{\omega}\hat{\psi}_r(k) + v_s(k)]\end{aligned} \tag{8.16}$$

where $\Delta\boldsymbol{i}_s^\tau(k+1)$ = $\hat{\boldsymbol{i}}_s^\tau(k+1)$ - $\hat{\boldsymbol{i}}_s(k+1)$, which is described as

$$\Delta\boldsymbol{i}_s^\tau(k+1) = -\frac{\Delta\tau_r}{\tau_r(\tau_r+\Delta\tau_r)}\frac{k_r T_s}{\sigma L_s}\hat{\psi}_r(k) \tag{8.17}$$

Based on the above, the variation of predicted stator current $\Delta i_s(k+1)$ can be expressed in (8.18) when ΔR_s and $\Delta\tau_r$ are taken into consideration simultaneously. The predicted flux-linkage error $\Delta\boldsymbol{\psi}_s(k+1)$ is described in (8.19).

$$\begin{aligned}&\Delta\boldsymbol{i}_s(k+1) = \Delta\boldsymbol{i}_s^R(k+1) + \Delta\boldsymbol{i}_s^\tau(k+1)\\ =&\frac{\Delta\tau_\sigma}{\tau_\sigma(\tau_\sigma+\Delta\tau_\sigma)}T_s i_s(k) - \frac{\Delta\tau_r}{\tau_r(\tau_r+\Delta\tau_r)}\frac{k_r T_s}{\sigma L_s}\hat{\psi}_r(k)\end{aligned} \tag{8.18}$$

$$\Delta\boldsymbol{\psi}_s(k+1) = \Delta\boldsymbol{\psi}_s^R(k+1) = -T_s\boldsymbol{i}_s(k)\Delta R_s \tag{8.19}$$

Therefore, the predicted stator current and flux-linkage deviations of PPTC with R_s and τ_r mismatches are evaluated under different operating conditions. The measured deviations are

obtained by the repetitive simulation implementations in the Matlab/Simulink environment. As shown in Fig. 8.3, the percentage of predicted stator current deviation increases significantly according to R_s and τ_r mismatches (14.8% with 200% R_s and τ_r at the nominal operating condition). More specifically, it is more sensitive to R_s variation. Similar trend can be observed in the test scenario of 150 rpm with 2 Nm, the predicted current error increases from 5.88 % to 10.96 %, as shown in Fig. 8.4. In terms of predicted stator flux-linkage deviation, the percentage of deviation reaches 23.0% with 200% R_s in Fig. 8.5. It is demonstrated that the percentage of stator flux-linkage deviation keeps constant as the variation of τ_r occurs. The three-dimensional diagram of predicted error with ΔR_s and $\Delta\tau_r$ is shown in Fig. 8.6. The predicted flux-linkage error is 16.8 % with 100 % ΔR_s.

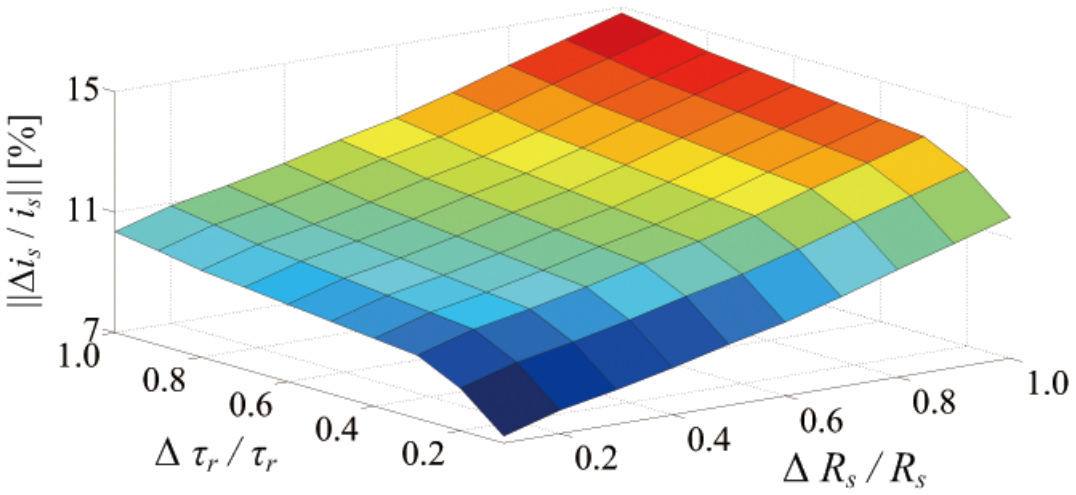

Figure 8.3: Predicted stator current deviation of PPTC with R_s and τ_r mismatches. (2772 rpm with 7.5 Nm).

8.3.2 Robust MRAS estimator

In this section, the robust encoderless MRAS estimator with online parameter identification algorithm is presented, to meet the control system's requirements for accuracy speed estimation and robustness improvement. In the proposed MRAS estimator, the voltage model is used as the reference model to estimate stator flux-linkage, while the current model is employed as the adaptive model, as shown in (8.20-8.21). $k_{p\omega}$ and $k_{i\omega}$ are the gains for the MRAS speed estimator.

$$\begin{aligned} \frac{d\hat{\boldsymbol{\psi}}_{\boldsymbol{s}}}{dt} &= u_s - \hat{R}_s \boldsymbol{i}_s \\ \frac{d\hat{\boldsymbol{\psi}}_{\boldsymbol{r}}}{dt} &= \frac{L_r}{L_m}\left(\frac{d\hat{\boldsymbol{\psi}}_{\boldsymbol{s}}}{dt} - L_s\sigma \cdot \frac{d\boldsymbol{i}_s}{dt}\right) \end{aligned} \tag{8.20}$$

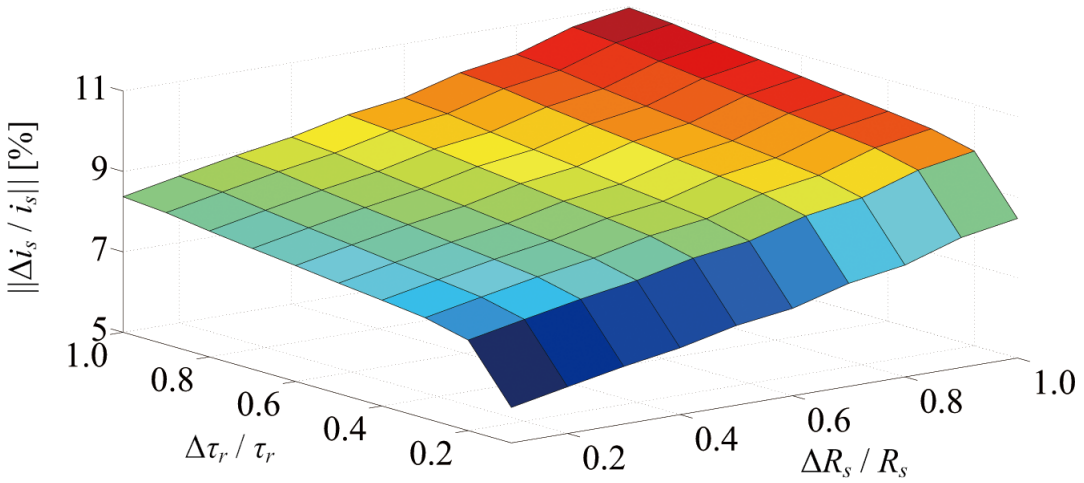

Figure 8.4: Predicted stator current deviation of PPTC with R_s and τ_r mismatches. (150 rpm with 2 Nm).

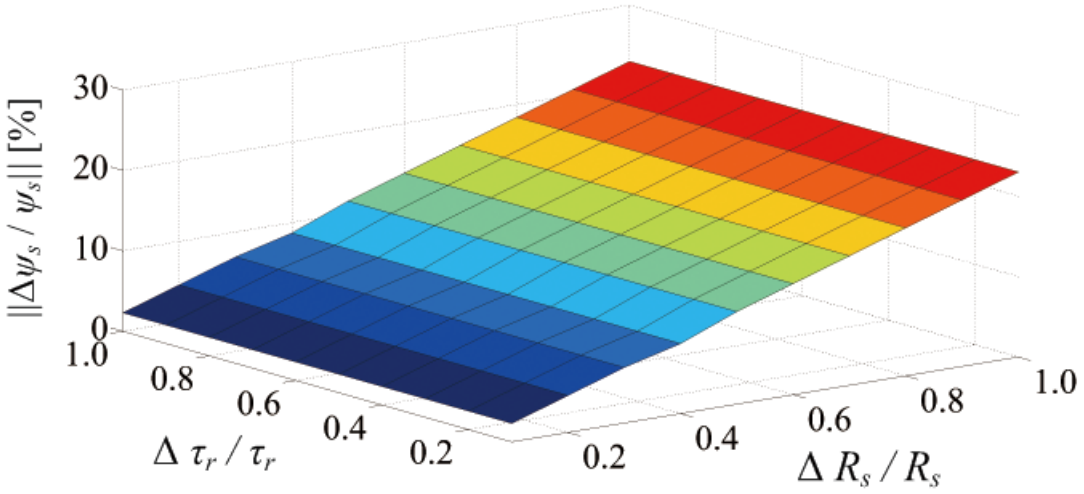

Figure 8.5: Predicted stator flux-linkage deviation of PPTC with R_s and τ_r mismatches. (2772 rpm with 7.5 Nm).

$$\begin{aligned}\frac{d\hat{\boldsymbol{\psi}}_{\boldsymbol{rI}}}{dt} &= \frac{L_r R_r}{L_m}\cdot \boldsymbol{i}_s - (\frac{R_r}{L_r} - j\hat{\omega}\cdot \boldsymbol{i}_s)\hat{\boldsymbol{\psi}}_{\boldsymbol{rI}} \\ &+ k_{p\omega}\hat{e}_{\psi r} + k_{i\omega}\int \hat{e}_{\psi r}dt\end{aligned} \tag{8.21}$$

The difference term $\hat{e}_{\psi r}$ is constructed according to the cross product of rotor flux-linkages estimated in the reference and adjustable models, which is forced to zero by the adaptive mech-

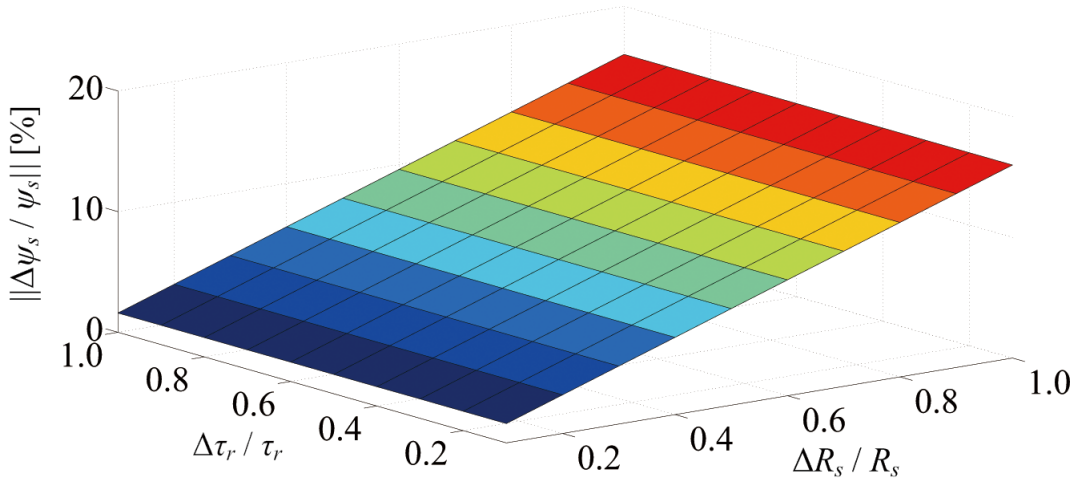

Figure 8.6: Predicted stator flux-linkage deviation of PPTC with R_s and τ_r mismatches. (150 rpm with 2 Nm).

anism with PI controller.

$$\hat{e}_{\psi r} = \hat{\boldsymbol{\psi}}_{\boldsymbol{r\alpha I}}\hat{\boldsymbol{\psi}}_{\boldsymbol{r\beta}} - \hat{\boldsymbol{\psi}}_{\boldsymbol{r\beta I}}\hat{\boldsymbol{\psi}}_{\boldsymbol{r\alpha}} \tag{8.22}$$

However, the variations of stator resistance and mutual inductance lead to the inaccuracy estimation of rotor speed and flux-linkage in the MRAS estimator, which subsequently leads to inevitable deviations in the prediction stage and unsatisfactory performance of PPTC. To enhance the robustness of the MRAS-based PPTC scheme, an online parameter identification algorithm in which stator resistance and rotor time constant are updated in a sequential structure, is presented. The dot product of stator current and rotor flux-linkage deviation is eliminated, to compensate the stator resistance according to the PI mechanism.

$$\begin{aligned} \hat{e}_{Rs} &= \boldsymbol{i}_{s\alpha} \cdot (\hat{\boldsymbol{\psi}}_{\boldsymbol{r\alpha I}} - \hat{\boldsymbol{\psi}}_{\boldsymbol{r\alpha}}) + \boldsymbol{i}_{s\beta} \cdot (\hat{\boldsymbol{\psi}}_{\boldsymbol{r\beta I}} - \hat{\boldsymbol{\psi}}_{\boldsymbol{r\beta}}) \\ \hat{R}_s &= k_{pRs}\hat{e}_{Rs} + k_{iRs}\int \hat{e}_{Rs}dt \end{aligned} \tag{8.23}$$

The dot product of stator current and rotor flux-linkage (defined as $\hat{\tau}_{r\_ref}$) is calculated in the reference model. The obtained dot product is compared with the estimated value ($\hat{\tau}_{rI}$) in the adjustable model, as shown in (8.24). The error between ($\hat{\tau}_{r\_ref}$) and ($\hat{\tau}_{rI}$) is constructed as a tuning parameter that goes though an integral process to update the reciprocal of $\hat{\tau}_r$.

$$\begin{aligned} \hat{e}_{\tau r} &= \hat{\tau}_{r\_ref} - \hat{\tau}_{rI} \\ &= \hat{\boldsymbol{\psi}}_{\boldsymbol{r\alpha}}\boldsymbol{i}_{s\alpha} + \hat{\boldsymbol{\psi}}_{\boldsymbol{r\beta}}\boldsymbol{i}_{s\beta} - L_m\boldsymbol{i}_{\boldsymbol{sd}}^2 \end{aligned} \tag{8.24}$$

where $i_{sd} = \cos(\theta)\boldsymbol{i}_{s\alpha} + sin(\theta)\boldsymbol{i}_{s\beta}, \theta = arctan(\frac{\hat{\boldsymbol{\psi}}_{\boldsymbol{r\alpha}}}{\hat{\boldsymbol{\psi}}_{\boldsymbol{r\beta}}})$.

$$\frac{1}{\hat{\tau}_r} = \frac{1}{\tau_r} + k_{i\tau r}\int \hat{e}_{\tau r}dt \tag{8.25}$$

The block diagram of robust MRAS estimator is shown in Fig. 8.7, which is one of the components in the robust MRAS-based PPTC controller in Fig. 8.8.

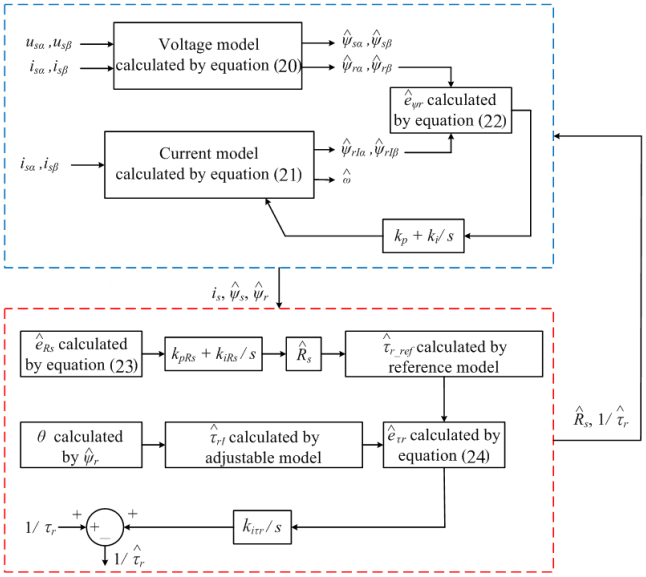

Figure 8.7: Block diagram of the robust MRAS estimator.

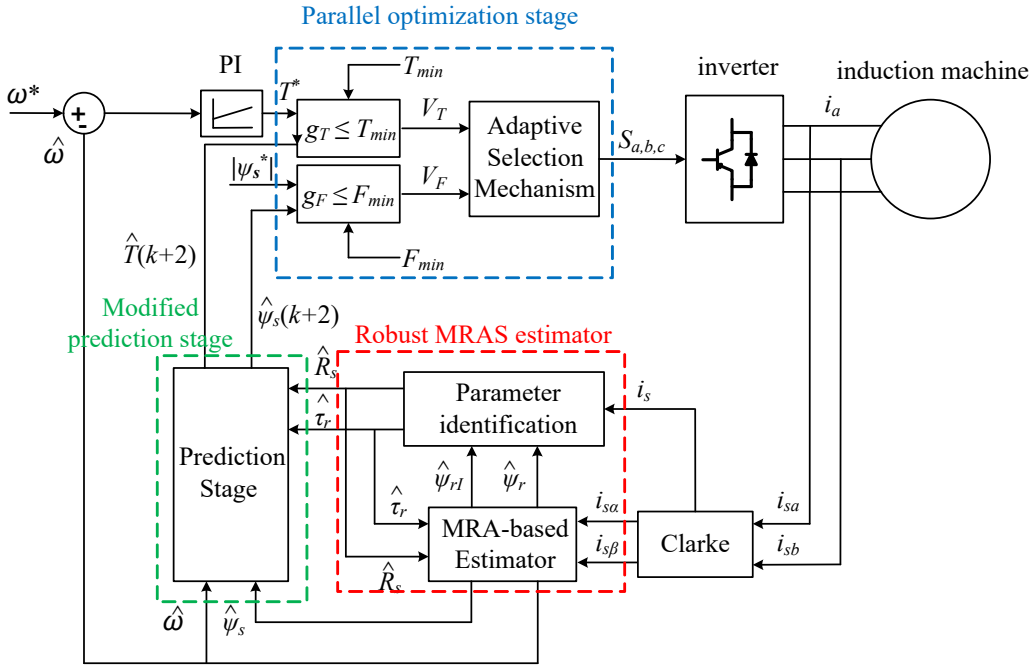

Figure 8.8: Block diagram of PPTC with robust MRAS estimator.

8.4 MRAS for FCS-PTC

8.4.1 Steady-state performance

To validate the performance of the proposed R-MRAS based PPTC scheme, steady-state experimental implementations are firstly conducted in two scenarios of low and rated rotor speed.

The waveforms of estimated stator flux-linkage in α and β axis ($\psi_{s\alpha,\beta}$), estimated and error rotor speed ($\hat{\omega}$ and $\Delta\omega$), electromagnetic torque (T) and stator current (i_s) are shown in Fig. 8.9 and Fig. 8.10. The tests are carried out at 300 rpm with 1 Nm and 2772 rpm with 7.5 Nm, respectively. In Fig. 8.10, it can be seen that the estimated rotor speed accurately tracks the measured value with less than 18 rpm deviation (defined by $\Delta\omega = \hat{\omega} - \omega$), which is similar to the speed tracking performance in Fig. 8.9. As illustrated in Fig. 8.9, the mean squared error of electromagnetic torque (T_{mse}) and stator current THD (i_{sTHD}) are 0.35 Nm and 8.6%, respectively. More specifically, it is presented in Fig. 10 that relatively higher T_{mse} (0.44 Nm) and lower i_{sTHD} (5.7%) are obtained when the IMs operate at rated speed and load torque. The performance metrics of the proposed method at the steady state are listed in TABLE 8.1. It is worth noted that although the speed deviation (18 rpm) is slightly higher at nominal rotor speed and load torque, the percent value (0.65 %) is significantly lower than that at 300 rpm, 1 Nm (4 %).

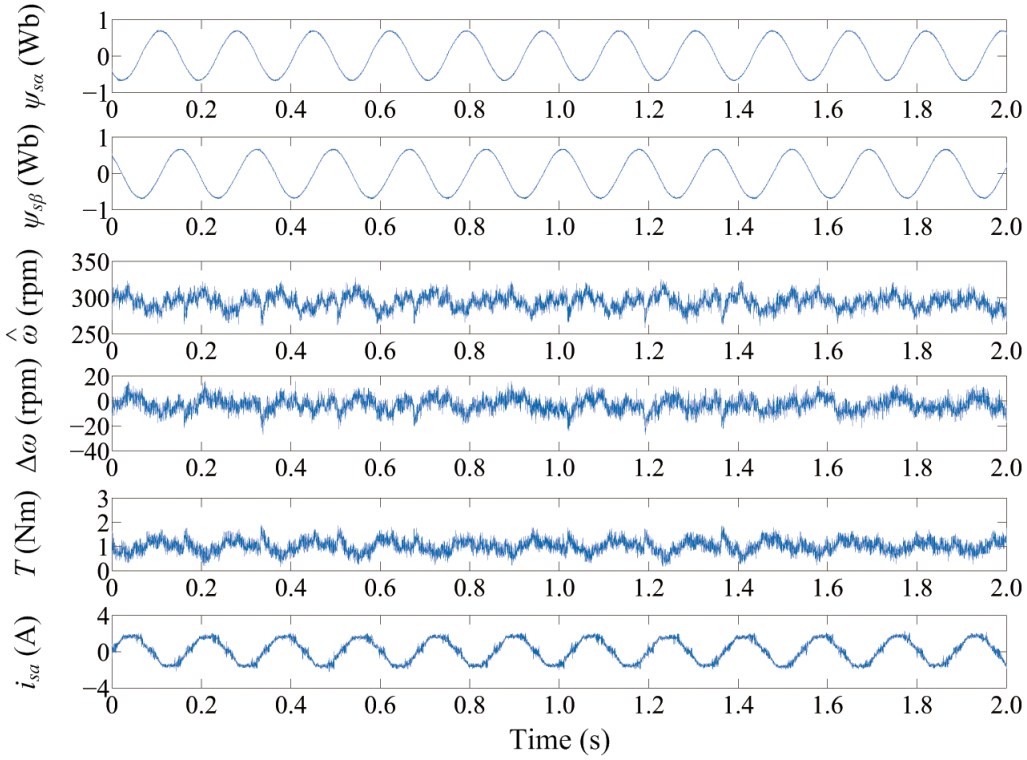

Figure 8.9: Measured waveforms in steady state for ω = 300 rpm, T = 1 Nm.

8.4.2 Steady-state performance

The second test is to validate the performance of speed reversal maneuver of the proposed method at a low speed range. The given rotor speed of the induction machine is reversed from 60 rpm to -60 rpm (2% of the rated speed). As shown in Fig. 8.11, the estimated rotor speed drops at t = 1.06 s and then reaches the reverse value at t = 1.2 s. During the whole reversal maneuver, the maximum speed deviation is 15 rpm. Specifically, the magnitude of estimated

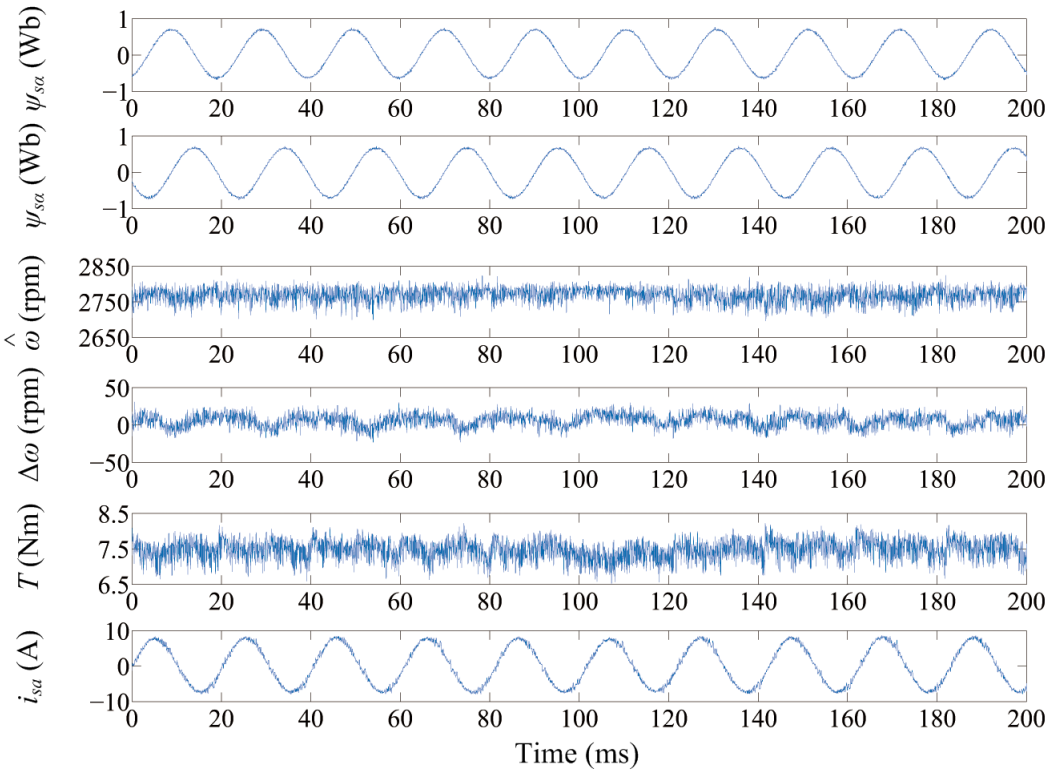

Figure 8.10: Measured waveforms in steady state for ω = 2772 rpm, T = 7.5 Nm.

Table 8.1: The performance metrics of R-MRAS based PPTC at steady-state

Feature	300 rpm, 1 Nm	2772 rpm, 7.5 Nm
$\Delta\omega$ [rpm]	12 (4%)	18 (0.65%)
T_{mse} [Nm]	0.35	0.44
i_{sTHD} [%]	8.6	5.7
$\|\|\Delta\psi_s\|\|$ [Wb]	0.05	0.04
f_{sw} [kHz]	0.80	3.74

stator flux-linkage remains stable ($\frac{||\Delta\psi_s||}{||\psi_s||} \leq 4\%$). It can be seen that T_{mse} is considerably low (0.21 Nm), and i_{sTHD} is 10.8 % without load torque.

8.4.3 Dynamic performance

In this section, the dynamic performance of the proposed method, namely the load step performance, load disturbance performance and speed step performance are evaluated. The first test is to operate the induction machine at 500 rpm with two 2 Nm load step changes. The load torque changes from 2 Nm to 4 Nm at t = 0.45 s and to 6 Nm at t = 1.4 s, respectively. In Fig. 8.12, it is indicated that the estimated rotor speed rises to 535 rpm and returns to original value in 0.4 s

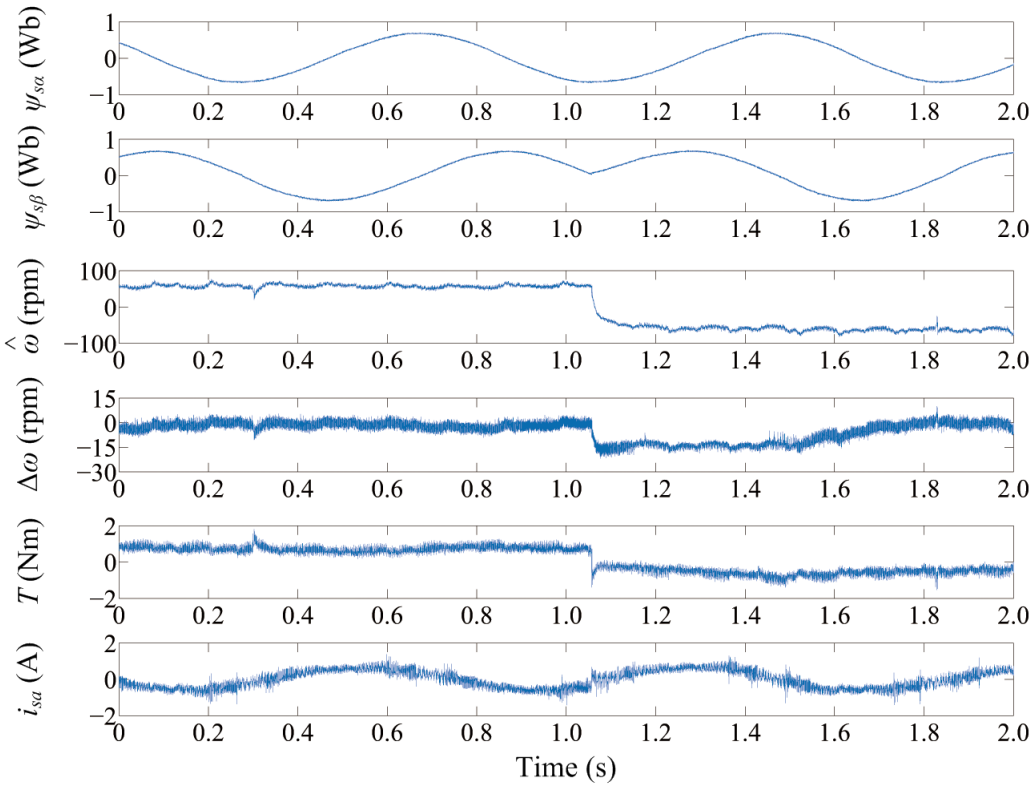

Figure 8.11: Measured waveforms of speed reversal maneuver from 60 rpm to -60 rpm.

when the torque step occurs. The maximum deviation between the estimated and measured rotor speed is 30 rpm. It is shown that low i_{sTHD} is achieved (5.4 %) and the maximum deviation of flux-linkage magnitude is 0.04 Wb.

Subsequently, the load disturbance behavior from 2 to 4 Nm is validated on the experimental platform, and the waveforms are presented in Fig. 8.13. The applied rotor speed is 600 rpm, while the load torque is given by the control panel. As shown in Fig. 8.13, the average deviation of rotor speed at steady-state is approximately 1.5%. The estimated rotor speed drops to 550 rpm when the load disturbance takes place, and the maximum $\Delta\omega$ is 45 rpm at the same time. In the term of electromagnetic torque and stator current, a 3 Nm load torque is employed at t = 0.4 s and a 4 Nm load torque is applied at t = 1.36 s with about 25% overshoot. Thanks to the merits of fine-tuned weighting factor at dynamic transient, the proposed method achieves low torque mean squared error (T_{mse} = 0.32 Nm) and small stator current harmonic distortion (i_{sTHD} = 5.6%).

At last, the experimental results of speed step performance are illustrated in Fig. 8.14. The induction machines are initially operated at 500 rpm with 3 Nm load torque, and then the reference value of rotor speed is set as 1000 rpm. The estimated rotor speed rises to 1080 rpm and then drops back to 1000 rpm in the duration of 0.1 s, and the maximum rotor speed error is 60 rpm. Meanwhile, the torque mean squared error and stator current THD of the proposed method are 0.38 Nm and 6.7%. The dynamic performance metrics of the proposed method are summarized in TABLE 8.2.

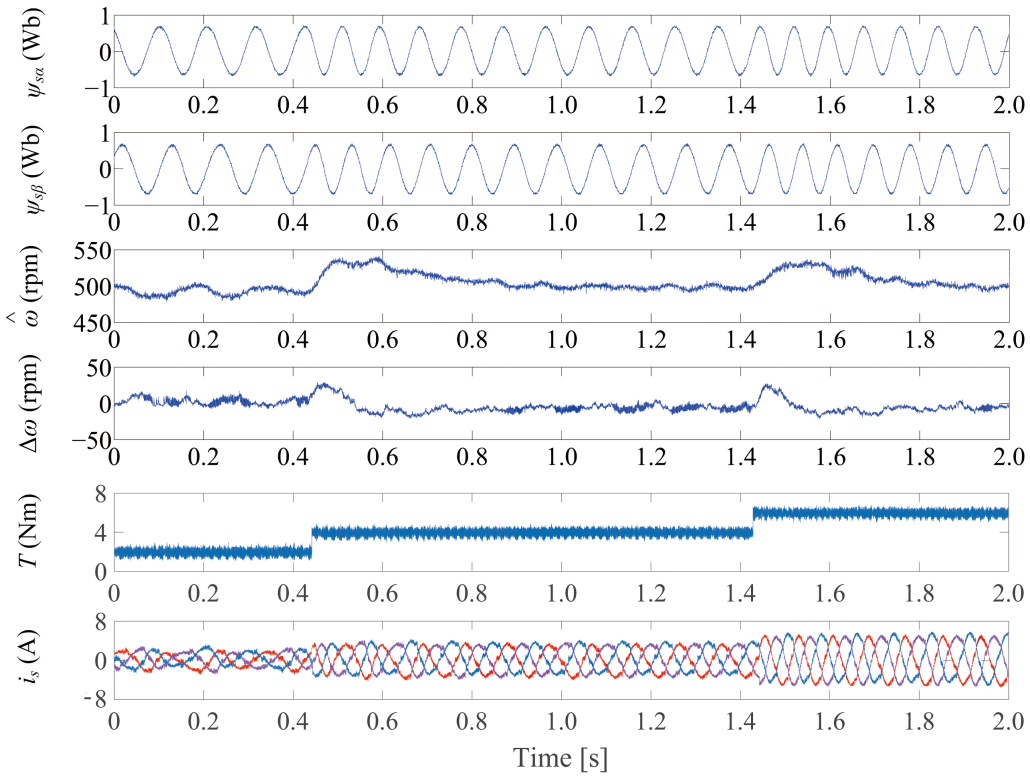

Figure 8.12: Load step performance of the proposed R-MRAS based PPTC from 2 Nm to 6 Nm at 500 rpm.

8.4.4 Robustness evaluation

To validate the robustness performance against parameter variations, the proposed method is compared with PPTC in [42] and MRAS-PTC in [95], respectively. The three algorithms are executed fairly that R_s and τ_r are changed in the same way. The robustness experiments of three algorithms against R_s deviation are performed at 150 rpm, in which the stator resistance reaches 200% initial value in 2 s. The control performance of PPTC is significantly degraded because it becomes instability when R_s reaches the peak value. Thanks to the R_s compensation by parameter identification algorithm, both R-MRAS based PPTC and MRAS-PTC show strong robustness to R_s variation. Compared with MRAS-PTC, the proposed algorithm obtains better tracking performance like lower estimated rotor speed (8 rpm) and torque deviation (0.19 Nm) in average, as well as lower stator current THD (9.7%).

The comparative results of τ_r mismatch among the three algorithms are illustrated as follows. In the implementation, the rotor time constant changes from 0.133 to 0.4 (200% deviation) at t = 1.0 s. It can be seen that PPTC shows smaller torque and stator current error than that of the counterpart MRAS-PTC. However, the τ_r variation generates a negative influence on the predicted value. The estimated rotor speed suffers from a 5.9 % deviation in MRAS-PTC without τ_r identification. Compared with MRAS-PTC, the proposed R-MRAS PPTC obtains accuracy rotor speed estimation (3.2%), as well as significantly reduction in torque deviation (0.2 Nm) and current THD (9.4%). It is indicated that the proposed algorithm achieves satisfactory steady-

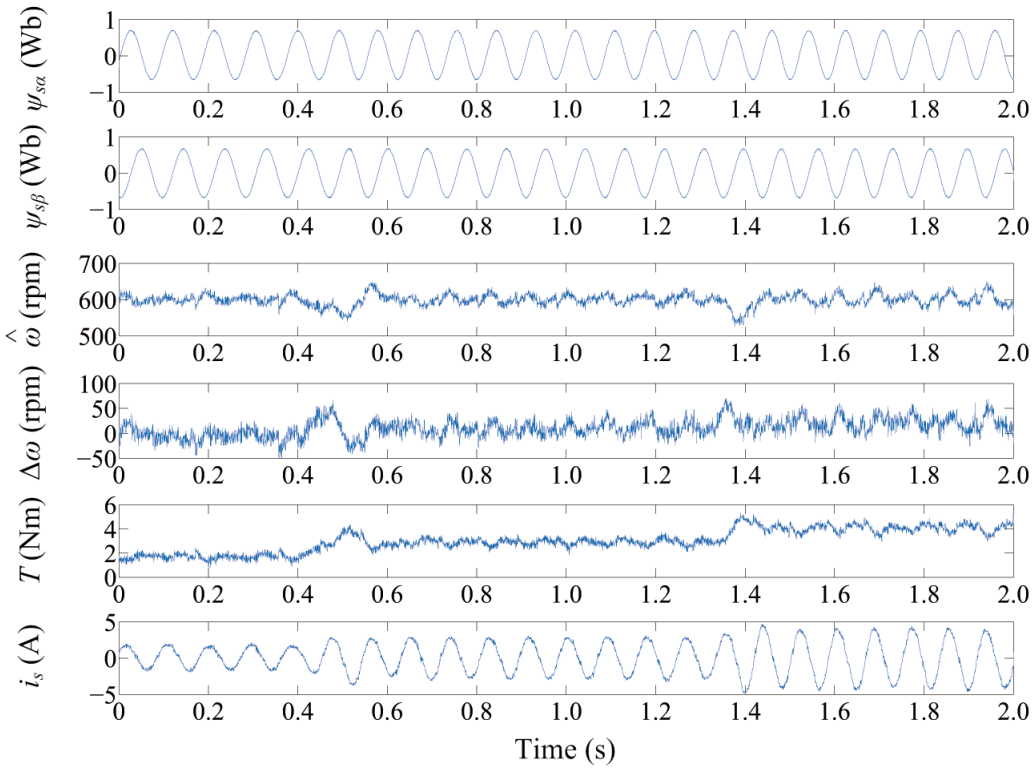

Figure 8.13: Load disturbance performance of the proposed R-MRAS based PPTC from 2 Nm to 4 Nm at 600 rpm.

state performance at a low speed.

Table 8.2: The performance metrics of R-MRAS based PPTC at dynamic-transient

Feature	load step	load disturbance	speed step
$\Delta\omega$ $[rpm]$	30	45	60
T_{mse} [Nm]	0.38	0.32	0.38
i_{sTHD} [%]	5.4	5.6	6.7
$\|\|\Delta\psi_s\|\|$ [Wb]	0.04	0.06	0.06
f_{sw} [kHz]	1.43	1.68	2.55 (at 1000 rpm)

8.5 Conclusion

In this chapter, the encoderless techonology for FCS-MPC schemes is introduced, which not merely estimates the rotor speed for the proposed model predictive controller but also improve the robustness against parameter mismatches. The influence of parameter mismatches on the

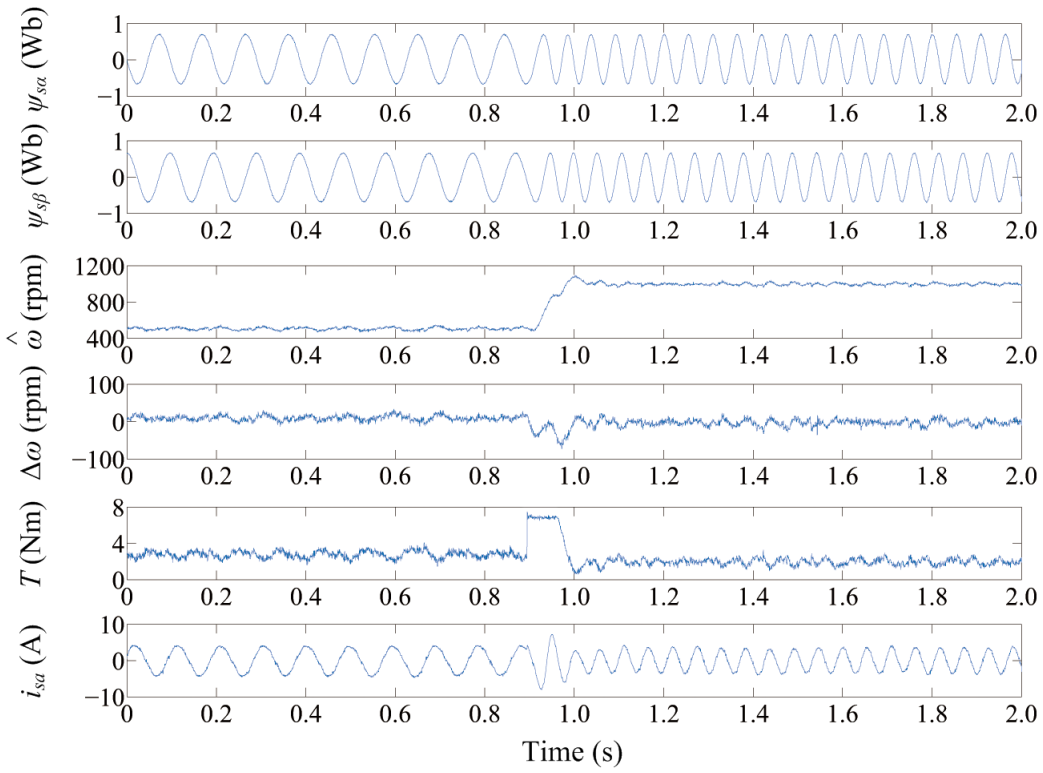

Figure 8.14: Speed step performance of the proposed R-MRAS based PPTC from 500 rpm to 1000 rpm with 3 Nm load.

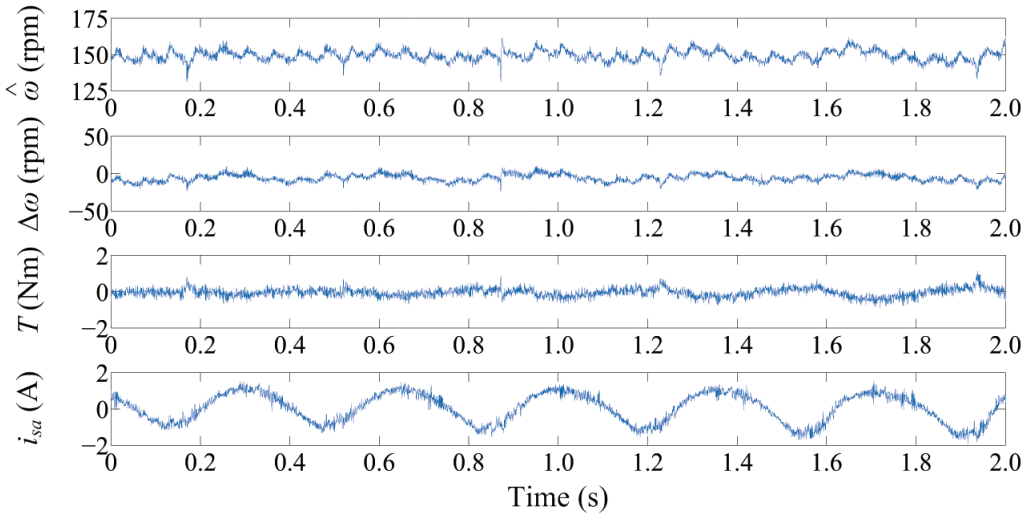

Figure 8.15: Robustness performance of the proposed R-MRAS based PPTC against 100 % R_s deviation.

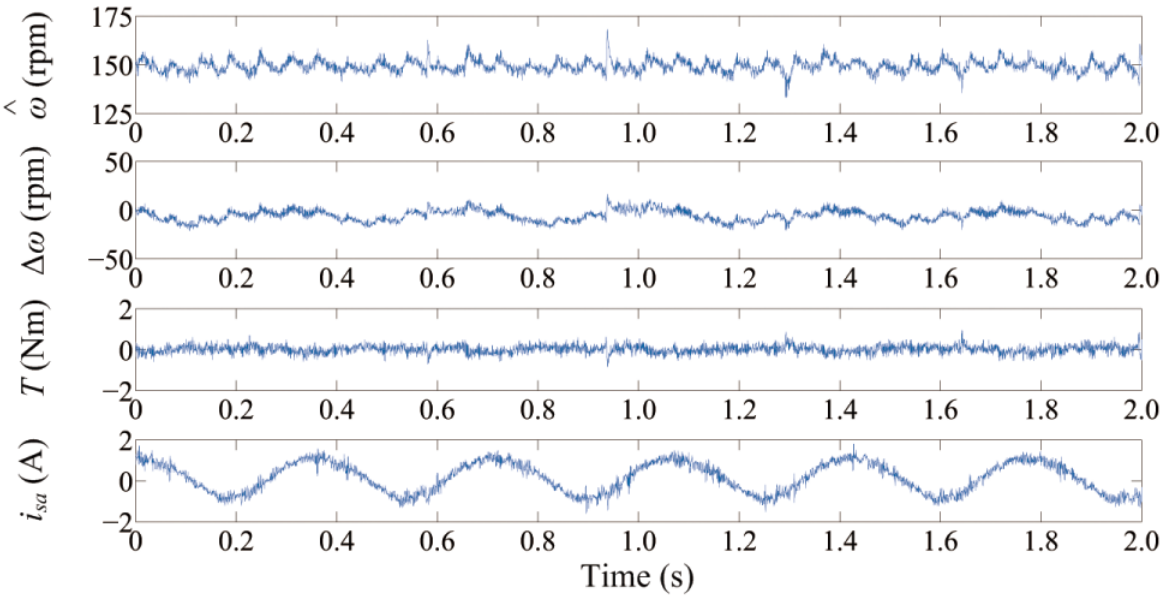

Figure 8.16: Robustness performance of the proposed robust MRAS-based PPTC against 200 % τ_r deviation.

FCS-MPC schemes are investigated. Moreover, the designed MRAS estimators are applied on the proposed FCS-MPC schemes, in which the stator resistance and rotor time constant are updated. It is validated by experimental implementation that the proposed algorithm achieves low speed and flux-linkage estimation deviations, as well as low torque mean squared error and current THD at both steady-state and dynamic transient.

CHAPTER 9

Conclusion

In this dissertation, MPC strategies with objective function reformulation are investigated, to achieve the increasing requirements arising from the rapid development of the power electronic and electrical drive systems. The state-of-the-art FCS-MPC schemes show the superiority of straightforward concept, simple implementation, flexible inclusion of constraints, fast dynamic response, low switching frequency and the ability to handle with multiple conflicting targets. With the tremendous development of the commercial digital processors, FCS-MPC has emerged as an alternative control strategy with satisfactory control performance in the field of power electronic and electrical drive systems.

In chapter 2 and 3, the basic principles of the control plant and FCS-MPC methods are introduced. Based on the above, FCS-MPC schemes with multiple control objectives for IM drives are formulated and experimentally evaluated in chapter 4. As can be seen, the predominate objective of FCS-PTC is electromagnetic torque and that of FCS-PCC is stator current. Compared with FCS-PCC, FCS-PTC achieves a smaller torque ripple but suffers from a worse current quality. Moreover, FCS-PTC shows a strong robustness against the variation of magnetizing inductance. On the contrary, FCS-PCC is less sensitive to the stator resistance mismatch.

In chapter 5, several weighting parameter optimization solutions are proposed for the multi-objective FCS-MPC schemes, to tackle the issue of weighting parameter design. It is promising to design the weighting parameters using an artificial neural network (ANN) approach, to offline obtain the optimal combination of the required parameters. Another solution is the splitting of the objective function combined with different optimization structures. By doing so, the weighting parameters are not required because the dimension of the reformulated tracking error terms is 1. A sequential, parallel and ensemble structure is designed to resolve the global optimum for the FCS-MPC optimization problem, respectively.

In chapter 6, the FCS-MPC optimization problem is resolved using a derivative projection, to improve the control performance at the steady state. To do so, the objective function is reformulated as the quadratic Euclidean-norm of the tracking deviation from a geometric perspective. An extension of finite control set is by the reformulated objective function, to overcome the

high ripples caused by the single control input in the entire sampling period. Moreover, a preselection principle is proposed to obtain a significant reduction on the computational burden of the proposed FCS-MPC scheme.

In chapter 7, a newly-developed gradient descent solution is proposed for the FCS-MPC schemes. The convexity of the quadratic programming (QP) problem is proved. Therefore, a deepest decrease occurs in the value of the reformulated objective function, as the control variable moves along with the direction of gradient descent. The convergence of the proposed gradient descent solution is confirmed. More specifically, special concerns, i.e., extension of finite set, selection of step size and the number of prediction horizon, have also been discussed.

In chapter 8, the encoderless technologies for the reformulated FCS-MPC schemes are investigated. A model reference adaptive system (MRAS) estimator is applied for FCS-MPC, which can not only estimates the rotor speed but also improves the robustness against parameter mismatches. The parameter sensitivity of the proposed is investigated. The proposed MRAS estimators for FCS-PTC and parallel structure FCS-MPC are experimentally verified.

APPENDIX A

List of publications

A.1 Journal papers

- **H. Xie**, L. Liu, Y. He, F. Wang, J. Rodríguez and R. Kennel, “Gradient Descent based Objective Function Reformulation for Finite Control Set Model Predictive Current Control with Extended Horizon", *Industrial Electronics, IEEE Transactions on*, 2021. (published)
- **H. Xie**, F. Wang, Q. Xun, Y. He, J. Rodríguez and R. Kennel, “A Low-Complexity Gradient Descent Solution with Backtracking Iteration Approach for Finite Control Set Predictive Current Control", *Industrial Electronics, IEEE Transactions on*, vol.69, no.5, pp.4522,4533, May.2022. doi: 10.1109/TIE.2021.3084164
- **H. Xie**, F. Wang, Y. He, J. Rodríguez and R. Kennel, “Encoderless Parallel Predictive Torque Control for Induction Machine Using A Robust Model Reference Adaptive System", *Energy Conversion, IEEE Transactions on*, vol.37, no.1, pp.232,242, March.2022. doi: 10.1109/TEC.2021.3102305
- **H. Xie**, F. Wang, Q. Xun, Y. He, J. Rodríguez and R. Kennel, “Iterative Gradient Descent Based Finite Control Set Predictive Current Control with Least Squares Optimized Duty Cycles", *IEEE Journal of Emerging and Selected Topics in Power Electronics*, 2021. (published)
- **Xie, H**.; Du, J.; Ke, D.; He, Y.; Wang, F.; Hackl, C.; Rodríguez, J.; Kennel, R. “Multistep Model Predictive Control for Electrical Drives A Fast Quadratic Programming Solution", *Symmetry*, 2022, 14, 626. https://doi.org/10.3390/sym14030626
- M. Novak, **H. Xie**, T. Dragicevic, F. Wang, J. Rodríguez and F. Blaabjerg, “Optimal Cost Function Parameter Design in Predictive Torque Control (PTC) Using Artificial Neural Networks (ANN)", *Industrial Electronics, IEEE Transactions on*, vol.68, no.8, pp.7309,7319, Aug.2021.

- F. Wang, **H. Xie**, Q. Chen, S.A. Davari, J. Rodríguez and R. Kennel, “Parallel Predictive Torque Control for Induction Machines Without Weighting Factors", *Power Electronics, IEEE Transactions on*, vol.35, no.2, pp.1779,1788, Feb.2021.
- Y. Tang, Y. He, F. Wang, **H. Xie**, J. Rodríguez and R. Kennel, “A Drive Topology for High-Speed SRM With Bidirectional Energy Flow and Fast Demagnetization Voltage", *Industrial Electronics, IEEE Transactions on*, vol.68, no.10, pp.9242,9253, Oct.2021.
- **H. Xie**, F. Wang, D. Ke, Y. Tang and R. Kennel, “Ensemble Optimization based Weighting Factor-less Predictive Torque Control for Induction Machines", *Transactions of China Electrotechnical Society*, 2021. (accepted)

A.2 Conference papers

- **H. Xie**, Q. Chen, Y. Tang, R. Kennel, F. Wang, A. Xia, Z. Zhang and J. Rodríguez, “Sliding-Mode MRAS based Encoderless Predictive Torque Control for Induction Machine", *2019 IEEE International Symposium on Predictive Control of Electrical Drives and Power Electronics (PRECEDE)*, 2019. doi: 10.1109/PRECEDE.2019.8753190 (Best paper award)
- **H. Xie**, F. Wang, Y. He, Y. Tang, J. Rodríguez and R. Kennel, “Sliding-Mode Disturbance Observer based Parallel Predictive Torque Controller for Induction Machine Drives", *2021 IEEE 12th Energy Conversion Congress & Exposition - Asia (ECCE-Asia)*, 2021. doi: 10.1109/ECCE-Asia49820.2021.9478975
- **H. Xie**, F. Wang, Y. He, Y. Tang, J. Rodríguez and R. Kennel, “Extended Kalman Filter based Encoderless Predictive Current Control for Induction Machine Drives", *2021 IEEE 12th Energy Conversion Congress & Exposition - Asia (ECCE-Asia)*, 2021. doi: 10.1109/ECCE-Asia49820.2021.9479124
- **H. Xie**, F. Wang, W. Zhang, C. Garcia, J. Rodríguez and R. Kennel, “Sliding Mode Flux Observer Based Predictive Field Oriented Control for Induction Machine Drives", *2020 IEEE 9th International Power Electronics and Motion Control Conference (IPEMC2020-ECCE Asia)*, 2020. doi: 10.1109/IPEMC-ECCEAsia48364.2020.9368086
- **H. Xie**, F. Wang, W. Zhang, C. Garcia, J. Rodríguez and R. Kennel, “Predictive Field Oriented Control based on MRAS Current Estimator for IM Drives", *2020 IEEE 9th International Power Electronics and Motion Control Conference (IPEMC2020-ECCE Asia)*, 2020. doi: 10.1109/IPEMC-ECCEAsia48364.2020.9367976
- **H. Xie**, Q. Xun, Y. Tang, F. Wang, J. Rodríguez and R. Kennel, “Robust Parallel Predictive Torque Control with Model Reference Adaptive Estimator for IM Drives", *2020 International Conference on Electrical Machines (ICEM)*, 2020. doi: 10.1109/ICEM49940.2020.9271013
- Q. Chen, **H. Xie**, R. Kennel, “Variable Switching Point Parallel Predictive Torque Control(VSP3TC) for Induction Motor", *2020 IEEE International Conference on Industrial Technology (ICIT)*, 2020. doi: 10.1109/ICIT45562.2020.9067317

- Y. He, Y. Tang, **H. Xie**, D. Ke, F. Wang, R. Kennel, “Power Quality Improvement for Grid-connected High-Speed Switched Reluctance Drive System", *2021 IEEE 12th Energy Conversion Congress & Exposition - Asia (ECCE-Asia)*, 2021. doi: 10.1109/ECCE-Asia49820.2021.9479157

- Y. He, Y. Tang, **H. Xie**, D. Ke and F. Wang, “Rotor Optimization for Two-phase High-speed Switched Reluctance Motor", *2021 IEEE 12th Energy Conversion Congress & Exposition - Asia (ECCE-Asia)*, 2021. doi: 10.1109/ECCE-Asia49820.2021.9479399

- Y. He, Y. Tang, **H. Xie**, F. Wang and R. Kennel, “Weighting-factor-less Model Predictive Direct Power Control for Three-Level NPC Rectifier", *2020 23rd International Conference on Electrical Machines and Systems (ICEMS)*, 2020. doi: 10.23919/ICEMS50442.2020.9291113

- Y. He, Y. Tang, **H. Xie**, F. Wang, J. Rodríguez and R. Kennel, “Performance Evaluation for an Optimized 4/2 High-speed SRM Fed by Active Front-end Rectifier", *2020 International Conference on Electrical Machines (ICEM)*, 2020. doi: 10.1109/ICEM49940.2020.9270814

- **H. Xie**, F. Wang, Y. He, L. Liu, J. Rodríguez and R. Kennel, “Cascaded Predictive Current Control with a Piecewise Approach for Induction Machine Drives", *2021 IEEE International Symposium on Predictive Control of Electrical Drives and Power Electronics(PRECEDE)*, Jinan, China, 2021, pp.81,85. doi: 10.1109/PRECEDE51386.2021.9680982

- L. Liu, **H. Xie**, D. Kong, Y. Yin, Y. Zhao, Z. Zhang and R. Kennel, “A Disturbance Observer-Based Integral Sliding Mode Control for Two-Level Power Converter", *2021 IEEE International Symposium on Predictive Control of Electrical Drives and Power Electronics(PRECEDE)*, Jinan, China, 2021, pp.232,242. doi: 10.1109/PRECEDE51386.2021.9680925

- K. Zuo, J. Du, H. Wang, Y. Gui, **H. Xie**, F. Wang and R. Kennel, “Model Variation Observer based Model Predictive Control for PMSM Drives", *2021 IEEE International Symposium on Predictive Control of Electrical Drives and Power Electronics(PRECEDE)*, Jinan, China, 2021, pp.594,599. doi: 10.1109/PRECEDE51386.2021.9681007 (Best paper award)

APPENDIX B

Nomenclature

General electrical variables:

$\boldsymbol{i}_s$	stator current
$\boldsymbol{i}_r$	rotor current
$\boldsymbol{\psi}_s$	stator flux
$\boldsymbol{\psi}_r$	rotor flux
R_s	stator resistance
R_r	rotor resistance
L_s	stator inductance
L_r	rotor inductance
L_m	magnetizing inductance
$\boldsymbol{u}_s$	stator voltage vector
ω	rotor angular speed
k_r	rotor coupling factor
R_σ	effective resistance of both windings
L_σ	transient stator inductance
τ_σ	transient time constant
p	number of pole pairs
J	moment of inertia
θ	rotation angle
T_L	load torque

Abbreviations:

AC	Alternating current
ANN	Artificial neural network
CCS-MPC	Continuous control set model predictive control
DB	Deadbeat
DC	Direct current
DTC	Direct torque control
DSP	Digital signal processor
FCS-MPC	Finite control set model predictive control
FCS-PCC	Finite control set predictive current control
FCS-PTC	Finite control set predictive torque control
FOC	Field oriented control
FPGA	Field programmable gate arrays
GD	Gradient descent
GSDMPC	Generalized sequential direct model predictive control
IM	Induction machine
LIM	Linear induction machine
LS	Least squares
MPC	Model predictive control
MRAS	Model reference adaptive system
OT	Optimal torque
PA	Pruning algorithm
PI	Proportional-integral
PMSM	Permanent magnet synchronous machine
PPTC	Parallel predictive torque control
PWM	Pulse width modulation
QP	Quadratic programming
SA	Sorting algorithm
SDA	Sphere docoding algorithm
SOC	System-on-chip
THD	Total harmonic distortion
VSI	Voltage source inverter
VV	Voltage vectors

List of Figures

List of Tables

Bibliography

[1] M. P. Kazmierkowski, L. G. Franquelo, J. Rodriguez, M. A. Perez, and J. I. Leon, "High-performance motor drives," *IEEE Industrial Electronics Magazine*, vol. 5, no. 3, pp. 6–26, 2011.

[2] N. P. Quang and J.-A. Dittrich, *Vector Control of Three-Phase AC Machines*. Springer Press, 2015.

[3] W. Leonhard, *Control of Electrical Drives*, 2nd ed. Berlin, Heidelberg: Springer-Verlag, 1996.

[4] F. Blaschke, "The principle of field orientation as applied to the new transvector closed-loop system for rotating-field machines," *Siemens Review*, vol. 34, no. 3, pp. 217–220, 1972.

[5] J. R. Domínguez, I. Dueñas, and S. Ortega-Cisneros, "Discrete-time modeling and control based on field orientation for induction motors," *IEEE Transactions on Power Electronics*, vol. 35, no. 8, pp. 8779–8793, 2020.

[6] I. Takahashi and T. Noguchi, "A new quick-response and high-efficiency control strategy of an induction motor," *IEEE Transactions on Industry Applications*, vol. IA-22, no. 5, pp. 820–827, 1986.

[7] R. E. Kodumur Meesala and V. K. Thippiripati, "An improved direct torque control of three-level dual inverter fed open-ended winding induction motor drive based on modified look-up table," *IEEE Transactions on Power Electronics*, vol. 35, no. 4, pp. 3906–3917, 2020.

[8] C. Rao, J. Rawlings, and D. Mayne, "Constrained state estimation for nonlinear discrete-time systems: stability and moving horizon approximations," *IEEE Transactions on Automatic Control*, vol. 48, no. 2, pp. 246–258, 2003.

[9] A. Linder, R. Kanchen, R. Kennel, and P. Stolze, *Model-based Predictive Control of Electric Drives*. Cuvillier Verlag, 2010.

[10] J. Rodriguez, C. Garcia, A. Mora, F. Flores-Bahamonde, P. Acuna, M. Novak, Y. Zhang, L. Tarisciotti, A. Davari, Z. Zhang, F. Wang, M. Norambuena, T. Dragicevic, F. Blaabjerg, T. Geyer, R. Kennel, D. Arab Khaburi, M. Abdelrahem, Z. Zhang, N. Mijatovic, and R. P. Aguilera, "Latest advances of model predictive control in electrical drives. part i: Basic concepts and advanced strategies," *IEEE Transactions on Power Electronics*, pp. 1–1, 2021.

[11] J. Rodriguez, C. Garcia, A. Mora, A. Davari, J. Rodas, D. F. Valencia Garcia, M. F. Elmorshedy, F. Wang, K. Zuo, L. Tarisciotti, F. Flores-Bahamonde, W. Xu, Z. Zhang, Y. Zhang, M. Norambuena, A. Emadi, T. Geyer, R. Kennel, T. Dragicevic, D. Arab Khaburi, Z. Zhang, M. Abdelrahem, and N. Mijatovic, "Latest advances of model predictive control in electrical drives. part ii: Applications and benchmarking with classical control methods," *IEEE Transactions on Power Electronics*, pp. 1–1, 2021.

[12] Y. Xi, D. Li, and S. Lin., "Model predictive control - status and challenges," *Acta Automatica Sinica*, vol. 39, no. 3, pp. 222–236, 2013.

[13] P. Karamanakos and T. Geyer, "Guidelines for the design of finite control set model predictive controllers," *IEEE Transactions on Power Electronics*, vol. 35, no. 7, pp. 7434–7450, 2020.

[14] P. Karamanakos, E. Liegmann, T. Geyer, and R. Kennel, "Model predictive control of power electronic systems: Methods, results, and challenges," *IEEE Open Journal of Industry Applications*, vol. 1, pp. 95–114, 2020.

[15] S. Kouro, P. Cortes, R. Vargas, U. Ammann, and J. Rodriguez, "Model predictive control—a simple and powerful method to control power converters," *IEEE Transactions on Industrial Electronics*, vol. 56, no. 6, pp. 1826–1838, 2009.

[16] P. Cortes, M. P. Kazmierkowski, R. M. Kennel, D. E. Quevedo, and J. Rodriguez, "Predictive control in power electronics and drives," *IEEE Transactions on Industrial Electronics*, vol. 55, no. 12, pp. 4312–4324, 2008.

[17] S. Vazquez, J. I. Leon, L. G. Franquelo, J. Rodriguez, H. A. Young, A. Marquez, and P. Zanchetta, "Model predictive control: A review of its applications in power electronics," *IEEE Industrial Electronics Magazine*, vol. 8, no. 1, pp. 16–31, 2014.

[18] A. Bemporad, M. Morari, V. Dua, and E. N. Pistikopoulos., "The explicit linear quadratic regulator for constrained systems," *Automatica*, vol. 38, no. 1, pp. 3–20, 2002.

[19] J. Rodriguez, J. Pontt, C. A. Silva, P. Correa, P. Lezana, P. Cortes, and U. Ammann, "Predictive current control of a voltage source inverter," *IEEE Transactions on Industrial Electronics*, vol. 54, no. 1, pp. 495–503, 2007.

[20] J. Rodriguez, M. P. Kazmierkowski, J. R. Espinoza, P. Zanchetta, H. Abu-Rub, H. A. Young, and C. A. Rojas, "State of the art of finite control set model predictive control in power electronics," *IEEE Transactions on Industrial Informatics*, vol. 9, no. 2, pp. 1003–1016, 2013.

[21] J. Rodriguez and P. Cortes, *Predictive Control of Power Converters and Electrical Drives*. Wiley-IEEE Press, 2012.

[22] T. Geyer, *Model Predictive Control of High Power Converters*. Willy Press, 2016.

[23] T. Faulwasser, M. A. Müller, and K. Worthmann, *Recent Advances in Model Predictive Control: Theory, Algorithms, and Applications*. Springer Press, 2016.

[24] A. Andersson and T. Thiringer, "Assessment of an improved finite control set model predictive current controller for automotive propulsion applications," *IEEE Transactions on Industrial Electronics*, vol. 67, no. 1, pp. 91–100, 2020.

[25] T. Geyer, G. Papafotiou, and M. Morari, "Model predictive direct torque control—part i: Concept, algorithm, and analysis," *IEEE Transactions on Industrial Electronics*, vol. 56, no. 6, pp. 1894–1905, 2009.

[26] A. A. Ahmed, B. K. Koh, and Y. I. Lee, "A comparison of finite control set and continuous control set model predictive control schemes for speed control of induction motors," *IEEE Transactions on Industrial Informatics*, vol. 14, no. 4, pp. 1334–1346, 2018.

[27] P. Cortes, J. Rodriguez, C. Silva, and A. Flores, "Delay compensation in model predictive current control of a three-phase inverter," *IEEE Transactions on Industrial Electronics*, vol. 59, no. 2, pp. 1323–1325, 2012.

[28] W. Xu, M. F. Elmorshedy, Y. Liu, J. Rodriguez, and C. Garcia, "Maximum thrust per ampere of linear induction machine based on finite-set model predictive direct thrust control," *IEEE Transactions on Power Electronics*, vol. 35, no. 7, pp. 7366–7378, 2020.

[29] P. Karamanakos and T. Geyer, "Model predictive torque and flux control minimizing current distortions," *IEEE Transactions on Power Electronics*, vol. 34, no. 3, pp. 2007–2012, 2019.

[30] P. Karamanakos, T. Geyer, and R. Kennel, "On the choice of norm in finite control set model predictive control," *IEEE Transactions on Power Electronics*, vol. 33, no. 8, pp. 7105–7117, 2018.

[31] P. Cortes, J. Rodriguez, D. E. Quevedo, and C. Silva, "Predictive current control strategy with imposed load current spectrum," *IEEE Transactions on Power Electronics*, vol. 23, no. 2, pp. 612–618, 2008.

[32] F. Wang, S. Li, X. Mei, W. Xie, J. Rodríguez, and R. M. Kennel, "Model-based predictive direct control strategies for electrical drives: An experimental evaluation of PTC and PCC methods," *IEEE Transactions on Industrial Informatics*, vol. 11, no. 3, pp. 671–681, 2015.

[33] F. Morel, X. Lin-Shi, J.-M. Retif, B. Allard, and C. Buttay, "A comparative study of predictive current control schemes for a permanent-magnet synchronous machine drive," *IEEE Transactions on Industrial Electronics*, vol. 56, no. 7, pp. 2715–2728, 2009.

[34] X. Zhang, L. Zhang, and Y. Zhang, "Model predictive current control for pmsm drives with parameter robustness improvement," *IEEE Transactions on Power Electronics*, vol. 34, no. 2, pp. 1645–1657, 2019.

[35] X. Liu, L. Zhou, J. Wang, X. Gao, Z. Li, and Z. Zhang, "Robust predictive current control of permanent-magnet synchronous motors with newly designed cost function," *IEEE Transactions on Power Electronics*, pp. 1–1, 2020.

[36] M. Xiao, T. Shi, Y. Yan, W. Xu, and C. Xia, "Predictive torque control of permanent magnet synchronous motors using flux vector," *IEEE Transactions on Industry Applications*, vol. 54, no. 5, pp. 4437–4446, 2018.

[37] Y. Zhang and H. Yang, "Two-vector-based model predictive torque control without weighting factors for induction motor drives," *IEEE Transactions on Power Electronics*, vol. 31, no. 2, pp. 1381–1390, 2016.

[38] M. Norambuena, J. Rodriguez, Z. Zhang, F. Wang, C. Garcia, and R. Kennel, "A very simple strategy for high-quality performance of ac machines using model predictive control," *IEEE Transactions on Power Electronics*, vol. 34, no. 1, pp. 794–800, 2019.

[39] Y. Zhang, B. Zhang, H. Yang, M. Norambuena, and J. Rodriguez, "Generalized sequential model predictive control of im drives with field-weakening ability," *IEEE Transactions on Power Electronics*, vol. 34, no. 9, pp. 8944–8955, 2019.

[40] S. A. Davari, M. Norambuena, V. Nekoukar, C. Garcia, and J. Rodriguez, "Even-handed sequential predictive torque and flux control," *IEEE Transactions on Industrial Electronics*, vol. 67, no. 9, pp. 7334–7342, 2020.

[41] C. A. Rojas, J. Rodriguez, F. Villarroel, J. R. Espinoza, C. A. Silva, and M. Trincado, "Predictive torque and flux control without weighting factors," *IEEE Transactions on Industrial Electronics*, vol. 60, no. 2, pp. 681–690, 2013.

[42] F. Wang, H. Xie, Q. Chen, S. A. Davari, J. Rodrguez, and R. Kennel, "Parallel predictive torque control for induction machines without weighting factors," *IEEE Transactions on Power Electronics*, vol. 35, no. 2, pp. 1779–1788, 2020.

[43] C. A. Rojas, J. R. Rodriguez, S. Kouro, and F. Villarroel, "Multiobjective fuzzy-decision-making predictive torque control for an induction motor drive," *IEEE Transactions on Power Electronics*, vol. 32, no. 8, pp. 6245–6260, 2017.

[44] Z. Zhang, Wei Tian, Wanyi Xiong, and R. Kennel, "Predictive torque control of induction machines fed by 3l-npc converters with online weighting factor adjustment using fuzzy logic," in *2017 IEEE Transportation Electrification Conference and Expo (ITEC)*, 2017, pp. 84–89.

[45] S. A. Davari, V. Nekoukar, C. Garcia, and J. Rodriguez, "Online weighting factor optimization by simplified simulated annealing for finite set predictive control," *IEEE Transactions on Industrial Informatics*, vol. 17, no. 1, pp. 31–40, 2021.

[46] P. Cortes, S. Kouro, B. La Rocca, R. Vargas, J. Rodriguez, J. I. Leon, S. Vazquez, and L. G. Franquelo, "Guidelines for weighting factors design in model predictive control of power converters and drives," in *2009 IEEE International Conference on Industrial Technology*, 2009, pp. 1–7.

[47] O. Machado, P. Martín, F. J. Rodríguez, and E. J. Bueno, "A neural network-based dynamic cost function for the implementation of a predictive current controller," *IEEE Transactions on Industrial Informatics*, vol. 13, no. 6, pp. 2946–2955, 2017.

[48] M. Novak, H. Xie, T. Dragicevic, F. Wang, J. Rodriguez, and F. Blaabjerg, "Optimal cost function parameter design in predictive torque control (ptc) using artificial neural networks (ann)," *IEEE Transactions on Industrial Electronics*, pp. 1–1, 2020.

[49] J. Zhang, T. Sun, F. Wang, J. Rodríguez, and R. Kennel, "A computationally efficient quasi-centralized dmpc for back-to-back converter pmsg wind turbine systems without dc-link tracking errors," *IEEE Transactions on Industrial Electronics*, vol. 63, no. 10, pp. 6160–6171, 2016.

[50] Y. Zhang and W. Xie, "Low complexity model predictive control—single vector-based approach," *IEEE Transactions on Power Electronics*, vol. 29, no. 10, pp. 5532–5541, 2014.

[51] X. Wu, W. Song, and C. Xue, "Low-complexity model predictive torque control method without weighting factor for five-phase pmsm based on hysteresis comparators," *IEEE Journal of Emerging and Selected Topics in Power Electronics*, vol. 6, no. 4, pp. 1650–1661, 2018.

[52] X. Wang and D. Sun, "Three-vector-based low-complexity model predictive direct power control strategy for doubly fed induction generators," *IEEE Transactions on Power Electronics*, vol. 32, no. 1, pp. 773–782, 2017.

[53] T. Geyer and D. E. Quevedo, "Multistep finite control set model predictive control for power electronics," *IEEE Transactions on Power Electronics*, vol. 29, no. 12, pp. 6836–6846, 2014.

[54] T. Geyer and D. E. Quevedo, "Performance of multistep finite control set model predictive control for power electronics," *IEEE Transactions on Power Electronics*, vol. 30, no. 3, pp. 1633–1644, 2015.

[55] C. Xia, Z. Zhou, Z. Wang, Y. Yan, and T. Shi, "Computationally efficient multi-step direct predictive torque control for surface-mounted permanent magnet synchronous motor," *IET Electric Power Applications*, vol. 11, no. 5, pp. 805–814, 2017.

[56] J. Zou, W. Xu, X. Yu, Y. Liu, and C. Ye, "Multistep model predictive control with current and voltage constraints for linear induction machine based urban transportation," *IEEE Transactions on Vehicular Technology*, vol. 66, no. 12, pp. 10 817–10 829, 2017.

[57] T. Dorfling, H. du Toit Mouton, T. Geyer, and P. Karamanakos, "Long-horizon finite-control-set model predictive control with nonrecursive sphere decoding on an FPGA," *IEEE Transactions on Power Electronics*, vol. 35, no. 7, pp. 7520–7531, 2020.

[58] A. Ayad, P. Karamanakos, and R. Kennel, "Direct model predictive current control strategy of quasi-z-source inverters," *IEEE Transactions on Power Electronics*, vol. 32, no. 7, pp. 5786–5801, 2017.

[59] R. Baidya, R. P. Aguilera, P. Acuña, S. Vazquez, and H. d. T. Mouton, "Multistep model predictive control for cascaded H-bridge inverters: Formulation and analysis," *IEEE Transactions on Power Electronics*, vol. 33, no. 1, pp. 876–886, 2018.

[60] Y. Luo and C. Liu, "Multi-vector-based model predictive torque control for a six-phase PMSM motor with fixed switching frequency," *IEEE Transactions on Energy Conversion*, vol. 34, no. 3, pp. 1369–1379, 2019.

[61] W. Hua, F. Chen, W. Huang, G. Zhang, W. Wang, and W. Xia, "Multivector-based model predictive control with geometric solution of a five-phase flux-switching permanent magnet motor," *IEEE Transactions on Industrial Electronics*, vol. 67, no. 12, pp. 10 035–10 045, 2020.

[62] Y. Zhang, Y. Peng, and H. Yang, "Performance improvement of two-vectors-based model predictive control of pwm rectifier," *IEEE Transactions on Power Electronics*, vol. 31, no. 8, pp. 6016–6030, 2016.

[63] H. T. Nguyen, E. Kim, I. Kim, H. H. Choi, and J. Jung, "Model predictive control with modulated optimal vector for a three-phase inverter with an lc filter," *IEEE Transactions on Power Electronics*, vol. 33, no. 3, pp. 2690–2703, 2018.

[64] S. Kouro, M. A. Perez, J. Rodriguez, A. M. Llor, and H. A. Young, "Model predictive control: Mpc's role in the evolution of power electronics," *IEEE Industrial Electronics Magazine*, vol. 9, no. 4, pp. 8–21, 2015.

[65] M. Aguirre, S. Kouro, C. A. Rojas, and S. Vazquez, "Enhanced switching frequency control in fcs-mpc for power converters," *IEEE Transactions on Industrial Electronics*, vol. 68, no. 3, pp. 2470–2479, 2021.

[66] P. Karamanakos, A. Ayad, and R. Kennel, "A variable switching point predictive current control strategy for quasi-z-source inverters," *IEEE Transactions on Industry Applications*, vol. 54, no. 2, pp. 1469–1480, 2018.

[67] Y. Zhang, D. Xu, and L. Huang, "Generalized multiple-vector-based model predictive control for PMSM drives," *IEEE Transactions on Industrial Electronics*, vol. 65, no. 12, pp. 9356–9366, 2018.

[68] X. Li, Z. Xue, X. Yan, L. Zhang, W. Ma, and W. Hua, "Low-complexity multi-vector-based model predictive torque control for PMSM with voltage pre-selection," *IEEE Transactions on Power Electronics*, pp. 1–1, 2021.

[69] Z. Zhang, H. Fang, F. Gao, J. Rodríguez, and R. Kennel, "Multiple-vector model predictive power control for grid-tied wind turbine system with enhanced steady-state control performance," *IEEE Transactions on Industrial Electronics*, vol. 64, no. 8, pp. 6287–6298, 2017.

[70] C. Xiong, H. Xu, T. Guan, and P. Zhou, "A constant switching frequency multiple-vector-based model predictive current control of five-phase PMSM with nonsinusoidal back EMF," *IEEE Transactions on Industrial Electronics*, vol. 67, no. 3, pp. 1695–1707, 2020.

[71] Z. Zhou, C. Xia, T. Shi, and Q. Geng, "Model predictive direct duty-cycle control for PMSM drive systems with variable control set," *IEEE Transactions on Industrial Electronics*, vol. 68, no. 4, pp. 2976–2987, 2021.

[72] Y. Wang, X. Wang, W. Xie, F. Wang, M. Dou, R. M. Kennel, R. D. Lorenz, and D. Gerling, "Deadbeat model-predictive torque control with discrete space-vector modulation for pmsm drives," *IEEE Transactions on Industrial Electronics*, vol. 64, no. 5, pp. 3537–3547, 2017.

[73] S.-W. Kang, J.-H. Soh, and R.-Y. Kim, "Symmetrical three-vector-based model predictive control with deadbeat solution for ipmsm in rotating reference frame," *IEEE Transactions on Industrial Electronics*, vol. 67, no. 1, pp. 159–168, 2020.

[74] Y. Yang, H. Wen, M. Fan, L. He, M. Xie, R. Chen, M. Norambuena, and J. Rodríguez, "Multiple-voltage-vector model predictive control with reduced complexity for multilevel inverters," *IEEE Transactions on Transportation Electrification*, vol. 6, no. 1, pp. 105–117, 2020.

[75] Z. Ni, A. Abuelnaga, and M. Narimani, "A novel high-performance predictive control formulation for multilevel inverters," *IEEE Transactions on Power Electronics*, vol. 35, no. 11, pp. 11 533–11 543, 2020.

[76] P. Acuna, C. A. Rojas, R. Baidya, R. P. Aguilera, and J. E. Fletcher, "On the impact of transients on multistep model predictive control for medium-voltage drives," *IEEE Transactions on Power Electronics*, vol. 34, no. 9, pp. 8342–8355, 2019.

[77] S. Boyd and L. Vandenberghe, *Convex Optimization*. Cambridge University Press, 2004.

[78] C. Ma, H. Li, X. Yao, Z. Zhang, and F. De Belie, "An improved model-free predictive current control with advanced current gradient updating mechanism," *IEEE Transactions on Industrial Electronics*, pp. 1–1, 2020.

[79] B. Long, Z. Zhu, W. Yang, K. T. Chong, J. Rodriguez, and J. M. Guerrero, "Gradient descent optimization based parameter identification for FCS-MPC control of LCL-type grid connected converter," *IEEE Transactions on Industrial Electronics*, pp. 1–1, 2021.

[80] S. Richter, T. Geyer, and M. Morari, "Resource-efficient gradient methods for model predictive pulse pattern control on an FPGA," *IEEE Transactions on Control Systems Technology*, vol. 25, no. 3, pp. 828–841, 2017.

[81] S. Richter, S. Mariéthoz, and M. Morari, "High-speed online mpc based on a fast gradient method applied to power converter control," in *Proceedings of the 2010 American Control Conference*, 2010, pp. 4737–4743.

[82] S. Richter, C. N. Jones, and M. Morari, "Computational complexity certification for real-time mpc with input constraints based on the fast gradient method," *IEEE Transactions on Automatic Control*, vol. 57, no. 6, pp. 1391–1403, 2012.

[83] S. Almér, S. Mariéthoz, and M. Morari, "Real-time solution of mixed-integer quadratic programs for hybrid control of power converters," in *2012 IEEE 51st IEEE Conference on Decision and Control (CDC)*, 2012, pp. 1948–1953.

[84] J. L. Jerez, P. J. Goulart, S. Richter, G. A. Constantinides, E. C. Kerrigan, and M. Morari, "Embedded predictive control on an fpga using the fast gradient method," in *2013 European Control Conference (ECC)*, 2013, pp. 3614–3620.

[85] S. Boyd, E. Busseti, S. Diamond, R. N. Kahn, K. Koh, P. Nystrup, and J. Speth, *Multi-Period Trading via Convex Optimization*, 2017.

[86] Y. Zhang, Bo Xia, and H. Yang, "A novel three-vectors-based model predictive flux control of induction motor drives," in *2016 IEEE 8th International Power Electronics and Motion Control Conference (IPEMC-ECCE Asia)*, 2016, pp. 367–373.

[87] H. Yang, Y. Zhang, P. D. Walker, N. Zhang, and B. Xia, "A method to start rotating induction motor based on speed sensorless model-predictive control," *IEEE Transactions on Energy Conversion*, vol. 32, no. 1, pp. 359–368, 2017.

[88] H. T. Nguyen and J.-W. Jung, "Finite control set model predictive control to guarantee stability and robustness for surface-mounted pm synchronous motors," *IEEE Transactions on Industrial Electronics*, vol. 65, no. 11, pp. 8510–8519, 2018.

[89] F. Tinazzi, P. G. Carlet, S. Bolognani, and M. Zigliotto, "Motor parameter-free predictive current control of synchronous motors by recursive least-square self-commissioning model," *IEEE Transactions on Industrial Electronics*, vol. 67, no. 11, pp. 9093–9100, 2020.

[90] P. Karamanakos, T. Geyer, and R. Kennel, "A computationally efficient model predictive control strategy for linear systems with integer inputs," *IEEE Transactions on Control Systems Technology*, vol. 24, no. 4, pp. 1463–1471, 2016.

[91] F. Wang, Z. Zhang, S. A. Davari, R. Fotouhi, D. Arab Khaburi, J. Rodrguez, and R. Kennel, "An encoderless predictive torque control for an induction machine with a revised prediction model and efosmo," *IEEE Transactions on Industrial Electronics*, vol. 61, no. 12, pp. 6635–6644, 2014.

[92] W. Sun, Y. Yu, G. Wang, B. Li, and D. Xu, "Design method of adaptive full order observer with or without estimated flux error in speed estimation algorithm," *IEEE Transactions on Power Electronics*, vol. 31, no. 3, pp. 2609–2626, 2016.

[93] D. Wang, K. Lu, and P. O. Rasmussen, "Improved closed-loop flux observer based sensorless control against system oscillation for synchronous reluctance machine drives," *IEEE Transactions on Power Electronics*, vol. 34, no. 5, pp. 4593–4602, 2019.

[94] M. Habibullah and D. D. Lu, "A speed-sensorless fs-ptc of induction motors using extended kalman filters," *IEEE Transactions on Industrial Electronics*, vol. 62, no. 11, pp. 6765–6778, 2015.

[95] F. Wang, Z. Chen, P. Stolze, J. Stumper, J. Rodrguez, and R. Kennel, "Encoderless finite-state predictive torque control for induction machine with a compensated mras," *IEEE Transactions on Industrial Informatics*, vol. 10, no. 2, pp. 1097–1106, 2014.

[96] J. Yang, W. Tang, G. Zhang, Y. Sun, S. Ademi, F. Blaabjerg, and Q. Zhu, "Sensorless control of brushless doubly fed induction machine using a control winding current mras observer," *IEEE Transactions on Industrial Electronics*, vol. 66, no. 1, pp. 728–738, 2019.

[97] P. Cao, X. Zhang, and S. Yang, "A unified-model-based analysis of mras for online rotor time constant estimation in an induction motor drive," *IEEE Transactions on Industrial Electronics*, vol. 64, no. 6, pp. 4361–4371, 2017.

[98] H. Xie, Q. Xun, Y. Tang, F. Wang, J. Rodríguez, and R. Kennel, "Robust parallel predictive torque control with model reference adaptive estimator for im drives," in *2020 International Conference on Electrical Machines (ICEM)*, vol. 1, 2020, pp. 1219–1224.

[99] L. Yan, F. Wang, P. Tao, and K. Zuo, "Robust predictive torque control of permanent magnet synchronous machine using discrete hybrid prediction model," *IEEE Transactions on Energy Conversion*, pp. 1–1, 2020.

[100] G. Wu, S. Huang, Q. Wu, C. Zhang, F. Rong, and Y. Hu, "Predictive torque and stator flux control for n*3-phase pmsm drives with parameter robustness improvement," *IEEE Transactions on Power Electronics*, vol. 36, no. 2, pp. 1970–1983, 2021.

[101] J. Chen and J. Huang, "Stable simultaneous stator and rotor resistances identification for speed sensorless im drives: Review and new results," *IEEE Transactions on Power Electronics*, vol. 33, no. 10, pp. 8695–8709, 2018.

[102] ——, "Alternative solution regarding problems of adaptive observer compensating parameters uncertainties for sensorless induction motor drives," *IEEE Transactions on Industrial Electronics*, vol. 67, no. 7, pp. 5879–5888, 2020.